# Quantum systems with balanced gain and loss, signatures of branch points, and dissociation effects

Habilitationsschrift
zur Erlangung der Lehrbefugnis
für das Fach Theoretische Physik
an der Universität Stuttgart

Vorgelegt von

Holger Cartarius

aus Böblingen

1. Institut für Theoretische Physik der Universität Stuttgart

2014

# Abstract

Gain and loss to the wave function of quantum mechanics can in a convenient way be modelled by effective non-Hermitian Hamiltonians. Imaginary contributions to the potential introduce source and drain terms for the probability amplitude. A special class of non-Hermitian Hamiltonians are those which possess a parity-time symmetry. In spite of their non-Hermiticity these Hamiltonians allow for real energy eigenvalues, i.e. the existence of stationary states in the presence of balanced gain and loss. This effect has been identified theoretically in a large number of quantum systems. Its existence has also been proved experimentally in coupled optical wave guides. The wave guides are, however, only optical analogues of quantum systems.

In the first part of this thesis it is shown from the theoretical side that Bose-Einstein condensates in a double-well setup are an ideal candidate for a first experimental realisation of a genuine quantum system with parity-time symmetry. When particles are removed from one well and coherently injected into the other the external potential is parity-time symmetric. To investigate the system the underlying time-independent and time-dependent Gross-Pitaevskii equations are solved numerically. It turns out that a subtle interplay between the nonlinearity of the Gross-Pitaevskii equation and the gain-loss effect leads to a complicated dynamics of the condensate wave function. However, the most important result is the existence of stationary states that are sufficiently stable to be observable in an experiment. Two suggestions for experimental realisations are presented. They are based on the idea of embedding the non-Hermitian parity-time-symmetric system into a larger structure described by a Hermitian Hamiltonian.

A further effect of non-Hermitian Hamiltonians are so-called exceptional points, at which two resonances coalesce such that both their eigenvalues and wave functions become identical. It is shown that an exceptional point can unambiguously be identified by a characteristic non-exponential decay of the resonances. With numerically exact calculations for the hydrogen atom in crossed electric and magnetic fields this effect is verified in an experimentally accessible quantum system.

The second part of the thesis is devoted to semiclassical Gaussian approximations to the Boltzmann operator, which have become an important tool for the investigation of thermodynamic properties of clusters of atoms at low temperatures. A numerically cheap frozen Gaussian approximation to the imaginary time propagator with a width matrix especially suited for the dynamics of clusters is developed. It is applied to the cases of $Ar_3$ and $Ar_6$. For these clusters classical-like transitions in one step from a bounded moiety to free particles are found for increasing temperatures. Additionally, the structure of the $Ar_6$ cluster is studied in the bound configuration and during the dissociation. Quantum

effects, i.e. differences with the purely classical case, manifest themselves in the low-temperature behaviour of the mean energy and specific heat as well as in a slight shift of the transition temperature. A first-order correction to the semiclassical propagator is used to improve the results of the calculation for $Ar_3$, and it is shown how the correction can be used to objectively assess the validity of the frozen Gaussian approximation.

# Inhaltsangabe

Gewinn- und Verlustbeiträge zur quantenmechanischen Wellenfunktion lassen sich sehr elegant durch effektive nichthermitesche Hamiltonoperatoren modellieren. Imaginäre Potentialbeiträge erzeugen Quellen und Senken der Wahrscheinlichkeitsdichte. Hamiltonoperatoren mit einer Paritäts-Zeit-Symmetrie bilden eine besondere Klasse nichthermitescher Operatoren. Trotz ihrer Nichthermitizität erlauben sie das Auftreten reeller Energieeigenwerte, d.h. die Existenz stationärer Zustände in der Gegenwart ausgeglichener Gewinn- und Verlustbeiträge. Dieser Effekt wurde in einer großen Anzahl von Quantensystemen theoretisch gefunden. Seine Existenz wurde darüber hinaus experimentell in gekoppelten optischen Wellenleitern nachgewiesen. Die Wellenleiter stellen jedoch nur ein optisches Analogon eines Quantensystems dar.

Im ersten Teil dieser Habilitationsschrift wird von theoretischer Seite gezeigt, dass Bose-Einstein-Kondensate in einer Doppelmulde ein idealer Kandidat für eine erste experimentelle Umsetzung eines originären Quantensystems mit Paritäts-Zeit-Symmetrie sind. Wenn Teilchen aus einer Mulde entfernt und kohärent in die andere eingekoppelt werden, besitzt das System eine Paritäts-Zeit-Symmetrie. Um es zu untersuchen, werden die zeitunabhängige und die zeitabhängige Gross-Pitaevskii-Gleichung numerisch gelöst. Dabei stellt sich heraus, dass das Wechselspiel zwischen der Nichtlinearität der Gross-Pitaevskii-Gleichung und dem Gewinn- und Verlustbeitrag zu einer komplizierten Dynamik der Kondensatwellenfunktion führt. Das wichtigste Ergebnis ist jedoch der Nachweis stationärer Zustände, die hinreichend stabil sind, um in einem Experiment beobachtbar zu sein. Es werden zwei Vorschläge für experimentelle Umsetzungen gegeben. Sie beruhen auf der Idee, das nichthermitesche System mit Paritäts-Zeit-Symmetrie in eine größere Struktur einzubetten, die durch einen hermiteschen Hamiltonoperator beschrieben wird.

Ein weiterer Effekt nichthermitescher Hamiltonoperatoren sind sogenannte exzeptionelle Punkte, an denen zwei Resonanzen so zusammenfallen, dass sie identische Eigenwerte und Wellenfunktionen aufweisen. Es wird gezeigt, dass ein exzeptioneller Punkt eindeutig durch einen charakteristischen nichtexponentiellen Zerfall der Resonanzen identifiziert werden kann. Mit numerisch exakten Rechnungen für das Wasserstoffatom in gekreuzten elektrischen und magnetischen Feldern wird dieser Effekt in einem experimentell zugänglichen Quantensystem nachgewiesen.

Der zweite Teil der Habilitationsschrift widmet sich semiklassischen gaußschen Näherungen des Boltzmannoperators, die zu einem wichtigen Hilfsmittel für die Untersuchung thermodynamischer Eigenschaften von Clustern aus Atomen bei niedrigen Temperaturen geworden sind. Eine numerisch günstige gaußsche Näherung des Imaginärzeitpropaga-

tors mit einer festen, besonders an die Dynamik von Clustern angepassten Breitenmatrix wird entwickelt. Die Methode wird auf $Ar_3$- und $Ar_6$-Cluster angewandt. Für diese Cluster werden bei ansteigender Temperatur nahezu klassische Übergänge in einem Schritt von einem festen Verbund zu freien Atomen gefunden. Zusätzlich wird die Struktur von $Ar_6$ im Clusterverbund und während der Dissoziation untersucht. Quanteneffekte, d.h. Unterschiede zum rein klassischen Fall, drücken sich im Niedertemperaturverhalten der mittleren Energie und der Wärmekapazität sowie in einer leichten Verschiebung der Dissoziationstemperatur aus. Eine Korrektur erster Ordnung zum semiklassischen gaußschen Propagator wird verwendet, um die Ergebnisse der Rechnungen für $Ar_3$ zu verbessern. Es wird darüber hinaus gezeigt, dass die Korrektur zur objektiven Beurteilung der Gültigkeit der gaußschen Näherung verwendet werden kann.

# Contents

# 1. Introduction

## 1.1. Motivation

Very often in quantum mechanics small isolated systems, i.e. those with a low number of degrees of freedom, are investigated. However, all systems are always in contact with an environment, which often cannot be ignored or even defines the dominating influence on the system, e.g. gain and loss effects. In many cases a very elegant way of investigating open quantum systems with reasonable effort, in particular to avoid expensive time-dependent calculations, is made possible by non-Hermitian Hamiltonians. In his book on non-Hermitian quantum mechanics Moiseyev [1] lists four main fields, in which non-Hermitian operators play a significant role, viz. the use of complex refractive indices in optics, the appearance of parity-time symmetry, simplification of numerical calculations, and cases of statistical mechanics in which the concepts of quantum mechanics are used. Two approaches will be the topic of this thesis. Firstly, gain and loss of the probability amplitude, i.e. a growth or decay of the wave function can be modelled by imaginary contributions to a non-Hermitian parity-time symmetric potential. Secondly, resonances, i.e. decaying but long-lived states can be studied with non-Hermitian Hamiltonians within the framework of the time-independent Schrödinger equation although the decay is a time-dependent process.

A special class of non-Hermitian Hamiltonians with complex potentials introducing explicitly gain and loss effects will cover the largest part of this thesis. Those non-Hermitian quantum systems which possess a parity-time symmetry, i.e. which commute with the parity-time operator, $[\mathcal{PT}, H] = 0$, have gained an increasing attention over the last years [2–13]. Bender and Boettcher [4] showed that these Hamiltonians exhibit remarkable properties. In particular, they found that completely real eigenvalue spectra are possible for specific ranges of the non-Hermitian contribution's strength. In contrast to solutions with complex eigenvalues, which incorporate a decay or growth of the wave function, real eigenvalue solutions represent true stationary states existing in spite of the gain and loss effects.

The effects of $\mathcal{PT}$-symmetric quantum systems are not only of theoretical nature. Recently first experimental observations of $\mathcal{PT}$ symmetry became possible in optical systems [2, 3]. Here, the analogy of Maxwell's equations with the Schrödinger equation in specific setups has been used to simulate $\mathcal{PT}$-symmetric quantum mechanics. Several suggestions for the realisation of $\mathcal{PT}$-symmetric optical systems have been made [6, 8, 10, 14–17] and the experimental realisation has been achieved by using a passive system

with only a loss term on one side [2] and by actively inducing gain and loss in a dual wave guide [3].

Despite this triumphal success of proving the existence of $\mathcal{PT}$ symmetry and its effects in optics the experimental observation in a genuine quantum system is still missing. The goal of the first part of this thesis is to present a true quantum system instead of an optical analogue with a realistic $\mathcal{PT}$-symmetric gain-loss effect that is potentially accessible in an experiment. It is the purpose of this part to demonstrate that the experimental realisation of $\mathcal{PT}$ symmetry in Bose-Einstein condensates trapped in a double-well potential [18] as suggested by Klaiman et al. [8] is a very promising approach. The $\mathcal{PT}$ symmetry is implemented by adding atoms coherently to the condensed phase in one well and by simultaneously removing them from the other.

Bose-Einstein condensates differ in one important aspect from many $\mathcal{PT}$-symmetric quantum systems studied earlier [4, 7, 11, 12, 19, 20]. At sufficiently low temperatures the condensate of weakly interacting Bosons is well described by the mean-field approximation of the Gross-Pitaevskii equation [21, 22]. In contrast to the Schrödinger equation the Gross-Pitaevskii equation is nonlinear. This means that even if an effective complex $\mathcal{PT}$-symmetric potential can be created for a Bose-Einstein condensate one still has to pay attention to the Gross-Pitaevskii nonlinearity $g|\psi|^2$ originating from the contact interaction of the atoms. Because of this nonlinearity choosing a $\mathcal{PT}$-symmetric potential alone does not guarantee the Hamiltonian to be $\mathcal{PT}$ symmetric, but the square modulus $|\psi|^2$ of the wave function must be an even function of the spatial coordinates as well. Therefore, it is not a priori granted that the effects of $\mathcal{PT}$ symmetry can be observed in such nonlinear systems. However, the studies of the mean-field limit of a Bose-Hubbard dimer [9, 23, 24] as well as optical systems with a Kerr nonlinearity [25–33] showed typical properties expected in the presence of $\mathcal{PT}$-symmetric potentials.

In this thesis it will be shown that, indeed, $\mathcal{PT}$-symmetric solutions with real eigenvalues can be found in realistic parameter ranges for an experimental observation. To do so, the Gross-Pitaevskii equation for a Bose-Einstein condensate in a $\mathcal{PT}$-symmetric double-well potential will be solved. This will be done on the level of a simple model in which idealised infinitesimally small delta traps in one dimension are studied as well as in a fully three-dimensional spatially extended structure. We will see that the nonlinearity fortunately does not destroy the stationary real eigenvalue solutions in $\mathcal{PT}$-symmetric potentials. However, it will introduce new features such as additional branch points and solutions which under variation of the gain-loss effect suddenly merge and vanish completely, or solutions emerging out of nowhere. A careful analysis in an appropriate analytic extension of the Gross-Pitaevskii equation will uncover the nature of these branch points. The $\mathcal{PT}$-symmetric eigenstates will turn out to possess nontrivial stability properties. Due to a subtle interplay between the nonlinearity and the non-Hermitian gain-loss contribution in the potential a stability change of one of these eigenstates sets in under variation of one of the system's parameters, and can, as will be shown, be related to the branch points. Furthermore, full time evolutions of condensate wave functions in the double well will show that the dynamical properties are very rich. The gain

and loss terms in the potential introduce instabilities, which allow for a destruction of the condensate by a fast growing wave function due to the gain term in the potential. However, stable regimes of the physical parameters are found. It is even possible to show that there are experimentally feasible ways to create the balanced gain and loss of a $\mathcal{PT}$-symmetric potential for a Bose-Einstein condensate. Two different possibilities for experimental realisations will be given. One is based on a larger closed system described by a Hermitian Hamiltonian, of which the $\mathcal{PT}$-symmetric double well will be a subsystem. The second possibility assumes that a directed flow of atoms coming from a reservoir can be incoupled to one well and atoms can be outcoupled from the other with the same approach.

The applicability of non-Hermitian quantum mechanics is by far not restricted to the case of balanced gain and loss. Resonances are a typical example, in which non-Hermitian Hamiltonians are very useful. By appropriate methods, e.g. the complex scaling approach [1, 34, 35], resonances can be uncovered in a time-independent calculation as complex eigenvalues of the stationary Schrödinger equation. Since resonances are decaying states this can be understood as a system with only loss. It is well known that resonances show characteristic effects not observable in Hermitian quantum systems describing bound states. Among these effects are so-called exceptional points [1, 36, 37], isolated points in a two-dimensional parameter space, at which two or even more eigenstates coalesce. Exceptional points have shown to exhibit distinct features and are able to influence a whole region of the parameter space in their vicinity. They lead to unusual results such as the permutation of eigenstates for a closed adiabatic loop in the parameter space or a special geometric phase [36]. The experimental verification of exceptional points was achieved in microwave cavities [38, 39].

As in the case of $\mathcal{PT}$ symmetry the experimental observation of an exceptional point in a true quantum system has still not been achieved so far. However, there is a large number of quantum systems in which theoretical studies predict their existence, e.g. atomic [40, 41] or molecular [42] systems, the scattering of particles at potential barriers [43], atom waves [44, 45], or non-Hermitian Bose-Hubbard models [9, 23, 24]. A suggestion, how an exceptional point could be detected unambiguously in atomic resonance spectra, will be given in this thesis. Resonances are expected to decay purely exponentially. However, it has been shown theoretically in several examples [24, 46–50] that this is not the case exactly at an exceptional point. The survival probability $S(t) = |\langle\psi(0)|\psi(t)\rangle|^2$ of an adequate superposition $\psi$ of these states decays exactly as $|1 - at|^2 \mathrm{e}^{-\Gamma_{\mathrm{EP}} t/\hbar}$, where $\Gamma_{\mathrm{EP}}$ is associated with the decay rate at the exceptional point and $a$ is a complex constant depending solely on the initial wave packet. The origin of this behaviour will be shown. Numerically obtained resonances of the hydrogen atom in crossed electric and magnetic fields will reveal that the unique decay signal will be observable in a realistic physical situation even if the parameter values are not exactly those of the exceptional point. This may open the possibility for a first experimental detection of exceptional points in a quantum system.

The topic of the second part of this thesis will be a different approach to systems

that possess a connection between bound and unbound states. The focus will be on a larger number of degrees of freedom which explicitly have to be taken into account in a calculation. An environment will only appear in terms of a given temperature that deposits some energy into the system. For the weak van der Waals interaction between rare gas atoms the thermal energy corresponding to a few Kelvin already suffices to have a dramatic impact. A dissociation of a bound cluster to free atoms can occur. This effect shall be studied.

Rare gas atomic clusters are a topic of ongoing research due to the rich variety of their thermodynamic properties in relatively simple systems. In particular, structural transformations, i.e. a change from one packing of the atoms to another with increasing energy, or phase transitions from a solid-like behaviour to a liquid-like have been studied extensively [51–57]. Of interest for an investigation of such transformations are thermodynamic mean values. Simple derivatives of the partition function such as the mean energy or the specific heat will provide important information. Any structural transformation will leave signals when these quantities are measured or calculated as functions of the temperature. Typically the mean energy exhibits a step and the specific heat shows a peak at the occurrence of a phase transition or transformation. Additional information may be gained with direct access to the structure.

Since the effects appear on an atomic scale and at low temperatures accurate quantum mechanical computation methods are essential. The Boltzmann operator at inverse temperature $\beta$, $K = \exp(-\beta H)$, (due to its form also called imaginary time propagator) is the most important quantity. Its trace yields the partition function $Z(\beta)$, and the thermal averages of every other observable follow from $\langle O \rangle_\beta = \mathrm{Tr}(K(\beta)O)/Z(\beta)$. However, precise calculations for multi-dimensional systems are still a challenge for today's numerical possibilities. For example, path-integral Monte Carlo methods [58–60] have been used to investigate rare gas clusters. For low temperatures they become already too expensive for a few dozen atoms, and efficient but sufficiently accurate approximations are required. These approximations have to reproduce quantum effects reliably since they will be of eminent importance at low temperatures. Still many questions are open. For example $Ne_{13}$ and $Ne_{38}$ [54, 56] might exhibit novel low temperature quantum effects, such as liquid-like zero temperature structures of $Ne_{38}$ as compared to a solid-like structure predicted from classical mechanics [61].

In this thesis one of these approximations will be introduced, extended to multi-dimensional systems, and then applied to argon clusters. The semiclassical approximation will be based on a frozen Gaussian propagator, i.e. a Gaussian wave function of which the width matrix in the exponent is fixed for all imaginary times (or temperatures) will be propagated. It is applied to two argon clusters of different size, viz. $Ar_3$ and $Ar_6$. They are simple and can be used to instructively present the principles of the method. However, despite their simplicity there are still open questions and even the trimer with only three atoms involved has attracted the interest of theoretical investigations for a long time [62–66]. Path-integral Monte Carlo calculations of the system [57] indicate a dissociation to three free atoms but cannot distinguish this process from

structural changes because the numerics suffers strongly from noise. With the semiclassical method developed in this thesis it will be possible to answer this question. The method will also uncover the differences between quantum and classical calculations, and thus assess the importance of quantum effects for the dissociation. A similar study will be done for the more complicated $Ar_6$ cluster. In contrast to the trimer, the specific heat and mean energy will not provide enough information to understand the whole structure of the cluster. An extension to the semiclassical frozen Gaussian method will be developed. It includes thermal mean values of the distances between all atoms.

The frozen Gaussian method is able to provide numerically well converged results with reasonable effort, and thus might be ideal for the study of thermodynamic properties of clusters. In spite of these advantages one has to be aware that they are approximations and not necessarily sufficiently accurate when quantum effects are expected to be strong [67]. Thus, the quality of the frozen Gaussian method will be evaluated in this thesis. It will be compared to numerically exact methods and the more flexible thawed Gaussian propagator, for which the Gaussian width matrix is allowed to change with (imaginary) time. For high-dimensional systems, when only approximations are feasible, one needs, however, an intrinsic method to estimate the approximation's quality. This can be achieved with the time-dependent perturbation approach developed by Pollak and coworkers [68, 69]. It connects the Gaussian semiclassical approximations with exact quantum mechanics. Its first-order correction helps to estimate the quality of the results and provides objective access to the validity of the Gaussian approximations. The first-order correction to the frozen Gaussian propagator will be developed for multidimensional systems and then be applied to the argon trimer. It will be possible to state that the frozen Gaussian method is sufficiently accurate for the dissociation processes of the clusters studied in this thesis.

## 1.2. Outline

Chapter 2 starts with a brief review of the basic properties of $\mathcal{PT}$-symmetric quantum systems and typical effects connected with them. In particular, the chapter will give a short introduction to the peculiarities of nonlinear Hamiltonians with a $\mathcal{PT}$-symmetric external potential. In chapter 3 the main topic of the first part of the thesis will be presented on the basis of a simple model, viz. the $\mathcal{PT}$-symmetric double-delta potential, and a fully three-dimensional double well. The time-independent Gross-Pitaevskii equation will be solved for both potentials and the eigenstates will be studied in dependence of the system's parameters. To do so, the strengths of the gain-loss effect and the nonlinearity will be varied. This will uncover surprising branch points not known from linear $\mathcal{PT}$-symmetric quantum systems. These branch points will be studied in more detail in chapter 4. For this purpose an appropriate analytic extension will be applied to the Gross-Pitaevskii equation, and additional states, not available without the extension, will complete the mathematical understanding of the branch points. The stability

of the stationary states of a condensate in a $\mathcal{PT}$-symmetric double-well potential will be investigated in chapter 5. This will reveal complicated structures following from the interplay between the nonlinearity and the gain-loss effect, which will also have a strong impact on the full dynamics, i.e. the simulation of a condensate with the time-dependent Gross-Pitaevskii equation in chapter 6. Two possibilities for an experimental realisation of a Bose-Einstein condensate in a $\mathcal{PT}$-symmetric double well will be evaluated in chapter 7. A switch to a linear quantum system, viz. the hydrogen atom in crossed electric and magnetic fields, is done in chapter 8. The possibility to detect exceptional points in the resonances of the system with their unique decay behaviour upon coalescence of two resonances will be demonstrated.

The second part of the thesis starts with an introduction of the frozen Gaussian imaginary time propagator and its application to the argon trimer in chapter 9. It will be shown how the method can be applied to multi-dimensional systems and reveal new information about the dissociation process of the cluster. In chapter 10 the method will be extended to a larger system, viz. the $Ar_6$ cluster and it will be shown how structural information can be accessed with low numerical costs within the semiclassical approximation. The first-order correction to the frozen Gaussian propagator will be added in chapter 11 and the quality of the approximation for the argon trimer will be evaluated.

# Part I.

# Quantum systems with non-Hermitian Hamiltonians modelling gain and loss

# 2. Balanced gain and loss in quantum systems

Before tackling the central question of the first part of the thesis, viz. the possibility of realising a $\mathcal{PT}$-symmetric quantum system with a Bose-Einstein condensate in a double well with gain and loss, we summarise basic expressions required for the following chapters. We first introduce gain and loss in Hamiltonians in section 2.1. This will be done with the help of complex potentials as explained in section 2.1.1. The resulting Hamiltonians will be non-Hermitian and will allow for the appearance of exceptional points, which are briefly reviewed in section 2.1.2. The basic idea, how the complex potentials are used to describe gain and loss for a Bose-Einstein condensate in the mean-field description of the Gross-Pitaevskii equation, is mentioned in section 2.1.3. Then the case of balanced gain and loss is introduced in section 2.2. To do so, the concept of $\mathcal{PT}$ symmetry in quantum systems is discussed in section 2.2.1 and then extended to nonlinear quantum systems in section 2.2.2.

## 2.1. Hamiltonians with gain and loss

### 2.1.1. Complex potentials

One application of non-Hermitian operators in quantum mechanics is the introduction of gain or loss for the probability amplitude. For example, complex potentials are used to implement reflection-free absorbers at boundaries of a finite fraction of the coordinate space included in a simulation in the case that in the true physical example no boundaries are present and outgoing waves may not be reflected [1]. However, they can also directly be exploited to simulate a growth or decay of a wave function in a certain region of the position space, i.e. the part which is considered to be the system of interest.

For a simple illustration let us consider a physical system with a time-independent Hermitian Hamiltonian $H$ of which we know the eigenstates $\phi_n(x)$ with energies $E_n$. We add a constant imaginary contribution $\mathrm{i}\Gamma$ to the potential and write down the time-dependent Schrödinger equation

$$(H + \mathrm{i}\Gamma)\,\psi(x,t) = \mathrm{i}\hbar\frac{\partial}{\partial t}\psi(x,t)\;. \tag{2.1a}$$

Obviously the states

$$\psi_n(x,t) = \phi_n(x)\mathrm{e}^{-\mathrm{i}(E_n+\mathrm{i}\Gamma)t/\hbar} = \phi_n(x)\mathrm{e}^{-\mathrm{i}E_nt/\hbar}\mathrm{e}^{\Gamma t/\hbar} \tag{2.1b}$$

with the square moduli

$$|\psi_n(x,t)|^2 = |\phi_n(x)|^2 \mathrm{e}^{2\Gamma t/\hbar} \tag{2.1c}$$

solve the Schrödinger equation. In this description a negative value of $\Gamma$ has exactly the form known from the decay of resonances. The probability amplitude shrinks exponentially in time. The interpretation is that the particle described by the wave function leaves the region in space in which the resonance is supposed to be localised. A positive value of $\Gamma$ describes exactly the opposite case, i.e. an exponential growth of the wave function in the spatial region of interest. In this case the interpretation is that the particle enters the region or, in other words, the probability to find the particle in the selected fraction of the position space is growing.

The meaning of the imaginary potentials can also be seen when the probability flux following from the time-derivative of the wave function's square modulus is calculated,

$$\frac{\mathrm{d}}{\mathrm{d}t}|\psi|^2 = \frac{\mathrm{i}}{\hbar}\left[\psi(H\psi)^* - \psi^*(H\psi)\right] \ . \tag{2.2}$$

With the assumption that a complex potential $V(\boldsymbol{r})$ appears in the Hamiltonian the result of this equation is an extended continuity equation,

$$\frac{\partial \rho}{\partial t} = 2\,\mathrm{Im}(V(\boldsymbol{r}))\rho - \mathrm{div}\boldsymbol{j} \ , \tag{2.3}$$

with $\rho = |\psi|^2$ and the usual probability flux density $\boldsymbol{j} = \mathrm{i}\hbar(\psi\nabla\psi^* - \psi^*\nabla\psi)/2m$. In this formulation the meaning of the terms source and drain becomes evident.

The use of imaginary potential contribution can always only be an effective description of the loss or gain for the wave function's amplitude. In every specific situation one has to be aware of the physical process that leads to a movement of the probability amplitude into or away from the system described by the non-Hermitian potential. A typical situation in which this description is applicable is a "large" closed system, of which we only consider a subsystem in all equations. An example to which we will come back in detail in chapter 7 is shown in figure 2.1. The "large" system is depicted in figure 2.1 (a). It consists of four wells created by the potential $V_{\mathrm{H}}(x)$. A possible distribution of the wave function is also shown. If we now are only interested in the inner part, i.e. the inner two wells, the smaller system might be described by the potential $V_{\mathrm{NH}}(x)$ shown in figure 2.1 (b). The dynamics in the larger system $V_{\mathrm{H}}(x)$ clearly allows for a shift of the probability distribution from the outer to the inner wells and the other way round. If one only looks at the wave function in the inner two wells, one notices an increase or a decrease of its norm within the subsystem. The smaller system, if only described by the real part shown in the figure, is not able to describe this shift since a wave function in the outer two wells does not exist in its description. However, if we include imaginary potential contributions, the gain and loss of the probability amplitude in the inner two wells can be retrieved. All descriptions with complex potentials in this thesis will be based on this relation. In every case the system will be considered to be a substructure of a larger closed physical system, which should be described by a Hermitian Hamiltonian.

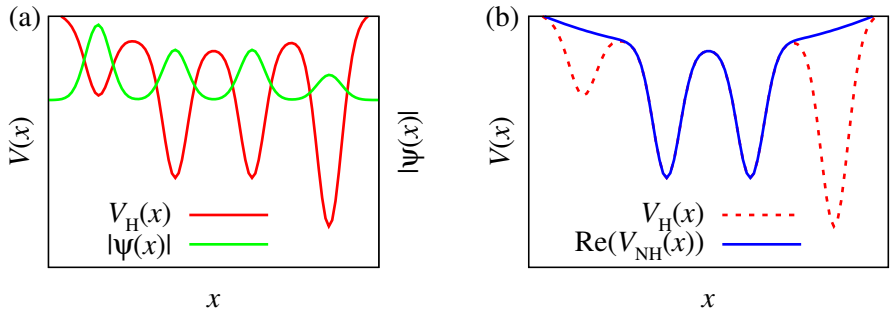


Figure 2.1.: (a) Potential $V_H(x)$ (red) of a "large" Hermitian system consisting of four wells with a possible probability distribution of the wave function (green). (b) Real part of a potential $V_{\mathrm{NH}}(x)$ of a "small" system (blue) embedded into the larger potential $V_{\mathrm{H}}(x)$.

### 2.1.2. Exceptional points

Always when non-Hermitian Hamiltonians are considered the possibility for exceptional points arises. Exceptional points are single points in an (at least) two-dimensional parameter space, at which two or even more eigenstates coalesce [1, 36, 37]. The term coalesce means that the eigenvalues *and* the eigenvectors become identical. This effect is not very common in quantum mechanics since a coalescence of two eigenstates of a Hermitian operator is impossible. However, in the case of non-Hermitian Hamiltonians exceptional points turn out to appear in a broad variety of systems. The most well known examples are found in quantum systems [9, 23, 24, 40–45, 70–72], and optics [8, 47, 73]. The experimental verification of their existence was achieved in microwave cavities [38, 39] and electronic circuits [74]. A detailed review can be found in reference [75].

The simplest explanation of some elementary properties of exceptional points can be given with an example. The non-Hermitian $2 \times 2$ matrix

$$\boldsymbol{M}(\kappa) = \begin{pmatrix} 1 & \kappa \\ \kappa & -1 \end{pmatrix} \tag{2.4}$$

depends on a single complex parameter $\kappa$, of which the real and imaginary parts span the two-dimensional parameter space required to adjust the exceptional points of the matrix. The eigenvalues

$$\lambda_1 = \sqrt{1+\kappa^2}\,, \tag{2.5a}$$

$$\lambda_2 = -\sqrt{1+\kappa^2} \tag{2.5b}$$

become obviously identical at the values $\kappa_1 = \mathrm{i}$ and $\kappa_2 = -\mathrm{i}$. The decisive fact is that $\lambda_1$ and $\lambda_2$ are two branches of the same analytic function and $\kappa_1$ and $\kappa_2$ are their two

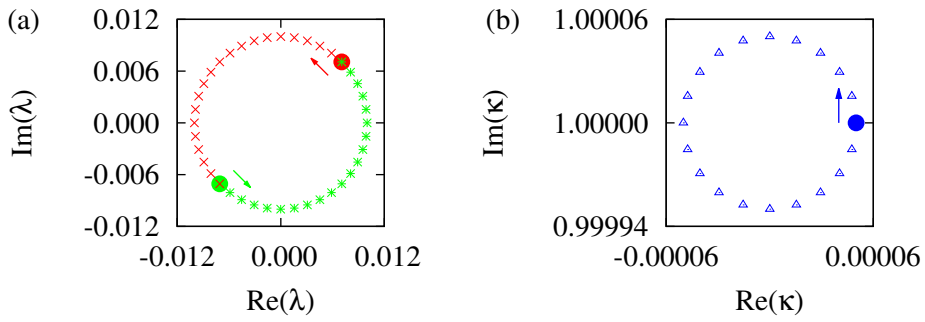


Figure 2.2.: (a) The eigenvalues $\lambda_1$ (red crosses) and $\lambda_2$ (green stars) are permuted and only perform together a closed loop in the complex plane for the closed parameter space circle shown in (b). The centre of the parameter space circle in (b) is the exceptional point $\kappa_1 = \mathrm{i}$. The filled circles indicate the initial points for the parameter and the eigenvalues, and the arrows mark the direction of progression.

branch points. In this case also the eigenvectors pass through a branch point singularity [37], as can be seen in the eigenvectors of the matrix (2.4), viz.

$$\boldsymbol{x}_1(\kappa) = \begin{pmatrix} -\kappa \\ 1 - \sqrt{1+\kappa^2} \end{pmatrix} , \tag{2.6a}$$

$$\boldsymbol{x}_2(\kappa) = \begin{pmatrix} -\kappa \\ 1 + \sqrt{1+\kappa^2} \end{pmatrix} . \tag{2.6b}$$

A very common method to detect exceptional points is to exploit the permutation of the eigenvalues for a closed loop in the parameter space, which is a consequence of encircling the branch point singularity. If the eigenvalues are traced continuously, they switch during their path from one Riemann surface to another, and thus end their path at the initial point of the other eigenvalue. This fact can be visualised nicely in the simple matrix model (2.4). Figure 2.2 (a) shows the eigenvalues $\lambda_1$ and $\lambda_2$ for the parameter values in figure 2.2 (b), which are located on a circle around the exceptional point $\kappa_1 = \mathrm{i}$. It is very clear that a continuous connecting of the points leads to a permutation of $\lambda_1$ and $\lambda_2$, i.e. each of the eigenvalues does not return to its starting point although the parameter space circle is closed. We will see that exceptional points are also an essential property of the systems with balanced loss and gain. The permutation behaviour will be an important tool to verify their presence.

The case briefly discussed in the example (2.4) is a so-called second-order exceptional point because two eigenvalues merge in a square root branch point. We denote it EP2. Higher orders are possible and have been discussed in models of physical systems [76–78]. We will in particular be confronted with a third-order exceptional point or EP3, i.e. a point in which three eigenstates coalesce.

An EP3 is typically connected with a cubic root branch point and the signal similar to that in figure 2.2 is a permutation of all three eigenvalues, i.e. eigenvalue 1 ends at the starting point of eigenvalue 2, eigenvalue 2 at the starting point of eigenvalue 3, and the third eigenvalue closes the path. However, there is also the possibility that a third-order exceptional point behaves under certain parameter variations like a second-order exceptional point. This can be understood with a very simple example. Let us assume that we calculated in a three-dimensional matrix model the characteristic polynomial

$$\lambda^3 + a\lambda^2 + b\lambda + c = 0 \tag{2.7a}$$

for the eigenvalues $\lambda$ and let us further assume that the coefficients $a$, $b$, and $c$ are either the physical parameters or can directly be controlled by them. Then $a = b = c = 0$ can be a third-order exceptional point of an appropriate system. Its cubic root nature can be revealed if only $c$ is varied and $a = b = 0$ are held constant,

$$\lambda^3 = -c \,, \tag{2.7b}$$

which leads to the three branches with $c = 0$ as branch point. However, if $a = c = 0$ are held constant and $b$ is varied, we find

$$\lambda^3 + b\lambda = \lambda(\lambda^2 + b) = 0 \,, \tag{2.7c}$$

clearly exhibiting the structure of a square root and an isolated eigenvalue not participating in the branch point. Thus, the same point in the parameter space can show different behaviours for different choices of parameter variations, which has to be kept in mind when a possible EP3 appears. The rigorous treatment of this situation can be found in reference [77].

### 2.1.3. Bose-Einstein condensates with complex potentials

Originally predicted theoretically in 1924 for quanta of light by Bose and Einstein [79, 80] a phase transition of a gas of atoms into a macroscopic superposition of the ground state, a Bose-Einstein condensate, was first observed experimentally in 1995 [81, 82]. It is well known that a Bose-Einstein condensate can, at sufficiently low temperatures, be described by the Gross-Pitaevskii equation [21, 22], which reads

$$-\frac{\hbar^2}{2m}\Delta\psi(\boldsymbol{x}) + \left[V(\boldsymbol{x}) + \frac{4\pi\hbar^2 a_\mathrm{s}}{m}|\psi(\boldsymbol{x})|^2\right]\psi(\boldsymbol{x}) = \mathrm{i}\hbar\frac{\mathrm{d}}{\mathrm{d}t}\psi(\boldsymbol{x}) \,, \tag{2.8}$$

where $m$ is the mass of one Boson, $a_\mathrm{s}$ the s-wave scattering length, and $V(\boldsymbol{x})$ describes an external potential forming a trap for the Bosons. It is the Hartree approximation of the corresponding many-particle equation for the dilute atomic gas, where the assumption that all atoms are in the quantum mechanical ground state is used. Additionally, the atoms interact via the weak and short-range van der Waals force. In the dilute gas

it can be described sufficiently exact by an s-wave scattering process, which leads in the mean-field approximation to the nonlinear contribution $\propto |\psi(\boldsymbol{x}, t)|^2$. Its strength is determined by the s-wave scattering length $a_\mathrm{s}$. Using magnetic fields acting on the hyperfine levels of the atoms and exploiting Feshbach resonances the scattering length can be tuned and $a_\mathrm{s}$ is an adjustable parameter of the system.

Although most examples of non-Hermitian Hamiltonians appear in the framework of the Schrödinger equation their applicability is not restricted to linear quantum mechanics. In the description of Bose-Einstein condensates with the Gross-Pitaevskii equation inelastic three-body collisions are usually implemented in terms of an imaginary loss potential because the only relevant effect for the condensate is a decline in the number of particles. The fate of the "lost" particles is not of further interest. Furthermore, non-Hermitian forms of the Gross-Pitaevskii equation provide access to the decay of the condensates with the complex scaling approach [83, 84], to transport phenomena [85], and to the theoretical study of dissipative optical lattices [27, 28, 86, 87]. They also made possible the discovery of exceptional points in stationary solutions of the Gross-Pitaevskii equation [45, 88] with the help of effects only visible in the complex neighbourhood of the physical parameters [45].

A loss or gain of particles can also in the limit of the Gross-Pitaevskii equation be modelled by imaginary contributions to the potential. They lead to a growth or decay of the wave function $\psi$ describing the whole condensate. Since the imaginary parts of the potential affect the probability amplitude of the whole condensate the physical interpretation of the process we have in mind is a *coherent* in- or outcoupling of the atoms. With this ansatz we are not considering individual atoms but the macroscopic wave function of the condensed phase. That is, in the example shown in figure 2.1 (a) we assume that the condensate occupies the whole systems of $V_\mathrm{H}(x)$, i.e. all four wells. The probability amplitude can shift its weight from one well to the other. In the non-Hermitian description with the complex potential, of which the real part is shown in figure 2.1 (b), the imaginary potential must cover exactly this process, which is achieved by adding imaginary parts to the potential $V(\boldsymbol{x})$ in the Gross-Pitaevskii equation (2.8). Loss terms, i.e. negative imaginary potential contributions, of exactly this type are also obtained in a derivation of a master equation modelling loss effects in cold atom systems when coherence is preserved [89, 90].

An important prerequisite for experiments with this type of gain or loss effects has already been fulfilled. To study the effects of complex potentials different fractions of the condensate in different parts of a trap (e.g. different wells in figure 2.1) must remain coherent, which is a nontrivial task in an experimental realisation. Shin et al. [91] demonstrated that it is possible to create a bidirectional coupling between BECs in an optical double-well potential by continuously outcoupling atoms with Bragg beams. A more direct approach was successfully accomplished by Gati et al. [92] by combining a three-dimensional harmonic trap with a one-dimensional periodic potential with large lattice spacing. Furthermore, electron beams have successfully been used to introduce loss in single sites of optical lattices [93], and an influx of atoms can be achieved by

exploiting different electronic states of the atoms to transfer them from a reservoir into one well of a trap [94].

We note that a theoretical approach similar to our study has been introduced by Graefe et al. in the investigation of a Bose-Hubbard dimer [9, 23, 24]. It differs, however, in one crucial aspect from the non-Hermitian description mentioned above. In the ansatz of Graefe et al. complex potentials were used on the single particle level. Only after the introduction of the complex potentials the mean-field limit was performed in a thorough calculation. Since the system obeys by construction particle number conservation there is also a difference in the interpretation of the complex potentials. The imaginary terms do not describe the loss or gain of individual particles but a decrease or increase of the probability to find one particle in the system of interest, and this probability is identical for all particles [24]. The result of the calculation is an equation similar to the Gross-Pitaevskii equation but with a different type of nonlinearity. It has the norm-independent shape $\propto |\psi(\boldsymbol{x},t)|^2/||\psi(\boldsymbol{x},t)||^2$, where $||\psi(\boldsymbol{x},t)||$ is the wave function's norm. Consequently the system exhibits a different dynamics. However, this does not influence the spectra of normalised stationary states.

## 2.2. Balanced gain and loss: $\mathcal{PT}$ symmetry

### 2.2.1. Quantum systems with $\mathcal{PT}$-symmetric Hamiltonians

A special form of potentials which allow for gain and loss introduced by imaginary parts are those which are parity-time symmetric. This term denotes quantum systems of which the Hamiltonian commutes with the $\mathcal{PT}$ operator, i.e.

$$[\mathcal{PT}, H] = 0 \,. \tag{2.9a}$$

The operator $\mathcal{P}$ is linear and describes spatial reflections, e.g. in one dimension

$$\mathcal{P}x = -x \,, \quad \mathcal{P}p = -p \,. \tag{2.9b}$$

The time reversal operator $\mathcal{T}$ is antilinear,

$$\mathcal{T}x = x \,, \quad \mathcal{T}p = -p \,, \quad \mathcal{T}\mathrm{i} = -\mathrm{i} \,. \tag{2.9c}$$

It was found by Bender and Boettcher [4] that non-Hermitian Hamiltonians obeying $\mathcal{PT}$ symmetry can have real eigenvalues and even completely real spectra. The example Bender and Boettcher introduced was the Schrödinger equation [4]

$$-\psi''(x) - (\mathrm{i}x)^N \psi(x) = E\psi(x) \,, \tag{2.10}$$

where $N$ is a parameter. For $N = 2$ this system represents the harmonic oscillator, which is Hermitian and has purely real eigenvalues $E$. This is also fulfilled for every integer

multiple of two. However, Bender and Boettcher found that the spectra are entirely real and positive for all values $N \geq 2$. This was surprising since the Hamiltonian is, e.g. for $N = 3$ definitely not Hermitian. However, it is simple to verify that it fulfils equation (2.9a). Only for $N < 2$ pairs of eigenvalues merge in exceptional points and become complex and complex conjugate.

The discovery of Bender and Boettcher initiated an ever increasing interest in $\mathcal{PT}$-symmetric systems in the last years in many fields of physics. It is discussed, e.g. in the context of quantum mechanics [13, 19, 20, 95–100], in quantum field theories [4, 5, 101–104], but also in microwave cavities [105], electronic devices [106, 107], and optics [6, 108]. The stationary Schrödinger equation was solved for scattering solutions [20] and bound states [19], where also mathematical questions in connection with the meaning of non-Hermitian Hamiltonians have been discussed [7, 11, 109]. Spectral singularities in $\mathcal{PT}$-symmetric potentials [12] turned out to be connected with the amplification of waves [110] and the lasing threshold [111]. Nonlinear $\mathcal{PT}$-symmetric quantum systems have been discussed for Bose-Einstein condensates described in a two-mode approximation [9, 23, 24, 112] and in model potentials [113]. For reviews see references [5, 6].

### Basic properties of $\mathcal{PT}$-symmetric quantum systems

In connection with the meaning of gain and loss $\mathcal{PT}$ symmetry represents a very special situation because it allows for the case that gain and loss to the probability amplitude are equally strong, i.e. balanced. To understand this behaviour we investigate the condition for a $\mathcal{PT}$-symmetric Hamiltonian. An explicit calculation of the commutator, again done in one dimension for simplicity,

$$[\mathcal{PT}, H] = \mathcal{PT}\left(\frac{p^2}{2m} + V(x)\right) - \left(\frac{p^2}{2m} + V(x)\right)\mathcal{PT} \tag{2.11}$$

$$= \left(V^*(-x) - V(x)\right)\mathcal{PT} \stackrel{!}{=} 0 \tag{2.12}$$

immediately shows that the potential has to fulfil the equation

$$V^*(-x) = V(x)\ , \tag{2.13}$$

i.e. its real part has to be a symmetric function of $x$ and its imaginary part has to be antisymmetric.

The potential is balanced, it has equally large imaginary parts with opposite sign on both sides of the $x$ axis. However, this is not sufficient for equally strong source and drain terms, which can be see in equation (2.3). Balanced gain and loss is only fulfilled if the square modulus of the wave function $\rho$ is also a symmetric function of $x$. This is fulfilled in the case of unbroken $\mathcal{PT}$ symmetry, i.e. in the case that also the wave function is an eigenstate of $\mathcal{PT}$,

$$\mathcal{PT}\psi = \lambda\psi\ . \tag{2.14}$$

The eigenvalue $\lambda$ has always the modulus 1 since $\mathcal{PT}$ is an idempotent antilinear operator. It can be set to 1 with an appropriate choice of the wave function's arbitrary global phase.

With the short calculation

$$H\mathcal{PT}\psi(x) = \mathcal{PT}H\psi(x) = \mathcal{PT}E\psi(x) = E^*\mathcal{PT}\psi(x) \tag{2.15}$$

and the knowledge of relation (2.14) for $\mathcal{PT}$-symmetric states it is easy to prove that all $\mathcal{PT}$-symmetric eigenstates of $H$ possess real eigenvalues, and all eigenstates of a $\mathcal{PT}$-symmetric Hamiltonian with real eigenvalues must be $\mathcal{PT}$ symmetric [5]. $\mathcal{PT}$-symmetric states have always symmetric square moduli since

$$|\psi(x)|^2 = \psi^*(x)\psi(x) = \mathcal{PT}\psi(-x)\psi(x) = \psi(-x)\mathcal{PT}\psi(x) = \psi(-x)\psi^*(-x) = |\psi(-x)|^2 \,. \tag{2.16}$$

Furthermore, equation (2.15) shows that if $\psi$ is an eigenstate of the $\mathcal{PT}$-symmetric Hamiltonian $H$ with the complex eigenvalue $E$ then also $\mathcal{PT}\psi$ is an eigenstate of $H$ with eigenvalue $E^*$. Consequently, complex eigenvalues appear always in complex conjugate pairs. These relations are valid for non-degenerate eigenvalues but similar relations can be found for degenerate ones. Genuine degeneracies will not appear in this thesis, and thus this case will not be considered further. We will only be confronted with exceptional points.

What does this mean for a quantum system? The complex $\mathcal{PT}$-symmetric potential describes spatially separated gain and loss terms for the probability amplitude. This opens for the wave function – or at least for its part in the system described by the $\mathcal{PT}$-symmetric potential – the possibility to grow or to decay, which is indicated by complex eigenvalues when eigenstates of the time-independent Schrödinger equation are calculated. To every growing state belongs a decaying solution with complex conjugate energy and $\mathcal{PT}$-conjugate wave function, and vice versa. A purely real energy describes a stationary state, i.e. a probability amplitude which stays constant in spite of the gain and loss present in the system. The state is $\mathcal{PT}$ symmetric, has a symmetric square modulus, and the source and drain terms are equally strong according to equations (2.13) and (2.3). For moderate strengths of the imaginary potential the probability flux from the source to the drain is constant such that the wave function does not change. With increasing strength of the gain and loss effect typically two real eigenvalue states merge in an exceptional point and become complex and complex conjugate. From this point on the case of balanced gain and loss is unsustainable. Thus, the system possesses two regimes in which completely different types of the system's dynamical behaviour exist. The transition from one type to the other can be controlled by a single parameter, viz. the magnitude of the source and drain terms of the potential. An example of these effects will be given in section 3.1.1, where the time-independent and time-dependent Schrödinger equations of the $\mathcal{PT}$-symmetric double-delta potential will be solved.

#### $\mathcal{PT}$ symmetry in optics

Due to the availability of gain or loss for the light intensity in electrodynamics via absorbing media and optical pumping the effects of $\mathcal{PT}$ symmetry also have become very important in optics. Subject of investigations are in particular wave guides [8, 14] and optical lattices [6, 10, 15–17, 114, 115]. Also in the development of lasers $\mathcal{PT}$ symmetry plays an important role [108, 116, 117]. The optical systems are directly relevant for quantum mechanics since in many cases the mathematical basis is equivalent. For example, the $\mathcal{PT}$-symmetric wave guide structure studied by Klaiman et al. [8] was described in paraxial approximation. Klaiman et al. investigated a light mode propagating in $z$ direction of which the $y$ component of the electric field $E_y$ is governed by the equation

$$\left(-\frac{\partial^2}{\partial x^2} + k^2 n^2(x)\right) \mathcal{E}_y(x) = \beta^2 \mathcal{E}_y(x) \tag{2.17}$$

with $E_y(x, z, t) = \mathcal{E}_y(x) \mathrm{e}^{\mathrm{i}(\omega t - \beta z)}$, the mode's wave number in vacuum $k$, and the refractive index $n(x)$. If $V(x) = k^2 n^2(x)^2$ is considered to be a potential, equation (2.17) is identical with the one-dimensional Schrödinger equation. Thus, these optical systems can be used to simulate quantum particles in a one-dimensional setup.

Also the features of a nonlinearity of the type $\propto |\psi(x)|^2$ have become very relevant for optics since it does not only appear in the mean-field description of Bose-Einstein condensates. $\mathcal{PT}$-symmetric optical setups of coupled dual wave guides including a Kerr nonlinearity show exactly the same structure in the underlying equations. They have been used to propose uni-directional wave guides [25] or the presence of solitons in gain-loss media [26–31]. The remarkable success of realising $\mathcal{PT}$ symmetry and $\mathcal{PT}$-symmetry breaking experimentally [2, 3] emphasises the relevance of these optical setups.

### 2.2.2. Nonlinearity and $\mathcal{PT}$ symmetry

The properties of $\mathcal{PT}$-symmetric Hamiltonians and their eigenstates shown so far are only true for the linear Schrödinger equation. In the case of the Gross-Pitaevskii equation special care has to be taken of the nonlinearity. The proves sketched in the last section rely on the linearity of the Hamiltonian. However, it is possible to gain some similar results for nonlinear quantum systems, which have been published already in reference [118] and are summarised in the following.

In the linear case the commutator relation (2.9a) is the starting point for all further calculations. In the nonlinear case we explicitly consider a nonlinearity in the Hamiltonian to proceed with the derivation of similar statements. Thus, we separate the Hamiltonian in a linear part $H_{\mathrm{lin}}$, which can be treated as before, and a nonlinear function $f(\psi)$ representing the nonlinearity. Then the time-independent variant of the Gross-Pitaevskii equation (2.8) reads

$$H_{\mathrm{lin}}\psi + f(\psi)\,\psi = \mu\psi \tag{2.18}$$

with the chemical potential $\mu$. The nonlinearity of the Gross-Pitaevskii equation $\propto |\psi|^2$ does not depend on the wave function's phase. We restrict the further discussion to this case and require

$$f\left(\mathrm{e}^{\mathrm{i}\chi}\psi\right) = f\left(\psi\right), \quad \chi \in \mathbb{R} \,. \tag{2.19}$$

When evaluating the commutator in equation (2.9a) we assume that the $\mathcal{PT}$ operator directly acts on the wave function in the nonlinearity,

$$\mathcal{PT} f\left(\psi\right) = f\left(\mathcal{PT}\psi\right)\mathcal{PT} \,, \tag{2.20}$$

which leads to

$$\mathcal{PT}\left[\left(H_{\mathrm{lin}} + f\left(\psi\right)\right)\psi\right] - \left[H_{\mathrm{lin}} + f\left(\mathcal{PT}\psi\right)\right]\mathcal{PT}\psi = 0 \,. \tag{2.21}$$

The relation (2.21) shows that the assumption (2.20) is reasonable since it is conform with the derivation of the Gross-Pitaevskii equation as Hartree approximation, where the solution $\psi$ is part of its self-consistent potential. In this description a symmetry operator cannot act only on the linear part of the Hamiltonian. It always has also to act on the wave function, and thus on the nonlinearity.

With the assumptions (2.19) and (2.20) and the meaning of the commutator from equation (2.21) it is possible to build up a notation which is very familiar to the linear case. This can be shown by the application of the $\mathcal{PT}$ operator on the Gross-Pitaevskii equation

$$H_{\mathrm{lin}}\mathcal{PT}\psi + f\left(\mathcal{PT}\psi\right)\mathcal{PT}\psi = \mu^{*}\mathcal{PT}\psi \,, \tag{2.22}$$

where $H_{\mathrm{lin}}$ was assumed to be $\mathcal{PT}$ symmetric. One property known from the linear case can immediately be recognised: the chemical potential $\mu$ appears in complex conjugate pairs, the corresponding eigenstates are $\psi$ and $\mathcal{PT}\psi$.

If we now assume that the wave function with a non-degenerate chemical potential $\mu$ is $\mathcal{PT}$ symmetric and use condition (2.19) we see from equation (2.22) that $\mu$ must be real. Conversely, if $\mu$ is a non-degenerate real eigenvalue (2.22) states that $\psi$ must be $\mathcal{PT}$ symmetric. In total we obtain for non-degenerate eigenstates the same relations between the $\mathcal{PT}$ symmetry of the states and the eigenvalues as in the linear Schrödinger equation. There are differences for genuine degeneracies as noted in reference [118]. However, this is not the topic of this thesis as mentioned above.

The nonlinear function $f(\psi)$ in the Gross-Pitaevskii equation (2.18) can be understood to belong to the potential of the nonlinear Hamiltonian. In this interpretation the conditions (2.19) and (2.20) relate the $\mathcal{PT}$ symmetry of the Hamiltonian with that of the wave function. If the linear part $H_{\mathrm{lin}}$ is $\mathcal{PT}$ symmetric it is possible that a $\mathcal{PT}$-symmetric wave function exists, which renders the total nonlinear Hamiltonian itself $\mathcal{PT}$ symmetric. Without a $\mathcal{PT}$-symmetric wave function the nonlinear Hamiltonian does not have to be $\mathcal{PT}$ symmetric. It can be added that not only the short-range contact interaction $\propto |\psi|^2$ fulfils the conditions (2.19) and (2.20). This is also true for two important long-range interactions, viz. Bose-Einstein condensates with a gravity-like

$1/r$ [119] or dipolar [120] interaction, c.f. also reference [118]. Thus, also Bose-Einstein condensates with these long-range interactions might exhibit $\mathcal{PT}$-symmetric solutions.

Finally, we want to summarise the results of this consideration since they will be used several times in the following chapters. If we consider non-degenerate eigenstates of the time-independent Gross-Pitaevskii equation (2.18) with a $\mathcal{PT}$-symmetric linear part of the Hamiltonian and a nonlinear part which fulfils the conditions (2.19) and (2.20) it can be stated that

- the eigenvalues are either real or occur in complex conjugate pairs,
- the eigenvalues are real if and only if the eigenstate itself is $\mathcal{PT}$ symmetric, and
- if $\psi$ is an eigenstate with complex chemical potential $\mu$ then also $\mathcal{PT}\psi$ is eigenstate with chemical potential $\mu^*$.

# 3. A model for a $\mathcal{PT}$-symmetric Bose-Einstein condensate

The effects of $\mathcal{PT}$-symmetric quantum systems have been studied in a wide class of models. A good candidate for an experimental realisation are Bose-Einstein condensates trapped in a double-well geometry, where on one side atoms are injected and on the other atoms are removed. This has to be done in a coherent manner if the wave function of the condensed phase is supposed to describe the $\mathcal{PT}$-symmetric or $\mathcal{PT}$-broken solutions. A proposal of realising a quantum system with $\mathcal{PT}$ symmetry on this basis was already given by Klaiman et al. [8]. Since the condensed phase is described by the nonlinear Gross-Pitaevskii equation new properties not known from linear quantum systems will arise, which have to be taken into account and studied carefully. To do so, we first introduce in section 3.1 a very simple system, viz. a potential shaped by two idealised attractive delta-traps, in which antisymmetric imaginary contributions will model the balanced source and drain of atoms. Delta functions have often been used to gain deeper insight with simple solutions [7, 11, 12, 19, 20, 121–128]. First we show that its linear variant exhibits the typical properties of $\mathcal{PT}$-symmetric quantum systems in section 3.1.1 and then study the solutions of the time-independent Gross-Pitaevskii equation for the double-delta trap in section 3.1.2. Finally we will do the same investigation for the example of a more realistic spatially extended double well in section 3.2. We will review the corresponding Gross-Pitaevskii equation in section 3.2.1, discuss the numerical methods used for the investigation in section 3.2.2 and then investigate the stationary states in one (section 3.2.3) and three (section 3.2.4) dimensions. This chapter is based on references [129–133], in which the results on stationary states of a Bose-Einstein condensate in a $\mathcal{PT}$-symmetric potential have been studied. Parts of the results for the spatially extended double well have been obtained together with Dennis Dast and Daniel Haag during their Master's theses [134, 135].

## 3.1. An idealised double-delta trap

The model we introduce in this first step is a Bose-Einstein condensate trapped in two delta-function shaped potential wells located at $x = \pm a/2$, where from one well condensate atoms are removed and atoms are added to the other. To simplify the discussion we reduce the system to one dimension. As will be shown later this is sufficient to describe all effects of the $\mathcal{PT}$-symmetric double well.

The consideration is done in the mean-field approach by the nonlinear Schrödinger equation, or Gross-Pitaevskii equation equation,

$$-\frac{\hbar^2}{2m}\frac{\mathrm{d}^2}{\mathrm{d}x^2}\psi(x) + \left[V(x) + \tilde{g}|\psi(x)|^2\right]\psi(x) = \tilde{\mu}\psi(x) \;, \tag{3.1}$$

which is well justified at sufficiently low temperatures. In the equation $m$ is the mass of one Boson, $\tilde{g}$ the strength of the contact interaction, which is proportional to the s-wave scattering length, and $\tilde{\mu}$ the chemical potential. The $\mathcal{PT}$-symmetric delta-function traps are described by the potential

$$V(x) = -(V_0 + \mathrm{i}\Gamma)\delta(x + a/2) - (V_0 - \mathrm{i}\Gamma)\delta(x - a/2) \;, \tag{3.2}$$

where the positive parameter $V_0$ determines the real part, i.e. the depths of the two symmetric wells. The gain and loss of the atoms are modelled by $\pm\Gamma$.

We will work with the dimensionless form of the Gross-Pitaevskii equation (3.1) and the potential (3.2), where the length is measured in units of $\ell_0 = \hbar^2/(2mV_0)$ and energies in units of $E_0 = 2mV_0^2/\hbar^2$. It reads

$$-\frac{\mathrm{d}^2}{\mathrm{d}x^2}\psi(x) - \left[(1 + \mathrm{i}\gamma)\delta(x + a/2) + (1 - \mathrm{i}\gamma)\delta(x - a/2)\right]\psi(x) \\ - g|\psi(x)|^2\psi(x) = \mu\psi(x) \;, \tag{3.3}$$

where $g$ is the dimensionless nonlinear interaction strength, and the real-valued parameter $\gamma$ determines the size of the gain and loss terms. Note that $g$ has been defined such that positive values describe an attractive contact interaction. The strength of the real part of the delta-function potentials is normalised to unity in the chosen units. Following the usual notation of the linear double-delta problem in textbook quantum mechanics, we will often substitute the chemical potential by

$$\mu = -\kappa^2 \;. \tag{3.4}$$

The potential (3.2) is complex and we cannot expect $\mu$ or $\kappa$ to be real. In particular, complex energies are known for $\mathcal{PT}$-broken states in quantum systems described by a $\mathcal{PT}$-symmetric potential. We are interested in all possible types of solutions, and thus we will quite generally search for solutions with $\kappa \in \mathbb{C}$.

### 3.1.1. Schrödinger equation of the $\mathcal{PT}$-symmetric double-delta potential

To be in a position to study the effects that emerge when the nonlinearity is turned on we first consider the case where the nonlinearity is absent, and then proceed to values $g > 0$. In particular, we want to show first that the very simple double-delta potential

incorporates the typical effects excepted of $\mathcal{PT}$-symmetric quantum systems in the linear Schrödinger equation.

We start with the linear variant of (3.3), i.e. with the Schrödinger equation

$$-\frac{\mathrm{d}^2}{\mathrm{d}x^2}\psi(x) - [(1+\mathrm{i}\gamma)\delta(x+a/2) + (1-\mathrm{i}\gamma)\delta(x-a/2)]\,\psi(x) = -\kappa^2\psi(x)\ . \tag{3.5}$$

We are only interested in bound states and do not consider scattering solutions of the Schrödinger equation. Hence, the wave functions must have the well-known form

$$\psi(x) = \begin{cases} A\,\mathrm{e}^{\kappa x} & x < -a/2 \\ C\,\mathrm{e}^{\kappa x} + D\,\mathrm{e}^{-\kappa x} & -a/2 < x < a/2 \\ B\,\mathrm{e}^{-\kappa x} & a/2 < x \end{cases}\ . \tag{3.6}$$

This ansatz leads only to physically relevant solutions for $\mathrm{Re}\,\kappa > 0$. Applying the continuity conditions leads to the system of linear equations (with the abbreviation $\kappa_0 = 1 + \mathrm{i}\gamma$),

$$\kappa_0 \mathrm{e}^{-\kappa a/2}\,C + (\kappa_0 - 2\kappa)\mathrm{e}^{\kappa a/2} D = 0\ , \tag{3.7}$$

$$(\kappa_0^* - 2\kappa)\mathrm{e}^{\kappa a/2}\,C + \kappa_0^* \mathrm{e}^{-\kappa a/2}\,D = 0\ . \tag{3.8}$$

It possesses nontrivial solutions if the secular equation

$$(1+\gamma^2)\mathrm{e}^{-2\kappa a} - (1 + \gamma^2 + 4\kappa^2 - 4\kappa) = 0 \tag{3.9}$$

is fulfilled. In general, this equation has to be solved numerically. In the units introduced above the equation depends on two remaining parameters, viz. the distance $a$ of the traps and the strength $\gamma$ of the gain-loss terms.

The eigenvalues $\kappa$ we obtained in the numerical root search are plotted as functions of the strength of the gain-loss parameter $\gamma$ in figure 3.1. Three different distances of the traps can be seen. The solutions exhibit the behaviour typical of $\mathcal{PT}$-symmetric non-Hermitian Hamiltonians: up to a critical value of the gain and loss parameter $\gamma$ there exist two real eigenvalues $\kappa$. One has to keep in mind that we have included a minus sign in the relation (3.4). Since the exponential decay parameter $\kappa$ is plotted the upper branch belongs to the state with lowest energy, i.e. the ground state, and the lower branch represents the excited state. At the critical value, which turns out to be an exceptional point, the eigenvalues and the eigenfunctions merge. Beyond the exceptional point the eigenvalues become complex, and complex conjugate. The time-dependence of the eigenstates of the Schrödinger equation (3.5) is given by $\exp(\mathrm{i}\kappa^2\,t) = \exp(\mathrm{i}(k_\mathrm{r}^2 - k_\mathrm{i}^2)t)\exp(-2k_\mathrm{r}k_\mathrm{i}t)$ (with $\kappa = k_\mathrm{r} + \mathrm{i}k_\mathrm{i}$), hence the mode with $k_\mathrm{i} > 0$ decays, and the mode with $k_\mathrm{i} < 0$ grows because all physically relevant solutions possess $k_\mathrm{r} > 0$.

Of course in the case $\gamma = 0$ the system corresponds to the well-know textbook example of the real double-delta potential. Then the solutions are $\cosh(\kappa x)$ (ground state) and

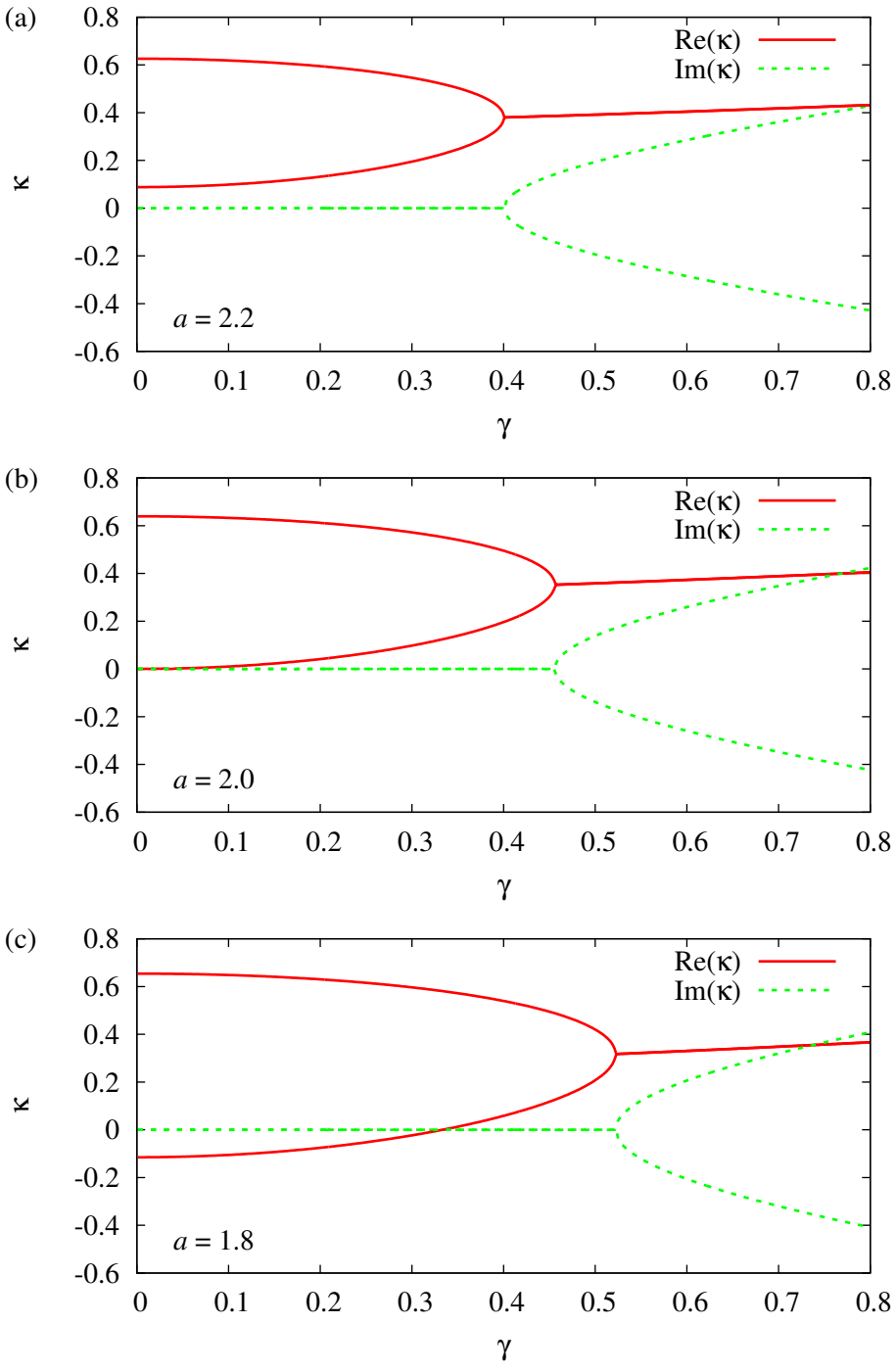


Figure 3.1.: Eigenvalues $\kappa$ of the Schrödinger equation (3.5) as functions of the gain-loss parameter $\gamma$ for three different distances of the delta-function traps, i.e. $a = 2.2$ (a), $a = 2.0$ (b), $a = 1.8$ (c).

$\sinh(\kappa x)$ (excited state) functions between the traps. It is also well-known that for $\gamma = 0$ the excited state disappears as soon as the distance between the two delta wells falls below a critical value. In the units of our system this critical value corresponds to $a = 2$. Indeed, from figure 3.1 (b) we see, that for $a = 2$, an excited state is only born as soon as gain and loss is switched on. For $\gamma = 0$ the formal second solution alongside the ground state is $\kappa = 0$. Such a state is not physical and does not exist. However, even with an infinitesimally small gain and loss contributions a second solution is supported by the two delta wells. For $a < 2$ a finite gain and loss threshold is required for the appearance of the second state as can be observed in figure 3.1 (c).

Below the branch point the wave functions are expected to possess $\mathcal{PT}$ symmetry. The need for wave functions to be $\mathcal{PT}$ symmetric if their energy $\mu = -\kappa^2$ is real, is expressed in the delta functions model in the following way: For real $\kappa$ the complex conjugate of the condition (3.7) is identical to the second (3.8). This means that pairs $(C, D)$ and $(D^*, C^*)$ fulfil the same equation, and hence $D = C^*$. Then one can conclude that $A = C + C^* e^{2\kappa a/2}$ and $B = Ce^{2\kappa a/2} + C^* = A^*$, i.e. we obtain in total $\psi^*(x) = \psi(-x)$, which is exactly a $\mathcal{PT}$-symmetric wave function.

The numerically obtained result confirming these properties can be seen in figure 3.2, in which the ratio of the coefficients $C$ and $D$ of the wave functions is shown in dependence of the gain-loss parameter $\gamma$. The modulus and the phase of this ratio are plotted. Below the branch point we expect and find $D = C^* = |C| \exp(-\mathrm{i}\varphi)$, the modulus of the ratio is 1, and the phase is twice the phase $\varphi$ of the coefficient $C$. As is known from the textbook example, the phase assumes the value of 0 for the (symmetric) ground state and $\pi$ for the (antisymmetric) excited state. For $\gamma \neq 0$ the phase $\varphi$ of the ground and the excited state quickly obtain nonvanishing values, where the ground state is more affected. The moduli and phases of the ratios of both states coincide at the branch point verifying the expected exceptional point. Beyond the branch point the moduli of the rations quickly evolve away from 1, the wave functions do no longer possess a symmetric modulus, and consequently they are $\mathcal{PT}$ broken.

In total, we find that the $\mathcal{PT}$-symmetric double-delta potential exhibits only two states, however, they are sufficient to reproduce all relevant properties of stationary states in $\mathcal{PT}$-symmetric quantum systems. Thus, the potential seems to be a good and simple candidate for the investigation of those properties with the nonlinear Gross-Pitaevskii equation.

### 3.1.2. Stationary solutions of the Gross-Pitaevskii equation with a delta-functions trap

#### Numerical method

For $g \neq 0$ we have solved the Gross-Pitaevskii equation (3.3) numerically using a procedure in which the energy eigenvalues are found by a five-dimensional numerical root search. The free parameters which have to be adjusted in such a way that a physically

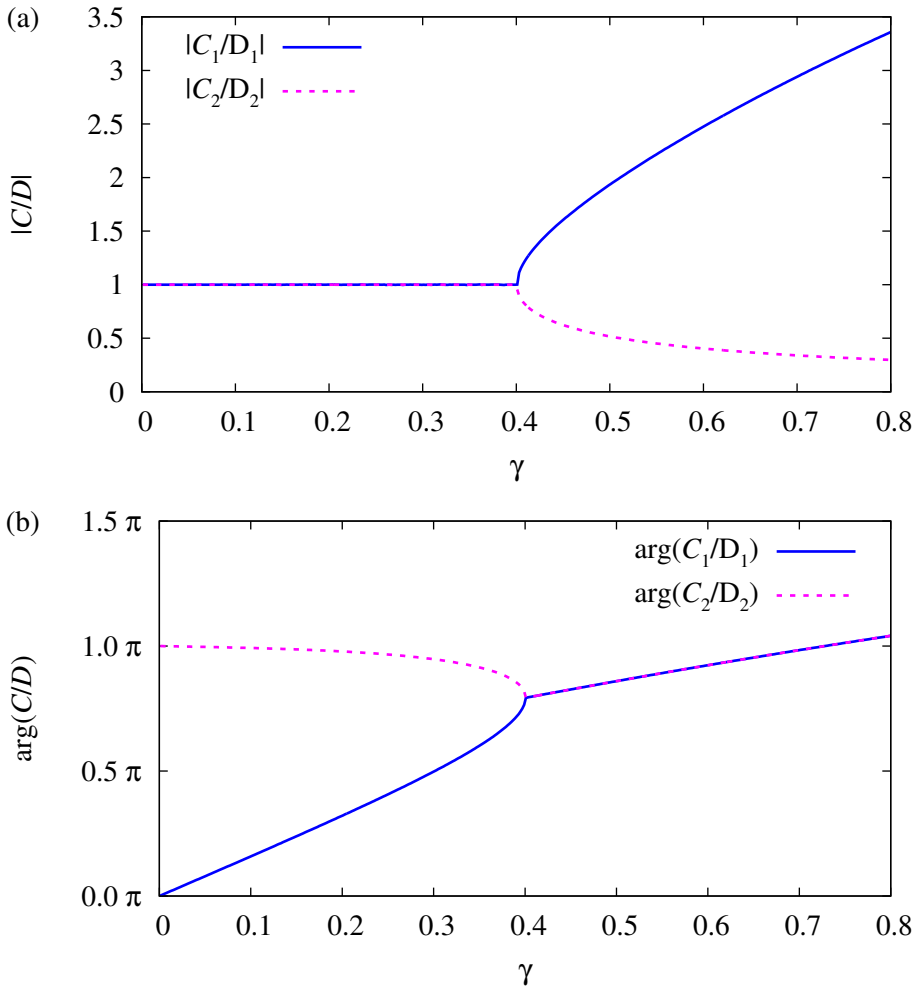


Figure 3.2.: Real parts (a) and imaginary parts (b) of the ratio of the coefficients of the wave functions in the region between the delta-function traps for vanishing nonlinearity and a distance of $a = 2.2$ as functions of the gain-loss parameter $\gamma$. For values of $\gamma$ below the bifurcation point the solid lines correspond to the ground state, the dashed lines to the excited state.

meaningful wave function is obtained are the complex eigenvalue $\kappa$ as well as initial conditions for the wave function and its derivative. Since the overall phase is arbitrary we can choose it such that $\psi(0)$ is a real number. Therefore five real parameters remain, viz. the real part of $\psi(0)$, and the real and imaginary parts of both $\psi'(0)$ and $\kappa$. Physically relevant wave functions must be square integrable and normalised. The normalisation is important since the Gross-Pitaevskii equation is nonlinear and the norm influences the form of the Hamiltonian. This gives in total five conditions which have to be fulfilled: The real and imaginary parts of $\psi$ must vanish for $x \to \pm\infty$, and the norm of the wave function must fulfil $||\psi|| - 1 = 0$.

Outside the delta-function traps the Gross-Pitaevskii equation (3.3) coincides with the free nonlinear Schrödinger equation, which has well known real solutions in terms of Jacobi elliptic functions (cf., e.g. [123, 136–138]). The function which solves the equation in the ranges $|x| > a/2$ for the attractive nonlinearity considered here and decays to zero for $|x| \to \infty$ is $\mathrm{cn}(\kappa x, 1) = \mathrm{sech}(\kappa x) = 1/\cosh(\kappa x)$. The numerically integrated wave functions exactly show this behaviour.

### Eigenvalues

Figure 3.3 shows the results for the real and imaginary parts of the eigenvalues $\kappa$ calculated for a trap distance of $a = 2.2$ and three different nonvanishing values of the nonlinearity parameter as functions of $\gamma$. The results for the case $g = 0$ are shown for comparison. Even with a strong nonlinearity present there always exist two branches of real eigenvalues, up to critical values $\gamma_{\mathrm{EP}}$, where the two branches merge. It can also be seen that branches of two complex conjugate eigenvalues appear. Unlike in the linear case they are not born at $\gamma_{\mathrm{EP}}$, but at smaller values of $\gamma$ where they bifurcate from the real eigenvalue branch of the ground state. As the nonlinearity is increased this bifurcation point is shifted to smaller values of $\gamma$, while the branches of the real eigenvalues practically retain their form and are shifted upwards. A similar observation can be made for negative values of $g$, i.e. a repulsive nonlinearity. In contrast to the attractive case the two complex conjugate eigenvalues then bifurcate from the excited state. However, the overall effect remains the same. There is always a range of $\gamma$ values, in which two real and two complex eigenvalues coexist.

This behaviour is obviously caused by the nonlinearity in the Gross-Pitaevskii equation and can also be observed in the mean-field limit of a non-Hermitian Bose-Hubbard dimer [9, 23, 24, 112]. In fact the different branches can be continuously transformed into each other: when, for fixed $\gamma$, we increase the nonlinearity from $g = 0$ in small steps to $g = 1$ and always take the solution of the previous step as input for the root search in the next step, the branch of complex conjugate eigenvalues which exists for $g = 0$ is continuously transferred to the branch of complex eigenvalues for $g = 1$ shown in figure 3.3. Likewise, starting from the branch of complex conjugate eigenvalues for $g = 1$ at any value of $\gamma$ in the range where four solutions exist and decreasing $g$ in small steps to $g = 0$ we end up on the branch belonging to the real eigenvalue of the ground state.

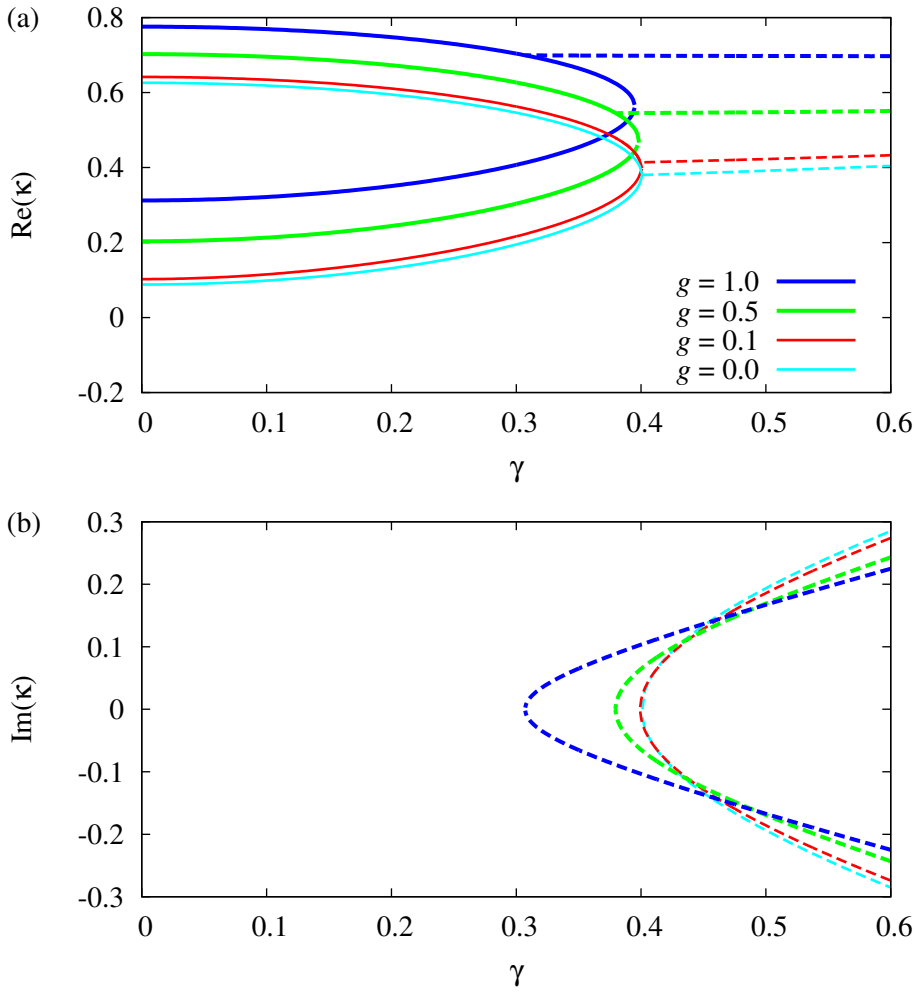


Figure 3.3.: Real (a) and imaginary (unless zero) (b) parts of the eigenvalues $\kappa$ of the full nonlinear equation (3.3) as functions of the gain-loss parameter $\gamma$ for $a = 2.2$ and four values of the nonlinearity parameter. Solid lines denote purely real eigenvalues, dashed lines complex conjugate eigenvalues. For $g \neq 0$ the complex conjugate eigenvalues bifurcate from the ground state branch before the branch point where the two real solutions coalesce.

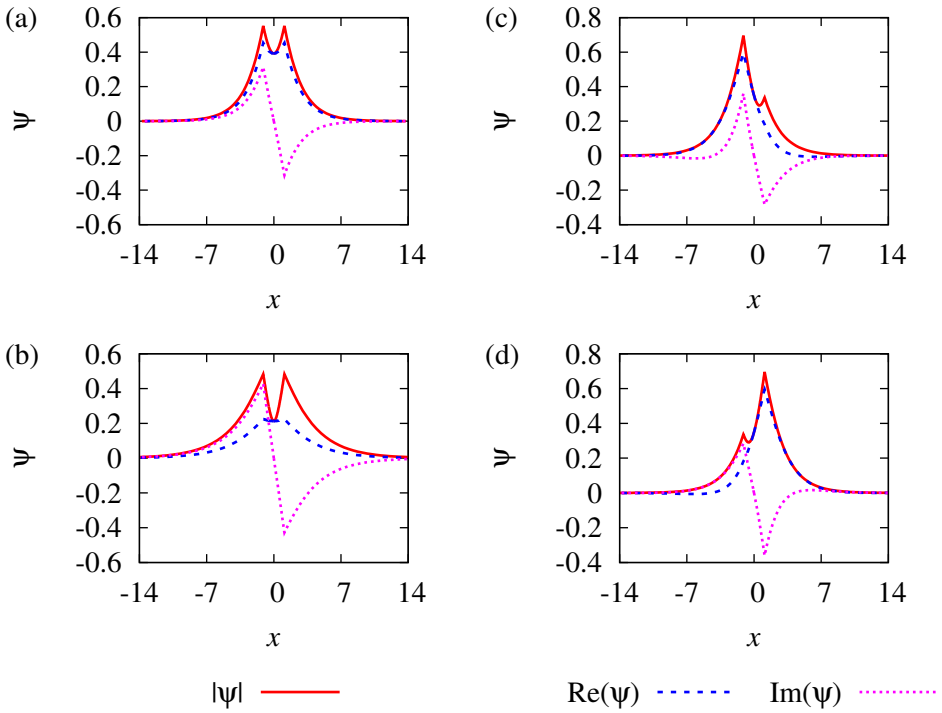


Figure 3.4.: Real and imaginary parts as well as the moduli of the wave functions of the eigenstates of the Gross-Pitaevskii equation (3.3) for $g = 0.5$, $a = 2.2$. Ground state (a) and excited state (b) for $\gamma = 0.35$, solution with $\mathrm{Im}\,\kappa > 0$ (c) and $\mathrm{Im}\,\kappa < 0$ (d) for $\gamma = 0.5$. In (a) and (b) the wave functions are $\mathcal{PT}$ symmetric, and the moduli are symmetric functions of $x$. The wave functions in (c) and (d) are no longer $\mathcal{PT}$ symmetric, their moduli are not symmetric functions of $x$.

### Wave functions

Examples of the wave functions corresponding to the energies of the case $g = 0.5$ and $a = 2.2$ shown in figure 3.3 are presented in figure 3.4. The results for the ground state and the excited state are shown in figures 3.4 (a) and (b), where the value $\gamma = 0.35$ below the critical value $\gamma_{\mathrm{EP}} \approx 0.4$ was used. With the choice used for the global phase in the numerical procedure the $\mathcal{PT}$ symmetry of the solutions is easy to recognise. Their real parts become even functions and their imaginary parts odd functions of $x$. Since $\mathcal{PT}$-symmetric wave functions have always a symmetric square modulus it immediately follows that the moduli of those wave functions are even functions of $x$. The symmetric square moduli can also be seen in figures 3.4 (a) and (b). This illustrates the important result of section 2.2.2 that the nonlinear Hamiltonian with gain and loss selects as eigenfunctions exactly those states in Hilbert space which render itself $\mathcal{PT}$ symmetric. This is a nontrivial result and needs the assumptions made in section 2.2.2. While the

delta-function potentials are $\mathcal{PT}$ symmetric, it is, on the level of the position space representation used here, not clear a priori that the Gross-Pitaevskii equation itself also obeys this symmetry since this requires the nonlinear potential term to fulfil exactly the symmetry found in the numerical results. In the ground state, which emerges from the symmetric real wave function for $\gamma = g = 0$, the symmetric contribution from the real part still dominates, while for the excited state, which originates from the antisymmetric solution for $\gamma = g = 0$, the antisymmetric contribution from the imaginary part prevails.

The $\mathcal{PT}$ symmetry of the wave functions is broken for the eigenstates with complex eigenvalues. Figures 3.4 (c) and (d) show as examples the wave functions obtained for $\gamma = 0.5$ for the corresponding pair of complex conjugate eigenvalues $\kappa$. It can be seen that the real and imaginary parts are no longer even or odd functions, and therefore the $\mathcal{PT}$ symmetry of both the wave functions and the nonlinear Hamiltonian is lost. The mode with positive imaginary part, as shown in figure 3.4 (c), is the one which decays. As expected it is more strongly localised in the trap with loss, while the mode with negative imaginary part in figure 3.4 (d) is the one which grows and is more strongly localised in the trap with gain.

It is important to note that all eigenstates with complex eigenvalues lose their physical relevance. They solve the nonlinear eigenvalue problem (3.3), but do not obey the corresponding *time-dependent* Gross-Pitaevskii equation. As soon as imaginary energy parts appear the square moduli of the wave functions grow or decay proportional to $\exp(-2\,\mathrm{Im}\,\kappa^2 t)$, and so does the nonlinear term in the Gross-Pitaevskii equation (3.3). Therefore strictly speaking multiplying these eigenstates with the usual time evolution factor $\exp(\mathrm{i}\kappa^2 t)$ only captures the *onset* of the temporal evolution of the two modes, for times $\mathrm{Im}\,\kappa^2 t \ll 1$.

At $\gamma_{\mathrm{EP}}$ we expect that the two eigenstates with real eigenvalues coalesce. Indeed, this is the case. In figure 3.5 we have plotted their wave functions for $a = 2.2$, $g = 0.5$ and values of $\gamma$ close to the critical point $\gamma_{\mathrm{EP}} \approx 0.4$. While slightly below the critical value minor deviations of the wave functions are still visible, in particular in the imaginary parts, no differences appears for $\gamma = 0.398$. Thus, also for a strong nonlinearity we find at $\gamma_{\mathrm{EP}}$ the properties characteristic of an exceptional point, i.e. the coalescence of both eigenvalues and eigenfunctions.

## 3.2. A Bose-Einstein condensate in a realistic double-well setup

### 3.2.1. Gross-Pitaevskii equation

We now turn to a more realistic description of the Bose-Einstein condensate and consider a spatially extended double-well potential in three dimensions. The Bose-Einstein condensate of atoms with mass $m$ is, again, described by the Gross-Pitaevskii equation,

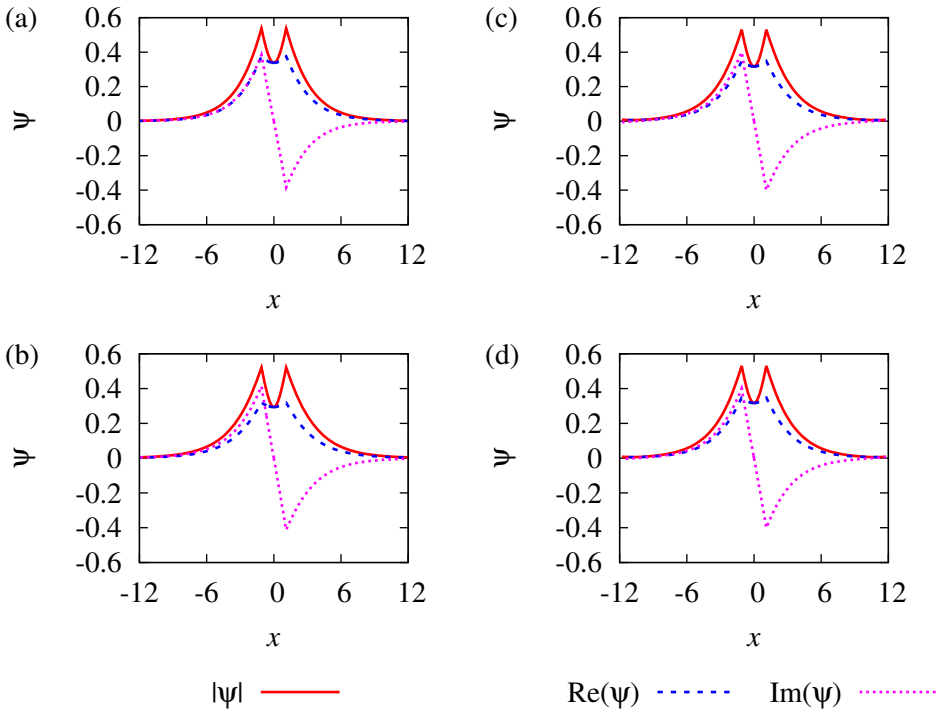


Figure 3.5.: Wave functions for $a = 2.2$ and $g = 0.5$ and values of $\gamma$ close to the exceptional point: ground state (a) and excited state (b) for $\gamma = 0.395$, ground state (c) and excited state (d) for $\gamma = 0.398$. While for $\gamma = 0.395$ still small differences are present, in particular in the imaginary part, the wave functions practically coincide at $\gamma = 0.398$.

where we now use its three-dimensional variant

$$-\frac{\hbar^2}{2m}\Delta\psi(\boldsymbol{x}) + \left[V(\boldsymbol{x}) + \frac{4\pi\hbar^2 a_\mathrm{s}}{m}|\psi(\boldsymbol{x})|^2\right]\psi(\boldsymbol{x}) = \mathrm{i}\hbar\frac{\mathrm{d}}{\mathrm{d}t}\psi(\boldsymbol{x}) \;, \tag{2.8}$$

or its time-independent form

$$-\frac{\hbar^2}{2m}\Delta\psi(\boldsymbol{x}) + \left[V(\boldsymbol{x}) + \frac{4\pi\hbar^2 a_\mathrm{s}}{m}|\psi(\boldsymbol{x})|^2\right]\psi(\boldsymbol{x}) = \tilde{\mu}\psi(\boldsymbol{x}) \;, \tag{3.10}$$

and assume a potential of the shape

$$V(\boldsymbol{x}) = \frac{m}{2}\omega_x^2 x^2 + \frac{m}{2}\omega_{y,z}^2(y^2+z^2) + v_0 e^{-\sigma x^2} + \mathrm{i}\tilde{\Gamma} x \mathrm{e}^{-\rho x^2} \;. \tag{3.11}$$

It consists of a three-dimensional harmonic trap with trapping frequencies $\omega_x$ for the $x$ direction and $\omega_{y,z}$ for the two remaining spatial coordinates. To form a double well it is superimposed with a Gaussian barrier in $x$ direction. This results in the one-dimensional

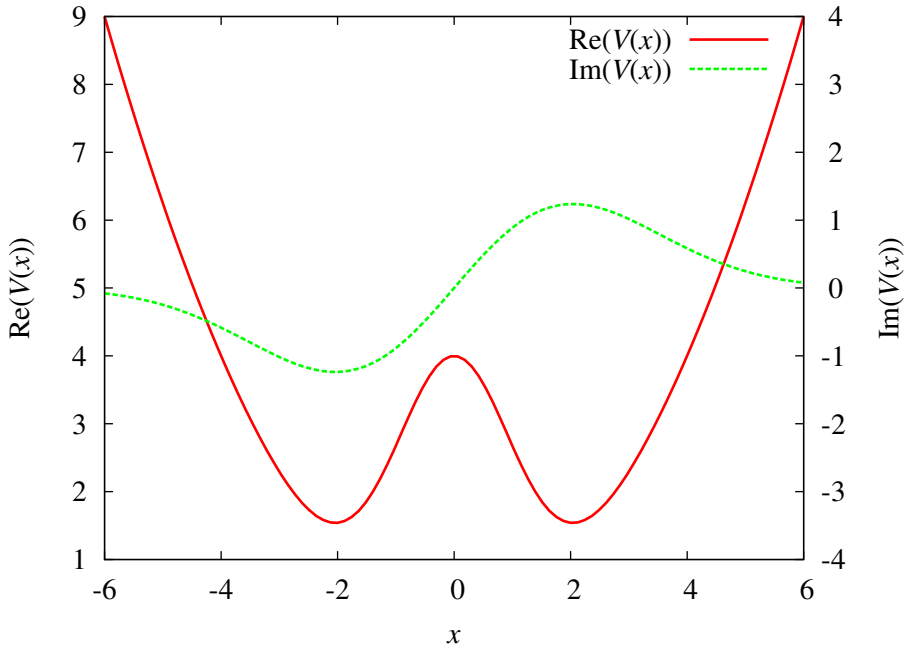


Figure 3.6.: Visualisation of the $\mathcal{PT}$-symmetric external potential in $x$ direction. The real part (solid line) defines the confinement of the condensed atom cloud, and the imaginary part (dashed line) describes the in-/outcoupling of atoms.

projection of the potential as shown in figure 3.6. It is obvious that the barrier has its maximum at $x = 0$. Its height is $v_0$ and the width of the Gaussian is given by $\sigma$. The imaginary contribution of strength $\tilde{\Gamma}$ is an effective description of a gain or loss of atoms. As can be confirmed by a simple calculation the external potential (3.11) is $\mathcal{PT}$ symmetric. As in the case of the double-delta trap we concentrate on the effects of the $\mathcal{PT}$-symmetric external potential and will keep the equations as simple as possible.

With the length scale $a_0 = \sqrt{\hbar/2m\omega_x}$ defined by the trap frequency in the direction of the double well and the unit of energy $E_0 = \hbar^2/2ma_0^2$ the dimensionless potential assumes the form

$$V(\boldsymbol{x}) = \frac{1}{4}x^2 + \frac{1}{4}\omega_{y,z}^2(y^2+z^2) + v_0 e^{-\sigma x^2} + \mathrm{i}\Gamma x \mathrm{e}^{-\rho x^2} \ . \tag{3.12}$$

Then the dynamics is governed by the time-dependent Gross-Pitaevskii equation. To obtain stationary solutions we solve its time-independent variant, viz.

$$\left(-\Delta + V(\boldsymbol{x}) - g|\phi(\boldsymbol{x})|^2\right)\phi(\boldsymbol{x}) = \mu\phi(\boldsymbol{x}) \ , \tag{3.13}$$

where the chemical potential $\mu$ has been introduced with the usual ansatz $\psi(\boldsymbol{x},t) = \phi(\boldsymbol{x})\mathrm{e}^{-\mathrm{i}\mu t}$. For the following calculations we keep the parameters $v_0 = 4$ and $\sigma = 0.5$

fixed. The width parameter $\rho$ of the imaginary gain-loss potential is chosen to be

$$\rho = \frac{\sigma}{2\ln(4v_0\sigma)} \ . \tag{3.14}$$

This choice guarantees that the extrema of the real and imaginary potential parts coincide, as is illustrated in figure 3.6. A one-dimensional description is obtained with the potential

$$V(x) = \frac{1}{4}x^2 + v_0 e^{-\sigma x^2} + \mathrm{i}\Gamma x \mathrm{e}^{-\rho x^2} \ , \tag{3.15}$$

in which only the $x$ direction is considered and all $y$ and $z$ terms are removed. Obviously it contains all the relevant information about the $\mathcal{PT}$ symmetry.

### 3.2.2. Variational Gaussian and numerically exact approach to the solutions of the Gross-Pitaevskii equation

We use two methods to solve the time-dependent and time-independent Gross-Pitaevskii equations (2.8) and (3.10). One is a Gaussian variational method [139–141]. It has been shown to provide highly precise stationary states with low numerical effort [142–144]. Since in our work it is applied for the first time to Bose-Einstein condensates in a $\mathcal{PT}$-symmetric complex potential we compare it to numerically exact solutions of the Gross-Pitaevskii equation in the one-dimensional case, in which the numerically exact wave functions can be integrated with a reasonable effort.

We use both methods to obtain only the two lowest modes with real energy, the ground state and the first excited state, as well as the two complex eigenvalue solutions with lowest real parts. Of course, the double-well potential has infinitely many states, which with increasing energy more and more converge to the equidistant levels of the harmonic oscillator in the linear case $g = 0$. It turned out, however, that only the states mentioned above are of interest. Further states differ considerably in energy, do not undergo bifurcations with those considered here, and are drastically less affected by the gain-loss contributions. Thus, they will not be considered in this and the following chapters.

The idea of the Gaussian variational method consists of the restriction to a Gaussian shaped wave function,

$$\psi(\boldsymbol{z}, \boldsymbol{x}) = \sum_{k=1}^{2} \mathrm{e}^{-\left[A_x^k (x-q_x^k)^2 + A_{y,z}^k (y^2+z^2)\right]} \mathrm{e}^{\mathrm{i}p_x^k (x-q_x^k) - \varphi^k} \ , \tag{3.16}$$

described by a small set of variational parameters, viz.

$$\boldsymbol{z}(t) = \left\{ A_x^k(t), A_{y,z}^k(t), q_x^k(t), p_x^k(t), \varphi^k \right\} \ . \tag{3.17}$$

In the case of the $\mathcal{PT}$-symmetric double-well setup it is reasonable to start with two Gaussian wave functions, where each of them is located in one of the wells. The widths of

the Gaussians are determined by the complex parameters $A_x^1$, $A_x^2$, $A_{y,z}^1$ and $A_{y,z}^2$. Since the relevant dynamics only affects the $x$ coordinate and the trap was assumed to be symmetric in $y$ and $z$ directions, we include in our ansatz the same symmetry for the Gaussian wave functions. The positions and corresponding momenta of both Gaussians are determined by the real coordinates $q_x^1$, $q_x^2$, $p_x^1$ and $p_x^2$. The amplitudes and phases are introduced via the complex variables $\varphi^1$ and $\varphi^2$. This leads in total to 16 real parameters completely defining the condensate wave function. Reducing the model to one dimension we end up with twelve real variables.

Certainly, the ansatz (3.16) cannot solve the time-dependent Gross-Pitaevskii equation (2.8) exactly. One way to find the "best" approximative solution with a wave function restricted to the Gaussian form (3.16) is the application of the McLachlan time-dependent variational principle [139],

$$\delta I = \delta ||\mathrm{i}\chi(\boldsymbol{z}(t), \boldsymbol{x}) - H\psi(\boldsymbol{z}(t), \boldsymbol{x})||^2 \stackrel{!}{=} 0 \,. \tag{3.18}$$

In this procedure the variation with respect to the parameters in the wave function $\chi$ is performed such that the functional $I$ is minimised. In a second step one sets $\dot{\psi} \equiv \chi$ and obtains the equations of motion, which in our case are of the form

$$\dot{A}_x^k = -4\mathrm{i}\left((A_x^k)^2 + (A_{y,z}^k)^2\right) + \mathrm{i}V_{2;x}^k \,, \tag{3.19a}$$

$$\dot{A}_{y,z}^k = -4\mathrm{i}\left((A_x^k)^2 + (A_{y,z}^k)^2\right) + \mathrm{i}V_{2;y,z}^k \,, \tag{3.19b}$$

$$\dot{q}_x^k = 2p_x^k + s_x^k \,, \tag{3.19c}$$

$$\dot{p}_x^k = -\operatorname{Re} v_{1;x}^k - 2\operatorname{Im} A_x^k s_x^k - 2\operatorname{Re} V_{2;x}^k q_x^k \,, \tag{3.19d}$$

$$\begin{aligned}\dot{\varphi}^k = {} & \mathrm{i}v_0^k + 2\mathrm{i}(A_x^k + A_{y,z}^k) - \mathrm{i}(p_x^k)^2 \\ & - \mathrm{i}p_x^k s_x^k + \mathrm{i}q_x^k v_{1;x}^k + \mathrm{i}q_x^k V_{2;x}^k q_x^k \,,\end{aligned} \tag{3.19e}$$

with

$$s_x^k = \frac{1}{2}(\operatorname{Re} A_x^k)^{-1}(\operatorname{Im} v_{1;x}^k + 2\operatorname{Im} V_{2;x}^k q_x^k) \,. \tag{3.19f}$$

The equations of motion (3.19a)-(3.19f) contain effective potential terms $\boldsymbol{v} = (v_0^1, \ldots, v_{1;x}^1, \ldots, V_{2;x}^1, \ldots)$ which are obtained from a system of linear equations, $\boldsymbol{K}\boldsymbol{v} = \boldsymbol{r}$, where the matrix $\boldsymbol{K}$ contains weighted overlap integrals of the Gaussians and the vector $\boldsymbol{r}$ consists of weighted Gaussian averages of all potential terms including the nonlinearity. The detailed form can be found in [131]. The dynamics of the condensate wave function is found by solving the ordinary differential equations (3.19a)-(3.19f) with a Runge-Kutta algorithm [145].

Stationary states or solutions of the time-independent Gross-Pitaevskii equation are found by the requirements $\dot{A}_x^k = \dot{A}_{y,z}^k = \dot{q}_x^k = \dot{p}_x^k = 0$ (12 conditions for real numbers), $\dot{\varphi}^1 = \dot{\varphi}^2$ (2 conditions). In the case of the double-delta trap we mentioned already the importance of normalised wave functions. Thus, we add the constraint $||\psi|| = 1$. Due

to the arbitrary global phase one of the 16 Gaussian parameters introduced above is free and 15 parameters must be varied to fulfil the 15 conditions. This is done with a 15-dimensional root search by applying a Powell hybrid method [145]. If we consider a one-dimensional condensate the root search reduces to 11 conditions which have to be fulfilled by 11 appropriately chosen parameters. This small difference exemplifies the high scalability of the variational Gaussian method. The increase of the dimension from one to three or a better flexibility due to a superposition of more than two Gaussians leads only to a moderate increase of the numerical effort.

The numerically exact integrations are carried out for the one-dimensional setup, where the computational costs are reasonable. Similar to the procedure in the double-delta case the stationary wave functions are integrated outward from $x = 0$ in positive and negative direction using a Runge-Kutta algorithm with initial values $\mathrm{Re}\,\psi(0), \psi'(0) \in \mathbb{C}$, and $\mu \in \mathbb{C}$. They have to be chosen such that the five conditions $\psi(\infty) \to 0$, $\psi(-\infty) \to 0$, and $||\psi|| = 1$ are satisfied. The conditions define square-integrable and normalised wave functions, i.e. the stationary states we are interested in.

### 3.2.3. Stationary states in one dimension

Figure 3.7 shows the results of the solution of the one-dimensional Gross-Pitaevskii equation. Let us, again, first concentrate on the linear case $g = 0$, which exhibits the typical behaviour known from other $\mathcal{PT}$-symmetric systems [top curve in (a) and rightmost curve in (b)]. Below a critical value $\Gamma_{\mathrm{EP}} \approx 0.04$ of the gain-loss parameter $\Gamma$ we find two real eigenvalues, corresponding to a ground state with completely symmetric wave function for $\Gamma = 0$ and an excited state, of which the wave function is completely antisymmetric for $\Gamma = 0$. At $\Gamma_{\mathrm{EP}} \approx 0.04$ the two solutions merge in an exceptional point, where we have confirmed that indeed the wave functions become identical. Increasing $\Gamma$ further we obtain two complex conjugate solutions. We also note that the agreement between the Gaussian approximation and the numerically exact solution is excellent.

Obviously the real eigenvalues do not vanish in the case $g \neq 0$. This is an important result since it indicates a persistence of the $\mathcal{PT}$ symmetry in the nonlinear quantum system. Non-decaying states are present. As derived in section 2.2.2 and checked for the double-delta potential in section 3.1.2 the corresponding wave functions must be $\mathcal{PT}$ symmetric. Can this also be seen in the spatially extended double well? The answer to this question is given in figures 3.8 (a) and (b), which show the wave functions belonging to both real eigenvalues for $g = 0.2$ and $\Gamma = 0.03$. The square moduli are symmetric functions of $x$. This confirms that the case of exact $\mathcal{PT}$ symmetry is fulfilled.

There are also, as in the linear case, states with complex eigenvalues and we know that these complex eigenvalue solutions belong to $\mathcal{PT}$-broken wave functions. This behaviour has been found to be present for the double-delta trap. Again, it is found in the double-well potential, cf. figures 3.9 (a) and (b). This has the crucial impact on the nonlinear Gross-Pitaevskii equation that the square moduli of the wave functions are not symmetric functions of $x$ and the $\mathcal{PT}$ symmetry of the Hamiltonian is destroyed.

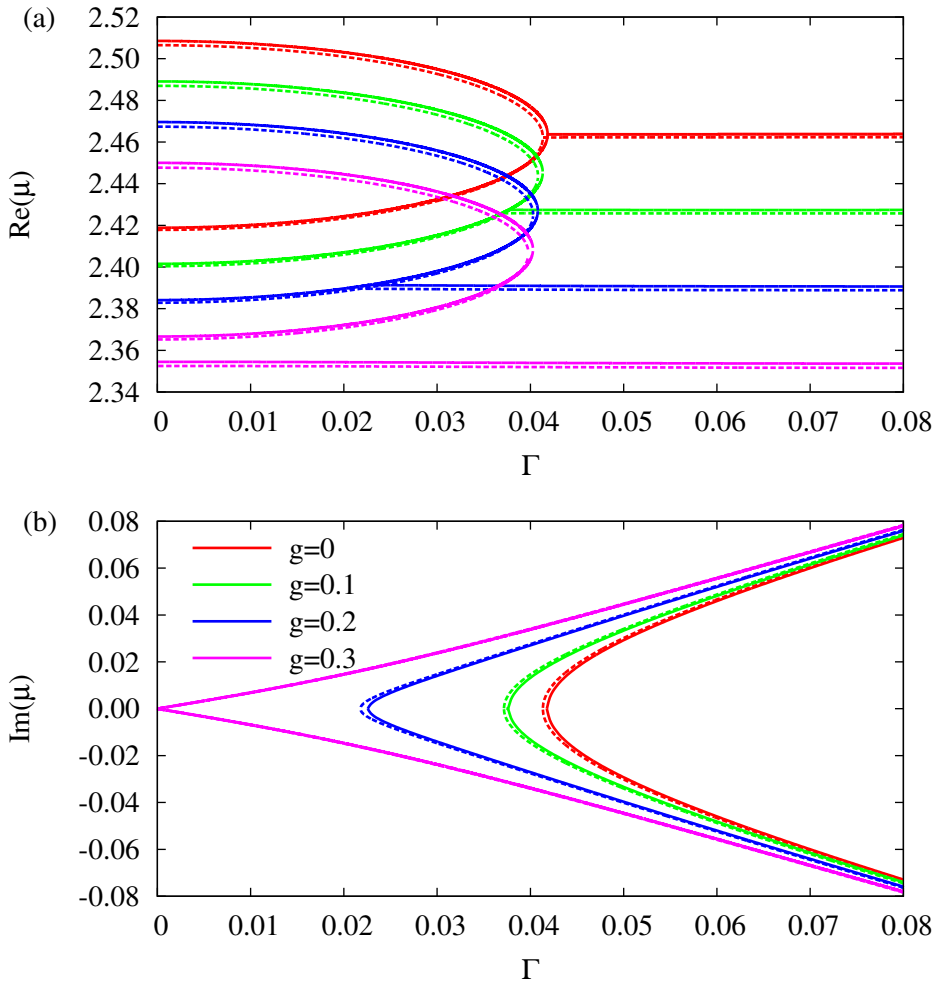


Figure 3.7.: Eigenvalues of the time-independent Gross-Pitaevskii equation for different values of the nonlinearity $g$ in dependence of the gain-loss parameter $\Gamma$. With increasing $g$ the real part of the energies decreases. The Gaussian approximation (solid lines) and the numerically exact solutions (dashed lines) are shown. Vanishing imaginary parts are not plotted. Two solutions with real eigenvalues are obtained up to a value $\Gamma_{\mathrm{EP}} \approx 0.04$, where they merge in an exceptional point. Two additional solutions with complex eigenvalues are obtained starting at a critical value $\Gamma_{\mathrm{cr}}$, where $\Gamma_{\mathrm{cr}} < \Gamma_{\mathrm{EP}}$ for $g \neq 0$.

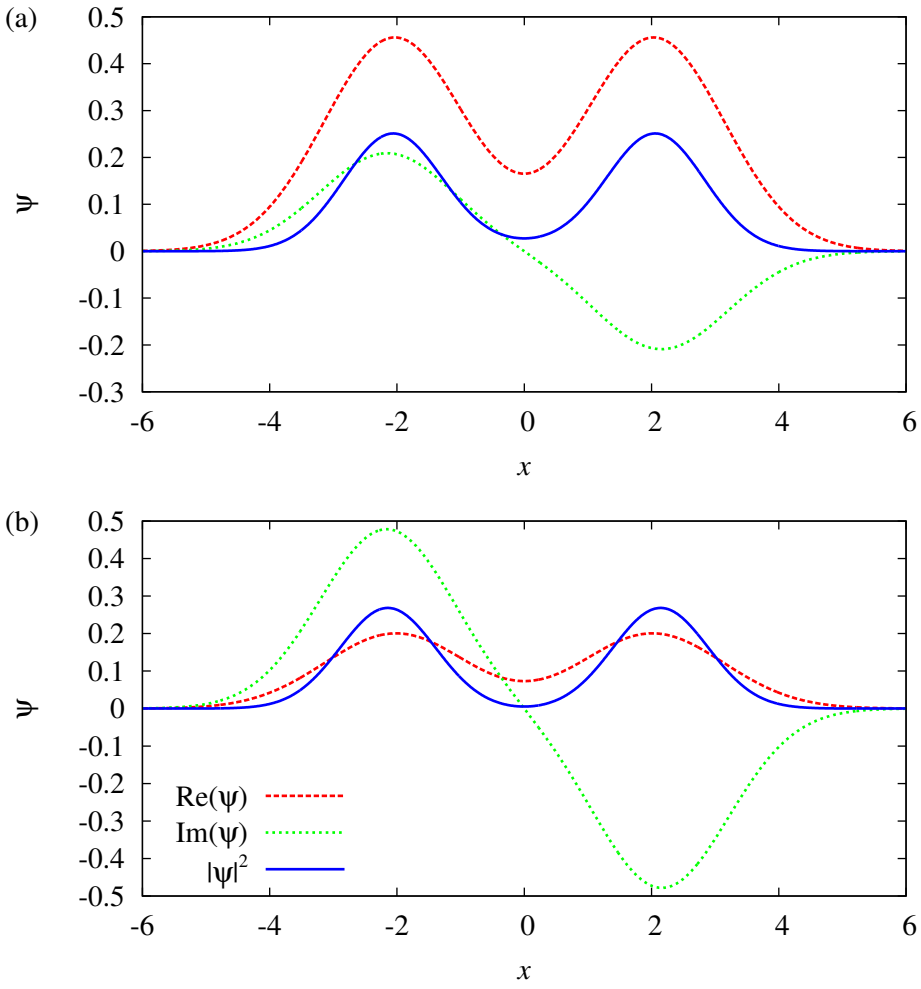


Figure 3.8.: Wave functions of the ground (a) and excited (b) eigenstates with real eigenvalues in the case $g = 0.2$ and $\Gamma = 0.03$. Only the Gaussian solutions are shown since they are almost identical with the numerically exact values. The square moduli of both wave functions are symmetric functions of $x$, preserving the $\mathcal{PT}$ symmetry of the nonlinear Hamiltonian.

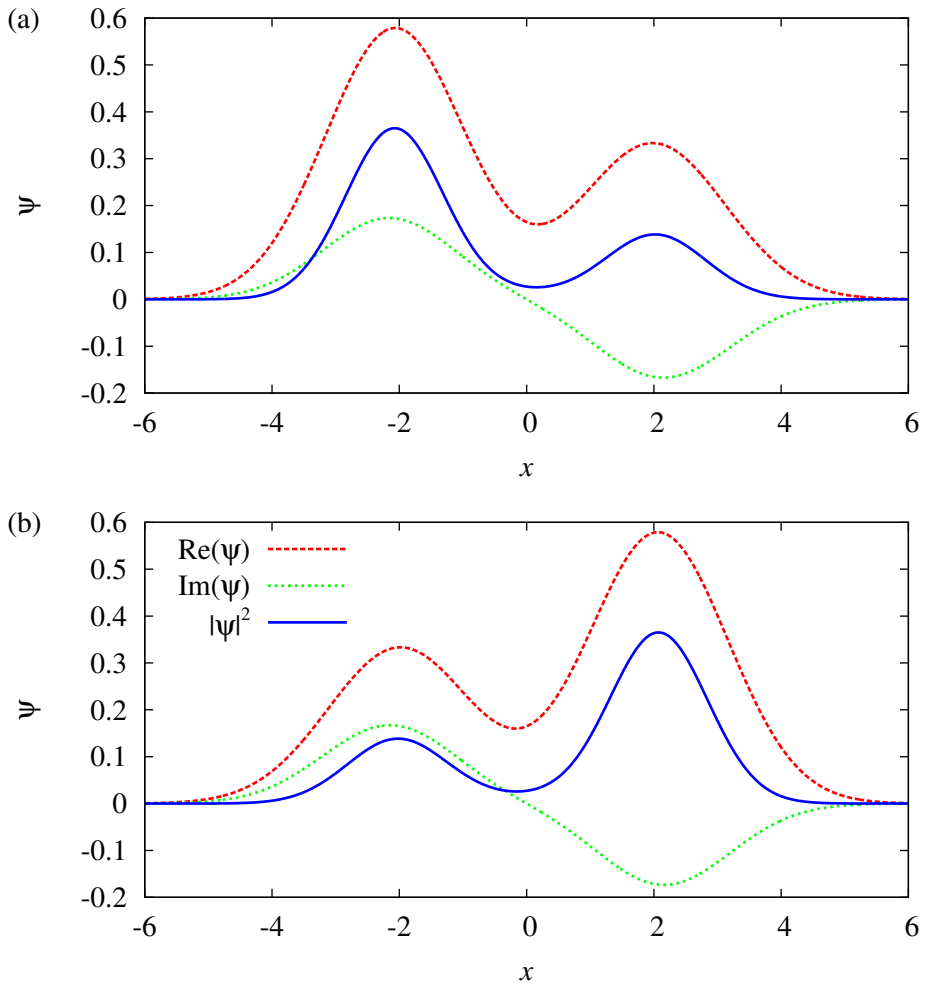


Figure 3.9.: Wave functions of the complex eigenvalue solutions with negative (a) and positive (b) imaginary part in the case $g = 0.2$ and $\Gamma = 0.03$. Again only the Gaussian wave functions are shown. The square moduli are not symmetric functions of $x$ and destroy the Hamiltonian's $\mathcal{PT}$ symmetry.

In section 3.1.2 we discussed a further crucial difference between the linear and the nonlinear system. In the linear case $g = 0$ the two complex eigenvalue solutions emerge exactly at the critical value $\Gamma_{\mathrm{EP}}$ at which the non-decaying eigenstates with real eigenvalues vanish. This does not hold for the nonlinear system, i.e. for $g \neq 0$. In the latter case the complex eigenvalue solutions are born at a value $\Gamma_{\mathrm{cr}} < \Gamma_{\mathrm{EP}}$. At the exceptional point $\Gamma_{\mathrm{EP}}$ only the real eigenvalue states vanish and new complex solutions do not appear. In figure 3.7 we observe exactly the same behaviour, which thus seems to be very generic. The effect can be related to the non-analyticity of the nonlinearity in the Gross-Pitaevskii equation and will be discussed in detail in chapter 4.

The critical parameter $\Gamma_{\mathrm{cr}}$, at which the wave functions breaking the $\mathcal{PT}$ symmetry of the potential appear, is shifted to lower values for increasing $g$. For the strongest value of the nonlinearity $g = 0.3$ chosen in figure 3.7 this results in a new scenario. Now there is no bifurcation from one of the real eigenvalue states at all. Symmetry breaking states are present for any value of $\Gamma$, even without any gain-loss effect. The symmetry breaking states for $\Gamma = 0$ are well known [146]. They possess real energies with values below those of the two symmetric states. Due to the attractive nonlinearity it is more favourable for the wave function to concentrate in one of the two wells. According to the potential's symmetry there exist two degenerate solutions, one with predominant probability in the left well and its reflected counterpart. As soon as the gain-loss parameter $\Gamma$ is switched on these two wave functions develop into two $\mathcal{PT}$-broken states with complex and complex conjugate eigenvalues $\mu$.

The different values $\Gamma_{\mathrm{EP}}$ at which the solutions with real eigenvalues merge and vanish, and $\Gamma_{\mathrm{cr}}$ at which those with complex complex eigenvalues are born leads to an interval $\Gamma_{\mathrm{cr}} < \Gamma < \Gamma_{\mathrm{EP}}$ in which both types of solutions, viz. $\mathcal{PT}$-symmetric and $\mathcal{PT}$-broken states, coexist. It has turned out that this is most conveniently summarised and discussed in the form of a phase diagram [131]. It is shown in figure 3.10. The appearance of the $\mathcal{PT}$-broken states does not only depend on the strength of the gain-loss parameter $\Gamma$. It is also crucially influenced by the strength of the nonlinearity. The stronger the nonlinearity $g$ is chosen the lower is the critical value $\Gamma_{\mathrm{cr}}$ at which the $\mathcal{PT}$-broken eigenstates emerge. This is indicated by the elliptic line separating the blue region with only $\mathcal{PT}$-symmetric states and the green area in which both $\mathcal{PT}$-symmetric and $\mathcal{PT}$-broken eigenstates are found. Beyond the value $\Gamma_{\mathrm{EP}}$, which only weakly depends on $g$, the $\mathcal{PT}$-symmetric states vanish and only the $\mathcal{PT}$-broken states are present. Two degenerate symmetry-broken wave functions are found already for $\Gamma = 0$ if the nonlinearity $g$ is attractive and strong enough as mentioned above.

### 3.2.4. Three-dimensional calculations and the importance of the one-dimensional solutions

Since only the $x$ coordinate is important for the $\mathcal{PT}$ symmetry of the potential (3.11) it is not surprising that the one-dimensional calculations considered so far already cover qual-

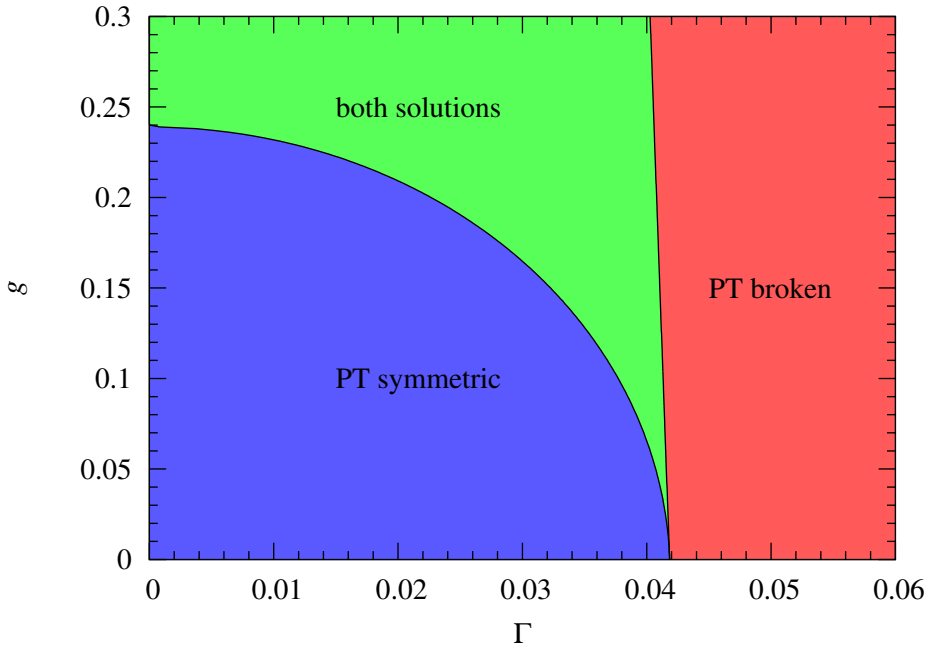


Figure 3.10.: In dependence of the gain-loss parameter $\Gamma$ and the nonlinearity $g$ three different regimes appear, in which only $\mathcal{PT}$-symmetric or only $\mathcal{PT}$-broken states are present, or both types of solutions coexist.

itatively all relevant effects. However, we want to go one step further and ask whether the one-dimensional calculations are also capable of providing precise quantitative predictions for a completely three-dimensional setup. To do so, we investigate simple but plausible assumptions on the two remaining directions and their influence on the energy eigenvalues. We will show that these assumptions lead to simple relations between the one-dimensional and the three-dimensional setup. The agreement of these relations with the fully three-dimensional calculation is very good.

The first effect of the two additional directions is clearly the interaction of the atoms in the condensate with the trapping potentials defined by the trap frequency $\omega_{y,z}$ in (3.12). If we assume that only the ground state of the corresponding oscillators is occupied, which is reasonable in the condensed phase, we obtain an energy shift by a value of $\Delta\mu = \omega_{y,z} = 2$ in the units introduced in section 3.2.1.

Since the Gross-Pitaevskii equation (3.10) contains also the nonlinear scattering term we have to take into account the normalisation integral for the energy contribution of the s-wave contact interaction. An estimate of the difference between the one- and three-dimensional contact energies can be extracted from its expectation value. We wish to describe the three-dimensional setup by an equivalent one-dimensional model, and thus

we demand that the expectation values of both contact energies are identical, viz.

$$\int_{\mathbb{R}^3} \mathrm{d}x\,\mathrm{d}y\,\mathrm{d}z\; g_{3\mathrm{D}}|\psi_{3\mathrm{D}}(\boldsymbol{x})|^4 \stackrel{!}{=} \int_{\mathbb{R}} \mathrm{d}x\; g_{1\mathrm{D}}|\psi_{1\mathrm{D}}(x)|^4 \;. \tag{3.20}$$

This leads to the relation

$$g_{3\mathrm{D}} = \frac{4\pi}{\omega_{y,z}} g_{1\mathrm{D}} \tag{3.21}$$

between the value $g_{1\mathrm{D}}$ which has to be used in the one-dimensional model such that it results in the same contact energy as a three-dimensional wave function with $g_{3\mathrm{D}}$. Again, we assumed that the harmonic oscillator ground state with its wave function $\psi_0$ is a good approximation for the directions $y$ and $z$. Furthermore, we used the product ansatz

$$\psi_{3\mathrm{D}}(\boldsymbol{x}) \approx \psi_{1D}(x)\psi_0(y)\psi_0(z) \;. \tag{3.22}$$

Of course, these simple considerations are only correct in the linear form of the Gross-Pitaevskii equation (3.10), i.e. with $g = 0$. However, in figure 3.11 we observe a remarkable agreement between the one-dimensional results based on the simple assumptions and the results of the fully three-dimensional calculations even for nonlinearities as large as $g_{1\mathrm{D}} \approx 0.3$. It is almost impossible to identify the differences.

In a further step one may assume that the one-dimensional description even becomes better when the geometry of the setup is designed to favour the spatial extension in only the $x$ direction. The previous calculations for the three-dimensional potential were carried out with a constant trapping frequency of $\omega_{y,z} = 2$. The trapping frequencies influence the condensate's shape, and thus it is expected that they have an impact on how precise the stationary solutions in one dimension can be transferred to solutions in three dimensions. The limit $\omega_{y,z} \to \infty$ effectively describes the one-dimensional potential because the widths of the wave function in $y$ and $z$ directions must vanish. Therefore the behaviour in the three-dimensional potential can be predicted more accurately by the one-dimensional solutions for higher values of $\omega_{y,z}$. Figure 3.12 confirms the convergence of the energy eigenvalues in the three-dimensional potential to the solutions in one dimension with increasing $\omega_{y,z}$. What is shown is the value of the ratio

$$r_\mu = \frac{\mu_{3\mathrm{D}} - \Delta\mu}{\mu_{1\mathrm{D}}} = \frac{\mu_{3\mathrm{D}} - \omega_{y,z}}{\mu_{1\mathrm{D}}}. \tag{3.23}$$

If the solutions in three dimensions are exactly described by the product ansatz (3.22) the ratio will be equal to one. Indeed, we observe convergence to unity for increasing values of $\omega_{y,z}$.

The convergence in the limit $\omega_{y,z} \to \infty$ is expected. What is, however, of greater interest is, at which values of the trapping frequencies the one-dimensional model becomes sufficiently accurate. We see from figure 3.12 that in particular for the stationary solutions with real eigenvalues, i.e. the $\mathcal{PT}$-symmetric states, one has rapid convergence. To achieve a good agreement between the solutions in one and three dimensions it is

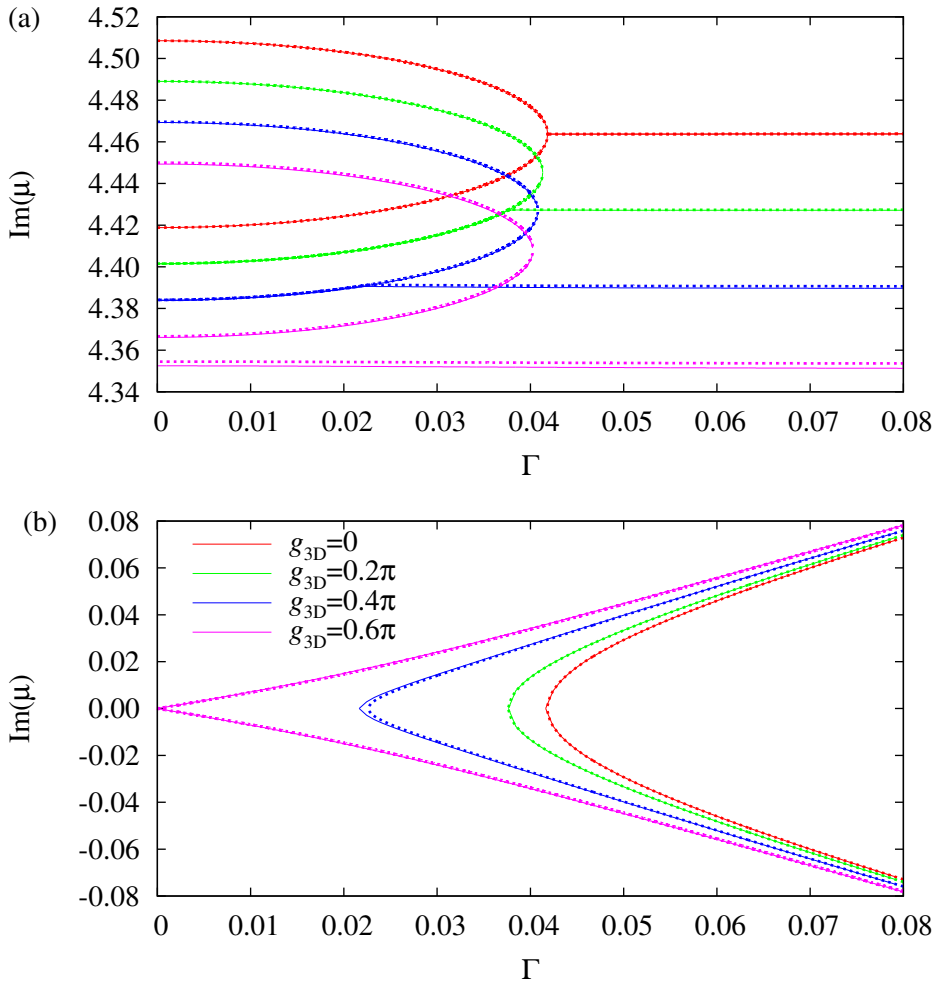


Figure 3.11.: The real (a) and nonvanishing imaginary (b) parts of the energy eigenvalues of the one-dimensional model (thick dotted lines) are compared with the fully three-dimensional calculations (thin solid lines). One observes a very good quantitative description by the simple one-dimensional treatment of the system. The differences can hardly be seen in the graph.

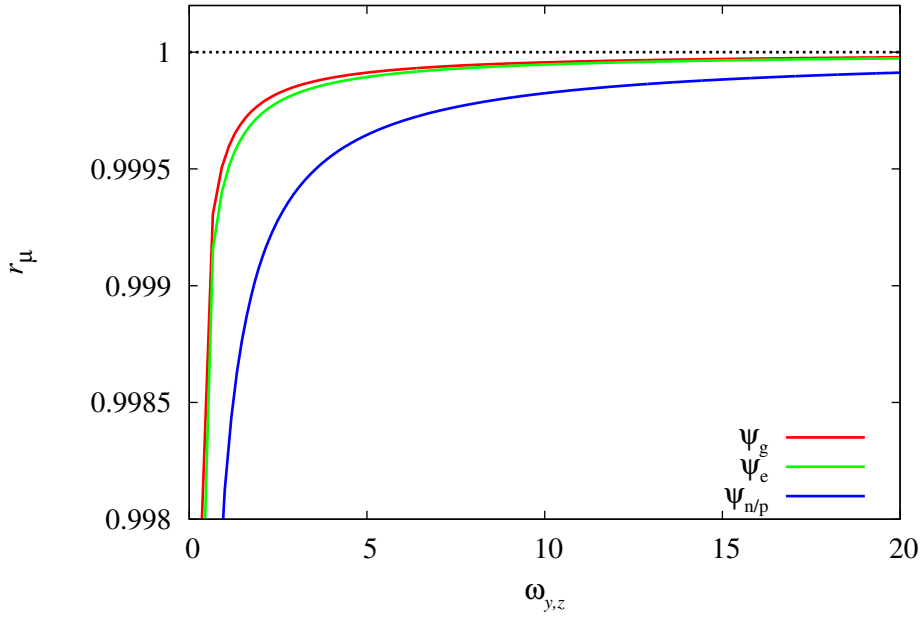


Figure 3.12.: Real part of the ratio (3.23) as a function of $\omega_{y,z}$ for the ground state $\psi_\mathrm{g}$, the excited state $\psi_\mathrm{e}$, and the $\mathcal{PT}$-broken states $\psi_\mathrm{n/p}$. All calculations are carried out for a nonlinearity of $g_\mathrm{3D} = 1.2\pi/\omega_{y,z}$, i.e. $g_\mathrm{1D} = 0.3$. For higher values of $\omega_{y,z}$ the ratio converges to unity, i.e. the agreement between the solutions in one and three dimensions becomes better and better. The $\mathcal{PT}$-symmetric solutions converge faster than the $\mathcal{PT}$-broken solutions.

obviously sufficient to choose a trapping frequency $\omega_{y,z}$ which is larger than that for the $x$ direction, i.e. in the units used for our calculation $\omega_{y,z} > 1$. This is remarkable since this does by far not mean that we are investigating a quasi one-dimensional setup. The spatial extension in $y$ and $z$ directions may be comparable to that in $x$ direction and it is still possible to extract quantitatively correct values from a simple and numerically less expensive one-dimensional calculation.

# 4. Branch points in the nonlinear Gross-Pitaevskii equation for systems with gain and loss

The eigenvalue spectra found in figures 3.3 and 3.7 revealed a structure which might be, at first glance, surprising. For different values of the gain-loss parameter both the double-delta trap discussed in section 3.1 and the spatially extended double well from section 3.2 possess a different number of stationary states. Obviously the strength of the corresponding gain-loss parameter has an influence on the number of possible solutions. There are bifurcation points at which two real eigenvalues merge and vanish without the appearance of new states, and there are further points at which complex conjugate eigenvalues are born without other states disappearing. On the one hand this observation is in contradiction to the known behaviour of linear $\mathcal{PT}$-symmetric quantum systems, where complex conjugate eigenvalues always appear exactly when two real eigenvalues vanish. The number of states is always preserved. On the other hand bifurcation points are well studied in nonlinear systems. From these studies one is also used to a preserved number of states. Only changes from real to complex eigenvalues or a change in the stability of some of the states are usually observed.

From a mathematical point of view the structures shown in figures 3.3 and 3.7 seem to be unsatisfactory. However, it is possible to give a simple explanation for the observed bifurcation scenarios. Its origin can be traced to the non-analyticity of the Gross-Pitaevskii equation. The square modulus in the nonlinear term $g|\psi|^2$ is responsible for the discontinuity in the number of states. This is shown by appropriate analytic continuations in section 4.1. They not only help to reveal the full structure at the bifurcation points, they also allow for "complete" spectra, in which states that seem to be missing in figures 3.3 and 3.7 are added. Additionally, the techniques of the continuations provide the necessary tools to identify the nature of the bifurcation points in terms of exceptional points [1, 36, 37], which is done in section 4.2.

Since the qualitative effects are identical for the double-delta trap and the spatially extended double well we restrict the discussion in this chapter to the simpler system, viz. the double-delta potential. This will provide the most illustrative description. Most of the results discussed here have been published already in references [129, 130, 147] and the chapter is based on these publications. A similar discussion for the spatially extended double well has been done in references [118, 131], and demonstrates that the

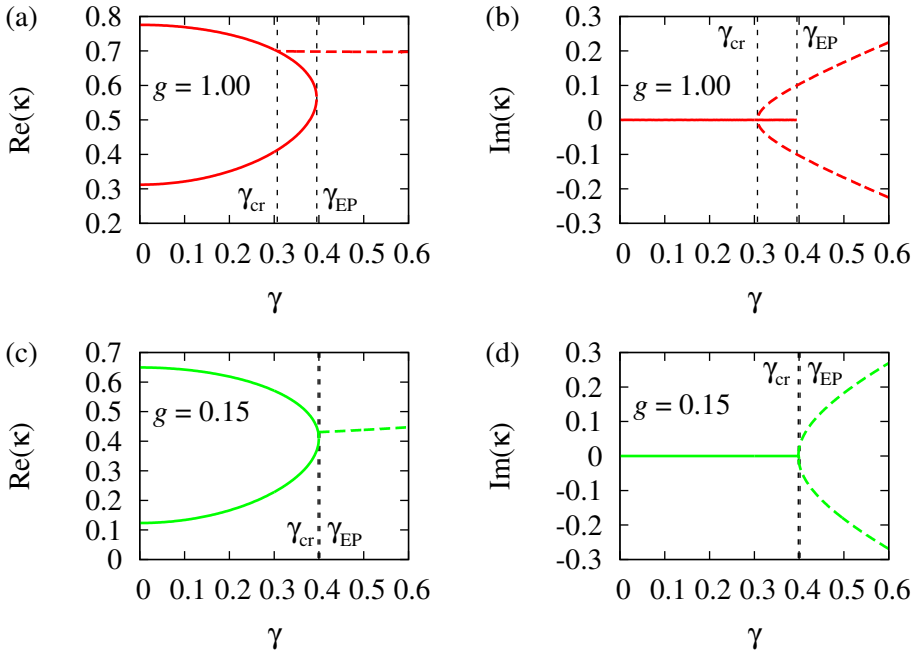


Figure 4.1.: Real parts [(a), (c)] and imaginary parts [(b), (d)] of the eigenvalues $\kappa$ of the full nonlinear equation (3.3) as functions of the gain-loss parameter $\gamma$ for $a = 2.2$ and the two values of the nonlinearity parameter $g = 1.00$ [(a) and (b)] and 0.15 [(c) and (d)]. Solid lines denote purely real eigenvalues, dashed lines complex conjugate eigenvalues. For $g \neq 0$ the complex conjugate eigenvalues bifurcate from the ground state branch at $\gamma_{\mathrm{cr}}$ before the branch point $\gamma_{\mathrm{EP}}$ where the two real solutions coalesce. Between $\gamma_{\mathrm{cr}}$ and $\gamma_{\mathrm{EP}}$ the $\mathcal{PT}$-broken and the $\mathcal{PT}$-symmetric branches coexist.

origin of the properties found for the double-delta system is not a peculiarity of the potential.

## 4.1. Analytic continuation

Figure 4.1 recapitulates the essential properties of the eigenvalues $\kappa$ for different non-vanishing values of the nonlinearity parameter $g$. For every value of $g$ a pair of real eigenvalues exists up to some value $\gamma_{\mathrm{EP}}$, where they coalesce at a branch point. Pairs of complex conjugate eigenvalues emerge at critical values $\gamma_{\mathrm{cr}} < \gamma_{\mathrm{EP}}$, where $\gamma_{\mathrm{cr}}$ decreases for increasing $g$. All examples have been calculated with $g \geq 0$, for which the complex conjugate eigenvalues bifurcate from the ground state. Note that this is the upper branch in figure 4.1 since $\kappa$ and not the energy $E = -\kappa^2$ is plotted. For $g < 0$ the complex eigenvalues branch off from the excited state. For sufficiently large nonlinearity

these solutions already appear for $\gamma = 0$. Thus one has ranges of $\gamma$ where two real and two complex conjugate eigenvalues coexist. The branching-off from the real eigenvalue changes continuously from the branch for $g = 0$.

### 4.1.1. A simple analytic continuation exploiting the symmetry of the wave functions

Pairs of complex conjugate eigenvalues emerge at the branch points only when the non-analytic term $|\psi(x)|^2$ in the Gross-Pitaevskii equation (3.3) is continued beyond the branch points. To do so we exploit in a first step the $\mathcal{PT}$ symmetry of the wave functions belonging to the real eigenvalue solutions. The choice of the arbitrary global phase of the wave functions shown in figure 3.4 has been such that

$$\mathcal{PT}\psi(x) = \psi^*(-x) = \psi(x) \tag{4.1a}$$

or in other terms

$$\mathcal{PT}\psi^*(x) = \psi(-x)\ . \tag{4.1b}$$

The formulation (4.1b) opens now a simple possibility for a continuation of the branches representing the $\mathcal{PT}$-symmetric states. For these states we may apply the replacement

$$g|\psi(x)|^2 \to g\,\psi(x)\psi(-x)\ , \tag{4.2}$$

which turns the non-analytic nonlinearity into an analytic function. Obviously the $\mathcal{PT}$-symmetric states will not be affected by this replacement since they fulfil exactly the symmetry (4.1b). Beyond the branch point $\gamma_{\mathrm{EP}}$ the analytic form allows for additional solutions not available with the correct Gross-Pitaevskii nonlinearity $g|\psi(x)|^2$. To calculate them we introduce the substitution (4.2) at all places in which the square modulus appears. We require, however, that the new wave functions fulfil the same conditions as in the non-continued case. In particular, they have to be normalised to unity. With the replacement (4.2) the norm condition reads

$$\int_{-\infty}^{\infty} \psi(x)\psi(-x)\mathrm{d}x \stackrel{!}{=} 1\ , \tag{4.3}$$

and has obviously two components. The integral may now assume a complex value. Thus, one has to add the condition that its imaginary part must vanish. This condition fixes the global phase of the wave function. It is no longer arbitrary. However, this does not contradict the free choice of the global phase we applied in section 3.1.2. Only with this choice, viz. that the wave function is real at the origin, the symmetry relation (4.1b), which was the starting point of our considerations in this section, is possible. Consequently, it turns out that numerically obtained $\mathcal{PT}$-symmetric wave functions for

real eigenvalues with the replacement (4.2) and the requirement (4.3) have a global phase exactly fixed to $\operatorname{Im}\psi(0) = 0$.

The method introduced above leads to a slightly modified numerical procedure as compared to section 3.1.2. The wave function is integrated outward from $x = 0$ with six initially chosen values, viz. the real and imaginary parts of $\psi(0)$, $\psi'(0)$, and $\kappa$. In addition to the two real requirements (4.3) the real and imaginary parts of $\psi$ still have to vanish for $x \to \pm\infty$, which results in a six-dimensional root search.

The result of this procedure is illustrated in figure 4.2. The analytic continuation shows that the number of solutions does not change at the branch point $\gamma_{\mathrm{EP}}$. Two additional solutions are obtained (dotted lines). The real and imaginary parts of the corresponding wave functions and their moduli are shown in figure 4.3. Obviously the states are no longer $\mathcal{PT}$ symmetric. Their imaginary part at the origin does not vanish, which is a result of the fixed global phase.

The results so far demonstrate that the inconsistency in the number of solutions can be related to the non-analytic character of the nonlinearity in the Gross-Pitaevskii equation. With a simple analytic continuation especially designed for a continuation of $\mathcal{PT}$-symmetric states it was possible to find a complete picture at one branch point, at which the number of states could be conserved. The continuation applied so far had the advantage that it was simple and could be found with apparent symmetry arguments. However, it still has two major drawbacks. The first is connected with the $\mathcal{PT}$-broken states with complex eigenvalues. These states do not fulfil the symmetry (4.1b), and thus are not available with the substitution (4.2). To obtain all states shown in figure 4.2 two different equations have to be solved! The second drawback lies in the second branch point $\gamma_{\mathrm{cr}}$. Even with the continuation applied so far the number of states is less for $\gamma < \gamma_{\mathrm{cr}}$. The pair of complex eigenvalues bifurcating from the ground state at $\gamma_{\mathrm{cr}}$ seem to come about without real-valued precursors. It will be the topic of section 4.1.2 to apply a full analytic continuation eliminating these two drawbacks.

### 4.1.2. Full analytic continuation

The procedure of the full analytic continuation [45, 112] is to express all complex quantities by two real-valued functions, either amplitude and phase, or real and imaginary parts. The non-analytic Gross-Pitaevskii equation then decomposes into two coupled real-valued differential equations which can be continued analytically by allowing all variables to obtain complex values.

We write for the wave function, the double-well potential and the eigenvalue

$$\psi = \psi_{\mathrm{r}} + \mathrm{i}\psi_{\mathrm{i}} \,, \tag{4.4}$$

$$V = V_{\mathrm{r}} + \mathrm{i}V_{\mathrm{i}} \,, \tag{4.5}$$

$$\text{and} \quad \kappa = \kappa_{\mathrm{r}} + \mathrm{i}\kappa_{\mathrm{i}} \,, \tag{4.6}$$

respectively. Inserting this separation into the Gross-Pitaevskii equation and sorting the

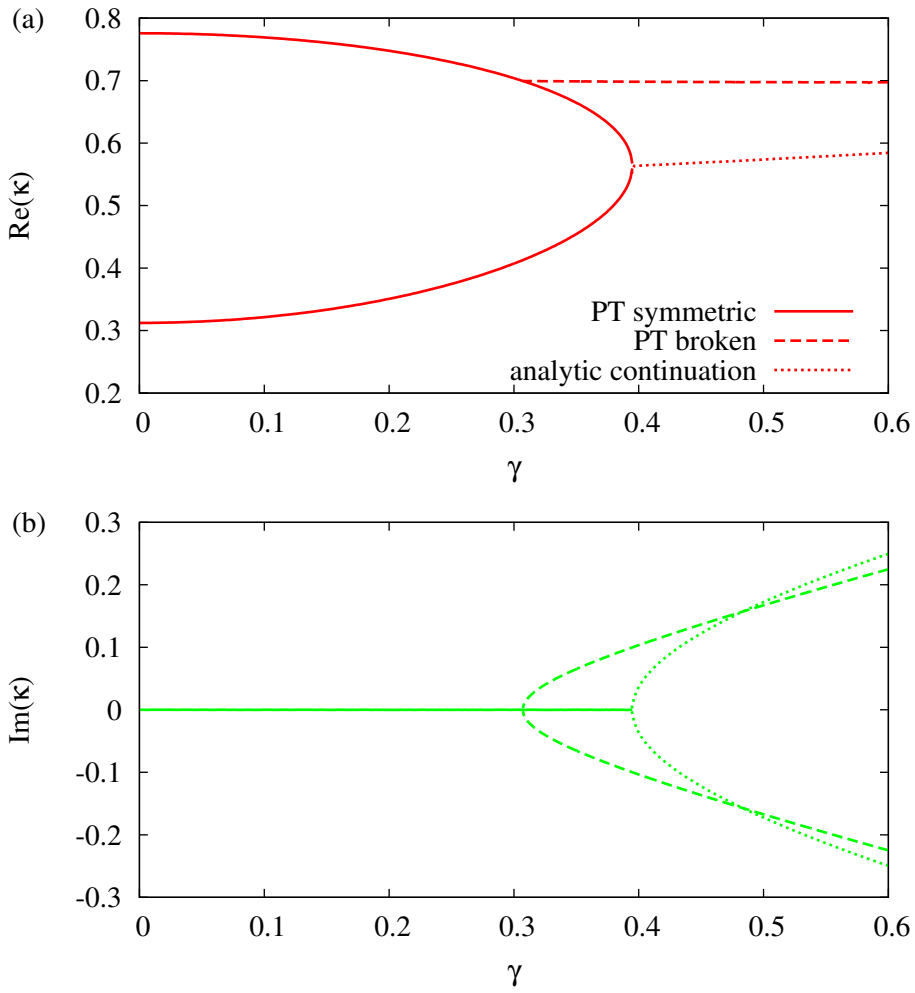


Figure 4.2.: Real (a) and imaginary (b) parts of the eigenvalues $\kappa$ for the states appearing at $g = 1$ for different values $\gamma$. Using the substitution $|\psi(x)|^2 \to \psi(x)\psi(-x)$ the analytic continuation beyond the branch point $\gamma_{\mathrm{EP}}$ of the two real $\mathcal{PT}$-symmetric eigenvalue states is obtained (dotted lines).

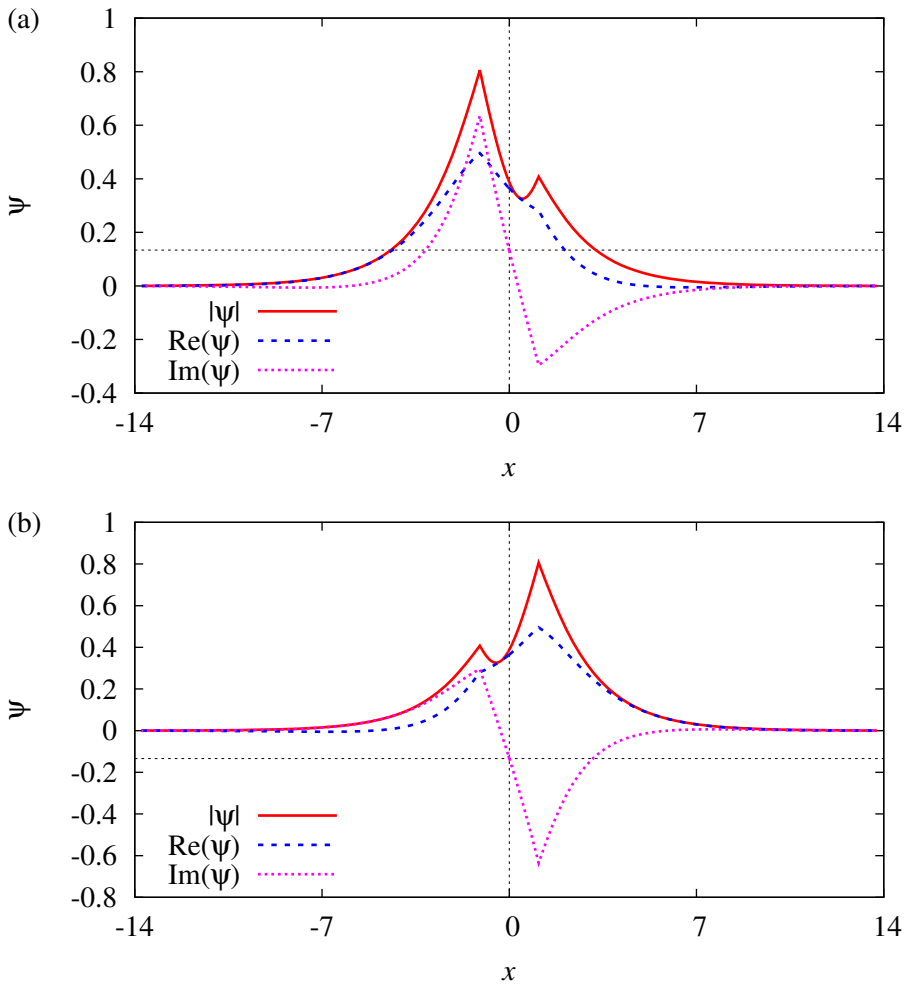


Figure 4.3.: Wave functions of the eigenstates belonging to the complex eigenvalues of the analytic continuation for $g = 1.0$, $a = 2.2$ and $\gamma = 0.5$. The eigenfunctions are not $\mathcal{PT}$ symmetric. The black dotted lines have been drawn to illustrate that $\mathrm{Im}\,\Psi(0) \neq 0$.

real and imaginary contributions leads to

$$-\psi_\mathrm{r}'' + V_\mathrm{r}\psi_\mathrm{r} - V_\mathrm{i}\psi_\mathrm{i} - g(\psi_\mathrm{r}^2 + \psi_\mathrm{i}^2)\psi_\mathrm{r} = \kappa_\mathrm{r}\psi_\mathrm{r} - \kappa_\mathrm{i}\psi_\mathrm{i} \,, \tag{4.7a}$$
$$-\psi_\mathrm{i}'' + V_\mathrm{r}\psi_\mathrm{i} + V_\mathrm{i}\psi_\mathrm{r} - g(\psi_\mathrm{r}^2 + \psi_\mathrm{i}^2)\psi_\mathrm{i} = \kappa_\mathrm{r}\psi_\mathrm{i} + \kappa_\mathrm{i}\psi_\mathrm{r} \,. \tag{4.7b}$$

The full analytic extension is implemented by allowing these real and imaginary parts of the wave functions and eigenvalues to become themselves complex:

$$\psi_\mathrm{r} = \psi_\mathrm{rr} + \mathrm{i}\psi_\mathrm{ri} \,, \tag{4.8a}$$
$$\psi_\mathrm{i} = \psi_\mathrm{ir} + \mathrm{i}\psi_\mathrm{ii} \,, \tag{4.8b}$$
$$\kappa_\mathrm{r} = \kappa_\mathrm{rr} + \mathrm{i}\kappa_\mathrm{ri} \,, \tag{4.8c}$$
$$\kappa_\mathrm{i} = \kappa_\mathrm{ir} + \mathrm{i}\kappa_\mathrm{ii} \,. \tag{4.8d}$$

This extension allows for continuing both the $\mathcal{PT}$-symmetric and the $\mathcal{PT}$-broken states beyond the corresponding branch points. The numerical procedure to find the solutions of the system of equations (4.7) is identical to that introduced in section 3.1.2. The initial values for $\psi_\mathrm{r}(0)$, $\psi_\mathrm{r}'(0)$, $\psi_\mathrm{i}'(0)$, and the two parts of the eigenvalue $\kappa_\mathrm{r}$ and $\kappa_\mathrm{r}$ have to be chosen such that $\psi_\mathrm{r}$ and $\psi_\mathrm{i}$ vanish for $x \to \pm\infty$ and the norm fulfils $\int(\psi_\mathrm{r}^2 + \psi_\mathrm{i}^2)\,\mathrm{d}x = 1$. Since all variables are complex numbers this results in 10 values which have to chosen in a root search such that 10 conditions are satisfied. The choice for the global phase introduced in section 3.1.2 is not affected by the analytic extension.

When plotting the eigenvalues we recombine the 4 real quantities $\kappa_\mathrm{rr}$, $\kappa_\mathrm{ri}$, $\kappa_\mathrm{ir}$, $\kappa_\mathrm{ii}$ into the real and imaginary parts of $\kappa$, i.e.

$$\kappa = (\kappa_\mathrm{rr} - \kappa_\mathrm{ii}) + \mathrm{i}(\kappa_\mathrm{ri} + \kappa_\mathrm{ir}) = \mathrm{Re}(\kappa) + \mathrm{i}\ \mathrm{Im}(\kappa) \,. \tag{4.9}$$

For the value of the nonlinearity parameter $g = 1$ the results for $\mathrm{Re}(\kappa)$ and $\mathrm{Im}(\kappa)$ are shown in figure 4.4. In addition to the two branches, which have already been uncovered with the previous ansatz, there are indeed two new branches of real-valued $\kappa$ for $\gamma \leq \gamma_\mathrm{cr}$. They merge at $\gamma_\mathrm{cr}$ and give rise to the complex conjugate pair of eigenvalues. Moreover, these two solutions are present even at $\gamma = 0$, where they refer to two degenerate eigenvalues.

It is remarkable that the spectra of the two additional states obtained by the analytic continuation become very similar to the spectra of the original $\mathcal{PT}$-symmetric solutions when $g$ is decreased. This is demonstrated in figure 4.5, where the spectra shown should be compared with those in figure 4.1. There is, however, one difference: the two additional solutions are degenerate at $\gamma = 0$ for any $g \neq 0$, while the eigenvalues of the two original $\mathcal{PT}$-symmetric states always have different values at this point.

For $g > 0$ the wave functions of the analytically continued states shown in figure 4.5 differ of course from those of the original real eigenvalues. They are illustrated for $g = 1.0$ in figure 4.6 for a few values of $0 \leq \gamma \leq \gamma_\mathrm{cr}$ to show their structure.

For $0 < \gamma < \gamma_\mathrm{cr}$ the complex extended wave functions possess four nonvanishing components. Nevertheless they are eigenfunctions of $\mathcal{PT}$ throughout in that their real

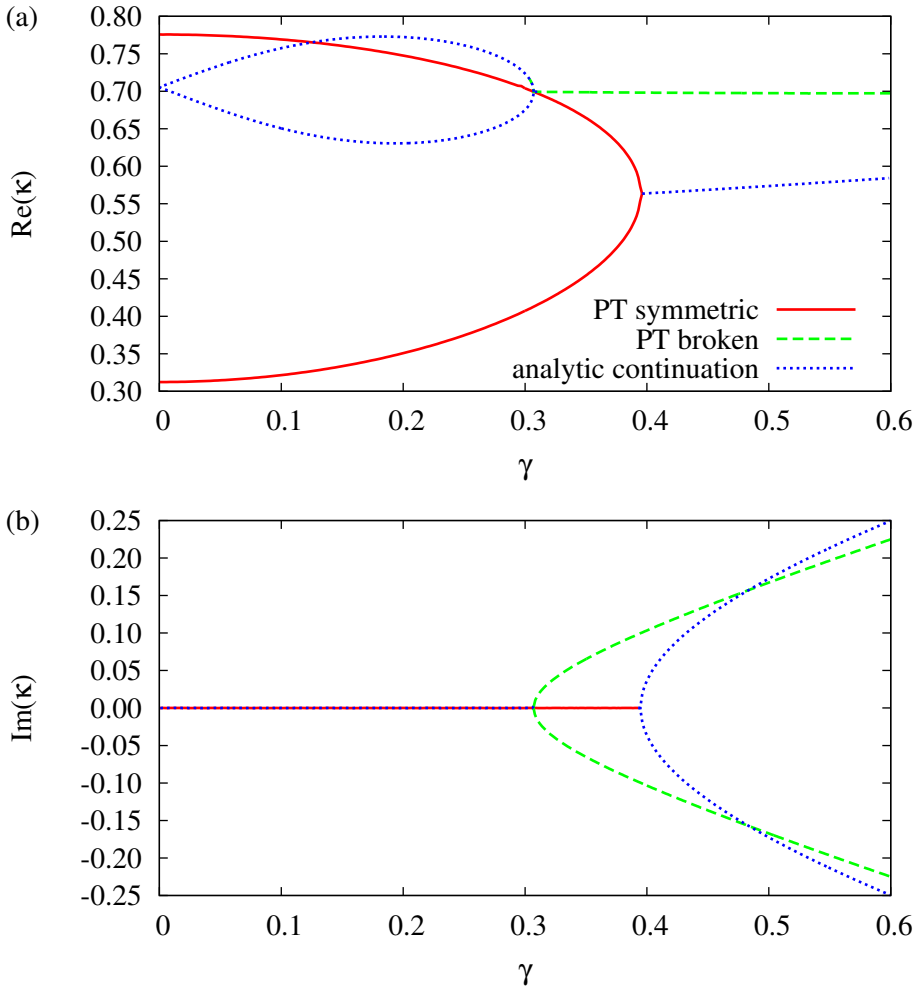


Figure 4.4.: Real Re($\kappa$) (a) and imaginary Im($\kappa$) (b) parts of the spectra after the analytical extension for $g = 1$. The red solid and green dashed lines represent the $\mathcal{PT}$-symmetric and $\mathcal{PT}$-broken states already known without any analytic continuation. The new states visible with the full analytic continuation (4.8a)-(4.8d), and the recombination (4.9) of the energies are marked by blue dotted lines. With these continued states the number of states does no longer change with $\gamma$.

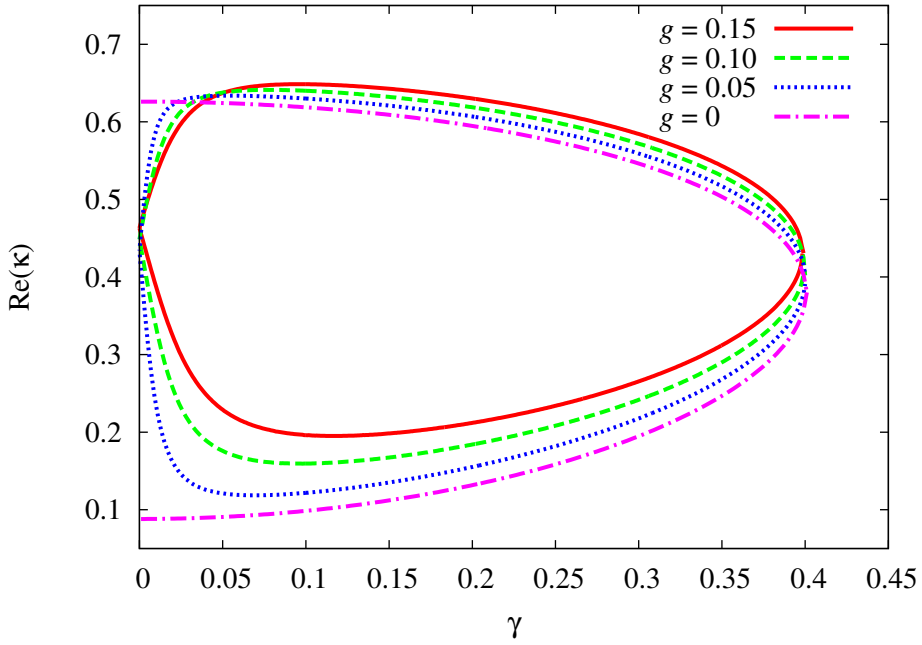


Figure 4.5.: Eigenvalues of the two branches emerging at $\gamma_{\mathrm{cr}}$ in the analytic continuation for $g = 0.15$ (red solid lines), $g = 0.10$ (green dashed lines), and $g = 0.05$ (blue dotted lines). For comparison the spectra of the $\mathcal{PT}$-symmetric states without the nonlinear term ($g = 0$) are also displayed.

parts $\mathrm{Re}(\psi)$ are symmetric and their imaginary parts $\mathrm{Im}(\psi)$ antisymmetric. Note that there is a nonvanishing imaginary part $\psi_{\mathrm{ri}}$ due to the analytic continuation even at $\gamma = 0$. At this point the two wave functions are associated with the same energy value as $\kappa_{\mathrm{ii}} = 0$, i.e. there is a genuine degeneracy, which is in contrast to the wave functions of the other two energies appearing for $\gamma = 0$. The imaginary part $\psi_{\mathrm{ii}}$ tends to zero when $\gamma_{\mathrm{cr}}$ is approached while another imaginary part $\psi_{\mathrm{ir}}$ – not due to the analytic continuation – emerges. At $\gamma_{\mathrm{cr}}$, the two wave functions become equal to themselves and to the third (original) state with which they coalesce. From this point onwards the states are found without the complex extension, in fact the parts invoked from the extension vanish. Note also, that the additional real part $\psi_{\mathrm{ii}}$ switches on and off at the endpoints of the interval $[0, \gamma_{\mathrm{cr}}]$ similarly to the behaviour of $\kappa_{\mathrm{ii}}$.

## 4.2. Exceptional point behaviour

As pointed out above the three eigenfunctions are identical at the point $\gamma_{\mathrm{cr}}$. Therefore the question arises whether or not this point is a third-order exceptional point. This is a crucial difference between the nonlinear Gross-Pitaevskii equation [112, 129–131]

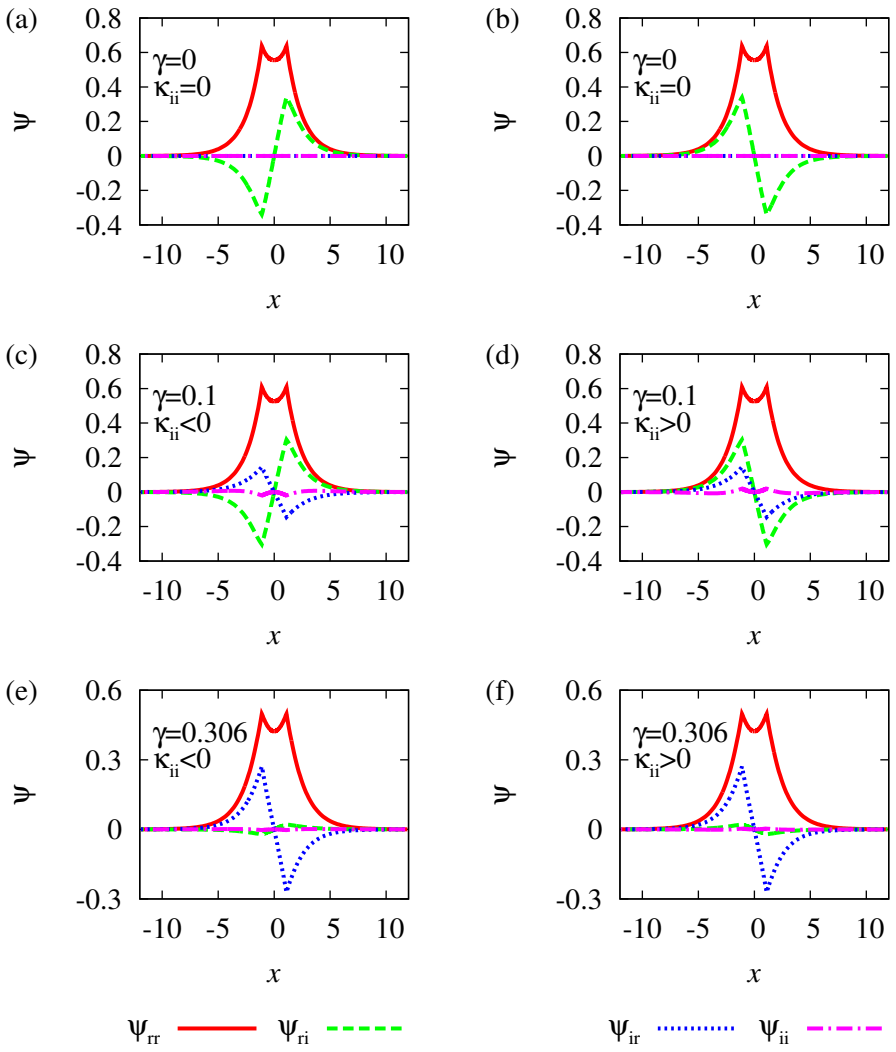


Figure 4.6.: Wave functions of the analytically extended solutions for a few values of $\gamma < \gamma_{cr}$ and $g = 1$. The right (left) column refers to the lower (upper) branch of the eigenvalues.

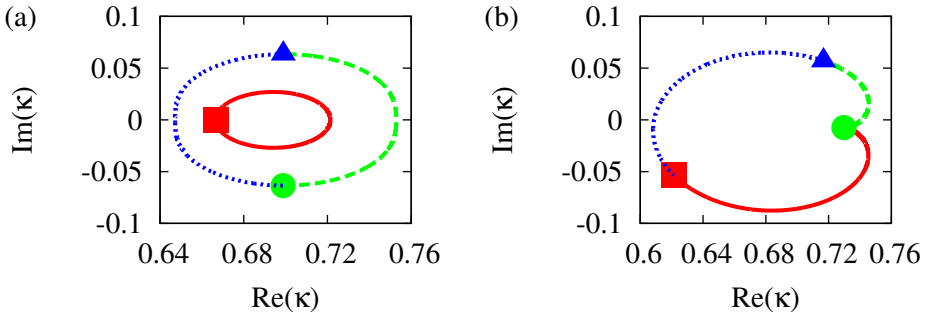


Figure 4.7.: Exceptional point behaviour: (a) Circle according to equation (4.10). For $\varphi = 0$ we have $\gamma = 0.312$ and the three states exist without complex continuation. The red square marks the ground state with real $\kappa$. Its trace on the parameter space circle is represented by the red solid line. The two states with positive and negative imaginary parts of the eigenvalues $\kappa$ are represented by the blue triangle (blue dotted line for $\varphi \neq 0$) and the green circle (green dashed line), respectively. (b) The same for the circle defined in equation (4.12), where the asymmetry parameter is varied.

and linear $\mathcal{PT}$-symmetric quantum systems, in which this additional point does not appear. As introduced in section 2.1.2 exceptional points are isolated singularities of the spectrum in the physical parameter space. We denote by EP2 the point where two states coalesce, i.e. their eigenvalues *and* their wave functions are identical; similarly, an EP3 denotes the point where three states coalesce (cf. section 2.1.2).

As a function of the parameter the levels and state vectors have typically a square root singularity at an EP2 and a cubic root singularity at an EP3. There are, however, special cases in which an EP3 exhibits features, which indicate a square root branch point [77] and special care has to be taken, when exceptional points are to be identified by their impact on the spectra. In the usual case, in which the correct root is observed the eigenvalues and the wave functions are interchanged at an EP2 (up to a possible phase of the latter, see e.g. [75]) when the exceptional point is encircled on a closed contour in parameter space. The three identical wave functions at $\gamma_{\mathrm{cr}}$ indicate an EP3, i.e. a cubic root branch point. For a closed contour around this point a cyclic permutation of all three eigenvalues and eigenfunctions is then expected.

To test numerically the precise character of the exceptional point one parameter must be extended into the complex plane. Confirmation is obtained by encircling the point of coalescence and checking the appropriate change of the eigenvalues and state vectors. Figure 4.7 (a) shows the result for a nonlinearity of $g = 1$ when the point $\gamma_{\mathrm{cr}} \approx 0.308$ is encircled in the complex extended $\gamma$ plane according to

$$\gamma(\varphi) = 0.308 + 0.04\mathrm{e}^{\mathrm{i}\varphi} , \qquad \varphi = 0 \ldots 2\pi . \tag{4.10}$$

One clearly sees that only the two complex eigenvalues interchange while the ground state remains unaffected. The same holds for the corresponding eigenfunctions. It thus appears that we deal with an EP2 corresponding to the merging of the two new eigenvalues.

However, as mentioned above this is not a clear identification of an EP2. For every EP3 there exists at least one special parameter variation under which it looks like an EP2 [77]. To uncover the true nature of the point at $\gamma_{\mathrm{cr}}$ we introduce a second and completely independent parameter variation. When we allow an arbitrarily small asymmetry for the real part of the double-well potential by considering

$$V_{\mathrm{asym}} = A\left[\delta(x - a/2) - \delta(x + a/2)\right] \ , \tag{4.11}$$

and encircle now the branch point around $A = 0$ in the complex extended $A$ plane along the line

$$A = 0.04\mathrm{e}^{\mathrm{i}\varphi} \ , \qquad \varphi = 0 \ldots 2\pi \ , \tag{4.12}$$

figure 4.7 (b) clearly points to an EP3. We stress that any other perturbation would produce the same result: the apparent EP2 which does not involve the third state becomes a true EP3 nesting together all three states as soon as the problem becomes disturbed, no matter of what nature and how small the disturbance may be. This behaviour is similar to that of a study of a simple matrix model by Demange and Graefe [77] where three coalescing eigenvectors can exhibit both the behaviour of second- or third-order exceptional point depending on the choice of parameters. The same behaviour has also been found in the investigation of pitchfork bifurcations occurring in Bose-Einstein condensates with dipolar interaction [78].

At this point its worthwhile to mention that simple matrix models covering all features of the nonlinear Gross-Pitaevskii equation can be constructed. These contain either only the three states forming the EP3 [147] or all four states of the double-delta model [118, 148]. Since these models allow for analytical expressions in many cases studied here, they help to get even more insight into the mathematical structures of the eigenvalues.

# 5. Stability of the stationary states

In sections 3.1.2, 3.2.3, and 3.2.4 we found stationary states of a Bose-Einstein condensate trapped in the attractive double-delta potential as well as in the more realistic spatially extended double well. Even though it is possible to show that these states exist under experimentally accessible conditions for the condensate and the trap, this does not give a definite answer to the question whether or not a condensate trapped in a double-well structure with $\mathcal{PT}$-symmetric gain and loss contributions will be observable in an experiment. It will only be observable if the eigenstates are dynamically stable with respect to quantum fluctuations. The first step to understand the dynamical properties of the condensate wave function is a linear stability analysis. This is the subject of this chapter.

We will first introduce the stability analysis in terms of the Bogoliubov-de Gennes equations in section 5.1 and then study the stability of the stationary states in section 5.2. This will uncover an unexpected behaviour of the stability change close to the critical point at which the $\mathcal{PT}$-broken states branch off from one of the truly stationary real eigenvalue states, which will be analysed in detail in section 5.3.

Parts of this chapter are based on articles which have already been published in references [131, 132]. Other parts are newer work, which has been submitted for publication [149, 150]. Parts of the data for the spatially extended double well have been produced together with Dennis Dast and Daniel Haag during their Master's theses [134, 135] and parts of the numerical calculations for the double-delta system have been done together with Andreas Löhle during his Bachelor's thesis [151].

## 5.1. Bogoliubov-de Gennes equations for a condensate in a $\mathcal{PT}$-symmetric double well

The linear stability is analysed by means of the Bogoliubov-de Gennes equations. Since there is no principle difference between the one-dimensional and the three-dimensional case the following discussion is reduced to the simpler one-dimensional form. As shown in section 3.2.4 this is also the relevant case since it covers already all effects of the $\mathcal{PT}$-symmetric potential. Thus, the one-dimensional consideration will also be the one which will be discussed in the following sections.

The Bogoliubov-de Gennes equations are derived under the assumption that a sta-

tionary state $\psi_0(x,t)$ is perturbed by a small fluctuation $\theta(x,t)$, i.e.

$$\psi(x,t) = \mathrm{e}^{-\mathrm{i}\mu t}\left[\psi_0(x) + \theta(x,t)\right] \ , \tag{5.1a}$$

where

$$\theta(x,t) = u(x)\mathrm{e}^{-\mathrm{i}\omega t} + v^*(x)\mathrm{e}^{\mathrm{i}\omega^* t} \ . \tag{5.1b}$$

With this ansatz and a linearisation in the small quantities $u$ and $v$ one obtains from the Gross-Pitaevskii equation the coupled system of the Bogoliubov-de Gennes differential equations,

$$\frac{\mathrm{d}^2}{\mathrm{d}x^2}u(x) = \left[V(x) - \mu - \omega - 2g|\psi_0(x)|^2\right]u(x) - g\psi_0(x)^2 v(x) \ , \tag{5.2a}$$

$$\frac{\mathrm{d}^2}{\mathrm{d}x^2}v(x) = \left[V^*(x) - \mu^* + \omega - 2g|\psi_0(x)|^2\right]v(x) - g\psi_0^*(x)^2 u(x) \ . \tag{5.2b}$$

In equation (5.1b) it can be seen that $\omega$ decides on the temporal evolution of the fluctuation. Real values of $\omega$ describe stable oscillations, whereas imaginary parts lead to a growth or decay of the fluctuation's amplitude. Thus, $\omega$ measures the stability of the stationary solution $\psi_0$ against small fluctuations.

Numerically the Bogoliubov-de Gennes equations are solved with the same method as the stationary states described in section 3.1.2, i.e. the wave functions $u$ and $v$ are integrated outward from $x = 0$. It can easily be seen that the Bogoliubov-de Gennes equations (5.2) are invariant under the transformation $u(x) \to u(x)\mathrm{e}^{\mathrm{i}\chi}$, $v(x) \to v(x)\mathrm{e}^{\mathrm{i}\chi}$ with a real phase $\chi$. Similarly to the procedure for the integration of the stationary states this symmetry can be exploited. The remaining initial values with which the integration has to be started are $u(0) \in \mathbb{C}$, $\mathrm{Re}(v(0))$, $u'(0) \in \mathbb{C}$, $v'(0) \in \mathbb{C}$, $\omega \in \mathbb{C}$. In a nine-dimensional root search they have to be chosen such that the conditions $u(\pm\infty) \to 0$, $v(\pm\infty) \to 0$, and

$$\int_{-\infty}^{\infty} |u(x) + v^*(x)|^2 \, \mathrm{d}x = 1$$

are fulfilled [131].

Two further symmetries can be exploited to reduce the number of independent stability eigenvalues which have to be calculated. The replacement $(u, v, \omega) \to (v^*, u^*, -\omega^*)$ leaves the ansatz (5.1b) invariant. Thus, if $\omega$ is a stability eigenvalue also $-\omega^*$ is a valid solution. Furthermore for every eigenvalue $\omega$ there is also one solution with the eigenvalue $\omega^*$ if the stationary state $\psi_0$ is $\mathcal{PT}$ symmetric. This can be verified by applying the $\mathcal{PT}$ operator to the Bogoliubov-de Gennes equations (5.2). Due to these two symmetries it is sufficient to search for stability eigenvalues with $\mathrm{Re}(\omega) > 0$ and $\mathrm{Im}(\omega) > 0$.

## 5.2. Stability of the stationary states

We are only interested in the stability of the true stationary states with real eigenvalues. As was mentioned in section 3.1.2 the states with complex eigenvalues are no

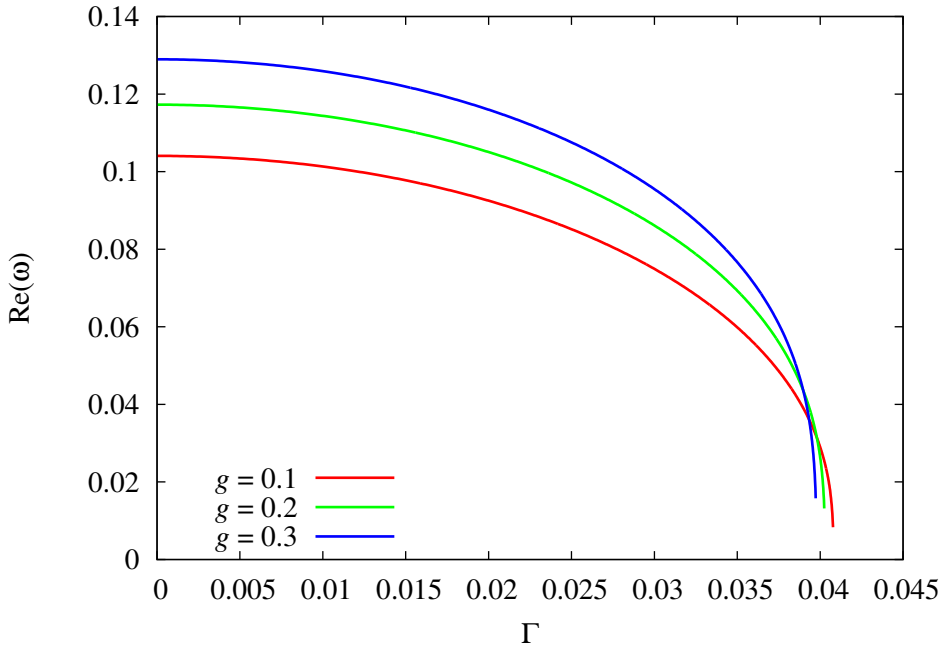


Figure 5.1.: Lowest stability eigenvalues of the excited states shown in figure 3.7 for the spatially extended double well and several values of the nonlinearity parameter $g$. The state exhibits only purely real eigenvalues $\omega$, and thus is stable as long as it exists.

stationary solutions of the time-dependent Gross-Pitaevskii equation. They grow or decay, and immediately introduce an explicit time-dependence in the nonlinear Hamiltonian. By contrast, the states with real eigenvalues are true stationary solutions of the time-dependent Gross-Pitaevskii equation, and might be observable in an experiment, if they turn out to be dynamically stable against small fluctuations. Thus, we study their stability properties.

Surprisingly, it is the excited state which turns out to possess the simplest stability structure, and we discuss it first. Figure 5.1 shows the lowest stability eigenvalue of the excited states presented in figure 3.7 for the spatially extended double well. Only real parts are drawn since all imaginary parts vanish. This holds for almost any value of the gain-loss parameter $\Gamma$ up to the value $\Gamma_{\mathrm{EP}}$ at which the state itself merges with the ground state and disappears. Thus, we conclude that the excited state seems to be stable as long as it exists. Eigenvalues of higher modes do not change this behaviour since they stay real.

More complicated – and more interesting – is the stability behaviour of the ground state. It is depicted in figure 5.2, in which the lowest stability eigenvalue of the ground states from figure 3.7 are shown. For every value of the nonlinearity strength $g$ there is a value of $\Gamma$ at which the stability changes. Below this value the eigenvalue $\omega$ is real

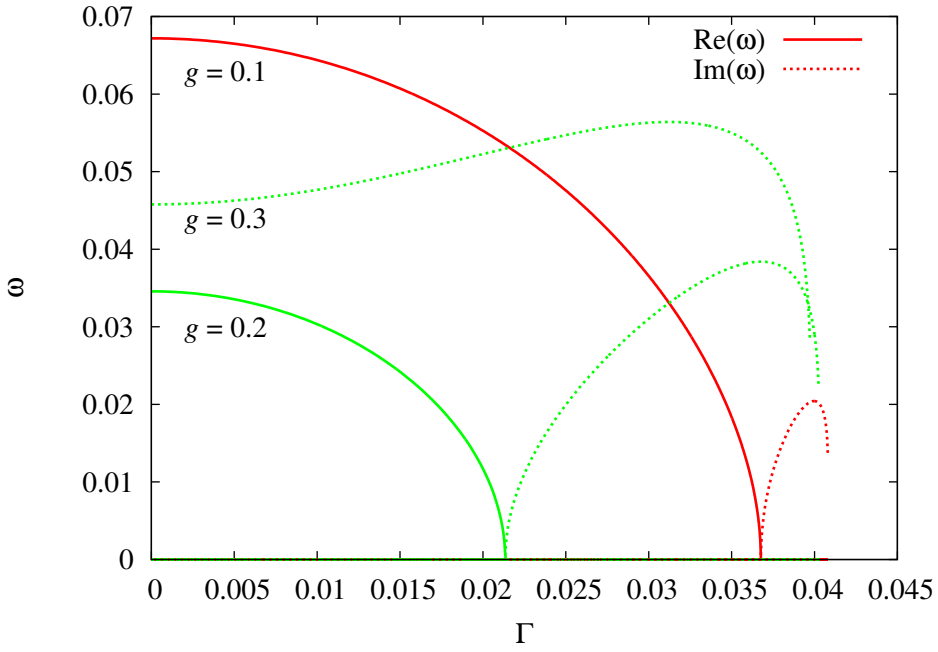


Figure 5.2.: Lowest stability eigenvalues of the ground states shown in figure 3.7 for the spatially extended double well and several values of the nonlinearity parameter $g$. Up to the critical value $\Gamma_{\mathrm{cr}}$ at which the $\mathcal{PT}$-broken states branch off from the ground state the eigenvalues are real, for larger values of $\Gamma$ they turn imaginary.

and the ground state is stable. Beyond this value $\omega$ turns from real to imaginary and renders the state unstable. A comparison with figure 3.7 shows that this point agrees reasonably well with the critical value $\Gamma_{\mathrm{cr}}$ at which the $\mathcal{PT}$-broken states branch off from the ground state. This indicates that the emergence of the $\mathcal{PT}$-broken solutions with their growing or decaying temporal behaviour introduce a source of instability.

One may ask the question why only the ground state and not the excited state is influenced by the instability introduced together with the appearance of the complex eigenvalue branches. At the critical value $\Gamma_{\mathrm{cr}}$ the ground state and the two emerging non-stationary solutions coalesce, i.e. even their wave functions are identical. Thus, they are very similar to each other around $\Gamma_{\mathrm{cr}}$ and it seems likely that small fluctuations in the wave function immediately introduce a significant overlap with the non-stationary waves destroying the ground state's stability. The ground state is affected because all calculations have been done with an attractive nonlinearity. With a repulsive nonlinearity the two complex eigenvalue modes branch off from the excited state and then also the excited state passes through the stability change.

## 5.3. Stability change close to branch points

It is well understandable that the complex eigenvalue solutions with their growing and decaying temporal evolution introduce an instability of the ground state. This leads to the expectation that the change of the stability will occur exactly at $\Gamma_{\mathrm{cr}}$. However, it is observed that this is not the case. The bifurcation and the stability change appear at slightly different values of the gain-loss parameter [149].

The discrepancy between the points of bifurcation and stability change seems to be surprising. It is also not found in all similar systems. The mean-field limit of a two-mode approximation with a Bose-Hubbard Hamiltonian [9, 23, 24, 112] does not show this effect. This model has, however, two crucial differences to the treatment of Bose-Einstein condensates with the full Gross-Pitaevskii equation in section 5.2. The latter system contains a harmonic trap in which infinitely many stationary states can be found, whereas the nonlinear two-mode system exhibits only four states, viz. the counterparts of the two $\mathcal{PT}$-symmetric and the two $\mathcal{PT}$-broken solutions visible in figure 3.7. Furthermore, the nonlinearity derived in [9, 23] is slightly different from that of the Gross-Pitaevskii equation. The equations of motion of the Bose-Hubbard dimer with its two modes $\psi_1$ and $\psi_2$ reads [112]

$$\mathrm{i}\frac{\mathrm{d}}{\mathrm{d}t}\begin{pmatrix}\psi_1\\ \psi_2\end{pmatrix} = \begin{pmatrix} g\frac{|\psi_1|^2}{|\psi_1|^2+|\psi_2|^2} - \mathrm{i}\gamma & v \\ v & g\frac{|\psi_2|^2}{|\psi_1|^2+|\psi_2|^2} + \mathrm{i}\gamma \end{pmatrix}\begin{pmatrix}\psi_1\\ \psi_2\end{pmatrix}\ , \tag{5.3}$$

i.e. the nonlinearity has the form $\sim |\psi|^2/||\psi||^2$. Hence, it does not depend on the norm of the wave function. Consequently, there might be two reasons for the appearance of the discrepancy. It could have its origin in the existence of higher modes influencing the ground state's stability or in the norm-dependence of the Gross-Pitaevskii nonlinearity.

It is the purpose of this section to clarify this question. To do so we revisit the model of a Bose-Einstein condensate trapped in an idealised double-delta potential. This system is described by the Gross-Pitaevskii equation, i.e. the contact interaction has the norm-dependent form $\sim |\psi(\boldsymbol{x}, t)|^2$. However, it exhibits only four stationary states of which two are $\mathcal{PT}$ symmetric and two are $\mathcal{PT}$ broken as in the two-mode model [9, 23, 24, 112]. Additionally, in a numerical study the structure of the nonlinearity can easily be changed such that the system's mathematical properties can be brought in agreement with the mean-field limit of the Bose-Hubbard dimer.

### 5.3.1. Stability in the vicinity of the bifurcation

The relevant question which has to be answered by our calculation is whether or not the discrepancy between the gain-loss parameters of the bifurcation and the stability change appears for the double-$\delta$ potential. Thus, we first write down the explicit form of the

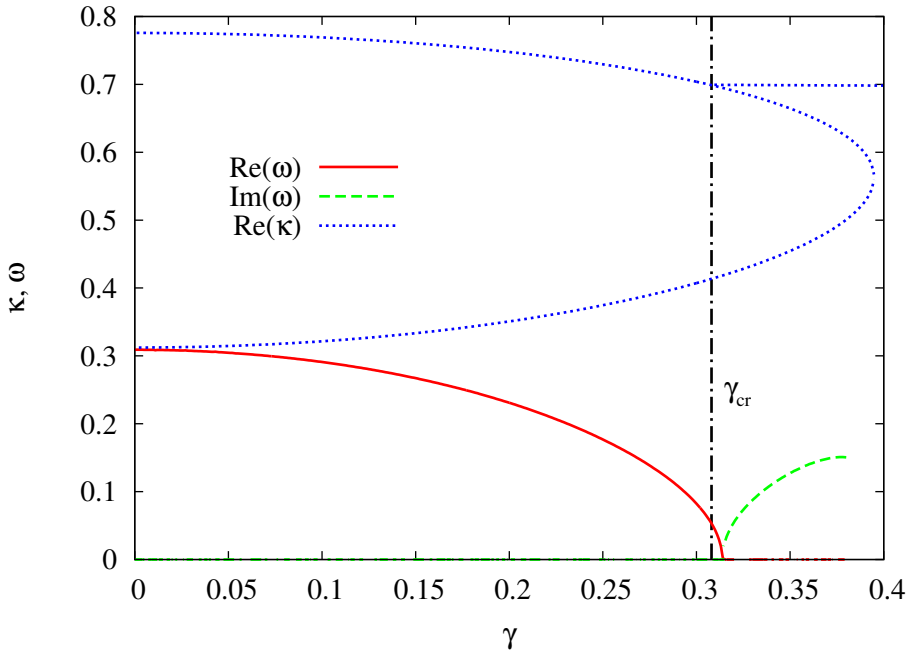


Figure 5.3.: Real (red solid line) and imaginary (green dashed line) part of the stability eigenvalue $\omega$ for the stationary ground state in the case $g = 1$. The stability change occurs at $\gamma_\omega \approx 0.3138$. To illustrate the bifurcation the real parts of $\kappa$ of all stationary states are also shown (blue dotted lines). The value $\gamma_{\mathrm{cr}} \approx 0.307$ is marked by the black dashed-dotted line. Obviously there is a discrepancy between both values.

Bogoliubov-de Gennes equations of the system,

$$\frac{\mathrm{d}^2}{\mathrm{d}x^2}u(x) = \big[-(1+\mathrm{i}\gamma)\,\delta\,(x+b) - (1-\mathrm{i}\gamma)\,\delta\,(x-b) + \kappa^2 - \omega - 2g|\psi_0(x)|^2\big]u(x) - g\psi_0(x)^2 v(x)\;, \quad (5.4a)$$

$$\frac{\mathrm{d}^2}{\mathrm{d}x^2}v(x) = \big[-(1-\mathrm{i}\gamma)\,\delta\,(x+b) - (1+\mathrm{i}\gamma)\,\delta\,(x-b) + (\kappa^2)^* + \omega - 2g|\psi_0(x)|^2\big]v(x) - g\psi_0^*(x)^2 u(x)\;, \quad (5.4b)$$

where we use again the energy $\mu = -\kappa^2$, and calculate the stability eigenvalue with $\mathrm{Re}(\omega) > 0$, $\mathrm{Im}(\omega) > 0$ for a range of $\gamma$ around the bifurcation, which is shown in figure 5.3 for $g = 1$. For increasing $\gamma$ the eigenvalue $\omega$ switches from real to imaginary at $\gamma_\omega \approx 0.3138$ marking the stability change. The bifurcation is visible in the real parts of $\kappa$ of all stationary states of the system. It is marked by the black dashed-dotted line.

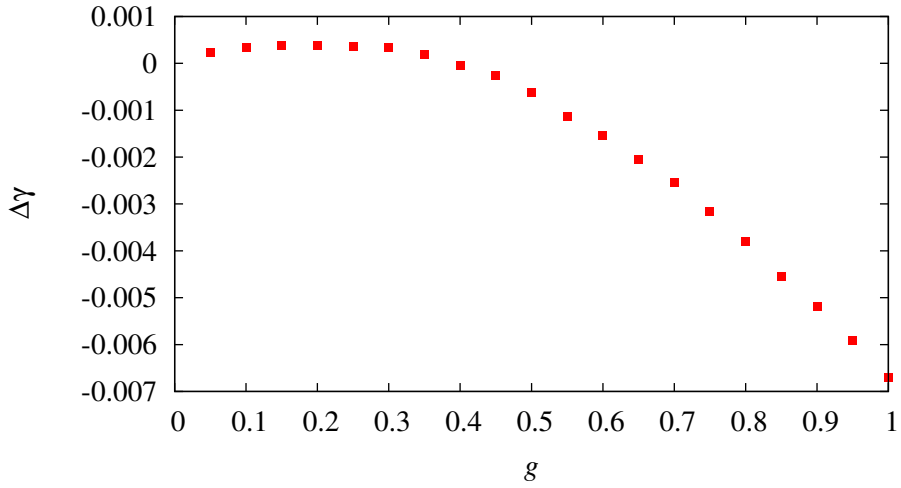


Figure 5.4.: Difference in between $\gamma_{\mathrm{cr}}$ and $\gamma_\omega$ as defined in equation (5.5) as a function of $g$. A strong dependence is clearly visible.

Obviously there is a discrepancy between $\gamma_{\mathrm{cr}}$ and $\gamma_\omega$. The difference

$$\Delta\gamma = \gamma_{\mathrm{cr}} - \gamma_\omega \tag{5.5}$$

is $\Delta\gamma \approx -0.0068$.

The system does not possess any further stationary states in addition to those shown in figure 3.3. Three of these four states are participating in the bifurcation at $\gamma_{\mathrm{cr}}$. Only the excited $\mathcal{PT}$-symmetric solution would be able to influence the dynamics of the ground state at a value $\gamma \neq \gamma_\omega$. However, it stays real for all parameters $\gamma$ shown in figure 5.3 and cannot cause any qualitative different behaviour of the ground state's dynamics. Thus, an influence of further states can be ruled out to be the reason for the discrepancy in the double-well system of section 3.2.

The remaining difference between the Gross-Pitaevskii equation and the two-mode system of references [9, 23, 24, 112] is the norm-dependence of the nonlinearity. Indeed, an influence of the norm is already present if the study done in figure 5.3 is repeated for different values of the nonlinearity parameter $g$. Figure 5.4 shows $\Delta\gamma$ as a function of $g$. A strong dependence is visible. Even the sign changes. For $g \lessapprox 0.4$ the ground state becomes unstable at $\gamma_\omega < \gamma_{\mathrm{cr}}$. For $g \to 0$ the discrepancy vanishes as expected.

### 5.3.2. Norm-independent variant of the Gross-Pitaevskii equation

An even clearer identification of $\Delta\gamma$ with the norm-dependence of the nonlinearity in the Gross-Pitaevskii equation (3.3) can be given with a small modification. The replacement

$$g|\psi|^2 \to \frac{g|\psi|^2}{\int |\psi|^2 \mathrm{d}x} \tag{5.6}$$

renders the Gross-Pitaevskii equation (3.3) norm-independent. Note that this is exactly the form of the mean-field limit in references [9, 23, 24, 112]. Since the stationary states are normalised to unity they are not influenced by the replacement. However, it influences the dynamics and also the linear stability. The Bogoliubov-de Gennes equations have to be adapted. Assuming again a small perturbation of the form (5.1a) and (5.1b) a linearisation in $u$ and $v$ leads us to

$$\begin{aligned}\frac{\mathrm{d}^2}{\mathrm{d}x^2}u(x) = \big[&-(1+\mathrm{i}\gamma)\,\delta\,(x+b) - (1-\mathrm{i}\gamma)\,\delta\,(x-b) \\ &+\kappa^2 - \omega - 2g|\psi_0(x)|^2\big]u(x) - g\psi_0(x)^2 v(x) \\ &- g|\psi_0(x)|^2\psi_0(x)S\ , \end{aligned} \tag{5.7a}$$

$$\begin{aligned}\frac{\mathrm{d}^2}{\mathrm{d}x^2}v(x) = \big[&-(1-\mathrm{i}\gamma)\,\delta\,(x+b) - (1+\mathrm{i}\gamma)\,\delta\,(x-b) \\ &+(\kappa^2)^* + \omega - 2g|\psi_0(x)|^2\big]v(x) - g\psi_0^*(x)^2 u(x) \\ &- g|\psi_0(x)|^2\psi_0^*(x)S \end{aligned} \tag{5.7b}$$

with the integral

$$S = \int \left[v(x)\psi_0(x) + u(x)\psi_0^*(x)\right]\mathrm{d}x\ . \tag{5.7c}$$

For a numerical solution of the modified Bogoliubov-de Gennes equations the value of $S$ is included in the root search, i.e. for the integration of the equations (5.7a) and (5.7c) a value for $S$ is guessed and subsequently compared with the result of equation (5.7c). Since $S$ is in general a complex value this increases the dimension of the root search to 11.

An example for a typical result is shown in figure 5.5. The discrepancy between the $\gamma$ values at which the bifurcation and the stability change occur vanishes. Both values agree as it is expected. This is true for all values of $g$. Thus, we conclude that the discrepancy appearing in figure 5.3 for the Gross-Pitaevskii equation is solely a result of the norm-dependent nonlinearity $\sim |\psi|^2$ in the Hamiltonian and is not a consequence of the interaction with higher excited states.

### 5.3.3. Discussion

The reason why the stability change does not occur exactly at the bifurcation can also be understood intuitively. Figure 3.3 shows that the value $\gamma_{\mathrm{cr}}$ of the bifurcation is not equal for all values of $g$. The same is true for the spatially extended double well and has been discussed in form of the phase diagram in figure 3.10. For $g = 0$ the two real eigenvalues $\kappa$ vanish in a tangent bifurcation and two complex eigenvalues emerge. Only for nonvanishing $g$ the additional pitchfork bifurcation at $\gamma_{\mathrm{cr}}$ exists and moves to smaller values of $\gamma$ for increasing $g$.

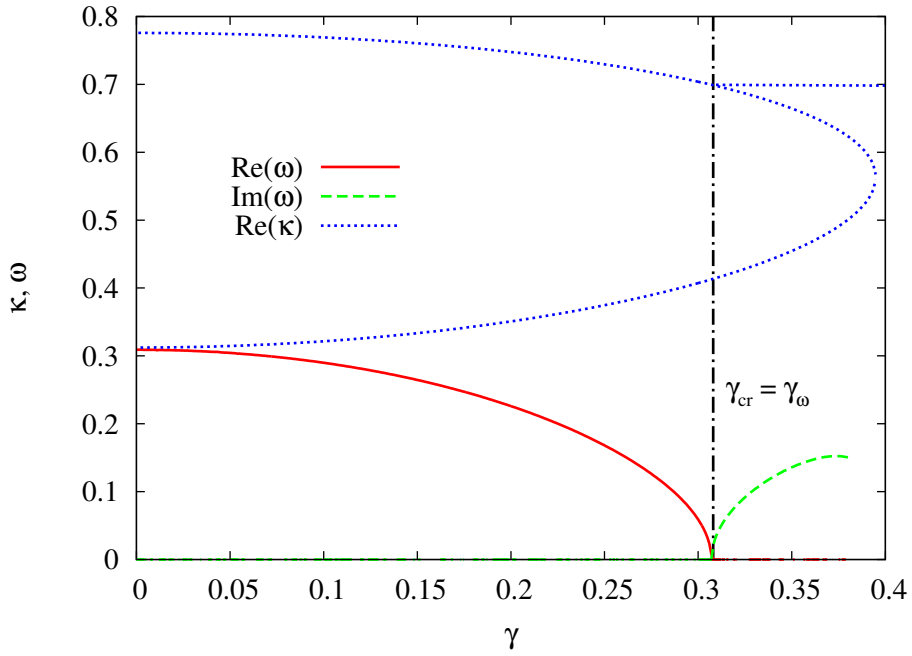


Figure 5.5.: The same as in figure 5.3 but for the modified Bogoliubov-de Gennes equations (5.7a)-(5.7c). Now the $\gamma$ values at which the bifurcation and the stability change occur agree perfectly.

If now the norm of a wave function changes, this can also be understood as a variation of $g$, i.e. a wave function with a norm $N^2 = ||\psi||^2$ has the same effect as a wave function with the norm 1 and a modified value

$$\tilde{g} = N^2 g \; . \tag{5.8}$$

Since the values $\gamma_{\mathrm{cr}}$ are different for $g$ and $\tilde{g}$ it is not surprising that a fluctuation changing the norm of the wave function may cause a qualitative change of the condensate's stability properties in the vicinity of $\gamma_{\mathrm{cr}}$.

In total the stability analysis tells us that stationary wave functions of Bose-Einstein condensates trapped in complex $\mathcal{PT}$-symmetric potential geometries exist, are stable, and should be observable in an experiment. In particular there is at least one state – the excited state in our example – which only exhibits real stability eigenvalues almost as long as it exists indicating a dynamically stable condensate in a wide range of the strength of the gain-loss contribution. To be precise, we have to add that also the excited state suffers from a discrepancy in its stability behaviour. The effect discussed here for the ground state also affects the exceptional point at which the two solutions with real eigenvalues merge. Thus, it might happen that the excited state becomes unstable shortly before it vanishes. However, this will only be restricted to a close vicinity of the exceptional point.

The second stationary state, i.e. the ground state in our example, shows a much more complicated stability behaviour promising a rich variety of dynamical effects, which are the subject of the following chapter. Its stability changes in a close vicinity of the critical point at which the $\mathcal{PT}$-broken states emerge. In the example of the spatially extended double well this means that the blue area indicating only $\mathcal{PT}$-symmetric states in the phase diagram 3.10 approximately defines the region in phase space, in which a stable condensed phase is possible.

# 6. Dynamics of a Bose-Einstein condensate in a $\mathcal{PT}$-symmetric double well

So far we have seen that the Gross-Pitaevskii equation of a Bose-Einstein condensate trapped in a $\mathcal{PT}$-symmetric double well possess stationary states with constant probability density in both wells. These stationary states are identified by real energies and have found to be stable if the gain-loss parameter and the nonlinearity are not too strong. The stability analysis in chapter 5 suggests that the dynamical properties will depend on a subtle interplay between the strengths of the nonlinearity and the gain-loss effect. This will be investigated in this chapter.

Before we study the influence of the nonlinearity on the dynamics, we recapitulate the basic dynamical properties of linear $\mathcal{PT}$-symmetric quantum systems in section 6.1. To do so, we pick up again the $\mathcal{PT}$-symmetric double-delta potential of which we studied already the stationary states in the linear case in section 3.1.1. Then we investigate the dynamics of a Bose-Einstein condensate in the $\mathcal{PT}$-symmetric double-well setup in section 6.2, where we consider the idealised double-delta trap (section 6.2.1) and the spatially extended potential (section 6.2.2). The critical norm-dependence of the stability of the ground state found in section 5.3 will also have an important influence on the dynamics. Its consequences on the dynamics in a system with gain and loss are discussed. Furthermore, we show that the two complex eigenvalue modes of the time-independent Gross-Pitaevskii equation branching off from the ground state, despite being no true stationary solutions of the time-dependent Gross-Pitaevskii equation, still possess an appreciable relevance for the dynamics in section 6.2.3. Finally, the dynamics is shown in a Bloch sphere-representation in section 6.2.4, which helps to gain further insight.

Again we restrict all discussions to the one-dimensional case since only the spatial direction with the antisymmetric gain an loss is of relevance for us. Furthermore, the discussion of the dynamics is much more illustrative in only one dimension than in a more complicated higher-dimensional space. The discussions in this chapter are adapted from references [130–132] in which the results presented here have already been published. Parts of newer results have been submitted for publication in reference [149] and will appear in a contribution to a conference proceeding [133]. Parts of the dynamical calculations with the split operator method for the nonlinear equations have been done

together with Daniel Haag during his Master's thesis [135].

## 6.1. Dynamics of the linear double-delta system

To better understand the dynamics of a Bose-Einstein condensate subject to balanced gain and loss it is instructive to look first at the temporal evolution of a quantum particle described by the linear Schrödinger equation in the $\mathcal{PT}$-symmetric double-delta potential. It exhibits typical dynamical properties of these systems, and the evolution of its probability amplitude provides a comprehensible insight.

The interesting regime in the parameter space is that in which $\mathcal{PT}$-symmetric eigenstates are present. When only growing or decaying modes exist the fate of the wave function is clear. As soon as there is an overlap with a growing mode, i.e. a solution of the stationary Schrödinger equation with a positive imaginary part in the energy, the wave function will grow exponentially in time. Each overlap with a decaying mode, i.e. an energy eigenstate with a negative imaginary contribution to the energy, will decay exponentially and vanish. Of course, at least the exponential growth for infinite times is not physical. It is a result of the constant imaginary potential contributions $\pm \mathrm{i}\gamma$ in the Schrödinger equation (3.5). In a realistic physical setup the gain term, e.g. the source of condensed atoms, will be finite and the constant influx of the probability amplitude (of particles) can only be held constant over a finite time span. Nevertheless, the only interesting dynamics over a longer time span will be given in the $\mathcal{PT}$-symmetric regime, i.e. when the initial wave function has only overlaps with stationary states with real energies.

The double-delta system exhibits exactly two eigenstates with real energies, viz. the ground and excited states shown in figure 3.1. To obtain a nontrivial dynamics we use as initial state the superposition

$$\psi(x,0) = \frac{1}{\sqrt{2}}(\psi_1(x) + \psi_2(x)) \tag{6.1}$$

and show its time evolution

$$|\psi(x,t)|^2 = \frac{1}{2}\left|\psi_1(x)\exp\left(i\kappa_1^2 t\right) + \psi_2(x)\exp\left(i\kappa_2^2 t\right)\right|^2 \tag{6.2}$$

for different values of the gain-loss parameter $\gamma$ in figure 6.1.

As expected for a closed two-state system, the probability density oscillates between the two delta-function wells for $\gamma = 0$, which is shown in figure 6.1 (a). With nonvanishing gain and loss we notice two effects, which can be observed in figures 6.1 (b) and (c). The frequency of the oscillation decreases, an effect which becomes stronger and stronger as the gain-loss parameter $\gamma$ is increased. Additionally, a deformation of the oscillation is observed, the phase difference between both wells is not exactly $\pi$. At some points in time the probability amplitude is low in both wells, at other times it is

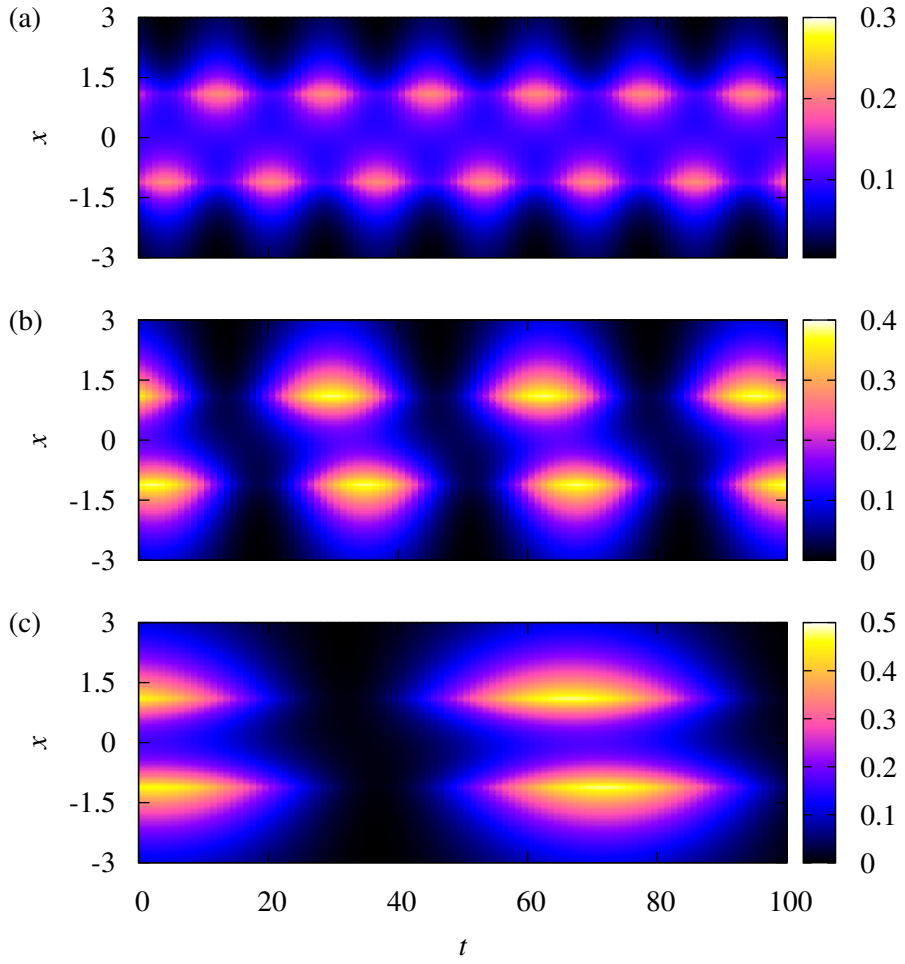


Figure 6.1.: Time evolution of the superposition (6.1) of the two eigenstates for different values of the gain-loss parameter: (a) $\gamma = 0$, (b) $\gamma = 0.35$, (c) $\gamma = 0.39$, close to the exceptional point at which both solutions vanish. Figure taken from [130].

high on both sides of the barrier. This also means that the total probability amplitude, integrated over the whole space, is not constant. This is only possible due to the gain and loss contributions. The probability can come from or move back to an external reservoir modelled by the imaginary potential contributions. Close to the branch point at which the two real energy solutions merge and vanish both effects reach their extremal cases. The oscillation frequency tends to zero and the probability density on both sides is almost identical and pulsates. We note that a similar behaviour has already been found by Klaiman et al. in the discussion of a wave guide with balanced gain and loss [8].

## 6.2. Dynamics in the nonlinear Gross-Pitaevskii equation with gain and loss

It is most instructive to investigate first a superposition similar to that in equation (6.1) for the linear case. This will give us the best insight into the similarities and the differences of the systems without and with nonlinearity. Furthermore the discussion in the context of the double-delta potential will exhibit the strongest similarities with the linear case of the previous section. Thus, we will first investigate the double-delta potential before we turn to the spatially extended double well, of which the numerics can be controlled better.

### 6.2.1. Gross-Pitaevskii equation with a $\mathcal{PT}$-symmetric double-delta potential

We use as initial states for the temporal evolution of a Bose-Einstein condensate in the double-delta trap a wave function of the type

$$\psi(x, t = 0) = \frac{1}{\sqrt{2}} \left(\phi_{\mathrm{g}}(x) + \phi_{\mathrm{e}}(x)\right) \ , \tag{6.3}$$

where $\phi_{\mathrm{g}}(x)$ and $\phi_{\mathrm{e}}(x)$ are the ground and excited state with real energy, respectively. In the nonlinear system the dynamics will not be restricted to the subspace of these two solutions, however, we will see that a discussion in this subspace will always provide an excellent description as long as the dynamics is stable. If we prepare the condensate in a state close to the stationary real eigenvalue solutions for values of the gain-loss parameter below the appearance of the $\mathcal{PT}$-broken states the influence of the latter is supposed to be negligible.

A second consequence of the nonlinearity is that the temporal evolution of individual sates in the Gross-Pitaevskii equation is not simply given by $\exp(\mathrm{i}\kappa^2 t)$. In particular, the time evolution of a superposition can no longer be obtained by simply multiplying the individual states by their time evolution factors. An explicit solution of the time-dependent Gross-Pitaevskii equation is required. In the numerics this is done by applying

the split operator method. This means that a representation of the wave function on a grid is used. Then the time-evolution operator

$$U(\Delta t) = \exp\left(-\frac{\mathrm{i}}{\hbar} H \Delta t\right) \tag{6.4}$$

with the nonlinear Hamiltonian $H$ of the Gross-Pitaevskii equation is applied to this wave function. To avoid a differential operator in the exponent of $U(\Delta t)$ the Hamiltonian is split into its kinetic ($T$) and potential ($V$) parts,

$$U(\Delta t) = \exp\left(-\frac{\mathrm{i}}{2\hbar} T t\right) \exp\left(-\frac{\mathrm{i}}{\hbar} V t\right) \exp\left(-\frac{\mathrm{i}}{2\hbar} T t\right) + O(t^3)\,. \tag{6.5}$$

For sufficiently small time steps $\Delta t$ the terms $O(t^3)$ can be ignored. If now a change form position representation to momentum representation of the wave function is done between the single parts of the time evolution operator, each application consists only of the multiplication of the wave function with a complex number at the respective positions on the grid.

In figure 6.2 we show the results for the time evolution of $|\psi(x,t)|^2$ of the initial superposition (6.3) for $a = 2.2$, the nonlinearity $g = 0.5$, and different values of the gain-loss parameter $\gamma$. For small values $\gamma$ we observe a behaviour, which is very similar to the linear case. The basic effects seem to be the same. The frequency decreases for stronger gain and loss, and there are time intervals in which the probability density in both wells is simultaneously large, or simultaneously almost completely extinguished.

For larger values of $\gamma$ the situation changes drastically. At the end of the time interval in figure 6.2 (c) for $\gamma = 0.275$ and for much shorter time in figure 6.2 (d) for $\gamma = 0.3$ we observe a dramatic increase of the probability amplitude in the well at $x = 1.1$ with gain. Even though we start with a high probability density in the well with loss eventually the well with gain wins. In the case $\gamma = 0.3$ this happens immediately without any oscillation prior to that.

We have seen in sections 5.2 and 5.3 that the bifurcation at which the $\mathcal{PT}$-broken states emerge introduces an instability. Thus, it is not very surprising that such an instability is also observable in the full dynamics. We even found that the bifurcation point is not a strict border due to norm-dependence of the Gross-Pitaevskii equation. However, the values $\gamma = 0.275$ and $\gamma = 0.3$ are far below the critical point $\gamma_{\mathrm{cr}} \approx 0.38$ where the two complex eigenvalues bifurcate from the ground state branch and smaller than the critical value $\gamma_{\mathrm{EP}} \approx 0.4$ where the two states coalesce. Thus, it seems to be unlikely that the results of the stability analysis are sufficient for explaining this diverging dynamics. A more careful study is required which will be done for the spatially extended double well.

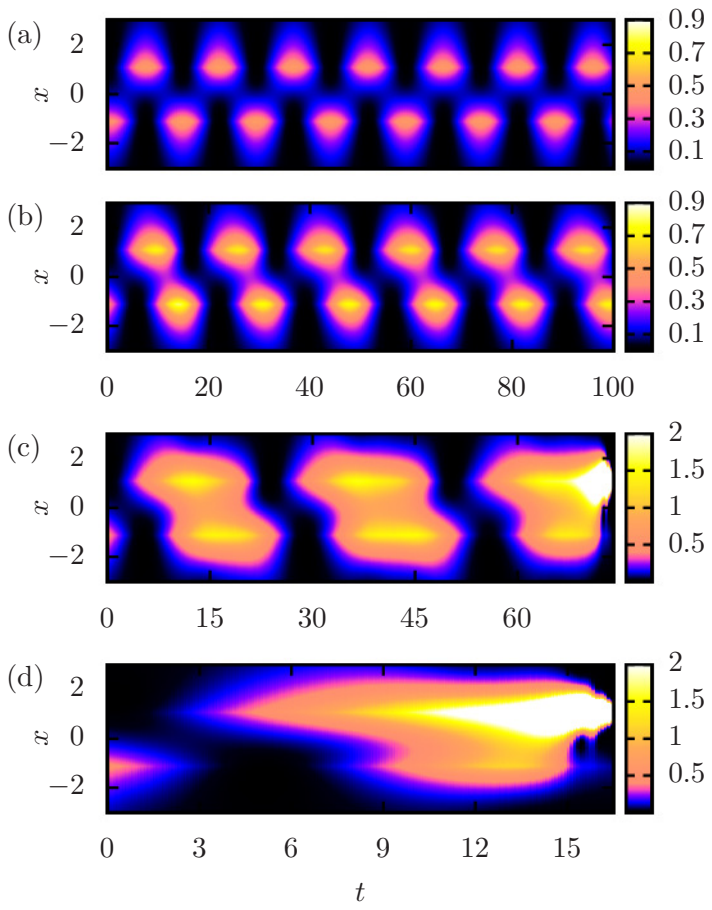


Figure 6.2.: Temporal evolution of a superposition of the two stationary solutions for $a = 2.2$ and $g = 0.5$ and different strengths of the gain-loss parameter: (a) $\gamma = 0$, (b) $\gamma = 0.2$, (c) $\gamma = 0.275$, (d) $\gamma = 0.3$. Figure taken from [130].

### 6.2.2. A Bose-Einstein condensate in the spatially extended double well

A reason for the unstable behaviour visible in figures 6.2 (c) and (d) is that with the temporal evolution of the wave function the norm of the state constantly varies in time, and with it the size of the nonlinear term in the Gross-Pitaevskii equation. Similar to the discussion of the stability eigenvalues in section 5.3.3 this effectively corresponds to a variation of $g$ in the stationary Gross-Pitaevskii equation, and acts as if one would constantly be moving through different eigenvalue diagrams of the type shown in figure 3.3. Therefore for a given value of $g$, the transition to the $\mathcal{PT}$-broken phase of the condensate can set in at values of $\gamma$ smaller than those of the bifurcation $\gamma_{\mathrm{cr}}$ and the exceptional point $\gamma_{\mathrm{EP}}$ for that value of $g$. This can be confirmed in a numerically exact propagation of such initial states for the spatially extended double well using the

split-operator method. In this system, a more careful study is possibly as compared to the double-delta potential since the singular character of the delta-functions leads to numerical instabilities during the propagation with the time evolution operator (6.5).

We start with a superposition of the ground and first excited state similar to that in equation (6.3) but now we introduce an additional phase parameter $\varphi$. The initial state then reads

$$\psi(x, t = 0) = \frac{1}{\sqrt{2}} \left( \phi_{\mathrm{g}}(x) + \mathrm{e}^{\mathrm{i}\varphi} \phi_{\mathrm{e}}(x) \right) \ , \tag{6.6}$$

where $\phi_{\mathrm{g}}(x)$ and $\phi_{\mathrm{e}}(x)$, as in equation (6.3), are the ground and first excited state, respectively.

In figures 6.3 (a), (b), and (c) we visualise the evolution of the probability amplitude of an initial wave packet with the phase $\varphi = \pi/2$ and $g = 0.2$. Several values of the gain-loss parameter between $\Gamma = 0$ (no gain and loss at all) and $\Gamma = 0.04$ were chosen. The behaviour of the wave packet is very similar to the linear system in section 6.1 or as in the optical wave guide studied by Klaiman et al. [8]. An oscillation of the probability amplitude between the two wells sets in, and the oscillation frequency decreases with increasing $\Gamma$. Close to the exceptional point at $\Gamma_{\mathrm{EP}} \approx 0.04$ the oscillation period tends to infinity. A detailed quantitative analysis reveals that the influence of the nonlinearity is only a slightly higher oscillation frequency as compared to the linear case $\Gamma = 0$. Note that in figure 6.3 with $\Gamma = 0.04$ a value at which the $\mathcal{PT}$-broken solutions already exist was chosen. In the example shown in figure 6.2 for the double-delta potential a strength of the gain-loss effect below the appearance of the complex eigenvalue solutions resulted already in a completely unstable dynamics.

The reason for the stable oscillations in the case of figure 6.3 (c) lies in the phase $\varphi$ in equation (6.6). It can be used to define whether or not the dynamics starts with an increasing or a decreasing norm of the wave functions. As can be seen in figures 6.3 (a)-(c) the initial configuration, as imposed by the phase $\varphi = \pi/2$, slides into a minimum of the overall probability to be in the double well. This start of the dynamics is obviously sufficient to guarantee a stable oscillation. With the norm of the wave function also the effective nonlinearity parameter

$$\tilde{g} = N^2 g \tag{5.8}$$

shrinks, which moves the appearance of the growing and decaying complex eigenvalue modes to larger values of the gain-loss parameter $\Gamma$ and stabilises the condensate.

The initial condition seems to be very important for the fate of the wave function. Indeed, a drastic qualitative change of the wave function's behaviour is observed in figure 6.3 (d), where the phase was chosen to be $\varphi = \pi$ and the gain-loss parameter was $\Gamma = 0.03$. For this strength of the gain-loss parameter $\mathcal{PT}$-broken states are present for $g = 0.2$, cf. figure 3.7. However, as we have seen in figure 6.3 (c), for which an even stronger $\Gamma$ was used, this does not necessarily lead to an infinite growth. More important is the slope of the norm, and as can be seen in figure 6.3 (d) the norm starts to climb to a maximum. The consequence is that also the effective $\tilde{g}$ in equation (5.8) grows and

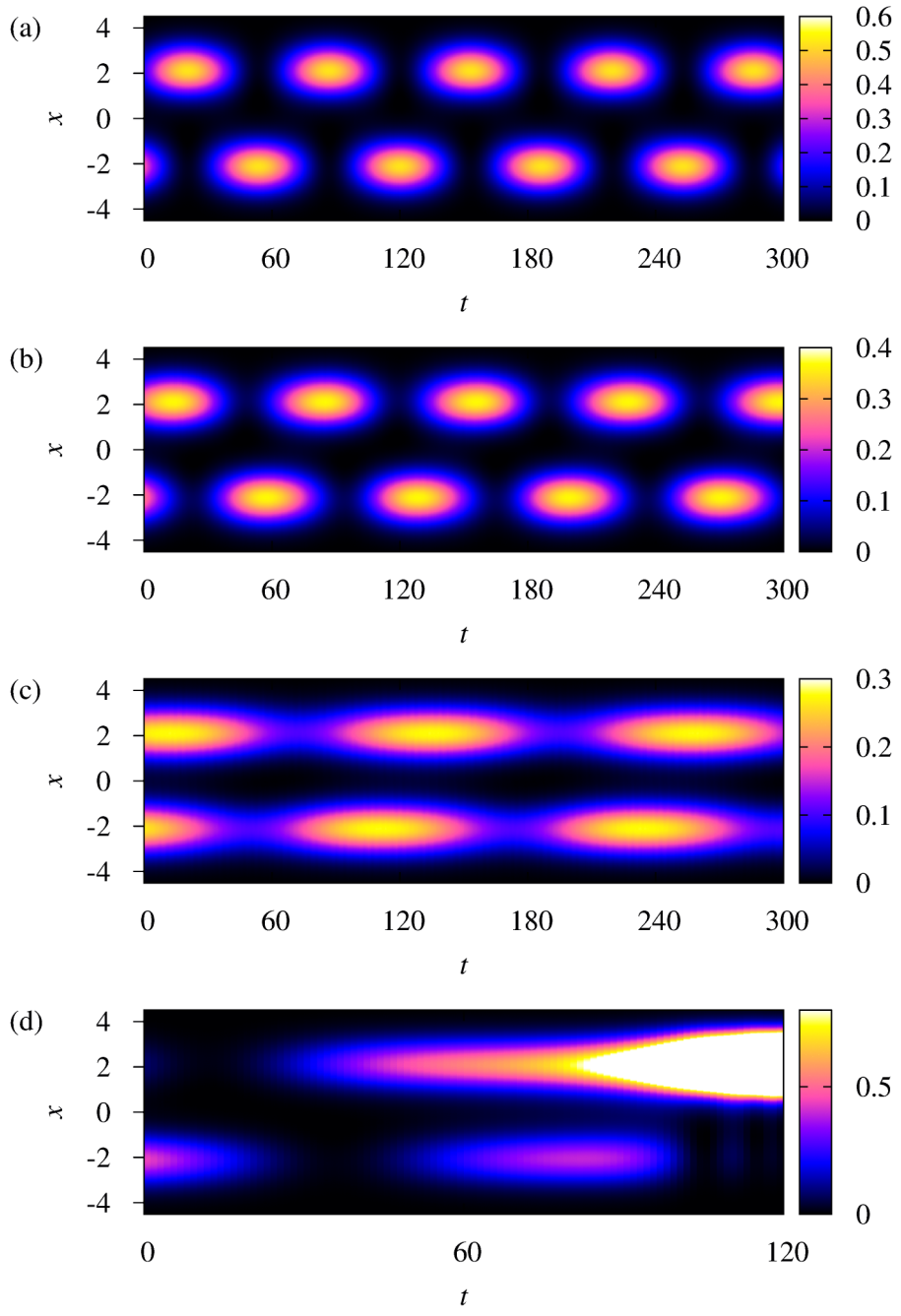


Figure 6.3.: Visualisation of the probability amplitude's spatial distribution as a function of time. The initial wave packet is defined by (6.6). In all calculations $g = 0.2$ was chosen. For the choice $\varphi = \pi/2$ stable oscillations are observable in the cases $\Gamma = 0$ (a), $\Gamma = 0.02$ (b), and $\Gamma = 0.04$ (c). For $\Gamma = 0.03$ and $\varphi = \pi$ we observe an explosion of the wave packet (d).

the whole system becomes totally unstable. The condensate does not oscillate between the wells. The probability amplitude tunnels into the well with gain ($x > 0$), which leads immediately to an "explosion" of the wave function, i.e. it grows beyond all limits. Of course this is only correct in our idealised description of the gain and loss effects with imaginary potentials, which correspond to infinitely large reservoirs. In a realistic situation this description will break down at some point.

We learn from these facts that in an experiment it is very important to control the maximum norm attained during an oscillation. If the norm and with it the the effective nonlinearity parameter $\tilde{g}$ exceed a critical value, the instability of the growing eigenmode with positive imaginary energy contribution acts on the dynamics. The result will be in all cases a growth of the probability amplitude – and the number of atoms – in the well with gain up to a certain breakdown level.

### 6.2.3. Significance of "stationary" solutions with complex eigenvalues

.

In section 3.1.2 we mentioned that the complex eigenvalue modes, visible for example in figure 3.3, are solutions of the time-independent Gross-Pitaevskii equation but not of its time-dependent counterpart. Strictly speaking, they lose their physical relevance. Due to the decay or growth of the probability amplitude mentioned above the nonlinear term $g|\psi|^2$ in the Hamiltonian becomes explicitly time dependent. Thus, the states are not true stationary solutions of the time-dependent Gross-Pitaevskii equation. They are, however, still useful to indicate the temporal evolution of the condensate. For example, it was possible above to explain the explosion of the condensate wave function in figure 6.2 (d) with the presence of the growing $\mathcal{PT}$-broken state.

Furthermore, it is possible to show that the complex eigenvalue solutions still can indicate the actual temporal evolution of an initial wave packet. In particular, for small times the prediction from the "stationary" complex eigenvalue solutions for the norm $N^2 = \int |\psi|^2 \,\mathrm{d}x$ describes very well the true onset of the growth as can be seen for an initial state with $\mathrm{Im}\,\mu > 0$ in figure 6.4.

To investigate the correspondence of the complex eigenvalue solutions with the exact time integration for longer times the difference

$$D = \frac{1}{N}\left(\sqrt{\int_{\text{right well}} |\psi|^2 \,\mathrm{d}x} - \sqrt{\int_{\text{left well}} |\psi|^2 \,\mathrm{d}x}\right) , \tag{6.7}$$

of the wave function's norm in the right and left wells is introduced, where $N$ signals the total norm. The quantity $D$ tells us how the probability density is distributed in both wells. A positive value signalises a higher probability density in the right well with gain, whereas a negative value indicates a concentration of the condensate's probability density in the left well with loss.

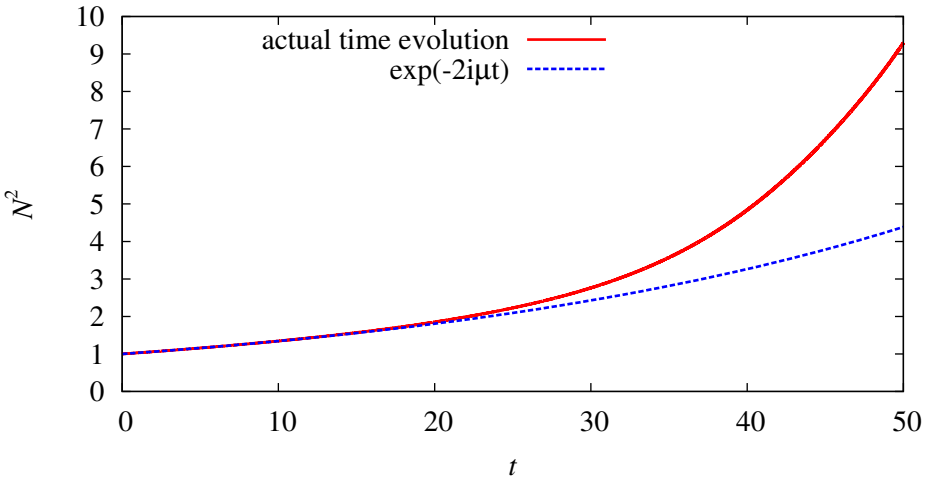


Figure 6.4.: Temporal evolution of the norm of an initial complex eigenvalue state with $\mathrm{Im}\,\mu > 0$. The parameters are $g = 0.2$ and $\Gamma = 0.03$.

In figure 6.5 we compare the norm difference $D$ of the correct temporal evolution with that of the complex eigenvalue solution with positive imaginary part, i.e. the growing state for the same parameters. Since the norm of the time evolved wave changes due to the gain-loss part of the potential we have to adapt the effective $\tilde{g}$ according to equation (5.8) in the stationary Gross-Pitaevskii equation such that both norm differences are comparable.

In figure 6.5 (a) $D$ is plotted for the initial condition and temporal evolution depicted in figure 6.3 (d). With increasing time the state first decays and the norm drops. This can already be seen in 6.3 (d). At low values of the norm the effective $\tilde{g}$ assumes values at which only the true stationary states with real eigenvalues and $D = 0$ exist. The latter property can be seen in the figure. However, at $t \approx 12$ the overlap with the growing eigenstate wins and the norm starts to grow. After some oscillations of $D$ we observe for times $t > 120$ that the norm differences of both calculations agree more and more. This indicates that the wave function initially prepared in a superposition of two eigenstates evolves into the shape of the growing eigenstate for long times. That is, the complex eigenvalue solution with positive imaginary part still has a meaning for long times although it is not a true stationary solution of the time-dependent Gross-Pitaevskii equation. A similar behaviour can be observed in figure 6.5 (b), where the initial state was the growing complex eigenvalue solution. Since we start with the increasing norm solution the agreement between both calculations sets in earlier.

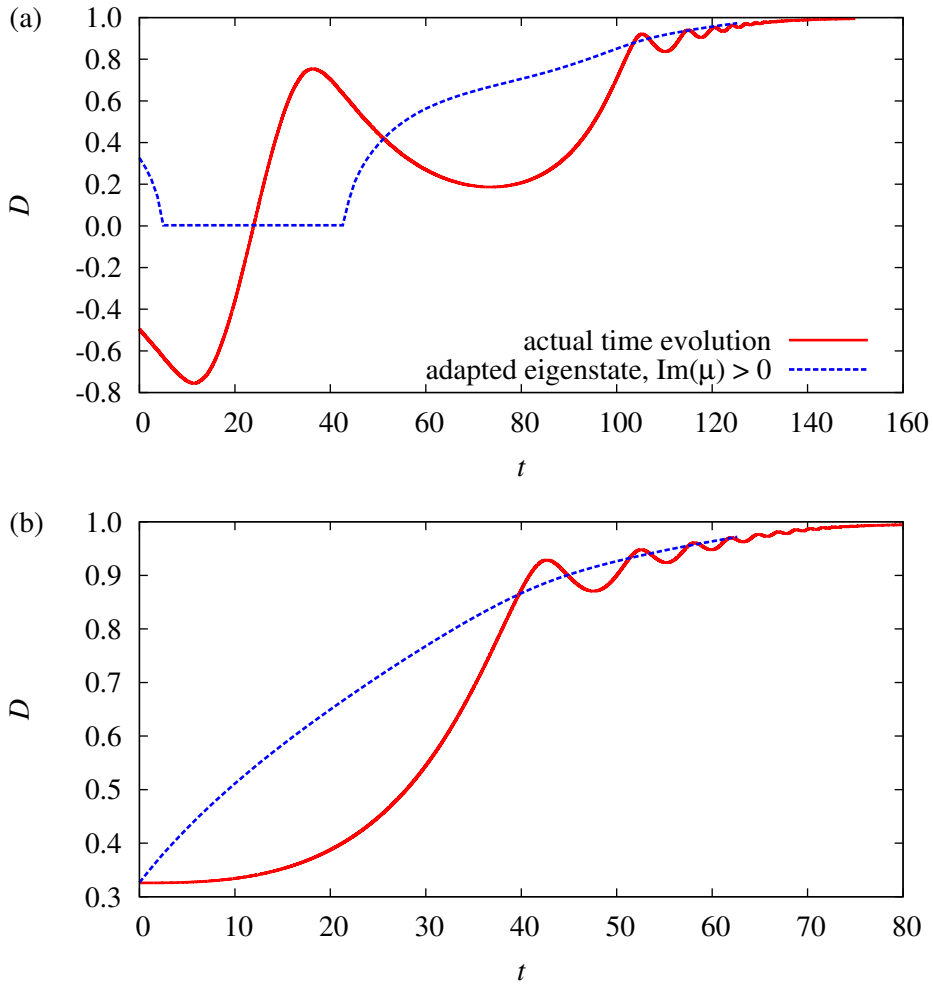


Figure 6.5.: Comparison of the norm difference $D$ of the correct temporal evolution with that of complex eigenvalue solutions. In (a) the same initial condition as in 6.3 (d) is depicted, whereas (b) shows the evolution of the complex eigenvalue state with positive imaginary part. In both cases the norm difference follows the growing complex eigenvalue state for long times. The gain-loss parameter $\Gamma$ was chosen to be 0.03 and the initial $g$ was 0.2.

### 6.2.4. Representation on a Bloch sphere

So far we have seen different regimes of the dynamics of initially $\mathcal{PT}$-symmetric states or a superposition of those. This gave a good overview about the important characteristics of wave functions evolving in a double-well structure with gain and loss: stable oscillations, the onset of instability to unlimited growth of the wave function, the influence of the norm on the dynamics, and the importance of solutions of the time-independent Gross-Pitaevskii equation with complex energies for the long-time evolution of non-stationary waves. A further analysis will give us more insight into the parameter space regions of stable and unstable dynamics. It turned out that this discussion is most conveniently done in a Bloch sphere representation [149] of the wave function, which will be introduced first.

#### Introduction of the Bloch sphere

Bloch sphere representations are very common in two-level systems. Basically a quantum state $|\psi\rangle$ evolving in a two-dimensional Hilbert space is determined by two complex coefficients, say, $a$ and $b$ via the expansion

$$|\psi\rangle = a|1\rangle + b|2\rangle \ . \tag{6.8}$$

Since the total norm is fixed to some value $N$ for a Hermitian Hamiltonian and the overall phase does not contain any information there remain two real parameters which define the whole dynamics. With, e.g. the relation

$$a = N\cos(\vartheta/2)\,\mathrm{e}^{\mathrm{i}\varphi} \ , \qquad b = N\sin(\vartheta/2) \ , \tag{6.9}$$

it is possible to map this dynamics onto the surface of a sphere with constant radius $N$, which corresponds to the fixed norm. The angle $\vartheta \in [0, \pi]$ describes the distribution of the amplitude on both states, and $\varphi \in [0, 2\pi)$ represents the phase difference between both coefficients.

The concept of a Bloch sphere representation has already been applied to a $\mathcal{PT}$-symmetric system, viz. the Bose-Hubbard dimer [23, 24] and its mean field limit. In this system the formalism is ideal to describe the dynamics since only two modes are present and, despite the non-Hermiticity of the Hamiltonian, the whole dynamics is norm-conserving [cf. equation (5.3)]. Both conditions are not fulfilled for the Bose-Einstein condensate in the double well. As we have seen the dynamics of the Gross-Pitaevskii equation with the gain and loss terms is not norm conserving. Furthermore the system has infinitely many modes, and thus the dynamics may rapidly leave the two-dimensional subspace which can be represented on a Bloch sphere. However, both difficulties can be dealt with.

In the following we show calculations of wave functions which initially are given by a superposition of the two real eigenvalue modes, the ground state $|\psi_\mathrm{g}\rangle$ and the first excited state $|\psi_\mathrm{e}\rangle$. Since they are not orthogonal the orthonormal basis states $|e_1\rangle = |\psi_\mathrm{g}\rangle$ are

introduced and $|e_2\rangle = \alpha(|\psi_\mathrm{e}\rangle - \langle\psi_\mathrm{g}|\psi_\mathrm{e}\rangle\,|\psi_\mathrm{g}\rangle)$ with an appropriate normalisation constant $\alpha$ built up with the Gram-Schmidt procedure. Any wave function can then be expanded as

$$|\psi\rangle = c_1\,|e_1\rangle + c_2\,|e_2\rangle + |\psi_\mathrm{err}\rangle\ , \tag{6.10}$$

where $|\psi_\mathrm{err}\rangle$ is the contribution outside the two-dimensional subspace. It addresses the second of the difficulties mentioned above. The nonlinear dynamics is not restricted to the subspace of $|e_1\rangle$ and $|e_2\rangle$. However, we found in all calculations that an expansion only in $|e_1\rangle$ and $|e_2\rangle$ remains a very good approximation. All results shown in this section fulfilled $\langle\psi_\mathrm{err}|\psi_\mathrm{err}\rangle < 0.004$, where the total norm is at least at the order of one.

The non-conserved norm can be tackled with the introduction of a third variable in the Bloch sphere coordinates. The representation is given by

$$c_1 = R\,\mathrm{e}^{\mathrm{i}\chi+\mathrm{i}\varphi}\cos\vartheta/2\ , \tag{6.11a}$$

$$c_2 = R\,\mathrm{e}^{\mathrm{i}\chi}\sin\vartheta/2\ , \tag{6.11b}$$

where $R$ describes a radius, $\vartheta$ measures the ratio of the contributions of the basis states, $\varphi$ their phase difference, and $\chi$ absorbs the arbitrary global phase of the numerically propagated wave functions. As long as the occupation of $|\psi_\mathrm{err}\rangle$ is small $R$ has the meaning of the total norm of the state. Strictly speaking the representation can no longer be called "Bloch sphere" since the dynamics is no longer restricted to a sphere. However, stable oscillations will remain on this sphere or in its vicinity, and for all other states the distance to the origin of the coordinate system (6.11) measures the norm.

### Meaning of special coordinates, symmetries and eigenstates

Before we will look at dynamical solutions of the Gross-Pitaevskii equation we will mark some special positions on the Bloch sphere to understand the evolution of the states better. As can be seen from the definition of the coordinates (6.11) the north pole of any sphere (i.e. of any norm) corresponds to the first basis state $|e_1\rangle$, which is identical with the ground state $|\psi_\mathrm{g}\rangle$ at the current norm. It is marked by the upper arrow in figure 6.6, which introduces the view we will use for the following visualisations of the dynamics. The second basis state points to the south pole, which is also shown in the figure by an arrow. All initial wave functions will be located on the yellow circle in the figure. It also represents a special property because it represents all sates with either $\varphi = 0$ or $\varphi = \pi$. The corresponding states (6.10) have, up to the global phase, purely real expansion coefficients. This means that due to the $\mathcal{PT}$ symmetry of the basis states all states on that circle are likewise $\mathcal{PT}$ symmetric.

The knowledge of the positions of the stationary eigenstates is also very helpful for the orientation in the Bloch sphere diagrams. They are shown as solid pink lines in figure 6.7. They appear as lines because each of the states exists for a certain range of the norm, and the sequence of all states forms the line. Clearly visible is the ground state which is pointing north for all radii, i.e. all norms. The first excited state lies for

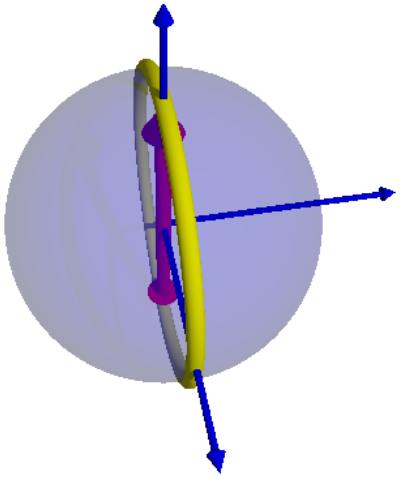

Figure 6.6.: Bloch sphere used for the representation of the dynamical solutions. The upper arrow marks the north pole identified with the first basis state. The lower arrow represents the second basis state pointing to the south pole. The temporal evolutions in figure 6.7 start on the yellow circle.

small norms exactly in the opposite direction and bends with increasing norm to the front side of the sphere since, due to its overlap with the ground state for nonvanishing nonlinearity, it does not exactly agree with the second basis state defining the south pole of all possible concentric spheres.

In the phase diagram 3.10 we see that the exceptional point, at which the ground and first excited state merge and vanish, depends slightly on the strength $g$ of the nonlinearity or, via the effective $\tilde{g}$ (5.8), on the norm of the wave function. For a given value of the gain-loss parameter $\Gamma$ it lies on a certain distance to the origin. In figure 6.7 (d) it can be seen. The two stationary states merge and form a closed circle in the diagram.

The two $\mathcal{PT}$-broken state are also drawn. They appear as solid pink lines emerging from the ground state. The state belonging to the energy with positive imaginary part heads to the right side of the sphere, whereas that with negative imaginary part in the energy leaves the sphere in the opposite direction.

### Discussion of dynamical solutions

As mentioned above all dynamical solutions start on the yellow circle on the Bloch sphere in figure 6.6. This corresponds to states normalised to unity which are $\mathcal{PT}$-symmetric superpositions of the two basis states. Figure 6.7 (a) has a vanishing gain-loss effect.

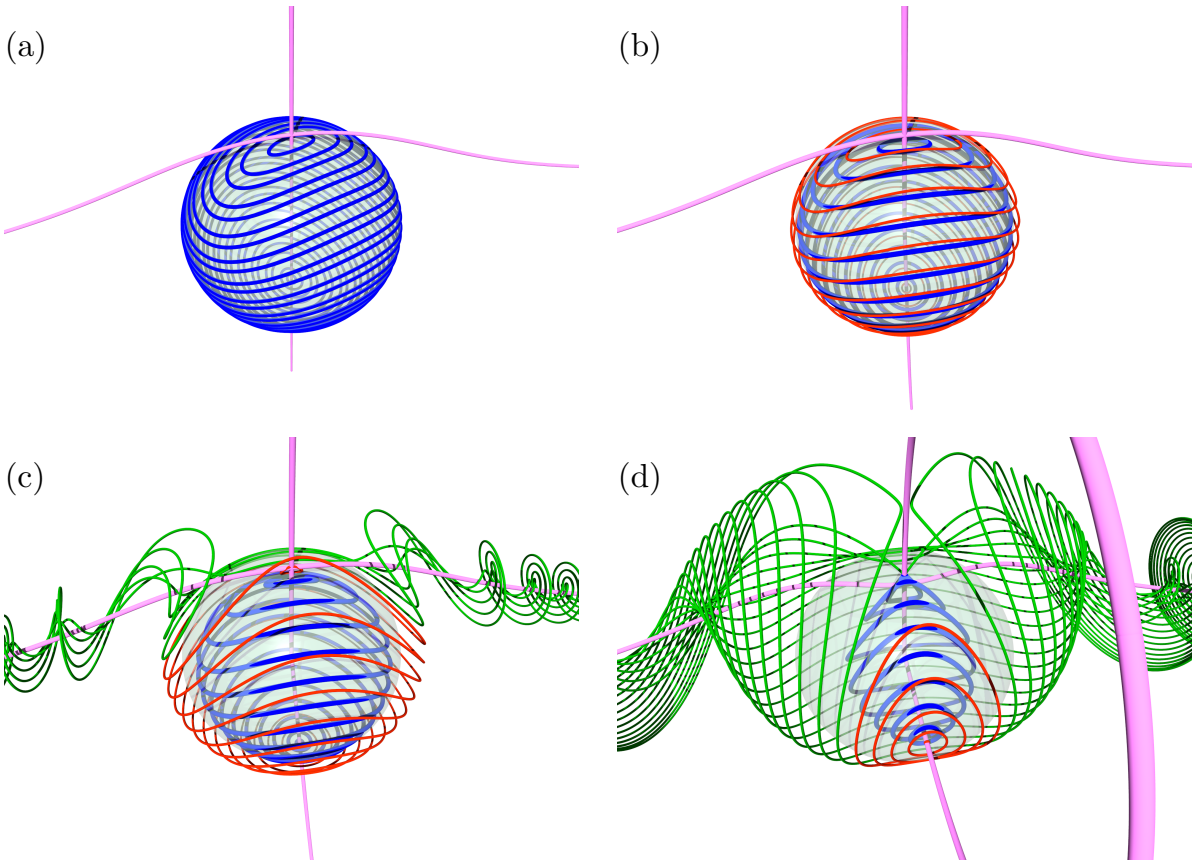


Figure 6.7.: Dynamics on the Bloch sphere for fixed $g = 0.2$ on the surface and different values of the gain-loss parameter: (a) $\Gamma = 0$, (b) $\Gamma = 0.0025$, (c) $\Gamma = 0.01$, (d) $\Gamma = 0.03$

This means, the Hamiltonian is Hermitian and the time evolution operator is unitary. Consequently the dynamics is norm-preserving and we obtain only stable oscillations bound to the sphere around the two stationary states. There is no influence at all from the two $\mathcal{PT}$-broken eigenstates.

More interesting is the dynamics with nonvanishing $\Gamma$. In figure 6.7 (b) it has the small value $\Gamma = 0.0025$ and we observe that the states are now evolving with non-constant radius, i.e. their norm changes. However, the oscillations are still stable. Among these stable oscillations we can distinguish two types. Waves starting at the front of the sphere (blue lines), between the two stationary states, immediately decrease in their norm and dive into the sphere. States starting on the rear side (red lines) start with an increasing norm and tend to larger radii before they return. We discussed already in section 6.2.2 that the start of the dynamics with increasing or decreasing norm is substantial for the fate of the wave packet. Here, we see that the Bloch sphere helps to predict which states will develop in which way. Stable and unstable initial conditions can be classified by

their assignment to a certain region on the sphere (e.g. front or rear side). This is the main value of the Bloch sphere representation.

The difference between the several types of the dynamical solutions becomes even clearer for stronger gain-loss contributions. In figure 6.7 (c) we observe for $\Gamma = 0.01$ that the first trajectories are leaving the sphere to infinite radii, i.e. they represent waves with diverging norm. They are shown as green lines and evolve from those states which started with an increasing norm. It can be seen in the figure that all green lines start on the rear side of the sphere. However, there are still oscillations, also starting with increasing norm (red lines), which still return to the sphere and do not diverge. To complete the picture we have to add the direction of the propagation of the diverging lines. The left $\mathcal{PT}$-broken state has a negative imaginary energy, i.e. it is the decaying state. Hence, the lines diverging to the left correspond in fact to dynamical solutions decaying from huge norms, participating in the dynamics in the vicinity of the sphere for a short time, and then leaving the sphere to the right following with increasing norm the $\mathcal{PT}$-broken state with positive imaginary energy contribution.

Of course, with increasing $\Gamma$ we observe that more and more unstable dynamical solutions appear. Indeed, this is the case as can be seen in figure 6.7 (d) for the value $\Gamma = 0.03$. A large number of the lines describes diverging wave functions. They are dominating the picture to a large extend. This is not surprising. The bifurcation in which the $\mathcal{PT}$-broken states emerge lies now inside the sphere and the eigenstates with complex energies exist already on the surface, which renders the ground state unstable. However, as was already seen in figure 6.3 (d) there are still possible initial conditions for which nonetheless stable oscillations are found. This is verified by the stable island around the excited state figure 6.7 (d). Even more, the stable island now defines the parameter space region in which initial conditions for a stable dynamics are found. Thus, one can deduce from the Bloch sphere representation in an easy manner which wave will diverge and which will evolve with moderate norm fluctuations in the vicinity of the sphere. For even larger $\Gamma$ this is not the case. At some value the stationary states will only exist within the sphere and there will be no stable dynamics on its surface.

# 7. Proposals for a realisation of a $\mathcal{PT}$-symmetric Bose-Einstein condensate

In chapters 3 to 6 we studied various properties of Bose-Einstein condensates trapped in a double well with balanced gain and loss. In all cases the addition and removal of particles was modelled by an imaginary potential which was designed such that the linear part of the Hamiltonian was $\mathcal{PT}$ symmetric. The actual process generating the imaginary potentials has not been considered. The imaginary potentials can, however, always only be an effective description of a true physical process. Since it was the aim of all considerations to finally realise a $\mathcal{PT}$-symmetric quantum system, we have to ask the question of how it will be possible to create a dynamics of a Bose-Einstein condensate which is identical to that generated by the $\mathcal{PT}$-symmetric complex potentials. In this chapter we will present two approaches to tackle this question.

The first approach is based on the idea of embedding the $\mathcal{PT}$-symmetric double well into a larger system, which itself is closed and described by a Hermitian Hamiltonian. The system must be designed such that it enables a directed probability flux from some fraction of the system into one of the two wells and a second directed flux from the second well into some other fraction ignored by the real part of the potential of the $\mathcal{PT}$-symmetric subsystem. The example we want to consider is a multi-well setup in a one-dimensional chain, where the potential minima of the wells are set to different energies such that the wave function tends to flow into the desired direction. Clearly, the simplest example is a four-well potential, where the $\mathcal{PT}$-symmetric double well is formed by the inner two wells. The outer two wells act as reservoirs, i.e. one is a source of atoms, the other a drain. Partially tilted multi-well structures, which could establish the required probability flux, are well accessible with today's experimental techniques [152–154].

In the second approach we assume that we have an external reservoir of atoms in the condensed phase and are able to in- and outcouple these atoms to the double-well setup by a directed flow of unbound atoms, i.e. atoms which are not affected by the trapping potential as long as we do not consider them to be part of the wave function in the double well. It is the aim to show that a coupling of these atoms to the double-well part of the condensate can replace the imaginary potentials in theoretical studies, and thus provide a good candidate for a physical process forming a $\mathcal{PT}$-symmetric Bose-Einstein

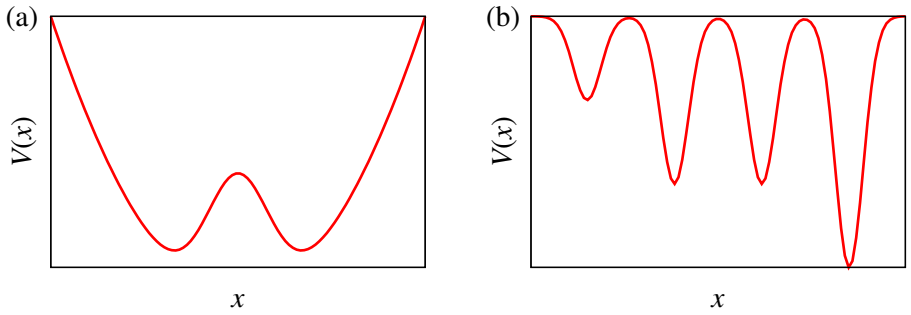


Figure 7.1.: Sketch of the potential considered in the previous chapters (a) and of the potential forming the closed four-well system capable of simulating the $\mathcal{PT}$-symmetric potential for the inner two wells (b).

condensate.

The first approach, viz. the four-well system, will be studied in section 7.1. We will start with simple linear matrix models describing the system in section 7.1.1. Then we will compare the four-well setup with a smaller $\mathcal{PT}$-symmetric system in section 7.1.2, and relate the simple model to a realistic Bose-Einstein condensate in section 7.1.3. In section 7.2 we will investigate the second approach, viz. the coupling of the double-well wave function to propagating waves with a directed flux to or from the two wells. First we will introduce the coupling approach in section 7.2.1, then study a coupling of a $\mathcal{PT}$-symmetric stationary state with an incoming and a further outgoing wave in section 7.2.2, and finally investigate whether a single wave carrying both the in- and outgoing flux is sufficient for the coupling method in section 7.2.3.

The results of the first part of this chapter have already been published and are based on reference [155]. A publication of the newer second part is in preparation. The computations have been done together with Manuel Kreibich during his PhD thesis and with Fabian Single during his Master's thesis [148].

## 7.1. A closed four-well system with an embedded $\mathcal{PT}$-symmetric double well

The setup of the trap used in the previous chapters has the form displayed in figure 7.1 (a), which has already been introduced in a similar way in figure 3.6. It is a simple double-well setup, where the influx and outflux of atoms can only be modelled by imaginary potential contributions. Now we want to investigate a system with a potential sketched in figure 7.1 (b). It consists of four wells, each of them separated from the others by a barrier. The total system is considered to be closed, i.e. we consider only energies for which no particle may leave the whole system, or we assume that an additional

(harmonic) trap exists. Due to an offset of the minima of neighbouring wells a tunnel current of the probability amplitude is possible for proper occupations of the wells. A suitable realisation could consist of an optical potential crated by a superposition of Gaussian laser beams, which would (without a further confinement due to, e.g. a harmonic trap) look like

$$V(\boldsymbol{r}) = \sum_{i=0}^{3} V_i \exp\left[-\frac{2x^2}{w_x^2} - \frac{2y^2}{w_y^2} - \frac{2(z-z_i)^2}{w_z^2}\right] , \tag{7.1}$$

where the values $V_i < 0$ represent the attractive maxima of the light intensity, the values $w$ are the width parameters, and the displacements of the potential minima in $z$ direction are given by the parameters $z_i$. The potential minima of the inner two wells are kept at the same level and their shape is created symmetrically with respect to the barrier between them such that they fulfil the condition for the real part of a $\mathcal{PT}$-symmetric potential.

### 7.1.1. A simple model for a Hermitian four-well system

It seems likely that the system introduced in figure 7.1 (b) is capable of providing an influx of the probability density from the outermost left well to the inner double-well structure and an outflux from the inner two wells to the outermost right well. The important question which has to be answered is, whether or not the system can be shaped such that the in- and outflux corresponds to that of the constant gain-loss parameters used in the previous chapters. To answer this question the system is reduced to its elementary parts and the corresponding dynamics is solved. In chapter 3 we have seen that the dynamics of the Bose-Hubbard dimer [9, 23, 24, 112] could be described with a very illustrative two-dimensional matrix model without losing the typical effects of $\mathcal{PT}$-symmetric systems. Thus, in the spirit of these works low-dimensional matrices are introduced, and we try to understand on this level the relation between a $\mathcal{PT}$-symmetric double well and the four-well setup of figure 7.1 (b).

In a first step we want to analyse the Schrödinger equation of both systems and their relation, i.e. the particle-particle interaction leading to the nonlinearity in the Gross-Pitaevskii equation is neglected. Also we want to keep the equations as simple as possible and introduce only the parameters really necessary for describing all effects. A relation to a real physical situation will be given later.

In the four-well setup we consider four modes $\psi_k$, $k \in 0, 1, 2, 3$ describing a wave function localised in one of the four wells. The wells are counted from left to right, and the observables will be the number of particles in each well described by the norm $n_k = |\psi_k|^2$. Then with these modes forming the vector $\Psi = (\psi_1, \psi_2, \psi_3, \psi_4)^{\mathrm{T}}$, the most

simple Hamiltonian including all required contributions reads

$$H^{(4)} = \begin{pmatrix} E_0(t) & -J_{01}(t) & 0 & 0 \\ -J_{01}(t) & 0 & -J_{12} & 0 \\ 0 & -J_{12} & 0 & -J_{23}(t) \\ 0 & 0 & -J_{23}(t) & E_3(t) \end{pmatrix} . \tag{7.2}$$

The two middle wells have been set to energies $E_1 = E_2 = 0$, and we consider only the offsets $E_0, E_3$ of the outer two wells we introduce to obtain the necessary dynamics. We allow for a coupling of the next nearest neighbour wells via the nonvanishing tunnelling amplitudes $J_{kl}$ in equation (7.2). All components may be time dependent. It is not the aim to construct a static potential but a setup, which is capable of reproducing the constant imaginary potential parts of, e.g. equations (3.2) or (3.11).

The most simple ansatz for the two-dimensional $\mathcal{PT}$-symmetric system with two modes located either in the left well ($\psi_1$) or in the right well ($\psi_2$), where $\Psi = (\psi_1, \psi_2)^{\mathrm{T}}$, is given by a matrix

$$H^{(2)} = \begin{pmatrix} \mathrm{i}\Gamma & -J \\ -J & -\mathrm{i}\Gamma \end{pmatrix} , \tag{7.3}$$

of which the real energies on the diagonal vanish in agreement with equation (7.2). The imaginary contributions $\pm\mathrm{i}\Gamma$ play the role of the parameter $\pm\mathrm{i}\Gamma$ in the double-well system (3.11) and model a gain or loss of atoms. To allow for $\mathcal{PT}$-symmetric solutions we have to couple the two modes via a tunnelling parameter $J$.

The matrix

$$\mathcal{P} = \begin{pmatrix} 0 & 1 \\ 1 & 0 \end{pmatrix} \tag{7.4}$$

interchanges the two modes, i.e. the wave functions localised in one of the two wells, and represents the parity operator in this system, whereas the time reversal operator is simply a complex conjugation. With these definitions it is easy to verify that the system (7.3) fulfils all properties of $\mathcal{PT}$-symmetric quantum systems. The two energy eigenvalues $E_\pm = \pm\sqrt{J^2 - \Gamma^2}$ are real for values of $\Gamma$ below the critical parameter $\Gamma = J$ and the corresponding eigenvectors are $\mathcal{PT}$ symmetric themselves. Beyond $\Gamma = J$ the eigenvalues are purely imaginary and the eigenvectors fulfil the relations $\Psi_{E_+} = \mathcal{PT}\Psi_{E_-}$ and vice versa.

### 7.1.2. Equivalence to the $\mathcal{PT}$-symmetric double well

The question is now whether the two systems agree. This will be the case if the dynamics of the observable quantities, i.e. the occupation densities $n_k(t) = |\psi_k(t)|^2$ of the two inner wells ($k \in 1, 2$) fulfil the same dynamical equations. Hence, the necessary task is to evaluate the equations of motion of the quantities $n_k$ in both systems.

From the Schrödinger equation for the four-well system one obtains in $\hbar$-scaled time ($t \to \hbar t$) the time derivatives

$$\partial_t n_1 = j_{01} - j_{12} \ , \tag{7.5a}$$
$$\partial_t n_2 = j_{12} - j_{23} \ , \tag{7.5b}$$
$$\partial_t j_{12} = 2J_{12}^2(n_2 - n_1) + J_{12}(J_{23}C_{13} - J_{01}C_{02}) \ , \tag{7.5c}$$

where the abbreviations $j_{kl} = \mathrm{i}J_{kl}(\psi_k\psi_l^* - \psi_k^*\psi_l)$ and $C_{kl} = \psi_k\psi_l^* + \psi_k^*\psi_l$ have been introduced. The same calculation for the non-Hermitian two-well matrix leads to

$$\partial_t n_1 = -j_{12} + 2\Gamma n_1 \ , \tag{7.6a}$$
$$\partial_t n_2 = j_{12} - 2\Gamma n_2 \ , \tag{7.6b}$$
$$\partial_t j_{12} = 2J^2(n_1 - n_2) \tag{7.6c}$$

with $j_{12} = \mathrm{i}J(\psi_1\psi_2^* - \psi_1^*\psi_2)$.

Obviously there are differences between the equations, however, a comparison of equations (7.5a)-(7.5c) with their counterparts (7.6a)-(7.6c) reveals that for the conditions

$$j_{01} = 2\Gamma n_1 \ , \tag{7.7a}$$
$$j_{23} = 2\Gamma n_2 \ , \tag{7.7b}$$
$$J_{01}C_{02} = J_{23}C_{12} \tag{7.7c}$$

we have an exact agreement of the time evolution of the occupation of the inner two wells of the four-well model with the two wells of the $\mathcal{PT}$-symmetric double well. The only remaining question is, whether or not the conditions (7.7a)-(7.7c) can be fulfilled with physically accessible parameters. A detailed calculation, which does not give more insight and does not need to be reproduced here, shows that this is indeed possible [155]. The result of the calculation are time-dependent conditions,

$$E_0(t) = E_0(\psi_k, \Gamma, J_{12}) \ , \tag{7.8a}$$
$$E_3(t) = E_3(\psi_k, \Gamma, J_{12}) \ , \tag{7.8b}$$
$$J_{01}(t) = J_{01}(\psi_k, \Gamma, J_{12}) \ , \tag{7.8c}$$
$$J_{23}(t) = J_{01}(\psi_k, \Gamma, J_{12}) \ , \tag{7.8d}$$

which can only be given in an implicit form. The important consequence is, however, that the four quantities $E_0(t)$, $E_3(t)$, $J_{01}(t)$, and $J_{23}(t)$ have to be adjusted in such a way that the conditions (7.7a)-(7.7c) with a constant value $\Gamma$ specified by the two-dimensional $\mathcal{PT}$-symmetric system are fulfilled. To control the energies $E_0(t)$ and $E_3(t)$ the potential minima have to be varied in a experiment. Also the off-diagonal matrix elements $J_{01}(t)$ and $J_{23}(t)$ are accessible in an experiment via the shape of the potential. To set their values their widths or heights of the potential barriers have to be shifted. It is important

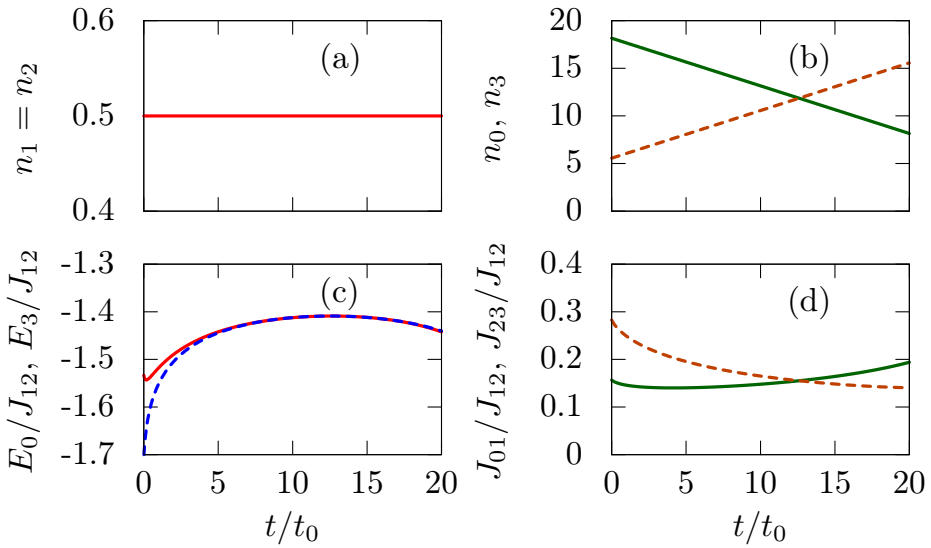


Figure 7.2.: Realisation of a $\mathcal{PT}$-symmetric stationary solution in the four-well system. (a) The populations $n_1$ and $n_2$ in the inner wells stay constant. (b) In the left well $n_0$ (solid green line) decreases constantly, whereas $n_3$ (dashed orange line) increases in the right well. (c) Required variation of the potential minima in the outer wells. (d) Necessary time-dependent values of the tunnelling amplitudes $J_{kl}$. All times are measured in units of $\hbar/J_{12}$. Figure taken from [155].

to note that all conditions can only be fulfilled with an appropriate distribution of the wave function in the beginning. That is, the possibility of embedding a $\mathcal{PT}$-symmetric double well in the larger Hermitian four-well system does not only depend on the correct choice of the external parameters as the potential but does also require an adequate initial state.

More interesting than the explicit form of the equations for $E_0(t)$, $E_3(t)$, $J_{01}(t)$, and $J_{23}(t)$ are examples showing a behaviour of the inner two wells which we expect for a $\mathcal{PT}$-symmetric system. The first example in figure 7.2 is a state we called stationary in chapter 3, i.e. it corresponds to a solution for which the probability amplitude is constant in the two $\mathcal{PT}$-symmetric wells. This corresponds to an eigenstate of the two-well system with a real energy and $\mathcal{PT}$-symmetric wave function. This quasi-stationary solution is obtained for the initial set $n_1(t=0) = n_2(t=0) = 1/2$, $\Gamma/J_{12} = 1/2$, which obviously already has the correct occupation.

Indeed, the occupation of the inner two wells stays constant for the time span shown in the figure. The amplitude of the wave function is always equal in both wells, which corresponds to the $\mathcal{PT}$ symmetry of the wave function as can be verified in figure 7.2 (a). The linear decrease of the probability amplitude in the left well and the increase in the right well as shown in figure 7.2 (b) verify the behaviour necessary for the constant value

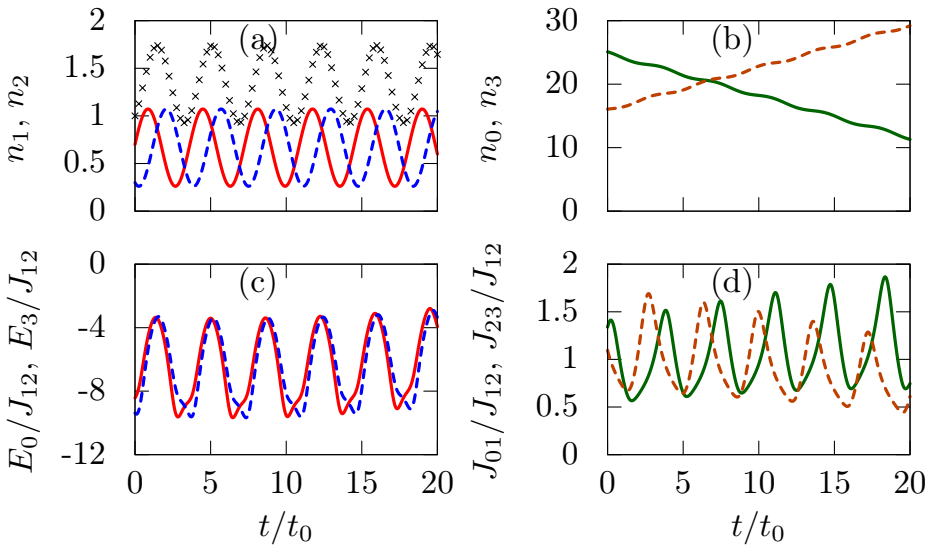


Figure 7.3.: Realisation of a dynamical $\mathcal{PT}$-symmetric solution in the four-well system. (a) The populations $n_1$ and $n_2$ in the inner wells oscillate around constant values with a phase relation $\Delta\varphi \neq \pi$. The black crosses represent the added amplitude of both wells. (b) Small oscillations are added to the decay of $n_0$ (solid green line) and the growth of $n_3$ (dashed orange line). (c) Required variation of the potential minima in the outer wells. (d) Necessary time-dependent values of the tunnelling amplitudes $J_{kl}$. Figure taken from [155].

of $\Gamma$ enforced by the $\mathcal{PT}$-symmetric double-well description. To achieve this situation a time-dependent adaption of the potential parameters is necessary, which can be done in moderate limits as follows from figures 7.2 (c) and (d). Of course the whole description will break down after some time since the constant influx from $n_0$ to $n_1$ is necessary and at some point in time $n_0$ will be too small to provide the required flux.

A dynamical property of $\mathcal{PT}$-symmetric quantum systems are the stable but phase shifted Rabi-like oscillations as for example obtained for the linear double-delta model in figure 6.1. If we want to describe the $\mathcal{PT}$-symmetric double well completely with the four-well model the latter one should also contain the correct time-dependent solution. To verify this the temporal evolution of the four modes is started with an initial condition including $n_1(t=0) = 0.7$, $n_2(t=0) = 0.3$, and $\Gamma/J_{12} = 1/2$. The result can be seen in figure 7.3. The stable oscillations are present, in both wells the probability amplitude oscillates around a mean value. In figure 6.1 we observed for nonvanishing gain-loss parameters that the total amplitude integrated over both wells also is not constant but oscillates in time. This happens due to the phase difference $\Delta\varphi \neq \pi$ between the oscillations in both wells and is possible due to the gain and loss effects. In the simple matrix model used in this section this effect must be visible in the added number $n_1 + n_2$, which is verified by the black crosses in figure 7.3 (a). We also observe that

the oscillations carry over to the occupation of the outer wells [figure 7.3 (b)] and the required potential parameters [figures 7.3 (c) and (d)].

### 7.1.3. Relation with a realistic Bose-Einstein condensate

The results of section 7.1.2 show that it is in principle possible to embed a $\mathcal{PT}$-symmetric system into a larger Hermitian system. With a correct variation of the larger system's shape it can exactly reproduce the description of balanced gain and loss in a subsystem. However, our aim is a realisation of this situation for a Bose-Einstein condensate. For this there are still three open questions. Firstly, so far we did not take care of the contact interaction $\sim |\psi|^2$, i.e. the nonlinearity in the Gross-Pitaevskii equation. Will the additional term in the Hamiltonian disturb the properties we found in section 7.1.2? Secondly, we did not consider realistic parameter values. Is it possible to relate the matrix $H^{(4)}$ with suitable potentials and typical interactions of atomic systems? Thirdly, we adjusted in section 7.1.2 directly the onset energies and tunnelling amplitudes. Is there a feasible procedure without the need for a permanent measurement of all condensate parameters?

These questions will be answered with an extension of the model. To take the contact interaction into account we add to the matrix (7.2) the Gross-Pitaevskii nonlinearity, such that

$$H^{(4)}_{\text{nonlin}} = H^{(4)} + g\,\text{diag}(|\psi_1|^2, |\psi_2|^2, |\psi_3|^2, |\psi_4|^2)\ . \tag{7.9}$$

Then the relation to the Gross-Pitaevskii equation is done via an explicit assumption for the four modes $\psi_k$, $k \in 0, 1, 2, 3$. We assume them to have the shape of a Gaussian wave function, i.e. the total wave function is given by a set of Gaussians,

$$\psi = \sum_{k=0}^{3} d_k \mathrm{e}^{-A_x x^2 - A_y y^2 - A_z (z-z_k)^2} \tag{7.10}$$

centred at the four potential minima $z_k$. To simplify the further calculation we assume the width parameters $A$ to be constant in time. Since all potential wells have the same width, we also assume that they are identical for each mode as already expressed in equation (7.10). With these assumptions the only dynamical variables in equation (7.10) are the amplitudes $d_k(t)$. With the potential (7.1) the Gross-Pitaevskii equation

$$\mathrm{i}\hbar\frac{\partial}{\partial t}\psi(\boldsymbol{r},t) = \left(-\frac{\hbar^2}{2m}\Delta + V(\boldsymbol{r}) + N\frac{4\pi\hbar^2 a_\mathrm{s}}{m}|\psi(\boldsymbol{r},t)|^2\right)\psi(\boldsymbol{r},t) \tag{7.11}$$

[cf. equation (3.1)] leads to a set of equations of motion for the $d_k(t)$. Using the four Gaussians in the ansatz (7.10) as (non-orthogonal) basis functions these equations of motion can be brought to a matrix form, which allows for an identification of the matrix elements $E_i$, $J_i$ in equation (7.2) with the potential (7.1) and the Gaussian parameters from equation (7.10) [155]. Thus, it is possible to relate all of the abstract variables in the matrix with real physical quantities.

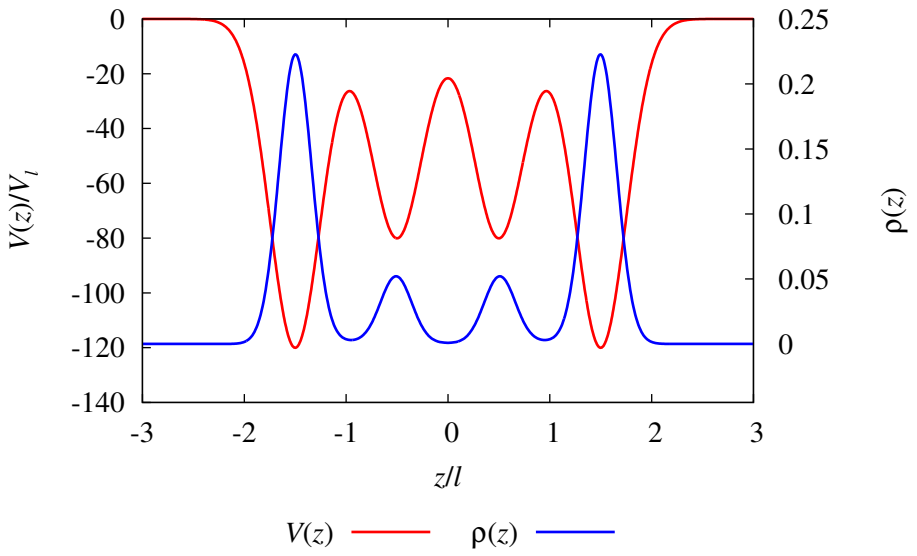


Figure 7.4.: Initial potential $V(z)$ and density $\rho(z)$ of the wave function before the adiabatic ramp (7.12) starts.

The last step is to find an applicable procedure. In principle it is possible to solve a system of equations similar to that in section 7.1.2 such that the nonlinear matrix model describes a nonlinear $\mathcal{PT}$-symmetric two-dimensional system. However, we want to obtain a procedure which is feasible in an experiment. In particular, it has to work without the need for always controlling all variables. The method is supposed to work with a predefined scheme. We will show an example for typical physical parameters. To do so, we assume a condensate of $N = 10^5$ atoms of $^{87}$Rb with $a_s$ set to 10.9 Bohr radii via a Feshbach resonance. The four wells are located at distances of $\ell = 2\,\mu$m. This distance is also used to define the unit of energy via $V_\ell = \hbar^2/(m\ell^2)$, i.e. $V_\ell/h = 29.1\,$Hz and the unit of time $t_\ell = \hbar/V_\ell = 5.47\,$ms.

The procedure starts with a symmetric potential with $V_1 = V_2 = -80V_\ell$ and $V_0 = V_3 = -122V_\ell$ and the widths $w_x = w_y = 4\ell$, $w_z = \ell/2$. For these conditions the ground state is calculated via minimising the mean field energy, i.e. the condensate is assumed to relax in this trap to the ground state. The result is visible in figure 7.4. As can be seen the condensate is mainly localised in the outer two wells, which is in particular important for the reservoir providing the gain to the inner double well. Then the potential is ramped adiabatically such that the virtual gain-loss parameter will follow the function

$$\Gamma(t) = \Gamma_f\,[1 - \cos(\pi t/t_f)]\ , \quad 0 < t < t_f \tag{7.12}$$

with $t_f = 70t_\ell$ and $\Gamma_f/J_{12} = 0.5$ shown in figure 7.5 (a). To achieve this behaviour the potential depths have to be adjusted according to figure 7.5 (b). Also the centres of the outer wells have to be moved a bit. Their displacements $\delta_k$ from their position on the

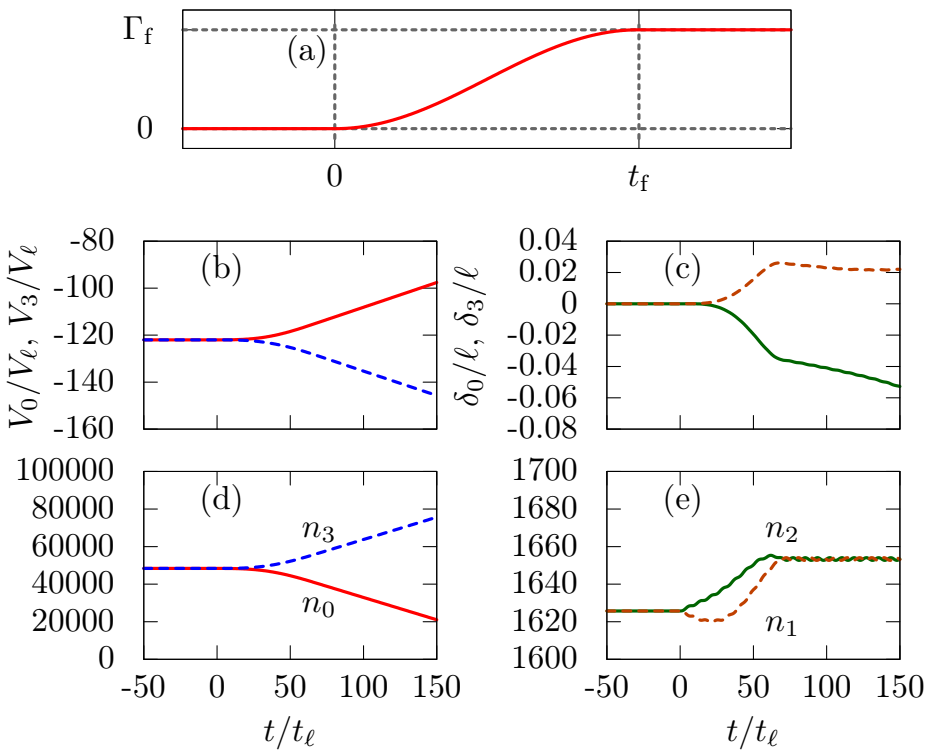


Figure 7.5.: (a) Time-evolution of the virtual gain-loss parameter Γ during the adiabatic ramp. (b) Required variation of the potential depths to obtain the ramp from (a). (c) Displacements $\delta_k$ of the outer two wells form their original positions. (d) Population of the two outer wells during the procedure. (e) Number of particles in the two inner wells. Starting with $t \approx 70$ a $\mathcal{PT}$-symmetric situation is achieved. Figure taken from [155].

equidistant grid is shown in figure 7.5 (c). However, we note that these displacements are small and just used to fulfil the necessary conditions. It has been checked that it is possible to keep the displacements at $\delta = 0$ without disturbing the conditions for the condensates considerably.

The result for the wave function can be seen in figures 7.5 (d) and (e). After the ramp achieved its final value at $t \approx 70$ we observe a constant loss of amplitude in well 0 and a constant gain in well 3. The two inner wells first experience a sudden change of the number of particles. However, after $t \approx 70$ all variations settle down and assume a constant value for all times shown in the figure. This is the desired $\mathcal{PT}$-symmetric condition. With balanced in- and outflux of particles the wave function in the inner two wells does not change at all. Again, it should be mentioned that the $\mathcal{PT}$-symmetric situation is only available for a certain time. The reservoirs $n_0$ and $n_3$ are not infinitely large, and thus after some time the necessary conditions for the constant and balanced

gain and loss can no longer be fulfilled.

Thus, we conclude that also in the nonlinear case of the Gross-Pitaevskii equation it is possible to consider a non-Hermitian $\mathcal{PT}$-symmetric system as a part of a larger closed Hermitian system accessible with today's experimental methods. We did this in a very simple calculation based on a matrix model, however, it was possible to relate the matrix elements with real physical parameters available in an experiment. The embedding of the double well in a multi-well structure also shows the relation of $\mathcal{PT}$-symmetric condensates with a transport process of a Bose-Einstein condensate in a titled optical lattice [44, 156–160].

## 7.2. Directed coupling to and from the double well

The second possibility we want to investigate for a possible realisation of a Bose-Einstein condensate subject to balanced gain and loss is based on a direct coupling of two Bose-Einstein condensates. Since the trapping in double-well potentials and an out-/incoupling of parts of the condensate are experimentally available [91, 92] this is a further promising approach. We will keep the discussion on a very elementary level to get the most illustrative insight. The emphasis is on the question whether or not a coupling setup can in principle be realised. The system we want to study is the double-delta potential introduced already in section 3.1. Here the two traps are infinitesimally thin and we only have to take into account two points in position space for the coupling since in all geometries the wave functions of the different condensate parts are supposed to have only an overlap within the delta traps.

### 7.2.1. Coupling approach

Before we will investigate possible geometries allowing for a coupling of two condensate parts at two isolated delta traps we first want to outline the approach how this coupling is implemented in the equations. Based on the Gross-Pitaevskii equation for the double-delta trap we now assume that we have two condensate modes $\psi_1$ and $\psi_2$, where each of them is exposed to the same attractive delta potential. We first consider only one point of interaction between the modes in a single-well setup and discuss the required relations for the individual setups in double-delta geometries later. In addition to the known Gross-Pitaevskii equation from section 3.1 we introduce a coupling with strength $\eta$ such that in the units from chapter 3 it reads

$$-\frac{\mathrm{d}^2}{\mathrm{d}x^2}\psi_1 - \delta(x-x_0)\psi_1 - g|\psi_1|^2\psi_1 + \eta\psi_2(x_0)\delta(x-x_0) = \mu_1\psi_1 \ , \tag{7.13a}$$

$$-\frac{\mathrm{d}^2}{\mathrm{d}x^2}\psi_2 - \delta(x-x_0)\psi_2 - g|\psi_2|^2\psi_2 + \eta\psi_1(x_0)\delta(x-x_0) = \mu_2\psi_2 \ . \tag{7.13b}$$

Will the coupling terms in equations (7.13a) and (7.13b) be capable of producing the imaginary potential contributions of the $\mathcal{PT}$-symmetric Gross-Pitaevskii equation (3.3)?

This is only possible if the coupling term can be seen as an imaginary potential contribution. i.e. we require, e.g. for equation (7.13a)

$$\eta\psi_2(x_0) = \mathrm{i}\gamma\psi_1(x_0) \;, \tag{7.14a}$$

which enforces

$$\gamma = -\mathrm{i}\eta\frac{\psi_2(x_0)}{\psi_1(x_0)} \;. \tag{7.14b}$$

Equation (7.14b) relates the non-Hermitian contribution the wave function $\psi_1$ would experience in the $\mathcal{PT}$-symmetric potential (3.2) with a coupling constant $\eta$ and the amplitude of both waves at position $x_0$. Since $\gamma$ was assumed to be a real positive constant in section 3.1, and we also want $\eta$ to describe a real positive coupling strength, the phase of the ratio $\psi_2(x_0)/\psi_1(x_0)$ is fixed:

$$-\mathrm{i}\eta\frac{\psi_2(x_0)}{\psi_1(x_0)} = -\mathrm{i}\eta\frac{|\psi_2(x_0)|}{|\psi_1(x_0)|}\mathrm{e}^{\mathrm{i}(\varphi_2-\varphi_1)} \stackrel{!}{=} \gamma \;, \tag{7.15}$$

where $\varphi_i$ is the phase of the complex number $\psi_i(x_0)$. This leads to

$$\varphi_2 = \varphi_1 + \frac{\pi}{2} \;, \tag{7.16a}$$

$$\eta = \gamma\frac{|\psi_1(x_0)|}{|\psi_2(x_0)|} \;. \tag{7.16b}$$

With the relations (7.16a) and (7.16b) the coupling term for the second wave function in equation (7.13b) reads

$$\eta\psi_1(x_0) = -\mathrm{i}\gamma\frac{|\psi_1(x_0)|^2}{|\psi_2(x_0)|^2}\psi_2(x_0) \;. \tag{7.17}$$

At first glance the coupling we produced seems to be asymmetric. Whereas with our ansatz the coupling term of wave function $\psi_1$ was forced to have the simple structure $\mathrm{i}\gamma\psi_1$ the non-Hermitian term we created for wave function $\psi_2$ is given by the more complex relation (7.17). However, if we calculate the source-drain term for the probability density established by an imaginary potential according to equation (2.3), we observe

$$\frac{\partial\rho_1}{\partial t} = 2\gamma|\psi_1(x_0)|^2 \;, \tag{7.18a}$$

$$\frac{\partial\rho_2}{\partial t} = -2\gamma\frac{|\psi_1(x_0)|^2}{|\psi_2(x_0)|^2}|\psi_2(x_0)|^2 = -2\gamma|\psi_1(x_0)|^2 \;. \tag{7.18b}$$

That is, the two fluxes of the probability density are opposite in direction and of the same strength. The probability density which is incoupled to one wave is outcoupled

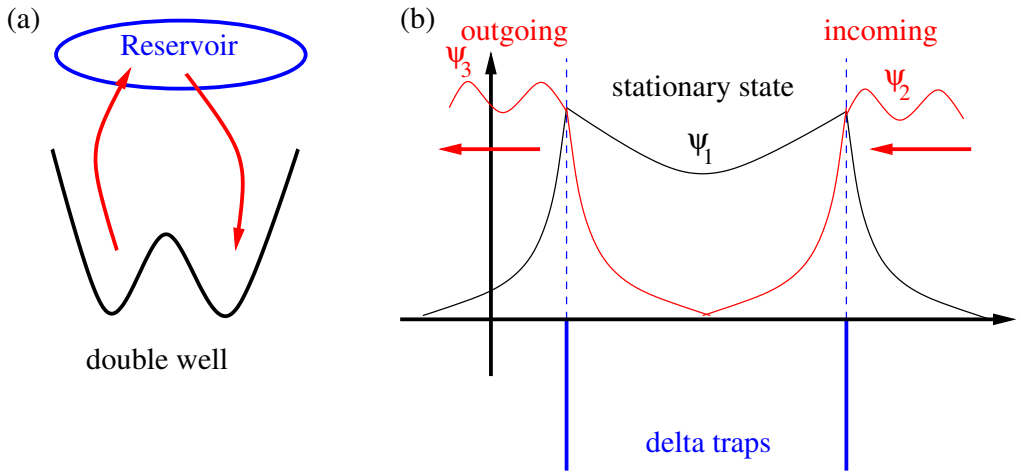


Figure 7.6.: (a) Idea of the coupling to a reservoir with directed atom flows. (b) Sketch of the one-dimensional model with delta traps modelling the coupling approach of (a).

from the other. Hence, our approach describes exactly the desired behaviour. One wave experiences a gain behaving exactly like that of an imaginary potential, whereas the other experiences a loss of the same amplitude.

We have to take care of one important property. From equation (7.15) we learn that the correct phase, which is important for the flux of the probability density, is completely determined by the phase relation of the wave function. It has to be constant for all times. Otherwise we will not be able to model constant source or drain terms. This can be adjusted if both states $\psi_1$ and $\psi_2$ are stationary and have the same energy $\mu$. Then their time-dependent phase $\mathrm{e}^{-\mathrm{i}\mu t}$ oscillates with the same frequency and the phase relation stays constant. Thus, we require $\mu_1 = \mu_2$ in equations (7.13a) and (7.13b). In the following we want to use the coupling approach for creating a fully $\mathcal{PT}$-symmetric environment. We will also show how the necessary conditions can be fulfilled.

### 7.2.2. Coupling to an incoming and an outgoing wave

We want to assume that we have outcoupled a condensate fraction from a reservoir and incouple the atoms to a stationary $\mathcal{PT}$-symmetric state. At the second trap we outcouple atoms, and afterwards they may propagate as a unbound wave. The outcoupling might be implemented with Bragg beams as experimentally performed in reference [91]. A sketch of the situation we have in mind is shown in figure 7.6 (a). The one-dimensional model, which is used for the calculations, is shown in figure 7.6 (b). It consists of three wave functions, of which $\psi_1$ is supposed to be the stationary $\mathcal{PT}$-symmetric solution. The wave $\psi_2$ is incoming, $\psi_3$ is outgoing. The general forms of the corresponding Gross-

Pitaevskii equations are

$$-\frac{\mathrm{d}^2}{\mathrm{d}x^2}\psi_1 - [\delta(x+a/2)+\delta(x-a/2)]\,\psi_1 - g|\psi_1|^2\psi_1 + \eta\psi_3(-a/2)\delta(x+a/2) + \eta\psi_2(a/2)\delta(x-a/2) = \mu\psi_1\ , \quad (7.19a)$$

$$-\frac{\mathrm{d}^2}{\mathrm{d}x^2}\psi_2 - [\delta(x+a/2)+\delta(x-a/2)]\,\psi_2 - g|\psi_2|^2\psi_2 + \eta\psi_1(a/2)\delta(x-a/2) = \mu\psi_2\ , \quad (7.19b)$$

$$-\frac{\mathrm{d}^2}{\mathrm{d}x^2}\psi_3 - [\delta(x+a/2)+\delta(x-a/2)]\,\psi_3 - g|\psi_3|^2\psi_3 + \eta\psi_1(-a/2)\delta(x+a/2) = \mu\psi_3\ . \quad (7.19c)$$

What happens with the waves $\psi_2$ and $\psi_3$ behind the coupling point is in principle not of further interest. However, we want to assume that the incoming wave function drops to zero due to the coupling. This corresponds to a complete incoupling and is certainly a very strict condition. As we will see it can be fulfilled by the bound and unbound solutions of the double-delta potential such that it does not mean any difficulty for us. The shapes of the wave functions in figure 7.6 (b) indicate already this behaviour. Similarly we assume that the whole outgoing wave originates completely from the condensate in the trap. This is clearly the most reasonable ansatz since there is absolutely no need for an interaction with an already existing unbound wave during the outcoupling process.

There are a few requirements on the wave functions we use for the coupling process. If we want to support a special $\mathcal{PT}$-symmetric wave function of those obtained in section 3.1.2 $\psi_2$ and $\psi_3$ must, on the declining side, be stationary states of the Gross-Pitaevskii equation with the same chemical potential $\mu$ to obey the constant phase relation (7.15). Furthermore, the in- and outcoupling must be such that it exactly replaces the imaginary potential of strength $\gamma$.

As already mentioned in section 3.1.2 the Jacobi elliptic functions are solutions of the time-independent Gross-Pitaevskii equation outside the delta traps [123, 136–138]. This will be our starting point for the construction of the waves we need to create the setup we have in mind. Since the in- and outflowing waves $\psi_2$ and $\psi_3$ are supposed to vanish far off the delta trap on one side we describe this part by the function

$$\psi_2(x) = \sqrt{\frac{2\kappa^2}{g}}\mathrm{cn}(\kappa(x-x_1),1) = \sqrt{\frac{2\kappa^2}{g}}\mathrm{sech}(\kappa(x-x_1)) = \sqrt{\frac{2\kappa^2}{g}}\frac{1}{\cosh(\kappa(x-x_1))}\ . \quad (7.20)$$

Note that this wave function automatically fulfils the energy condition if $\kappa$ is chosen such that $\mu = -\kappa^2$ with the chemical potential $\mu$ of the stationary state. With the free

parameter $x_1$ it is possible to adjust the value of the wave function at the coupling point $x = a/2$, which can be used to set via equation (7.16b) the strength $\gamma$ of the intended imaginary potential even if we have no influence on the coupling parameter $\eta$. The sole restriction is that the amplitude of $\psi_2(a/2)$ can only be in the interval $(0, \sqrt{2\kappa^2/g}]$.

With these steps $\psi_2(x)$ is completely defined on the left hand side of the delta trap at $x = a/2$. With the continuity conditions at delta functions also the right hand side is given, it just has to be integrated with a standard integrator. Thus, we have found the entire form of the wave function $\psi_2$. The same procedure can be applied to search for the necessary wave $\psi_3$. It turns out in the numerical solutions that the wave functions also carry the required flux of the probability amplitude, as is expected from the construction. The decaying parts described by the $\mathrm{sech}(\kappa(x - x_1))$-functions have no flux. The whole in- and outcoupling is done by the "free" part of the wave on the other side of the delta trap. This flux has exactly the same size and direction as that of the stationary wave function $\psi_1$ between the two attractive delta potentials.

Since only the maximum height $\sqrt{2\kappa^2/g}$ of the wave functions at the coupling point restricts the available feeder wave functions it seems very likely to find adequate solutions. Unfortunately, this is not completely true. We found in chapter 5 that the stability of the wave functions is important. Already the stability properties of the stationary states are very complex and needed a detailed investigation. The same is true for the unbound waves needed as feeders in this section. An extensive stability analysis has been done [148]. The analysis revealed that it is indeed possible to find solutions which fulfil all requirements to support the $\mathcal{PT}$-symmetric stationary states. This is in particular true for the excited of the two stationary states. For the ground state it is more difficult.

Figure 7.7 shows a simulation of the wave functions found for the case $g = 1$, $a = 1.1$, and $\gamma = 0.1$ with the split operator method. The excited state (left column) shows a stable behaviour until $t \approx 15$. For larger times we observe perturbations first in the feeder functions $\psi_2$ (middle row) and $\psi_3$ (bottom row) which carry over to the quasi stationary state (top row). The perturbations are the result of the singular delta potential, for which the time evolution is hard to simulate. In this respect the choice of the double-delta potential does not seem to be the simplest ansatz. The ground state is even earlier affected by the perturbations as can be seen in the right column of figure 7.7. The important result is, however, that the $\mathcal{PT}$-symmetric situation is kept for some time and obviously correctly described by the coupling of $\psi_1$ with the two unbound waves.

### 7.2.3. Coupling to a single external wave

Finally we want to evaluate the possibility of coupling only two waves such that at least one of them experiences the same effect as in a $\mathcal{PT}$-symmetric external potential. Of course, this will be much more challenging to realise as the previous example with three interacting wave functions, however, it is again the purpose to investigate whether the equations of a setup of this kind can be brought in agreement with the expectation we have from the $\mathcal{PT}$-symmetric non-Hermitian system. Again, we reduce the problem to

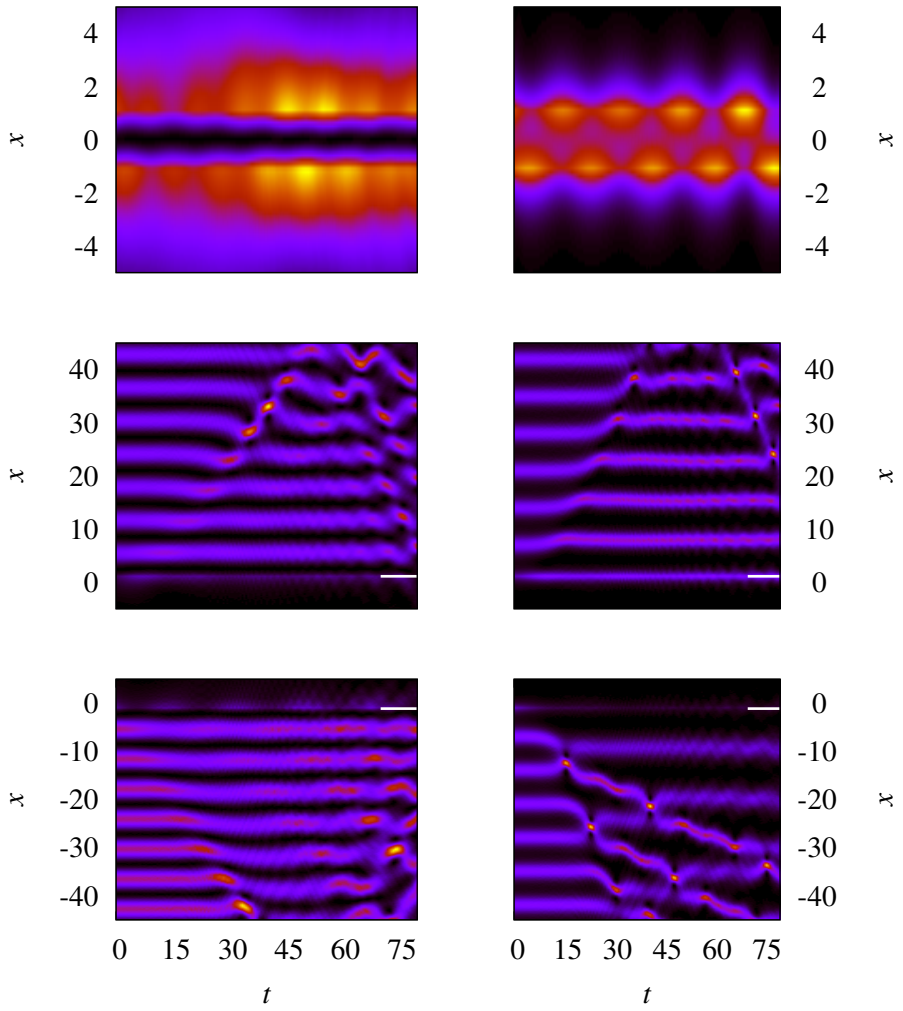


Figure 7.7.: Simulation of the coupling of two unbound wave functions to the stationary ground (right) and excited (left) state of the $\mathcal{PT}$-symmetric double-delta potential from section 3.1 with $g = 1$, $a = 1.1$, and $\gamma = 0.1$ (cf. figure 3.3). Shown are from top to bottom the wave functions $\psi_1$, $\psi_2$, and $\psi_3$. The white lines in the figures of the feeder functions indicate the coupling points, i.e. the positions of the delta traps. Figure taken from [148].

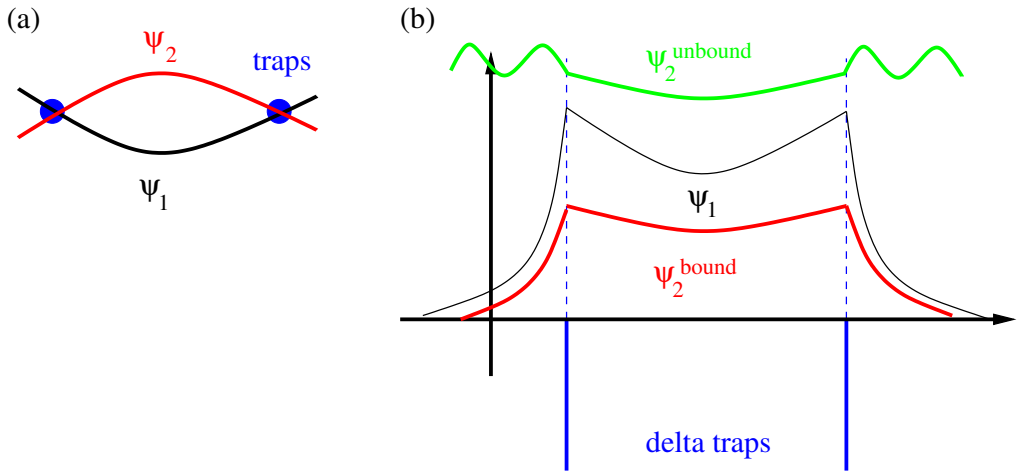


Figure 7.8.: (a) Top view of a geometry of a virtual setup with two one-dimensional condensates overlapping only at two infinitesimally thin attractive delta potentials. (b) The stationary $\mathcal{PT}$-symmetric state $\psi_1$ (black) can either be coupled to a second bound state (red) or an unbound wave function (green).

one dimension, use the double-delta model, and assume that the coupling is only present in the two infinitesimally thin delta traps. The equations of this model are given by

$$-\frac{\mathrm{d}^2}{\mathrm{d}x^2}\psi_1 - [\delta(x+a/2)+\delta(x-a/2)]\,\psi_1 - g|\psi_1|^2\psi_1 + \eta\,[\psi_2(-a/2)\delta(x+a/2)+\psi_2(a/2)\delta(x-a/2)] = \mu_1\psi_1\,, \quad (7.21a)$$

$$-\frac{\mathrm{d}^2}{\mathrm{d}x^2}\psi_2 - [\delta(x+a/2)+\delta(x-a/2)]\,\psi_2 - g|\psi_2|^2\psi_2 + \eta\,[\psi_1(-a/2)\delta(x+a/2)+\psi_1(a/2)\delta(x-a/2)] = \mu_2\psi_2\,, \quad (7.21b)$$

where, as in the previous example, $\psi_1$ will be the stationary $\mathcal{PT}$-symmetric state we are interested in.

A virtual geometry in agreement with our assumptions is shown in figure 7.8 (a). It consists of two quasi one-dimensional condensates overlapping only in the two attractive delta potentials. Figure 7.8 (b) displays two possibilities for the second wave function $\psi_2$. We can either assume that $\psi_2$ is also a bound state or that it is similarly to section 7.2.2 an unbound state. We will study both possibilities in the following.

### Conditions at the coupling points

We want that the $\mathcal{PT}$-symmetric stationary state $\psi_1$ is exposed to an in- and outflux of the probability density in exact agreement with the action of the imaginary potentials

with strength $\gamma$. With the calculations from section 7.2.1 this leads immediately to the conditions [cf. equation (7.16a)]:

$$\varphi_2(a/2) = \varphi_1(a/2) + \frac{\pi}{2} \,, \tag{7.22a}$$

$$\varphi_2(-a/2) = \varphi_1(-a/2) - \frac{\pi}{2} \,, \tag{7.22b}$$

where $\varphi_i$ is the phase of wave function $i$. This already indicates that not all wave functions can be combined such that the correct behaviour of the flux at the delta traps is present. Additionally we want, as in section 7.2.2, that this phase relation is constant in time. This is a further restriction leading to the condition that the chemical potentials of both states must be identical.

### Coupling of two bound states

The energy condition tells us immediately that, if we want to couple two bound states such that they form a $\mathcal{PT}$-symmetric situation, these two states have to be almost the same solutions of the Gross-Pitaevskii equation. They have only to differ in one aspect. To ensure that the flux of the probability density is flowing in the correct direction and that the result of equation (7.17) is met (If one wave function experiences a gain at the coupling point the other is exposed to a loss and vice versa.), $\psi_2$ has to solve the same Gross-Pitaevskii equation as $\psi_1$ but with opposite sign of $\gamma$. The result will be the spatially reflected state $\psi_1(-x)$. The global phase of the solutions is arbitrary and this is the sole freedom we have for $\psi_2$. In total we can write down the wave function as

$$\psi_2(x) = \mathrm{e}^{\mathrm{i}\theta}\psi_1(-x) \,, \tag{7.23a}$$

$$\text{i.e. } \varphi_2(x) = \varphi_1(-x) + \theta \,. \tag{7.23b}$$

With the knowledge that both states are $\mathcal{PT}$ symmetric we have furthermore

$$\varphi_1(x) = -\varphi_1(-x) \,, \tag{7.24a}$$

$$\varphi_2(x) = -\varphi_2(-x) \,. \tag{7.24b}$$

After combining these relations we obtain

$$\varphi_1(a/2) = -\varphi_1(-a/2) = -\varphi_2(a/2) = \varphi_2(-a/2) = -\frac{\pi}{4} \,, \tag{7.25a}$$

$$\theta = 0 \,. \tag{7.25b}$$

The important consequence of equation (7.25a) is that only $\mathcal{PT}$-symmetric states with $\varphi(-a/2) - \varphi(a/2) = \pi/2$ are acceptable. This restricts the number of possible solutions drastically. However, as can be seen in figure 7.9 there are combinations of the nonlinearity $g$ and the desired gain-loss parameter $\gamma$ for which these solutions exist. Similarly to the phase diagram 3.10 the lines $\gamma_{\mathrm{EP}}$ at which the stationary real eigenvalue

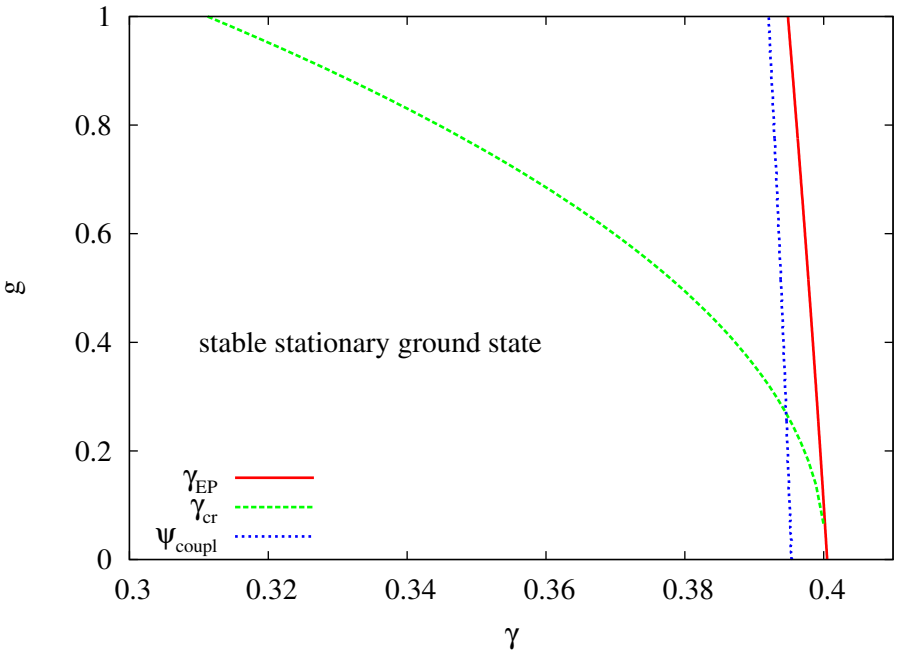


Figure 7.9.: Similarly to the phase diagram 3.10 the lines $\gamma_{\mathrm{EP}}$ at which the stationary real eigenvalue states vanish (red solid line) and $\gamma_{\mathrm{cr}}$ at which the complex $\mathcal{PT}$-broken states emerge (dashed green line) are shown. Only in the area below the dashed green line stable solutions for the ground state are possible. The blue dotted line indicates solutions $\psi_{\mathrm{coupl}}$ for a ground state which is suitable for a coupling to a second one.

states vanish (red solid line) and $\gamma_{\mathrm{cr}}$ at which the complex $\mathcal{PT}$-broken states emerge (dashed green line) are shown. Possible solutions which are suitable for a coupling of a stationary state with its spatially reflected counterpart are only available for the ground state. They are indicated by the blue dotted line in the figure.

In chapter 5 we learnt that, for an attractive nonlinearity, the ground state becomes unstable close to $\gamma_{\mathrm{cr}}$. Roughly speaking, stable solutions of the ground state exist only below the dashed green line. The region in which the desired solutions $\psi_{\mathrm{coupl}}$ are stable is rather small and these states are close to both $\gamma_{\mathrm{EP}}$ and $\gamma_{\mathrm{cr}}$, which does not guarantee a stable evolution as can be concluded from the dynamical investigations in chapter 6. Indeed, we find that the numerical propagation of these wave functions very early becomes unstable [148]. However, these instabilities can again be referred to the singular behaviour of the double-delta potential which is highly prone to tiny numerical perturbations. Thus, we conclude that in principle it is possible to combine two $\mathcal{PT}$-symmetric states such that one forms the balanced gain and loss for the other and vice versa. For the situations we investigated these states are dynamically unstable. Probably there are better values for the distance $a$ of the delta traps. Anyway, a realistic setup will have

a completely different parameter space and might provide better conditions. This topic needs a study of its own, which is not the subject of this work.

### Coupling of a bound with an unbound state

The last aspect we want to add is the coupling of the $\mathcal{PT}$-symmetric bound solution $\psi_1$ with a single unbound wave $\psi_2$. Certainly, this would be the most challenging experimental task since one needs a propagating wave passing both wells such that it causes a gain in the first and a loss in the second or the other way round. Nevertheless we wish to give some comments on the theoretical practicability of a setup of this kind.

As in the previous cases the decisive question is whether or not the conditions (7.16a) and (7.16b) for the implementation of the imaginary gain-loss term can be fulfilled. Since we wish to have balanced gain and loss terms we conclude from the requirement for the modulus of the wave function (7.16b)

$$|\psi_2(a/2)| = |\psi_1(a/2)|\frac{\gamma}{\eta} = |\psi_1(-a/2)|\frac{\gamma}{\eta} = |\psi_2(-a/2)| \,, \tag{7.26}$$

where we exploited that $\psi_1$ is $\mathcal{PT}$ symmetric, and thus $\psi_2$ possesses a symmetric modulus. That is, we need to find an unbound wave of which the modulus is equal at positions $x = -a/2$ and $x = a/2$. Furthermore, the phase relations (7.22a) and (7.22b) have still to be fulfilled which demands

$$\varphi_2(a/2) - \varphi_2(-a/2) = \varphi_1(a/2) - \varphi_1(-a/2) + \pi = 2\varphi_1(a/2) + \pi \tag{7.27}$$

for a $\mathcal{PT}$-symmetric $\psi_1$. The third condition which has to be fulfilled follows as in the previous cases from the chemical potential. The phase relation must hold for any time, and hence the energies of both states must be identical $\mu_2 = \mu_1 < 0$.

This energy condition is the weakest requirement. At first glance it seems to be a contradiction that we search for an unbound solution with negative energy for a potential given only by two negative delta functions. However, for negative values of $g$, i.e. an attractive contact interaction, negative chemical potentials are possible. The attractive forces lead to oscillations in the density $|\psi_2(x)|$. It turns out that the oscillations of the moduli of these solutions are periodic, which is very helpful to ensure condition (7.26). Numerical investigations also revealed that it is possible to find among these solutions also those which additionally comply with the phase relation (7.27) [148].

In summary, we note that it is also possible to find an unbound solution of the Gross-Pitaevskii equation with an attractive double-delta potential which is capable of simultaneously providing gain at one of the delta traps and loss at the other for a $\mathcal{PT}$-symmetric stationary state. The only drawback is that these solutions turn out to have a complicated stability pattern, i.e. it is hard to find examples which prove to be stable in a numerical solution of the time-dependent Gross-Pitaevskii equation.

# 8. A unique decay signal of resonances at an exceptional point

Exceptional points [1, 36, 37] appeared already in several aspects of the Bose-Einstein condensates in a $\mathcal{PT}$-symmetric potential structure considered so far. We observed two types of them and their structure has been investigated in detail in chapter 4. The value of the gain-loss parameter, at which the two $\mathcal{PT}$-symmetric modes with real eigenvalues vanish, was identified as a second-order exceptional point, i.e. a square root branch point in the spectrum. The two corresponding eigenstates of the Gross-Pitaevskii equation coalesce. We have seen that already for lower strengths of the gain-loss effect two $\mathcal{PT}$-broken states with complex energies branch off from one of the two real energy modes. This happens in a third-order exceptional point, which was explored in section 4.2. However, exceptional points are a very common phenomenon in non-Hermitian quantum systems. They do by far not require the presence of both gain and loss or even its balanced variant. Most commonly they are discussed in the context of resonances, i.e. long-lived decaying states. In the notation used in the previous chapters, this means a presence of only loss.

Exceptional points have shown to exhibit prominent effects not observable in their absence in the case of Hermitian Hamiltonians with potentials describing bound state spectra. Although exceptional points are single points in an (at least) two-dimensional parameter space they influence a whole region of parameters in their vicinity and lead to unusual results as the permutation of eigenstates for a closed adiabatic loop in the parameter space or a special type of a geometric phase [36]. Besides the systems studied so far they have recently been detected in a large number of physical applications. Examples are known for optical systems such as unstable lasers [73], wave guides [8], and optical resonators [47]. In quantum systems the existence of exceptional points has been proved theoretically, e.g. in atomic [40, 41] or molecular [42] spectra, in the scattering of particles at potential barriers [43], in atom waves [44, 45], and in non-Hermitian Bose-Hubbard models [9, 23, 24]. The experimental verification of their physical nature was achieved in microwave cavities [38, 39] and electronic circuits [74].

Despite this success an experimental observation in a true quantum system is still lacking. Resonances at an exceptional point exhibit, however, a unique decay behaviour [24, 46–50] and it is the purpose of this chapter to demonstrate that this can open the possibility for the first experimental detection of exceptional points in an atomic quantum system. In section 8.1 we review how in every quantum system exhibiting exceptional points a unique time behaviour of the survival probability leads to an unambiguous

fingerprint of the branch point singularity. To verify the existence of this signal in a true quantum system we show that it appears for the hydrogen atom in crossed electric and magnetic fields in section 8.2. A discussion of the results and an outlook to possible detection methods is added in section 8.3. The chapter is based on reference [161] in which its contents has already been published.

## 8.1. Fingerprint of exceptional points in the time behaviour of the survival probability

Many properties of exceptional points might be used to detect them in resonance spectra. For example, the permutation of eigenstates for a closed loop in the parameter space has been exploited in an experiment in a microwave cavity [38]. Another approach aims to the unique decay behaviour of the resonances if the parameters of the system are adjusted exactly at an exceptional point. It has been shown theoretically in a two-dimensional model [46], in optical microspirals [47], in a non-Hermitian Bose-Hubbard model [24], and in complex crystals [48, 49] as well as experimentally for Rabi oscillations in a microwave cavity [50] that when the spectrum of a non-Hermitian Hamiltonian has an exceptional point the decay of the resonances forming the coalescence is no longer purely exponential. The characteristic time evolution of the survival probability

$$S(t) = |\langle\psi(0)|\psi(t)\rangle|^2 \tag{8.1}$$

then has for a broad range of initial conditions exactly the form

$$S(t) = |1 - at|^2 \mathrm{e}^{+2\mathrm{Im}(E_{\mathrm{EP}})t/\hbar} \,, \tag{8.2}$$

where $E_{\mathrm{EP}}$ is the complex energy of the resonance state at the exceptional point and $a$ is a complex constant depending solely on the initial wave packet. The resonance decay rate (inverse lifetime) is defined as

$$\Gamma_{\mathrm{EP}} = -2\mathrm{Im}(E_{\mathrm{EP}}) > 0 \,. \tag{8.3}$$

This behaviour is in clear contrast to the purely exponential decay far away from an exceptional point. The only special condition which has to be fulfilled such that this behaviour appears is that the initial wave packet should populate both the exceptional point eigenstate $|\psi_{\mathrm{EP}}\rangle$ and its complimentary state $|\chi\rangle$ as obtained from the Jordan chain formalism but no other state. In the two-dimensional subspace of the resonances forming the exceptional point these two states form a basis, see section 9.2 of reference [1] for the mathematical details.

This unusual situation can be explained with a short calculation first shown in this simple form by Moiseyev [161]. At an exceptional point parameter $\lambda_{\mathrm{EP}}$ we have $\hat{H}(\lambda)|\psi_j\rangle =$

$E_j|\psi_j\rangle$ such that for $\lambda \to \lambda_{\mathrm{EP}}$ two eigenvalues degenerate, $E_j - E_{j'} \to 0$ (i.e. upon coalescence $E_j = E_{j'} \equiv E_{\mathrm{EP}}$) and also the corresponding eigenstates coalesce $\psi_j \to \psi_{j'}$ (up to a phase factor i [1], i.e. upon coalescence $\psi_j = \mathrm{i}\psi_{j'} \equiv \psi_{\mathrm{EP}}$) such that

$$\hat{M}|\psi_{\mathrm{EP}}\rangle = 0 \tag{8.4}$$

where

$$\hat{M} = \hat{H} - E_{\mathrm{EP}} \tag{8.5}$$

and $\Gamma_{\mathrm{EP}} = -2\mathrm{Im}(E_{\mathrm{EP}})$ is the decay rate of the system.

If we now consider only a two-dimensional subspace of the whole Hilbert space spanned by a basis consisting of $|\psi_{\mathrm{EP}}\rangle$ and its complimentary state $|\chi\rangle$ for the initial wave packet the $2 \times 2$ matrix representation of $\hat{M}$ is

$$\boldsymbol{M} = \begin{pmatrix} E_{\mathrm{EP}} & 1 \\ 0 & E_{\mathrm{EP}} \end{pmatrix} - \begin{pmatrix} E_{\mathrm{EP}} & 0 \\ 0 & E_{\mathrm{EP}} \end{pmatrix} = \begin{pmatrix} 0 & 1 \\ 0 & 0 \end{pmatrix} , \tag{8.6}$$

for which $\boldsymbol{M}^2 = 0$. Therefore

$$\begin{aligned} \boldsymbol{U}(t \leftarrow 0) &= \mathrm{e}^{-\mathrm{i}\boldsymbol{H}t/\hbar} = \mathrm{e}^{-\mathrm{i}E_{\mathrm{EP}}t/\hbar}\mathrm{e}^{-\mathrm{i}\boldsymbol{M}t/\hbar} \\ &= \mathrm{e}^{-\mathrm{i}E_{\mathrm{EP}}t/\hbar} \sum_n \frac{(-\mathrm{i}\boldsymbol{M}t/\hbar)^n}{n!} \\ &= \mathrm{e}^{-\mathrm{i}E_{\mathrm{EP}}t/\hbar}(\boldsymbol{I}_{2\times 2} - \mathrm{i}\boldsymbol{M}t/\hbar)\,. \end{aligned} \tag{8.7}$$

Consequently for any initial state $|\psi(t=0)\rangle$ which is a linear combination of $|\psi_{\mathrm{EP}}\rangle$ and its complimentary state $|\chi\rangle$ we obtain

$$\langle\psi(t=0)|\boldsymbol{U}(t \leftarrow 0)|\psi(t=0)\rangle = \mathrm{e}^{-\mathrm{i}E_{\mathrm{EP}}t/\hbar}(1 - \mathrm{i}t\langle\psi(t=0)|\boldsymbol{M}|\psi(t=0)\rangle/\hbar) \tag{8.8}$$

and for real values of $\langle\psi(t=0)|\boldsymbol{M}|\psi(t=0)\rangle$ the survival probability is given by

$$\begin{aligned} S(t) &= |\langle\psi(t=0)|\boldsymbol{U}(t \leftarrow 0)|\psi(t=0)\rangle|^2 \\ &= \left(1 + [\langle\psi(t=0)|\boldsymbol{M}|\psi(t=0)\rangle/\hbar]^2 t^2\right) \mathrm{e}^{+2\mathrm{Im}(E_{\mathrm{EP}})t/\hbar}\,. \end{aligned} \tag{8.9}$$

For complex values of $\langle\psi(t=0)|\boldsymbol{M}|\psi(t=0)\rangle$ an additional term linear in $t$ is added. Certainly, the quadratic dependence for short times is not surprising. What is important here is that there are no terms of order higher than $t^2$ so that the time dependence remains $t^2$ for all times. This provides a unique fingerprint proving unambiguously the presence of an exceptional point since the power series expansion of equation (8.7) stopping after the linear term requires the presence of an exceptional point. The effect even remains in a larger vicinity around the branch point singularity. Observations which are similar to exceptional points but not connected to true branch points as narrow avoided crossings for Wannier-Stark resonances [162] are not sufficient.

## 8.2. Non-exponential decay of resonances in spectra of the hydrogen atom

The most fundamental quantum objects which contain exceptional points are atoms in static external magnetic and electric fields. As such they are accessible to both experimental and theoretical methods, and thus ideally suited for studying the influence of exceptional points on quantum systems. Indeed, the existence of branch points in the resonance spectra of the hydrogen atom in crossed electric and magnetic fields was found numerically [41, 163]. Here the two field strengths play the role of two controllable parameters necessary to set the system at the exceptional points. We now want to demonstrate that the unique time signature of the survival probability exactly at the exceptional point parameters also appears in a detectable form in spectra of the hydrogen atom.

In our study the resonances are calculated numerically exact by the diagonalisation of a matrix representation of the Hamiltonian. Without relativistic corrections and finite nuclear mass effects [164] the Hamiltonian reads in atomic units

$$H = \frac{1}{2}\boldsymbol{p}^2 - \frac{1}{r} + \frac{1}{2}\gamma L_z + \frac{1}{8}\gamma^2(x^2+y^2) + fx \;, \tag{8.10}$$

where $L_z$ is the $z$ component of the angular momentum, and the field strengths $f = E/\mathrm{E}_0$ and $\gamma = B/\mathrm{B}_0$ are measured in units of $\mathrm{E}_0 = 5.14 \times 10^{11}\,\mathrm{V/m}$ and $\mathrm{B}_0 = 2.35 \times 10^5\,\mathrm{T}$. The strengths of the electric and magnetic fields are labelled $f$ and $\gamma$, respectively. We exploit the fact that the parity with respect to the $(z = 0)$-plane is a constant of motion and include in all our calculations only resonances with even $z$-parity.

To uncover the decaying unbound resonance states we use the complex rotation method [1, 34, 35], for which the coordinates of the system $\boldsymbol{r}$ are replaced with the complex rotated ones $\boldsymbol{r}\mathrm{e}^{\mathrm{i}\vartheta}$. For the application of the complex rotation method to hydrogen spectra see [165]. This procedure renders the resonance wave functions square integrable so that that they are automatically included in the spectrum as new discrete eigenstates with complex eigenvalues in the matrix representation. The real parts of the complex energies represent their energies and the imaginary parts their widths (lifetimes). After introducing complex dilated semiparabolic coordinates [166] the Schrödinger equation of the Hamiltonian (8.10) assumes in a basis representation the form of a generalised eigenvalue problem

$$\boldsymbol{A}(\gamma, f)\Psi = 2|b|^4 E \boldsymbol{B}\Psi \tag{8.11}$$

with a complex symmetric matrix $\boldsymbol{A}(\gamma, f)$ and a real symmetric matrix $\boldsymbol{B}$. In this equation $b$ is the complex dilation parameter and $E$ the complex resonance energy. The eigenstates can be normalised such that $(\Psi_i|\boldsymbol{B}|\Psi_j) = \delta_{ij}$, where the round braces indicate an inner product in which complex parts originating exclusively from the complex dilation parameter $b$ are not conjugated, which is the appropriate inner product for

complex scaled wave functions (c-product, cf. references [1, 35]). Note that this normalisation does not hold at an exceptional point where each of the two states is orthogonal to itself [1].

### 8.2.1. Construction of an adequate signal

We first demonstrate that the decay signal of the probability density according to equation (8.8),

$$S_{\mathrm{m}}(t) = \exp\left[2\mathrm{Im}(E_{\mathrm{EP}})t\right] \left|1 - \mathrm{i}(\Psi_0|\boldsymbol{M}|\Psi_0)t\right|^2 \ , \tag{8.12a}$$

can be found in the quantum spectrum of the hydrogen atom in a large region around the exceptional point, where in our case the matrix $\boldsymbol{M}$ of equation (8.5) is given by

$$\boldsymbol{M} = \boldsymbol{A}(\gamma, f)/(2|b|^4) - E_{\mathrm{EP}}\boldsymbol{B} \ . \tag{8.12b}$$

The subscript m of $S_{\mathrm{m}}$ in equation (8.12a) is given in order to emphasise the fact that the survival probability is calculated here using the matrix representation of the Hamiltonian given by equation (8.12b). This is to distinguish from the direct evaluation of the survival probability as discussed later [equation (8.17)]. For this purpose we calculate resonance spectra for several small distances $\delta$ to the exceptional point at $(f_{\mathrm{EP}}, \gamma_{\mathrm{EP}})$ in the space of the two field strengths, i.e. we use

$$f = f_{\mathrm{EP}}(1-\delta), \quad \gamma = \gamma_{\mathrm{EP}}(1-\delta) \ . \tag{8.13}$$

For small $\delta$ the two eigenstates $\Psi_1$ and $\Psi_2$ belonging to the branch point singularity can be identified clearly. Note, however, that due to roundoff errors in the numerical calculations $\delta$ never ever gets strictly the value 0. As we will show even when $\delta \neq 0$, i.e. when we have two *almost* degenerate states and the spectrum is *complete* the fingerprint of the exceptional points (strictly obtained only exactly at the coalescence of two eigenstates) on the survival probability is still pronounced. This will be important for an experimental verification since also in an experiment there will never be the possibility to adjust the exact mathematical condition of an exceptional point.

It is well known for exceptional points that $\Psi_1$ and $\Psi_2$ converge to the single independent eigenstate with the phase relation

$$\Psi_{\mathrm{EP}} = \Psi_1 = \mathrm{i}\Psi_2 \tag{8.14}$$

for $\delta \to 0$ [1]. A complete basis in the corresponding two-dimensional subspace is spanned by $\Psi_{\mathrm{EP}}$ and the complementary vector $\Psi_{\mathrm{a}}$,

$$(\boldsymbol{A}(\gamma, f) - 2|b|^4 E_{\mathrm{EP}}\boldsymbol{B})\Psi_{\mathrm{a}} = \Psi_{\mathrm{EP}} \ , \tag{8.15}$$

where $\Psi_{\mathrm{a}}$ is essential for a decay signal of the form (8.12a) [46]. Despite the convergence of $\Psi_1$ and $\Psi_2$ to the same state it is possible to extract an adequate superposition of $\Psi_{\mathrm{EP}}$ and $\Psi_{\mathrm{a}}$, viz.

$$\Psi_0 = \sqrt{(1 + 1/\sqrt{\delta})/2}\,\Psi_1 + \sqrt{(1 - 1/\sqrt{\delta})/2}\Psi_2 \ . \tag{8.16}$$

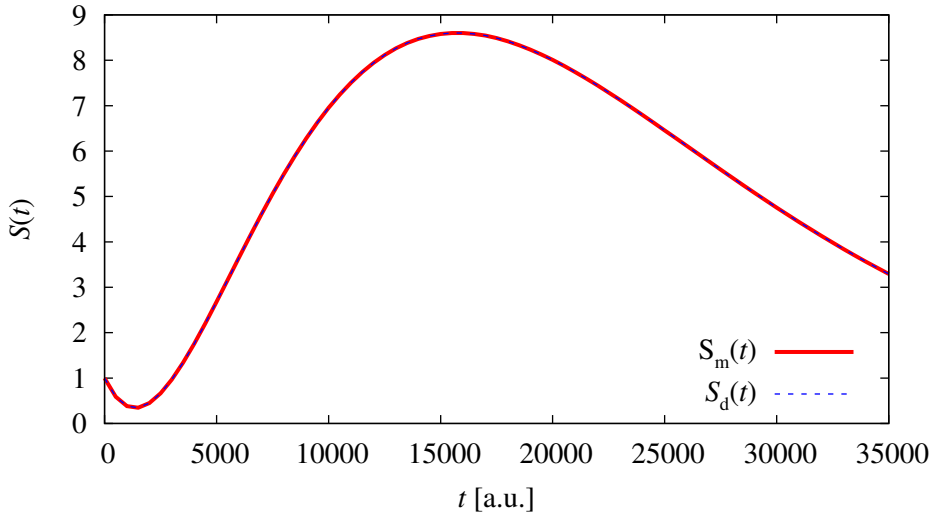


Figure 8.1.: Survival probability for the resonances at the exceptional point labelled 8 in reference [163] with an offset of $\delta = 10^{-5}$. Shown are the direct evaluation $S_{\mathrm{d}}(t)$ according to equation (8.17) and the expected form $S_{\mathrm{m}}(t)$ of equation (8.12a) including a linear term in $t$ besides the exponential decay. Note that on the scale of the figure the survival probabilities calculated by both methods are not distinguishable. Since we use here the c-product rather than the regular scalar product the survival probability can assume values larger than one. This non-physical behaviour results from the way we normalise $\Psi_0$ [see equation (8.16)]. As we will show later this problem disappears when the initial wave packet is prepared by using a laser excitation of the field-free ground state.

As we get closer to the exceptional point when $\delta \to 0$ the amplitudes of $\Psi_1$ and $\Psi_2$ approach infinitely large values. However, the initial wave packet $\Psi_0$ remains c-normalised.

We choose the exceptional point labelled 8 in table I of reference [163] at the field strengths $f = 0.0002177$ and $\gamma = 0.004604$, and with the complex energy $E_{\mathrm{EP}} = -0.022135 - 0.00006878\mathrm{i}$ (all values in atomic units). The survival probability for the superposition (8.16) is plotted in figure 8.1 for an offset $\delta = 10^{-5}$. At an exceptional point we expect a decay of the survival probability in the form (8.12a). The corresponding numerical result is shown with the solid red line in figure 8.1, where we found $(\Psi_0|M|\Psi_0) = (3.83 - 4.58\mathrm{i}) \times 10^{-4}$. Since we use here the c-product [1, 35] rather than the regular scalar product the survival probability can assume values larger than one for the mathematical choice given in equation (8.16). Additionally, we calculate the survival probability directly without any assumption about its shape close to an exceptional

point, i.e. we evaluate

$$S_{\mathrm{d}}(t) = \left| \sum_i (\Psi_0|\boldsymbol{B}|\Psi_i)(\Psi_i|\boldsymbol{B}|\Psi_0) \exp\left(-\mathrm{i}E_i t\right) \right|^2 , \tag{8.17}$$

where we use 100 eigenvectors of the matrix diagonalisation in the energy vicinity of the exceptional point for the basis states $\Psi_i$. The blue dashed line in figure 8.1 shows the results of the latter method. As can be seen clearly both methods agree very well, which proves that the description of the decay with the linear term in (8.12a) is correct.

Obviously the polynomial contribution influences the decay significantly. The unique time behaviour of the resonances at an exceptional point is a relevant effect in matter waves and can unambiguously be found for atomic resonances.

The typical time signal of an exceptional point is even present at larger distances $\delta$. In figure 8.2 (a) we plot the direct evaluation (8.17) for the same exceptional point as in figure 8.1 but for several different offsets $\delta = 10^{-8} \ldots 10^{-2}$. For all of these distances the two vectors belonging to the branch point are well defined. Almost all calculations provide exactly the same results. Only for $\delta = 10^{-2}$ we observe a slight difference to the other calculations. At this distance also the validity of the matrix representation (8.12a) including only the two components associated with the exceptional point breaks down, however, the differences are still small. The corresponding line $S_{\mathrm{m}}(t)$ is included in the figure. For all other values of $\delta$ shown we checked that the results of both methods agree completely, which demonstrates that the structure of equation (8.7), which is only fulfilled in the presence of an exceptional point, survives in a larger vicinity around the branch point. The signal keeps its unique structure. To verify that we obtain the correct vectors $\Psi_1$ and $\Psi_2$ in all calculations we plot the modulus

$$d = \langle \Psi_1 + \mathrm{i}\Psi_2 | \Psi_1 + \mathrm{i}\Psi_2 \rangle \tag{8.18}$$

in figure 8.2 (b). According to the phase relation (8.14) $d$ must vanish in the limit $\delta \to 0$. Exactly this behaviour is found.

### 8.2.2. Excitation with a laser

So far we demonstrated that it is possible to find an adequate superposition of the two eigenvectors, however, we want to show furthermore that this signal can be excited in a realistic case. Is it possible to occupy such a superposition in an experimental situation? To investigate this question we assume a hydrogen atom in external fields, where the electron is in the orbital $2p$, $m = 0$, for which any perturbation due to the fields we use can be ignored. The eigenstates at the exceptional point are excited with a laser polarised linearly along the direction of the static magnetic field. We use a Gaussian pulse shape of the form

$$E(\omega) \sim \exp\left(-\sigma(\omega - \omega_0)^2\right) , \quad \omega_0 = \mathrm{Re}(E_{\mathrm{EP}}) - E_{\mathrm{I}} , \tag{8.19}$$

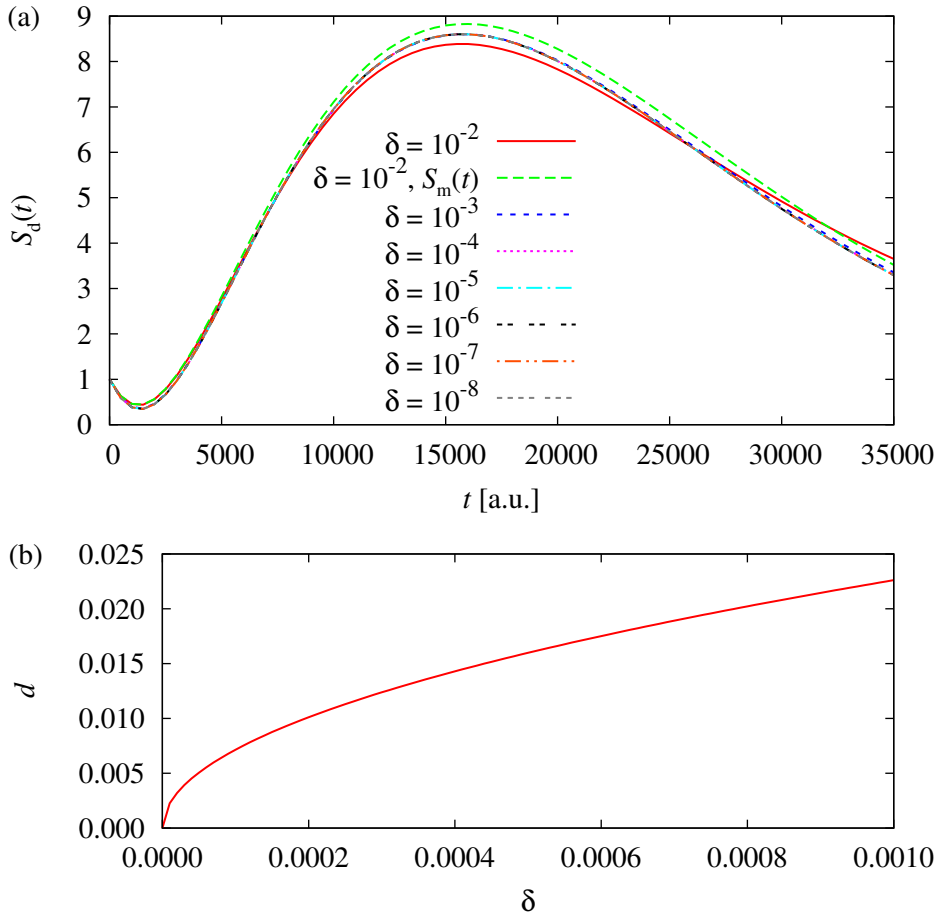


Figure 8.2.: (a) Survival probability $S_\mathrm{d}(t)$ for the same exceptional point as in figure 8.1 but for several different offsets $\delta = 10^{-8} \ldots 10^{-2}$. Small deviations only appear for the largest $\delta = 10^{-2}$. In this case also a small difference to the shape $S_\mathrm{m}(t)$ at an exceptional point becomes observable. (b) The modulus $d = \langle \Psi_1 + \mathrm{i}\Psi_2 | \Psi_1 + \mathrm{i}\Psi_2 \rangle$ vanishes at the exceptional point as is expected due to the phase relation (8.14).

where $E_\mathrm{I}$ is the energy at the initial state $\Psi_\mathrm{I}$ ($2p$, $m = 0$). The width was chosen to be $\sigma = 1000/\omega_0$. Then the occupation amplitude for a transition to eigenstate $\Psi_i$ of the Hamiltonian is

$$A_i = \int \mathrm{d}\omega\, E(\omega) \frac{(\Psi_\mathrm{I}|D|\Psi_i)}{E_{2p_z} - E_\mathrm{EP} + \hbar\omega} \tag{8.20}$$

with the dipole operator $D$ for the present choice of the light pulse.

Figure 8.3 (a) shows the occupation probability $|A_i|^2$ versus real part of the energy for the states in the vicinity of the branch point. One can see that the two states connected with the branch point (marked with filled blue circles) have an occupation probability almost three orders of magnitude larger than all other states. This does not tell us, however, whether or not an adequate superposition of the two dominating states similar to the mathematical case in equation (8.16) can be achieved. Thus, we construct the normalised state

$$\Psi_\mathrm{F} = \frac{\tilde{\Psi}_\mathrm{F}}{\sqrt{(\tilde{\Psi}_\mathrm{F}|\boldsymbol{B}|\tilde{\Psi}_\mathrm{F})}}\,, \qquad \tilde{\Psi}_\mathrm{F} = \sum_i A_i \Psi_i \tag{8.21}$$

populated by the laser with the states shown in figure 8.3 (a). The survival probability is calculated according to equation (8.17) with $\Psi_\mathrm{F}$ instead of $\Psi_0$. Figure 8.3 (b) shows the results. The small oscillations are due to the weaker excitations of the neighbouring states. They disappear for a pulse denser in frequency space. The dominating signal is still formed by the two states associated with the exceptional point. The linear part in the time behaviour (8.12a) is weaker than in the mathematical case $\Psi_0$ of equation (8.16), however, it is present and is expressed in the non-exponential decay. After the division by the exponential part the polynomial contribution of the physical (observable) survival probability calculated for the initial wave packet $\Psi_\mathrm{F}$ [see equation (8.21)] is given by

$$S_\mathrm{d,p}(t) = S_\mathrm{d}(t) / \exp\left(2\mathrm{Im}(E_\mathrm{EP})t\right). \tag{8.22}$$

To demonstrate that the origin of this signal is in fact the structure (8.12a) originating from an exceptional point we calculated the matrix element $(\Psi_\mathrm{F}|M|\Psi_\mathrm{F}) = (0.226 + 5.25\mathrm{i}) \times 10^{-5}$. The line $|1 - \mathrm{i}(\Psi_\mathrm{F}|M|\Psi_\mathrm{F})t|^2$ is not distinguishable from the full numerical result presented in figure 8.3 (b).

## 8.3. Discussion and possible detection methods

Any quantum system exhibiting exceptional points shows a time evolution of the form (8.7) for two resonances exactly at an exceptional point, i.e. the decay includes a quadratic term as in equation (8.9) which is distinct from the typical exponential decay apart from branch point singularities. Here it is important to note that this effect is not only observable exactly at the parameters of the exceptional point but can rather be seen in a large neighbourhood. In our study we found it still for a relative offset of the parameters of $\delta = 10^{-2}$.

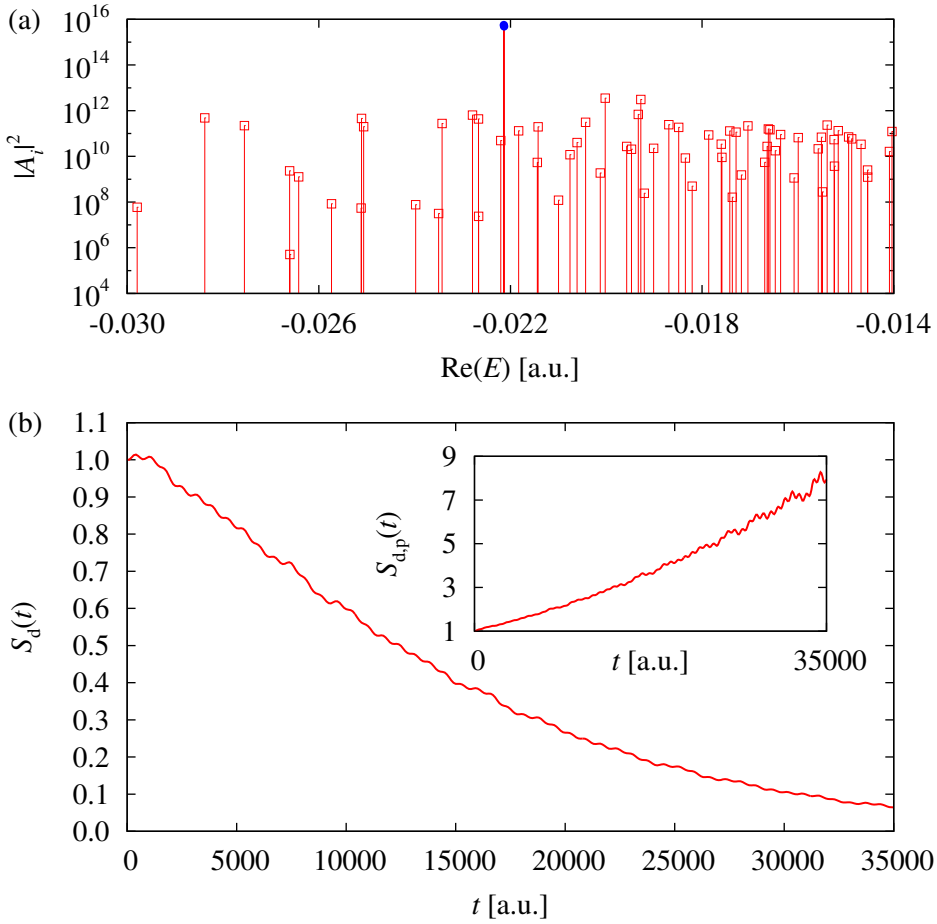


Figure 8.3.: (a) Occupation probabilities $|A_i|^2$ in arbitrary units for resonances in an energy vicinity of the exceptional point. The two resonances connected with the exceptional point are marked with blue (filled) circles. On the scale of our plot the two almost degenerate states are not distinguishable. (b) Survival probability for the excited state $\Psi_F$, which is prepared by using a laser to excite the field-free ground state [see equation (8.21)]. The division by the exponential part in the inset demonstrates the presence of the polynomial contribution. The behaviour of the survival probability as presented here is exactly as the analytical expression given in equation (8.12a).

The signal is not just a mathematical artefact but it is possible to excite an adequate superposition of the eigenvector at an exceptional point and its associate counterpart in a realistic physical situation. The quadratic term significantly influences the survival probability we found for the hydrogen atom in crossed electric and magnetic fields. It is an effect that leaves clear signatures in the decay of resonances in quantum systems and obviously opens a new possibility to detect an unambiguous fingerprint of an exceptional point accessible with experimental methods. It might such facilitate the first experimental detection of exceptional points in a true quantum system.

In the realistic physical situation shown in figure 8.3 the survival probability describes the decay of a resonance state in time. A possible experimental procedure would contain a repeated measurement of the decaying occupation of such a state. This can presumably be detected with a second laser as already indicated [46]. There are, however, further possibilities.

Purely exponentially decaying resonances lead to a Lorentzian line shape in the spectrum. From this profile it is possible to extract the position, i.e. the energy, and the width of the resonance state. For a decay of the form (8.7) including the linear contribution the signal in the spectrum has the shape

$$(1 - \mathrm{i}at)\mathrm{e}^{-\mathrm{i}\tilde{E}_{\mathrm{EP}}t/\hbar} \quad \rightarrow \quad \frac{b + c\Gamma + d\Gamma^2}{[(E - E_{\mathrm{EP}})^2 + \Gamma_{\mathrm{EP}}^2/4]^2} \,, \tag{8.23}$$

which clearly differs from a Lorentz profile. An extraction of the time signal from the spectrum is possible and has already been used for microwave cavities [50] via a Fourier transform. The harmonic inversion method [167] provides an even better possibility. It can be adapted such that it exactly fits to the non-exponential decay signal. Then it can be exploited to unambiguously identify if the linear part in equation (8.7) is present [168]. Thus, it can tell without any doubt whether or not an exceptional point has been found.

In this context we should mention that the ultra-strong magnetic and electric fields we have used in our calculations are due to our computational limitations to exceptional points associated with low-lying resonance positions. However, the phenomenon discussed here appears for highly excited resonances as well. In such cases much weaker and feasible external fields are required to observe the unique survival probability of a wave packet, which initially populates mainly the two almost degenerate states associated with the exceptional point.

# Part II.

# From bound to unbound states – dissociation effects of small clusters

# 9. The frozen Gaussian imaginary time propagator and its application to the $Ar_3$ cluster

Starting with this chapter we want to deal with a completely different approach to systems that possess a connection between bound and unbound states. The considerations in the last chapters were all basically done at zero temperature. For the Bose-Einstein condensates we assumed that all atoms are in the condensed phase, which is only possible at vanishing temperature. Also for the ionisation process of the hydrogen atom in chapter 8 we did not take into account a thermal occupation of the energy levels. Only the laser was interacting with the electron. Since the electronic excitations considered in this process are far beyond thermal energies this is an excellent approximation.

Now we want to turn to processes in which thermal energies are dominating the energy landscape. For the weak van der Waals interaction between rare gas atoms temperatures of a few Kelvin are already sufficient to drastically influence their structures. Clusters of these atoms can be dissociated completely. Rare gas atomic clusters are a topic of ongoing research partially due to the rich variety of their thermodynamic properties. Extensive studies have been carried out on structural transformations or phase transitions [51–57]. Properties of particular interest include the mean energy and specific heat. Computations on clusters of light atoms, e.g. $Ne_{13}$ and $Ne_{38}$ [54, 56], predict novel low temperature quantum effects such as liquid-like zero temperature structures of $Ne_{38}$ in contrast to a solid-like structure prediction from classical mechanics [61].

The features in the mean energies or specific heats of such systems appear usually at low temperatures so that accurate quantum mechanical computational methods are essential. Accurate calculations for multi-dimensional systems, however, are challenging. Path-integral Monte Carlo methods [58–60] have been used to investigate rare gas clusters with up to a few dozen atoms. However, they become expensive for low temperatures and approximations are necessary. It is the purpose of this chapter to introduce a semiclassical approximation based on a frozen Gaussian propagator, and to apply it to a very simple and instructive example, viz. the argon trimer, which has attracted the interest of theoretical investigations for a long time [62–66]. Its dissociation process has been discussed recently in an extensive study [57]. In spite of its apparent simplicity with only three atoms involved, the thermodynamic properties at low temperatures $T < 40\,\mathrm{K}$ still include open questions. In particular, path-integral Monte Carlo calculations of the

system [57] indicate a dissociation of the three atoms at temperatures $T \gtrapprox 35\,\mathrm{K}$ but cannot distinguish this process from structural changes. With the semiclassical Gaussian approximations discussed in this chapter we are able to provide well converged numerical mean energies and specific heats which exhibit an unambiguous classical-like dissociation at $T \approx 20\,\mathrm{K}$. We will also address the question of how important quantum effects are for the dissociation. Influences on the low temperature behaviour of the mean energy and the specific heat will become observable and we will see that the transition temperature is shifted to a slightly lower value.

In section 9.1 we define the Gaussian semiclassical approximation to the thermal operator, introduce the systems we are interested in (section 9.1.1), review the so-called thawed Gaussian (section 9.1.2) propagator, for which the Gaussian width parameters are allowed to change with temperature, and develop a new multi-dimensional form of its frozen Gaussian counterpart (section 9.1.3), for which the Gaussian width parameters are constants. As we will show the latter one will be capable of competing with the more flexible thawed Gaussian methods. The results for the argon trimer based on these semiclassical Gaussian methods are then presented in section 9.2. After introducing the system (section 9.2.1) and comparing the Gaussian methods (section 9.2.2) we discuss the influence of an artificial confining potential required for numerical convergence on the thermodynamic properties (section 9.2.3), and investigate the dissociation in the classical and the quantum case (section 9.2.4). A final discussion with an outlook to possible technical extensions in section 9.3 concludes the chapter.

The results have already been published in reference [169], on which the chapter is based.

## 9.1. Thermal operator for clusters and Gaussian approximations

In the following we introduce a semiclassical approximation to the Boltzmann (imaginary time) operator $\exp(-\beta H)$. Recently, new variants of semiclassical initial value representations have been adopted to problems involving the Boltzmann operator. The time evolved Gaussian method developed by Mandelshtam and coworkers [53, 170] has successfully been applied to atomic clusters [53, 54, 56, 170, 171] and dissipative systems [67]. It is based on the imaginary time propagation of a Gaussian wave packet of the form

$$\langle \boldsymbol{x}|g\rangle = \left(\pi^{3N}|\det \boldsymbol{G}(\tau)|\right)^{-1/4} \exp\left(-\frac{1}{2}[\boldsymbol{x}-\boldsymbol{q}(\tau)]^{\mathrm{T}}\boldsymbol{G}(\tau)^{-1}[\boldsymbol{x}-\boldsymbol{q}(\tau)]+\gamma(\tau)\right)\,, \quad (9.1)$$

where for a cluster with $N$ atoms the vectors are $3N$-dimensional and $\boldsymbol{G}(\tau)$ is a $3N\times 3N$-dimensional symmetric matrix of width parameters.

Despite the fact that it reduces the infinite number of degrees of freedom of the exact quantum mechanical propagator to a "low" number of Gaussian parameters the time

evolved Gaussian method may still become expensive for high-dimensional systems. It belongs to the so-called *thawed* Gaussian methods, where the matrix of Gaussian width parameters $\boldsymbol{G}(\tau)$ changes with time. The number of the resulting equations of motion scales with $N^2$. This can become difficult when dealing with clusters of several dozen atoms. Thus, Mandelshtam and coworkers introduced the single-particle ansatz [53], in which the width matrix $\boldsymbol{G}(\tau)$ is reduced to a block-diagonal structure by only taking into account correlations of the coordinates of one particle and ignoring the inter-particle connections. This approximation leads to a linear scaling ($6N$) with the number of atoms.

From a numerical point of view it is much cheaper to use *frozen* Gaussian representations of the thermal operator, in which the time-dependent width matrix $\boldsymbol{G}(\tau)$ in equation (9.1) is replaced by a constant matrix. The number of the remaining equations of motion which have to be solved scale as $3N$. Such a formalism has been provided by Zhang et al. [69]. One objective of this chapter is to apply the frozen Gaussian approach to the Boltzmann operator for a cluster of atoms. We will show that by an adequate nondiagonal choice of the constant width matrix, the frozen Gaussian method can accurately describe the mean energy, the specific heat, and signatures of dissociation processes. To do so, we will present a simple procedure to find a well suited shape for the width matrix. The results we obtain are of the same quality as the single-particle ansatz thawed Gaussian methodology, even though the frozen Gaussian variant leaves much less freedom to the Gaussian wave packet (constant width).

### 9.1.1. Hamiltonian and observables

In our study we consider a cluster of $N$ atoms with only internal forces depending on the distance between the atoms, i.e. the Hamiltonian in mass scaled coordinates has the form

$$H = -\frac{\hbar^2}{2}\sum_{i=1}^{N}\Delta_i + \sum_{j<i} V(|\boldsymbol{r}_i - \boldsymbol{r}_j|)\ , \tag{9.2}$$

where $\Delta_i$ is the Laplacian of particle $i$ and $V(|\boldsymbol{r}_i - \boldsymbol{r}_j|)$ describes the two-body interaction between particles $i$ and $j$, whose positions are given by the vectors $\boldsymbol{r}_i$. In the Gaussian representations used in this chapter it is necessary to evaluate integrals over a product of the potential with a coherent state, which are typically of the form

$$\langle h(\boldsymbol{q})\rangle = \int_{-\infty}^{\infty} \mathrm{d}\boldsymbol{x}^{3N}\, \langle \boldsymbol{x}|g(\{y_i\})\rangle^2 h(\boldsymbol{x})\ , \tag{9.3}$$

where $\langle \boldsymbol{x}|g(\{y_i\})\rangle$ is a normalised coherent state in $\boldsymbol{x}$, which depends on a set of parameters $\{y_i\}$ usually including Gaussian positions $\boldsymbol{q}$ and a width matrix $\boldsymbol{G}$, e.g.

$$\langle \boldsymbol{x}|g\left(\{y_i\} = \{\boldsymbol{q}, \boldsymbol{G}\}\right)\rangle = \left(\pi^{3N}|\det \boldsymbol{G}|\right)^{-1/4} \exp\left(-\frac{1}{2}[\boldsymbol{x}-\boldsymbol{q}]^{\mathrm{T}}\boldsymbol{G}^{-1}[\boldsymbol{x}-\boldsymbol{q}]\right)\ . \tag{9.4}$$

The function $h(\boldsymbol{x})$ stands for the potential or one of its derivatives. The $3N$-dimensional vectors $\boldsymbol{x}$ and $\boldsymbol{q}$ combine the coordinates of all $N$ atoms. It is essential for practical applications to reduce the numerical integrations as much as possible. Based on the facts that any central potential can be fitted by a sum of Gaussians and that a Gaussian in the distance $r_{ij} = |\boldsymbol{r}_i - \boldsymbol{r}_j|$ centred at the origin remains a Gaussian in Cartesian coordinates, Frantsuzov et al. [53] suggested the implementation of the interaction potential in terms of sums of Gaussians,

$$V(|\boldsymbol{r}_i - \boldsymbol{r}_j|) = \sum_p c_p \mathrm{e}^{-\alpha_p r_{ij}^2}, \qquad r_{ij} = |\boldsymbol{r}_i - \boldsymbol{r}_j| \,, \tag{9.5}$$

so that all integrals of the form (9.3) can be evaluated analytically. This is of great advantage in numerical computations and is used for the work presented in this chapter.

To investigate the thermodynamic properties of the cluster we calculate the partition function $Z(\beta)$ by evaluating Gaussian initial value representations of the thermal operator

$$K(\beta) = \mathrm{e}^{-\beta H} \,, \tag{9.6}$$

where $\beta = 1/(\mathrm{k}T)$ is the inverse temperature and $Z(\beta) = \mathrm{Tr}(K(\beta))$. We are interested in the mean energy $E = \mathrm{k}T^2 \partial \ln Z/\partial T$ and the specific heat $C = \partial E/\partial T$. In our calculations we use two different semiclassical propagators based on a frozen and on a thawed Gaussian representation, where in both cases the Bloch equation

$$-\frac{\partial}{\partial \tau}|\boldsymbol{q}_0, \tau\rangle = H|\boldsymbol{q}_0, \tau\rangle \tag{9.7}$$

connected with the propagator (9.6) is approximately solved for a coherent state $|\boldsymbol{q}_0, \tau\rangle \approx |g(\{y_i\}, \tau)\rangle$ with either constant or variable Gaussian width parameters.

### 9.1.2. Thawed Gaussian representation

The thawed Gaussian representation of the thermal operator is the most versatile since it allows both the positions and widths of the Gaussian wave packet to vary with time. We consider the summarised time evolved Gaussian approximation (TEGA) suggested by Frantsuzov et al. [53, 170],

$$\begin{aligned}\langle \boldsymbol{x}|K_{\mathrm{TG}}(\tau)|\boldsymbol{x}'\rangle = \int \frac{\mathrm{d}\boldsymbol{q}^{3N}}{(2\pi)^{3N}} \frac{\exp[2\gamma(\tau/2)]}{\det[\boldsymbol{G}(\tau/2)]} \\ \times \exp\left(-\frac{1}{2}[\boldsymbol{x} - \boldsymbol{q}(\tau/2)]^{\mathrm{T}} \boldsymbol{G}(\tau/2)^{-1} [\boldsymbol{x} - \boldsymbol{q}(\tau/2)]\right) \\ \times \exp\left(-\frac{1}{2}[\boldsymbol{x}' - \boldsymbol{q}(\tau/2)]^{\mathrm{T}} \boldsymbol{G}(\tau/2)^{-1} [\boldsymbol{x}' - \boldsymbol{q}(\tau/2)]\right) \,,\end{aligned} \tag{9.8}$$

which is constructed from the coherent state

$$\begin{aligned}\langle \boldsymbol{x}|g(\{y_i\}=\{\boldsymbol{q}(\tau),\boldsymbol{G}(\tau)\})\rangle &= \langle \boldsymbol{x}|g(\boldsymbol{q}(\tau),\boldsymbol{G}(\tau))\rangle \\ &= \left(\pi^{3N}|\det \boldsymbol{G}(\tau)|\right)^{-1/4}\exp\left(-\frac{1}{2}[\boldsymbol{x}-\boldsymbol{q}(\tau)]^{\mathrm{T}}\boldsymbol{G}(\tau)^{-1}[\boldsymbol{x}-\boldsymbol{q}(\tau)]\right) . \quad (9.9)\end{aligned}$$

One can then readily write down the partition function as:

$$Z_{\mathrm{TG}} = \int \frac{\mathrm{d}\boldsymbol{q}^{3N}}{(2\sqrt{\pi})^{3N}}\frac{\exp[2\gamma(\tau/2)]}{\sqrt{\det[\boldsymbol{G}(\tau/2)]}} . \quad (9.10)$$

The width matrix $G(\tau)$ is symmetric positive definite. The Gaussian parameters follow the equations of motion in imaginary time $\tau$,

$$\frac{\partial}{\partial\tau}\boldsymbol{G}(\tau) = -\boldsymbol{G}(\tau)\langle\nabla\nabla^{\mathrm{T}}V(\boldsymbol{q}(\tau))\rangle\boldsymbol{G}(\tau) + \hbar^2\mathbf{1} , \quad (9.11a)$$

$$\frac{\partial}{\partial\tau}\boldsymbol{q}(\tau) = -\boldsymbol{G}(\tau)\langle\nabla V(\boldsymbol{q}(\tau))\rangle , \quad (9.11b)$$

$$\frac{\partial}{\partial\tau}\gamma(\tau) = -\frac{1}{4}\mathrm{Tr}\left[\langle\nabla\nabla^{\mathrm{T}}V(\boldsymbol{q}(\tau))\rangle\boldsymbol{G}(\tau)\right] - \langle V(\boldsymbol{q}(\tau))\rangle , \quad (9.11c)$$

where $\langle\dots\rangle$ represents Gaussian averaged quantities of the form (9.3), which can be evaluated analytically for a potential (9.5) expressed in terms of Gaussians [53], and $\mathbf{1}$ is the $3N\times 3N$-dimensional identity matrix. The boundary conditions

$$\boldsymbol{q}(\tau\approx 0) = \boldsymbol{q}_0 , \qquad G(\tau\approx 0) = \hbar^2\mathbf{1}\tau , \qquad \gamma(\tau\approx 0) = -V(\boldsymbol{q}_0)\tau , \quad (9.12)$$

are derived by demanding that in the limit $\tau\to 0$ the Gaussian approximation reduces to the identity operator.

In the framework of a Gaussian propagator the thawed Gaussian representation is usually the most accurate approximation to the exact quantum result due to the large freedom in the parameters, as has recently been demonstrated for a double well potential [172]. However, it is also the numerically most expensive method. The number of equations of motion for the width matrix (9.11a) scales with $N^2$, and the matrix operations at each time step even scale with $N^3$. This drastic increase in the required computing resources is the most critical drawback of the method. An attempt for combining the advantages of a thawed Gaussian propagator, where some matrix elements are still governed by the equations of motion (9.11a)-(9.11c), and avoiding the drawback of the expensive numerical effort to evaluate it, is achieved with the so-called "single-particle ansatz" of Frantsuzov et al. [53]. This ansatz, or variations of it, have been applied to several types of clusters [53, 54, 171]. It uses a block-diagonal matrix $\boldsymbol{G}(\tau)$, where $3\times 3$ symmetric matrices representing one particle along the diagonal are the only non-vanishing matrix elements. Then the equations of motion (9.11a)-(9.11c) are only

solved for the $3 \times 3$ blocks and only the corresponding $3 \times 3$ blocks of $\langle \nabla \nabla^{\mathrm{T}} V(\boldsymbol{q}(\tau)) \rangle$ are included. In the single-particle ansatz the number of equations scales with $N$ instead of $N^2$, however, one loses information in the non-diagonal $3 \times 3$ blocks, which are set to 0. Since the Gaussian propagators are in practical applications usually evaluated in Cartesian coordinates, in which the motions of the particles do not separate, important correlations between the particles are ignored. Thus, one expects that compared to the case of a full matrix the single-particle ansatz may lead to results of poorer quality.

In what follows we will call the full matrix variant of the thawed Gaussian propagator FC-TG (fully coupled thawed Gaussian, also referred to as the "fully coupled variational-Gaussian-wave-packet Monte Carlo" in reference [53]) and the single-particle ansatz will be called SP-TG (single-particle thawed Gaussian, "single-particle variational-Gaussian-wave-packet Monte Carlo" in reference [53]). For the argon trimer we will compare these respective approximations for the thermodynamic properties derived from the partition function using two variants of a frozen Gaussian propagator.

### 9.1.3. Frozen Gaussian representation

The frozen Gaussian representation of the thermal operator suggested by Zhang et al. [69] is based on a multi-dimensional frozen Gaussian coherent state

$$\begin{aligned}\langle \boldsymbol{x}|g(\{y_i\} = \{\boldsymbol{p}(\tau), \boldsymbol{q}(\tau), \boldsymbol{\Gamma}\})\rangle &= \langle \boldsymbol{x}|g(\boldsymbol{p}(\tau), \boldsymbol{q}(\tau), \boldsymbol{\Gamma})\rangle \\ &= \left(\frac{\det(\boldsymbol{\Gamma})}{\pi^{3N}}\right)^{1/4} \exp\left(-\frac{1}{2}[\boldsymbol{x} - \boldsymbol{q}(\tau)]^{\mathrm{T}}\boldsymbol{\Gamma}[\boldsymbol{x} - \boldsymbol{q}(\tau)] + \frac{\mathrm{i}}{\hbar}\boldsymbol{p}^{\mathrm{T}}(\tau) \cdot [\boldsymbol{x} - \boldsymbol{q}(\tau)]\right) , \quad (9.13)\end{aligned}$$

where $\boldsymbol{\Gamma}$ is in general a $3N \times 3N$-dimensional constant width matrix with positive eigenvalues, and $\boldsymbol{q}(\tau)$ and $\boldsymbol{p}(\tau)$ describe the dynamical variables. The summarised frozen Gaussian approximation to the propagator reads

$$\begin{aligned}\langle \boldsymbol{x}'|K_{\mathrm{FG}}(\tau)|\boldsymbol{x}\rangle = \det(\boldsymbol{\Gamma}) \exp\left(-\frac{\hbar^2}{4}\mathrm{Tr}(\boldsymbol{\Gamma})\tau\right) \sqrt{\det\left(2\left[\mathbf{1} - \exp(-\hbar^2\boldsymbol{\Gamma}\tau)\right]^{-1}\right)} \\ \times \exp\left(-\frac{1}{4}[\boldsymbol{x}' - \boldsymbol{x}]^{\mathrm{T}}\boldsymbol{\Gamma}[\tanh(\hbar^2\boldsymbol{\Gamma}\tau/2)]^{-1}[\boldsymbol{x}' - \boldsymbol{x}]\right) \\ \times \int_{-\infty}^{\infty} \frac{\mathrm{d}\boldsymbol{q}^{3N}}{(2\pi)^{3N}} \exp\left(-2\int_0^{\tau/2} \mathrm{d}\tau' \langle V(\boldsymbol{q}(\tau'))\rangle - [\bar{\boldsymbol{x}} - \boldsymbol{q}(\tau/2)]^{\mathrm{T}}\boldsymbol{\Gamma}[\bar{\boldsymbol{x}} - \boldsymbol{q}(\tau/2)]\right) \quad (9.14)\end{aligned}$$

with $\bar{\boldsymbol{x}} = (\boldsymbol{x}' + \boldsymbol{x})/2$ and the Gaussian averaged potential $\langle V(\boldsymbol{q}(\tau))\rangle$ is as defined in equation (9.3). Taking the trace yields the partition function [69]

$$\begin{aligned}Z_{\mathrm{FG}}(\tau) = \mathrm{Tr}\left[K_{\mathrm{FG}}(\tau)\right] = \sqrt{\det(\boldsymbol{\Gamma})} \exp\left(-\frac{\hbar^2}{4}\mathrm{Tr}(\boldsymbol{\Gamma})\tau\right) \sqrt{\det\left(\left[\mathbf{1} - \exp(-\hbar^2\boldsymbol{\Gamma}\tau)\right]^{-1}\right)} \\ \times \int_{-\infty}^{\infty} \frac{\mathrm{d}\boldsymbol{q}^{3N}}{(2\pi)^{N/2}} \exp\left(-2\int_0^{\tau/2} \mathrm{d}\tau' \langle V(\boldsymbol{q}(\tau'))\rangle\right) . \quad (9.15)\end{aligned}$$

The numerical evaluation is relatively simple since one only needs to solve the $3N$ imaginary time equations of motion

$$\frac{\partial \boldsymbol{q}(\tau)}{\partial \tau} = -\boldsymbol{\Gamma}^{-1}\langle \nabla V(\boldsymbol{q}(\tau))\rangle \tag{9.16}$$

for the Gaussian positions $\boldsymbol{q}(\tau)$ and only one configuration space integration over the initial positions $\boldsymbol{q}(\tau = 0)$ has to be performed.

As in the case of the SP-TG propagator the numerical scaling in the evaluation of the two-body potential terms is $N^2$. The numerical advantage of the frozen Gaussian propagator as compared to the FC-TG or SP-TG methods is due to the constant width matrix, i.e. one has only to propagate the equations of motion (9.16), whose number scales with $N$. Additionally, functions of the width matrix $\boldsymbol{\Gamma}$ can be evaluated in advance and do not have to be repeated at every time step since $\boldsymbol{\Gamma}$ does not evolve in time. On the other hand, the width matrix $\boldsymbol{\Gamma}$ is a parameter of the system and its actual choice has a critical impact on the quality of the results [69]. It is not trivial to find a good choice of $\boldsymbol{\Gamma}$, however, the problem simplifies when all particles are identical.

For $N$ identical particles the simplest structure for $\boldsymbol{\Gamma}$ is a diagonal matrix with identical width elements, i.e. a multiple of the $3N \times 3N$ identity matrix,

$$\boldsymbol{\Gamma}_1 = \Gamma \mathbf{1} \, , \tag{9.17}$$

with only one parameter $\Gamma$. This ansatz treats all particles equally, is very simple to implement, and has the lowest numerical cost due to the diagonal structure of the matrix in Cartesian coordinates. However, it ignores the fact that a correct description of the cluster has to contain both the free motion of the centre of mass and the relative motion determined by the particle-particle interaction potential (9.5).

In a frozen Gaussian approximation the exact partition function of a free particle is obtained in the limit of a vanishing Gaussian width [cf. equation (9.15)], whereas the optimum width for the relative coordinates can be deduced from a harmonic approximation around the minimum of the particle-particle interaction potential and has a finite value. A separation of the free motion of the centre of mass from the internal degrees of freedom should be avoided since it complicates the structure of the equations of motion by introducing numerically more expensive terms such as a non-diagonal mass matrix. Considering the thawed Gaussian propagators we note that the FC-TG is capable of correctly describing the free centre of mass motion when it is combined with an internal potential independently of the choice of the coordinate system, whereas this is not fulfilled for the SP-TG [53, 173].

In the following we suggest a procedure based on an adequate choice of the width matrix which allows for a correct description of the free centre of mass motion without changing the structure of the equations. To simplify, we restrict our description to the case of three particles, a generalisation to an arbitrary number of particles is straightforward. It is plausible that in a system of coordinates $\boldsymbol{R}_i$ for the centre of mass

$$\boldsymbol{R}_{\mathrm{cm}} = \frac{1}{3}\left(\boldsymbol{r}_1 + \boldsymbol{r}_2 + \boldsymbol{r}_3\right) \tag{9.18a}$$

and the two relative positions

$$\boldsymbol{R}_1 = \boldsymbol{r}_1 - \boldsymbol{r}_2 \ , \tag{9.18b}$$
$$\boldsymbol{R}_2 = \boldsymbol{r}_1 - \boldsymbol{r}_3 \tag{9.18c}$$

a diagonal matrix structure is a good choice. In these coordinates the centre of mass is separated and we introduce the Gaussian width parameter $D_1$ for its motion. The Gaussian approximation becomes exact for the centre of mass motion in the limit $D_1 \to 0$. Since all particles are equal and there is no motivation for distinguishing between the propagation of the individual relative coordinates, we use one single parameter $D_2$ for the remaining coordinates. The matrix which then is applied to the coordinates (9.18a)-(9.18c) is

$$\boldsymbol{\Gamma}_{\mathrm{cmc}} = \begin{pmatrix} \boldsymbol{D}_1 & \boldsymbol{0} & \boldsymbol{0} \\ \boldsymbol{0} & \boldsymbol{D}_2 & \boldsymbol{0} \\ \boldsymbol{0} & \boldsymbol{0} & \boldsymbol{D}_2 \end{pmatrix} \ , \tag{9.19}$$

where $\boldsymbol{D}_1$ and $\boldsymbol{D}_2$ are $3 \times 3$ diagonal matrices with coefficients $D_1$ and $D_2$, respectively, and $\boldsymbol{0}$ is a $3 \times 3$ matrix of zeros. The most efficient way to evaluate the frozen Gaussian partition function is to keep its structure (9.15) in Cartesian coordinates and to transform the width matrix into the Cartesian system $\boldsymbol{r}_1$, $\boldsymbol{r}_2$, $\boldsymbol{r}_3$, i.e.

$$\boldsymbol{\Gamma} = \begin{pmatrix} (\boldsymbol{D}_1 + 2\boldsymbol{D}_2)/3 & (\boldsymbol{D}_1 - \boldsymbol{D}_2)/3 & (\boldsymbol{D}_1 - \boldsymbol{D}_2)/3 \\ (\boldsymbol{D}_1 - \boldsymbol{D}_2)/3 & (\boldsymbol{D}_1 + 2\boldsymbol{D}_2)/3 & (\boldsymbol{D}_1 - \boldsymbol{D}_2)/3 \\ (\boldsymbol{D}_1 - \boldsymbol{D}_2)/3 & (\boldsymbol{D}_1 - \boldsymbol{D}_2)/3 & (\boldsymbol{D}_1 + 2\boldsymbol{D}_2)/3 \end{pmatrix} \ . \tag{9.20}$$

This procedure requires the implementation of a full width matrix in the numerical evaluation of the frozen Gaussian thermal operator but avoids a full mass matrix and a change in the structure of the propagator. The results for the argon trimer presented in section 9.2.2 will show that despite its simplicity this choice leads to results which are competitive with the SP-TG propagator even though this variant of the frozen Gaussian propagator is much cheaper to evaluate numerically.

To distinguish the frozen Gaussian propagator with the matrix structure of equation (9.20) from its diagonal variant we will refer in the following to the two approximations as 2P-FG (two-parameter frozen Gaussian) and 1PD-FG (one-parameter diagonal frozen Gaussian), respectively.

Table 9.1.: Parameters used in the Gaussian fit (9.5) of the Morse potential (9.21).

| $p$ | $c_p$ [cm$^{-1}$] | $\alpha_p$ [Å$^{-2}$] |
|---|---|---|
| 1 | $3.296 \times 10^5$ | 0.6551 |
| 2 | $-1.279 \times 10^3$ | 0.1616 |
| 3 | $-9.946 \times 10^3$ | 6.0600 |

## 9.2. The argon trimer

### 9.2.1. Atomic parameters and numerical procedure

To be able to compare our results with previous investigations of the argon trimer [57, 66] we express the pairwise interaction by means of a Morse potential

$$V(r_{ij}) = D\left(\exp\left[-2\alpha(r_{ij} - R_\mathrm{e})\right] - 2\exp\left[-\alpha(r_{ij} - R_\mathrm{e})\right]\right) \ , \tag{9.21}$$

where $r_{ij}$ is the distance between particles $i$ and $j$. The Morse parameters are listed in reference [66] and have been chosen such that the Morse potential reflects a previous fit to experimental results [174]. They are $D = 99.00\,\mathrm{cm}^{-1}$, $\alpha = 1.717\,$Å, and $R_\mathrm{e} = 3.757\,$Å. Using the three sets of Gaussian parameters listed in table 9.1 we achieved a very accurate Gaussian fit to this Morse potential with a standard deviation smaller than $0.4\,\mathrm{cm}^{-1}$ in the relevant region between $r = 3.2\,$Å and $r = 6\,$Å around the minimum. As will become clear below this deviation is much smaller than effects due to the Gaussian approximation used to calculate the quantum mean energy, i.e. differences with the previous studies of the system [57, 66] do not originate from the Gaussian fit of the potential, which is only introduced to accelerate numerical computations.

In numerical evaluations of the partition function it is essential to restrict the position space integrations [cf. $\boldsymbol{q}$ integrations in equations (9.10) and (9.15)] to a reasonable region of the configuration space containing all relevant information about the thermodynamics of the cluster. Usually, this is done by introducing an additional steep potential [51] located at a certain distance $R_\mathrm{c}$ from the centre of mass $\boldsymbol{R}_\mathrm{cm}$, e.g.

$$V_\mathrm{c}(\boldsymbol{r}) \propto \sum_{i=1}^{N} \left( \frac{\boldsymbol{r}_i - \boldsymbol{R}_\mathrm{cm}}{R_\mathrm{c}} \right)^{20} \tag{9.22}$$

(cf. reference [52]) or, as implemented in our numerics, by restricting the sampling points $\boldsymbol{q}(\tau = 0)$ in the integrations to values $|\boldsymbol{q} - \boldsymbol{R}_\mathrm{cm}| < R_\mathrm{c}$. One focus of our discussion will be on the influence of this artificial confinement of the atoms. Often the potential is chosen to be very restrictive [51–54, 171]. In this chapter we will show that such a restrictive choice can have a drastic influence on the dissociation process as was already discussed in a classical context many years ago [62]. This may have implications on other studies of atomic clusters. With the confining potential the Monte Carlo sampling in $\boldsymbol{q}$ is done

with a standard Metropolis algorithm, where we followed the procedure suggested by Frantsuzov et al. explained in detail in reference [53].

The optimum width parameter connected with the atom-atom interaction in the two parameter ansatz (9.20) of the frozen Gaussian propagator was found to be $D_2 = 25\,\text{Å}^{-2}$ by using several choices, monitoring the results, and comparing them to the thawed Gaussian methods. For this choice of the parameter $D_2$ the low-temperature mean energy is minimised, and thus represents the best approximation to the ground level. The observation of the smallest energy value in the limit $T \to 0$ can be used as an additional criterion for the choice of the width matrix independently of the availability of a second method such as the thawed Gaussian propagator. We note that one can also monitor the relative amplitude of higher-order corrections to the Gaussian approximation [68, 69, 172] as a function of the width parameters.

A value of $D_1 = 0.1\,\text{Å}^{-2}$ is already small enough to lead to the best possible description of the free centre of mass motion. Using even smaller values for $D_1$ did not change the results, so we decided to use this value to have a well conditioned matrix of which the eigenvalues do not differ too much in their order of magnitude. The parameter for a diagonal matrix in the 1PD-FG propagator representing the best middle ground between $D_1$ and $D_2$ is $\Gamma = 20\,\text{Å}^{-2}$. It was selected with the method described for $D_2$ above. In a previous study of the frozen Gaussian imaginary time propagator it was found that the optimum choice for the width parameter is almost independent of the temperature [69], this was also confirmed in our study of the argon trimer. We found that the radius of the confining sphere does not have a significant influence on the optimum choice for the width matrices. Indeed, by checking several values as described above, it turned out that working with the same values for all computations was the best choice.

### 9.2.2. Comparison of the Gaussian imaginary time propagators

First we investigate the different methods introduced in section 9.1 for the evaluation of the quantum partition function for the argon trimer. To compare our results with the previous path-integral Monte Carlo calculation by Pérez de Tudela et al. [57] we select one of their parameter sets and calculate the mean energy and the specific heat for the argon trimer enclosed by a confining sphere with a radius of 10 Å, which is the weakest confinement applied in their study. Our results obtained with the four Gaussian propagators described above are also compared with the corresponding derivatives of the classical partition function

$$Z_{\text{cl}} = \left(\frac{\text{k}T}{2\pi\hbar^2}\right)^{3/2N} \int \text{e}^{-\beta V(\boldsymbol{q})}\,\text{d}\boldsymbol{q}^{3N}\ . \tag{9.23}$$

They are presented in figure 9.1. To allow for the comparison with the path-integral Monte Carlo computations of reference [57] in figure 9.2 we subtracted for this figure the exact kinetic energy of the free centre of mass $E_{\text{cm}} = 3/2\text{k}T$ from our values, which,

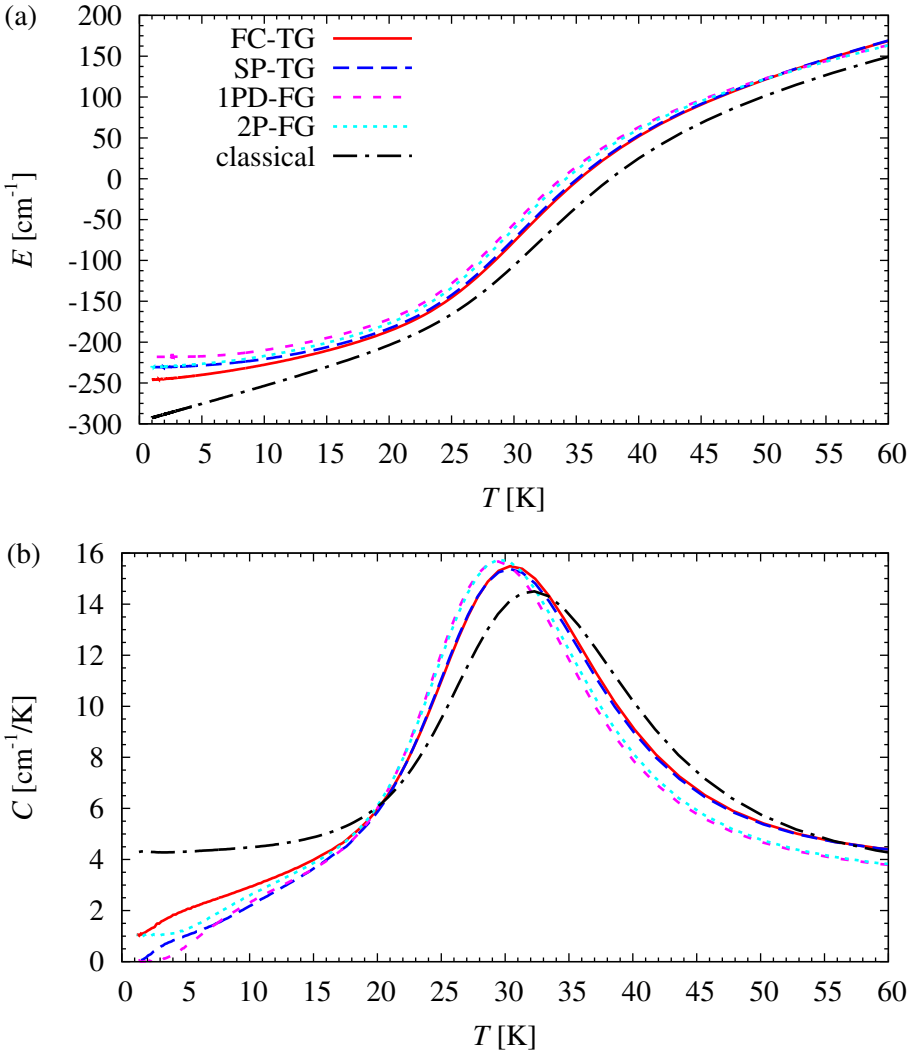


Figure 9.1.: Mean energy (a) and specific heat (b) of the argon trimer calculated for a confining radius of $R_c = 10$ Å. Results are provided for the thawed Gaussian approximations FC-TG and SP-TG, the frozen Gaussian approximations 1PD-FG, 2P-FG, and the classical theory.

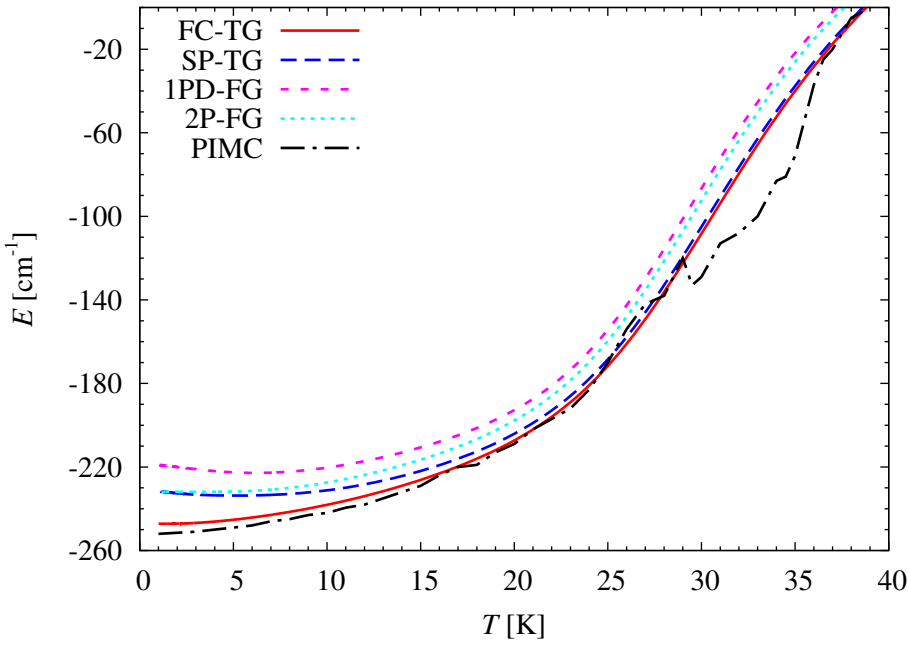


Figure 9.2.: Comparison of the mean energy obtained with the Gaussian methods FC-TG, SP-TG, 1PD-FG, and 2P-FG with the path-integral Monte Carlo (PIMC) values taken from reference [57]. The kinetic energy of the free centre of mass motion is subtracted from our results to allow for the comparison.

in the calculation, always include the energy of the whole cluster including the centre of mass translation.

The four semiclassical methods are in reasonably good agreement with each other and the classical results, however, there are quantitative differences. One can expect that the thawed Gaussian imaginary time propagator with a full matrix (FC-TG) provides the best approximation to the exact quantum results, and indeed the mean energy obtained with that method shows the best correspondence with the path-integral Monte Carlo computations of reference [57] (cf. figure 9.2). In particular, in the low-temperature limit the FC-TG propagator gives the best approximation ($E = -246\,\mathrm{cm}^{-1}$) to the ground state energy [57] of $-252.44\,\mathrm{cm}^{-1}$. Even though the FC-TG method is the most versatile propagator applied here, it still assumes a Gaussian form of the atom's wave functions and shows a slight difference as compared to the numerically exact path-integral Monte Carlo ground state energy. For higher temperatures there appear larger deviations as compared to the path-integral Monte Carlo results of reference [57], however, the latter ones are not very accurate due to the larger statistical error with increasing temperature. The semiclassical Gaussian approximations are expected to describe the partition function and its derivatives at higher temperatures even better than at low temperatures since they converge to the correct answer in the classical limit. We can thus assume that

our results are more accurate as the temperature increases. The differences between our results and those of reference [57] at higher temperatures $T \gtrapprox 30\,\mathrm{K}$ become even clearer when considering the specific heat. Our Gaussian calculations indicate a direct transition from the bound cluster to the completely dissociated situation with three free atoms, whereas such a clear conclusion is not possible with the path-integral Monte Carlo calculations of reference [57]. This transition is discussed in more detail in the next two sections.

It is also expected that the worst approximation in the low-temperature limit is obtained by the 1PD-FG ansatz. As was mentioned in section 9.1.3 the diagonal width matrix does not treat the free centre of mass motion correctly. This manifests itself as a large deviation of the mean energy from the correct value for $T \to 0$. The energy calculated with the diagonal frozen Gaussian width matrix increases for temperatures below 5 K, and this is definitely wrong. This deficiency is overcome with the 2P-FG matrix as presented in equation (9.20). It leads to a considerably lower mean energy in the low-temperature limit, which is closer to the exact ground level and is also closer to the FC-TG energy values, which can be considered to provide the best values of all methods used here.

More interesting, however, is the comparison of the 2P-FG and the SP-TG propagators. As reported in previous investigation of larger clusters [53] the single-particle thawed Gaussian approximation shows results for the mean energy and the specific heat which are qualitatively in agreement with the full matrix case. Quantitative differences have been reported and can also be found in our calculations for temperatures $T \lessapprox 45\,\mathrm{K}$. The differences with respect to the full matrix results increase with decreasing temperature. However, as can be seen in figure 9.1 (a) the description of the mean energy of the SP-TG and the 2P-FG methods is of similar quality at very low temperatures. This is a remarkable finding since the evaluation of the single-particle thawed Gaussian propagator is more expensive than the frozen Gaussian due to the need to propagate the width matrix elements in time.

By contrast, the specific heat curve of the 2P-FG propagator is closer to that of the 1PD-FG than to the two thawed Gaussian approximations, which agree very well with each other. It seems that in the temperature region around the transition from the bound to the dissociated cluster, a thawed Gaussian can provide a better description. However, the deviation is small and vanishes for weaker external confinements. An example for such a weaker confinement is shown in figure 9.3, in which the comparison of figure 9.1 is repeated for a confinement of $R_\mathrm{c} = 32\,\mathrm{\AA}$. Here, down to a temperature of 18 K the two thawed Gaussian approximations and the 2P-FG propagator provide almost identical results. The lines lie on top of each other both for the mean energy and the specific heat. Only the 1PD-FG values deviate a bit from the three other methods.

In summary, we can state that the thawed Gaussian propagator with a full matrix provides the best approximation which deviates in the low-temperature limit only slightly from the exact result and almost reaches the ground level for $T \to 0\,\mathrm{K}$. In all cases in which the high accuracy of the full matrix thawed Gaussian propagator is not required

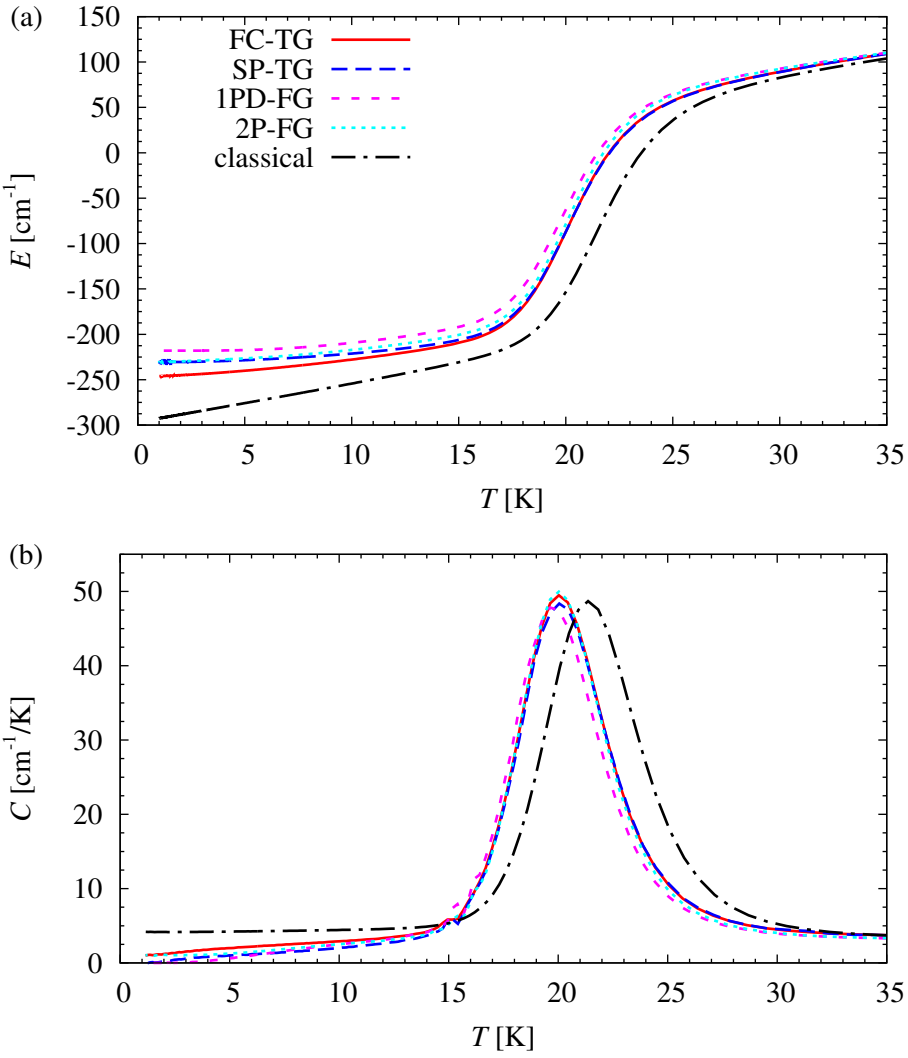


Figure 9.3.: Mean energy (a) and specific heat (b) of the argon trimer calculated with the Gaussian approximations FC-TG, SP-TG, 1PD-FG, 2P-FG, and classically for $R_c = 32\,\text{Å}$.

or in which the integration of the equations of motion for the width parameters of a full matrix is too expensive, the frozen Gaussian ansatz with two parameters (2P-FG) seems to be the best choice. It provides the same quality of results as the single-particle thawed Gaussian propagator but is much easier to evaluate since no integrations of parameters of the width matrix are required.

### 9.2.3. Dissociation and the influence of the confining sphere

Before we discuss the dissociation process in more detail we have to investigate the influence of the confining sphere on the mean energy and the specific heat. While often a very restrictive value of the confining radius $R_c$ is chosen [51–54, 171], our calculations demonstrate that its value significantly affects the thermodynamic properties of the clusters unless large values, drastically exceeding a few Ångströms, are used. Figure 9.4 shows the mean energy of the argon trimer for several confinements $R_c$ in a purely classical calculation [figure 9.4 (a)] and an evaluation of the quantum partition function with the 2P-FG propagator [figure 9.4 (b)], which, as was discussed in section 9.2.2, describes the quantum behaviour correctly. The values $R_c = 2.6\,\text{Å}, 4\,\text{Å}$, and $10\,\text{Å}$ have already been used in reference [57]. The qualitative behaviour of these three curves differs strongly. In particular, the mean energy for $R_c = 10\,\text{Å}$ shows a significant increase of the slope for temperatures above 20 K. In reference [57] this was regarded as an indication that this radius allows for a total fragmentation of the cluster. However, the mean energy for higher temperatures reveals that this is not fulfilled completely. We included the line for $E = (9/2)\mathrm{k}T$ in the figure, which corresponds to three free particles. The mean energy for the restriction $R_c = 10\,\text{Å}$ does not reach that line even at $T = 70\,\text{K}$. However, for the weaker restrictions $R_c = 15 \ldots 35\,\text{Å}$ one can observe that actually a total fragmentation takes place and that for $T \gtrapprox 40\,\text{K}$ the energy is identical to that of three free particles. In figure 9.4 (a) we also included the line $E = V_0 + 6\mathrm{k}T$ with the potential minimum $V_0 = -296\,\text{cm}^{-1}$. This line corresponds to the classical expectation at low temperatures for the internal rotations and oscillations of the trimer plus the energy of the free centre of mass.

Even though the behaviour at very low ($T \leq 15\,\text{K}$) and high temperatures ($T > 35\,\text{K}$) agrees well for all confinements $R_c > 15\,\text{Å}$ the transition itself obviously depends more critically on the value of $R_c$. It is clear that a confining radius $R_c = 10\,\text{Å}$ is too restrictive and does not describe the cluster correctly. A significantly larger confining radius $R_c > 30\,\text{Å}$ is required. For the largest confining radii used in figure 9.4 we observe convergence, i.e. a further expansion of the confining sphere does not change the results significantly.

We note that it becomes increasingly difficult to converge the Monte Carlo integrations for the classical and the 2P-FG partition function for increasing $R_c$. Similarly, the large error bars in the path-integral Monte Carlo calculation of reference [57] indicate that in their computations a radius of $R_c = 10\,\text{Å}$ was already challenging. Nevertheless, the results presented in figure 9.4 demonstrate that the added effort of increasing

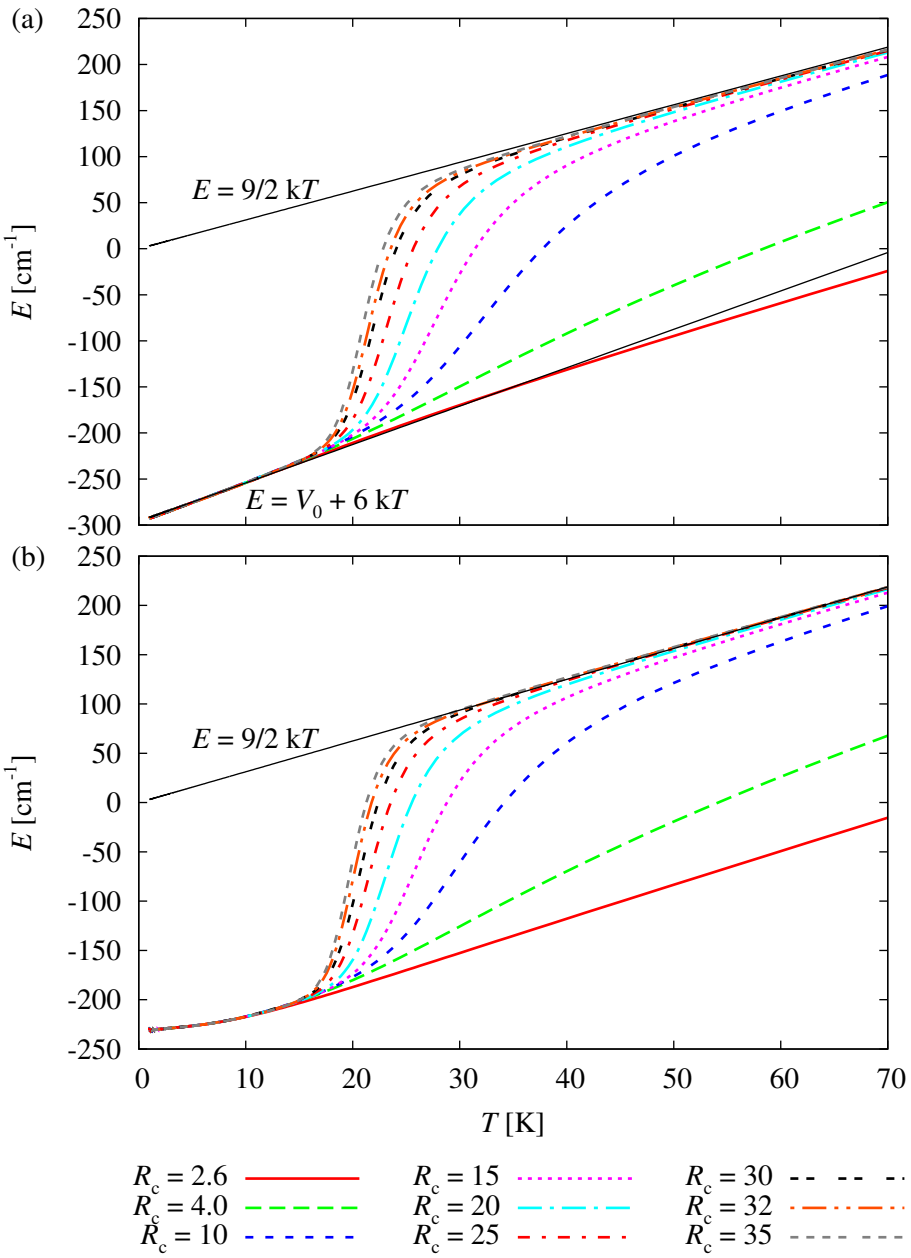


Figure 9.4.: Comparison of the mean energy of the argon trimer for different confining radii $R_c$ (in Å) in classical (a) and quantum calculations with the 2P-FG partition function (b). We also added the thin black lines $E = 9/2kT$ representing three free particles and $E = V_0 + 6kT$ with the potential minimum $V_0 = -296\,\mathrm{cm}^{-1}$ for the classical low-temperature behaviour.

$R_c$ beyond 30 Å is essential. The necessity for a thorough investigation of the correct boundary conditions is already known from classical investigations of atomic clusters. Etters and Kaelberer [62] demonstrated the negative influence of too restrictive boxes on the classical average energy.

### 9.2.4. Dissociation from classical and quantum perspectives

With a confinement of $R_c = 32$ Å the cluster can be regarded as converged with respect to $R_c$. The artificial confinement does not have a further noticeable influence on the thermodynamic properties. This allows us to discuss the features observed in the mean energy and the specific heat in more detail. Additionally, the various Gaussian propagators used to obtain the quantum properties agree with each other to a high precision, so that we may consider them as converged in the sense that the choice of Gaussian method has no further influence.

As can be seen in figure 9.3 the qualitative behaviour in the quantum and classical cases is almost the same. The cluster is bound at low temperatures, shows a relatively sharp transition, and is completely dissociated for temperatures $T > 33$ K. For very low temperatures the classical mean energy exhibits the expected behaviour $E \propto 6kT$ [cf. also figure 9.4 (a)] for the system (free centre of mass, rotations and oscillations of the internal degrees of freedom), whereas the FC-TG mean energy (best approximation, see section 9.2.2) converges to a value close to that of the ground level. Further differences between the classical and quantum mechanical results are found in the transition region. It is shifted to slightly lower temperatures in the quantum calculations as compared to the classical. All quantum calculations show a maximum of the specific heat at 20 K, while the classical maximum is at 21.5 K. One reason for this shift is the presence of the zero point energy in the quantum system. As is already obvious in figure 9.4 the classical and quantum results agree very well in the high-temperature limit, since both trend to the case of three free particles. Thus, we conclude that the transition observed in the cluster of three argon atoms is a classical phenomenon. The only difference between classical and quantum mechanics is in the temperature at which the transition occurs. We note that Etters and Kaelberer [62] reported a "liquid-gas transition" identified by the absence of bounded atom configurations in a classical investigation of the system with "free-surface boundary conditions", i.e. without a confining sphere, at $T = 20$ K, which is in good agreement with our results.

Our finding of a classical-like complete dissociation of the trimer in one step differs from the conclusions of Pérez de Tudela et al. [57]. While the mean energy in the calculations of reference [57] for $R_c = 10$ Å shows a larger and larger slope for increasing temperatures up to $T = 40$ K we observe already a decrease of the slope for temperatures $T > 30$ K. The difference relative to the path-integral Monte Carlo calculations becomes even more pronounced in the specific heat. Pérez de Tudela et al. [57] report that they find an "apparent" maximum which evolves with the radius $R_c$ of the confinement and appears slightly below 40 K for $R_c = 10$ Å. The absence of an unambiguous maximum

was seen as an indication for structural changes of the cluster instead of a proper "phase transition". Although the dissociation of the cluster is not fully achieved for such a strong confinement, it is clear from the Gaussian methods used in this chapter that already for $R_c = 10\,\text{Å}$ a pronounced peak in the specific heat indicating the dissociation of the system at $T \approx 30\,\text{K}$ is present (cf. figure 9.1). Describing the cluster with a weaker confinement correctly reveals the unambiguous dissociation without intermediate structural modification as discussed above.

The very low temperature found for the dissociation of the cluster may also be important for rare gas clusters in general. As was already discussed [57], even for a confining sphere with $R_c = 10\,\text{Å}$, the transition temperature of $T \approx 35\,\text{K}$ is lower than temperatures discussed for structural transformations or a "melting" of clusters. Features indicating such changes have, e.g. been found beyond 40 K for argon [175]. If one considers that the dissociation temperature is actually even lower ($T \approx 20\,\text{K}$, c.f. figure 9.3), one necessarily concludes that it is wrong to ignore the influence of the confining sphere on such properties. In larger neon clusters ($Ne_{13}$ and $Ne_{38}$) features in the mean energy or the specific heat which were related to structural changes, have been reported between 6 K and 8 K [51, 53, 54]. These temperatures are lower than the dissociation found here, however, one may expect that at least a partial dissociation can set in much earlier in larger clusters since they contain higher energies. In the numerical simulations [51, 53, 54] the confining radii are chosen such that no atom can leave the cluster during the time evolution. Our results indicate that such a constraint might be too restrictive and lead to incorrect conclusions. A partial or full dissociation can influence structural transformations and may even set in before structural changes of an artificially confined cluster can occur.

## 9.3. Discussion and possible extensions

In this chapter we investigated the argon trimer by means of semiclassical Gaussian approximations to the Boltzmann operator. We introduced a new matrix structure for a frozen Gaussian variant of the imaginary time propagator which is capable of correctly dealing with the free centre of mass motion of a cluster of atoms in Cartesian coordinates. With this matrix structure we were able to show that the frozen Gaussian propagator is, in spite of its simplicity, competitive with numerically more expensive thawed Gaussian variants. In particular, the frozen Gaussian method provides the same quality thermodynamic results as the so-called single-particle thawed Gaussian propagator, which in addition to the time-dependent variables of the frozen Gaussian requires the time evolution for the elements of a block-diagonal width matrix. This is especially true in the low-temperature limit, where quantum effects become important and the form of the semiclassical approximation is supposed to have the largest influence. Our results suggest that the frozen Gaussian ansatz with two parameters (2P-FG) introduced in this chapter is the method of choice in all cases in which the higher accuracy of the

full matrix thawed Gaussian propagator is not required or in which the integration of the equations of motion for the width parameters of a full matrix is too expensive.

The evaluation of the mean energy and the specific heat for the cluster of three argon atoms demonstrated that a previous investigation of the system [57] used too restrictive confinements to describe the dissociation behaviour of the system correctly. Above $T = 15\,\mathrm{K}$ the cluster directly dissociates into three free atoms, as is evident from the Gaussian calculations presented in this chapter. This dissociation is almost purely classical, the influence of quantum mechanics is only found in a convergence to the ground state energy instead of the classical potential minimum for $T \to 0$ and in a slight shift of the three-body dissociation transition to higher classical temperatures ($\Delta T \approx 1.5\,\mathrm{K}$) which we attribute to the zero point energy of quantum mechanics. The clear and pronounced transition found in this chapter supports the conclusion of reference [57] that the dissociation of the atoms from the cluster is important when reconfigurations of the internal structure are considered. Our results strongly indicate that the confinement to very small spheres usually applied in the calculation of the partition function and values deduced from it [52–54, 171] might be too restrictive to fully understand the low-temperature behaviour of the clusters. The dissociation can set in before structural changes or a melting can be observed. To make a clear statement on this question it is necessary to advance the investigations done here to clusters with higher numbers of atoms. In particular, the cases of $Ar_6$ [176], $Ar_{13}$ [176–178], $Ne_{13}$ [53] or $Ne_{38}$ [54] examined recently are of special interest.

On the technical side, it is known that both the frozen and thawed Gaussian propagators used here are, in the framework of a generalised time-dependent perturbation theory [179, 180], the lowest-order approximations in a series converging to the exact quantum propagator [68, 69, 172]. Higher orders can help to understand the thermodynamic properties better and to verify the results obtained here with a higher accuracy. Furthermore, the corrections obtained by the evaluation of higher-order terms provides objective access to the quality with which the Gaussian approximations reflect the quantum effects in the system studied. They are the topic of chapter 11.

# 10. Dissociation of $Ar_6$ and structural information with the frozen Gaussian method

In the last sections we investigated a very simple cluster, viz. the argon trimer with the frozen Gaussian imaginary time propagator, and studied physical quantities following directly from the partition function. The mean energy and the specific heat are obtained as simple derivatives. Often it is, however, important to know more than just these two properties. One important example are structural transformations or phase transitions from one packing to another [51–57]. Of course, every of these transformations will leave its signature in the specific heat or the mean energy. They will cause unambiguous signals in these variables, and thus it will be possible to detect at which temperature a transformation is occurring. However, often more information is required. For example, if a switch from one structure to another is studied, it is important to know which alignment of the atoms is present. A very detailed knowledge of the structure of the atoms is available via the inter-particle distances. To obtain their values it is very common to compute the radial pair correlation function between particles $i$ and $j$ at positions $\boldsymbol{r}_i$ and $\boldsymbol{r}_j$, respectively,

$$p_{ij}(r) = \langle \delta(|\boldsymbol{r}_i - \boldsymbol{r}_j| - r) \rangle_\beta = \mathrm{Tr}\left[K(\beta)\delta(|\boldsymbol{r}_i - \boldsymbol{r}_j| - r)\right] \ , \tag{10.1}$$

where $\langle\rangle_\beta$ is the thermal average at inverse temperature $\beta$ and $K(\beta) = \mathrm{e}^{-\beta H}$ represents the imaginary time propagator at the same temperature [53]. This quantity provides information about the distribution of the distances occurring at every temperature. In the form (10.1) it is expensive to calculate, however, it can more easily be accessed via its Fourier transform [53].

It is the purpose of this chapter to show that the frozen Gaussian method introduced in chapter 9 can be used to obtain a numerically cheap and easy way to the distances of the atoms in clusters. The mean values and the variances of the distances $d_{ij}$ between atoms $i$ and $j$ can directly be accessed and provide a very clear information of how the atoms are arranged in the cluster. Since the distances $d_{ij}$ of the single pairs can be calculated in parallel with the same Monte Carlo sampling all of these values can be calculated with low numerical extra cost. This provides for $N$ atoms $N(N-1)/2$ independent values, whereas in the pair correlation function (10.1) small differences in the mean distances might be hidden below broad distributions.

We introduce the semiclassical approximations of the mean distances and their variances in terms of the frozen Gaussian imaginary time propagator developed in section 9.1. To do so, we introduce mean values and variances for inter-atomic distances with the frozen Gaussian method (section 10.1.1) and add their thawed Gaussian variant (section 10.1.2). Then we apply the method to the $Ar_6$ cluster in section 10.2. After a short introduction of the system (section 10.2.1) we will investigate derivatives of the partition function (section 10.2.2) and the structural information (section 10.2.3). A discussion in section 10.3 concludes the chapter. The system is slightly more complicated than the trimer and promises more features, which will in particular be interesting for the structure. A publication of the data presented here is in preparation [181].

# 10.1. Structural information with the semiclassical Gaussian method

## 10.1.1. Frozen Gaussian mean values and variances

### Propagator

In section 9.1.3 we obtained for the frozen Gaussian imaginary time propagator the symmetrised form

$$\begin{aligned}\langle \boldsymbol{x}'|K_{\mathrm{FG}}(\tau)|\boldsymbol{x}\rangle = \det(\boldsymbol{\Gamma})\exp\left(-\frac{\hbar^2}{4}\mathrm{Tr}(\boldsymbol{\Gamma})\tau\right)\sqrt{\det\left(2\left[\mathbf{1}-\exp(-\hbar^2\boldsymbol{\Gamma}\tau)\right]^{-1}\right)}\\ \times\exp\left(-\frac{1}{4}[\boldsymbol{x}'-\boldsymbol{x}]^{\mathrm{T}}\boldsymbol{\Gamma}[\tanh(\hbar^2\boldsymbol{\Gamma}\tau/2)]^{-1}[\boldsymbol{x}'-\boldsymbol{x}]\right)\\ \times\int_{-\infty}^{\infty}\frac{\mathrm{d}\boldsymbol{q}^{3N}}{(2\pi)^{3N}}\exp\left(-2\int_0^{\tau/2}\mathrm{d}\tau'\langle V(\boldsymbol{q}(\tau'))\rangle-[\bar{\boldsymbol{x}}-\boldsymbol{q}(\tau/2)]^{\mathrm{T}}\boldsymbol{\Gamma}[\bar{\boldsymbol{x}}-\boldsymbol{q}(\tau/2)]\right)\end{aligned} \tag{9.14}$$

with $\bar{\boldsymbol{x}}=(\boldsymbol{x}'+\boldsymbol{x})/2$ and the Gaussian averaged potential $\langle V(\boldsymbol{q}(\tau))\rangle$ from equation (9.3). It is the basis for the variables we need in addition to the partition function

$$\begin{aligned}Z_{\mathrm{FG}}(\tau)=\mathrm{Tr}\left[K_{\mathrm{FG}}(\tau)\right]=\sqrt{\det(\boldsymbol{\Gamma})}\exp\left(-\frac{\hbar^2}{4}\mathrm{Tr}(\boldsymbol{\Gamma})\tau\right)\sqrt{\det\left(\left[\mathbf{1}-\exp(-\hbar^2\boldsymbol{\Gamma}\tau)\right]^{-1}\right)}\\ \times\int_{-\infty}^{\infty}\frac{\mathrm{d}\boldsymbol{q}^{3N}}{(2\pi)^{N/2}}\exp\left(-2\int_0^{\tau/2}\mathrm{d}\tau'\langle V(\boldsymbol{q}(\tau'))\rangle\right)\ .\end{aligned} \tag{9.15}$$

The width matrix is of the shape (9.20) but we do not restrict our discussion to three dimensions. Thus, we assume the generalised matrix

$$\boldsymbol{\Gamma}=\begin{pmatrix}(\boldsymbol{D}_1+2\boldsymbol{D}_2)/3 & (\boldsymbol{D}_1-\boldsymbol{D}_2)/3 & (\boldsymbol{D}_1-\boldsymbol{D}_2)/3 & \\ (\boldsymbol{D}_1-\boldsymbol{D}_2)/3 & (\boldsymbol{D}_1+2\boldsymbol{D}_2)/3 & (\boldsymbol{D}_1-\boldsymbol{D}_2)/3 & \cdots\\ & \ddots & & \end{pmatrix}\ . \tag{10.2}$$

It still consists only of two relevant parameters since we work only with a monoatomic cluster and all pairwise inter-atomic forces are considered to be identical. Only the centre of mass motion has to be distinguished from that. The $3 \times 3$ diagonal matrices $\boldsymbol{D}_1$ and $\boldsymbol{D}_2$ describe the three spacial directions of one particle. Since also the spacial dimensions are equivalent the best choices are, again, multiples of the unity matrix, such that two scalar coefficients $D_1$ and $D_2$ have to be chosen, i.e.

$$\boldsymbol{D}_1 = D_1 \mathbf{1}_{3\times 3} \ , \quad \boldsymbol{D}_2 = D_2 \mathbf{1}_{3\times 3} \ . \tag{10.3}$$

### Thermal averages of structural information

In chapter 9 we used already the simple thermal averages requiring only the partition function $Z(\beta)$, viz. the mean energy $E = \mathrm{k}T^2 \partial \ln Z/\partial T$ and the specific heat $C = \partial E/\partial T$. However, $K(\beta)$ provides access to the thermal average of any observable $O$ via

$$\bar{O}^{(\mathrm{FG})} = \langle O \rangle_\beta = \frac{\mathrm{Tr}(K_{\mathrm{FG}}(\beta) O)}{Z_{\mathrm{FG}}(\beta)} \ , \tag{10.4}$$

which we exploit in this chapter to gain access to the structural information. A well suited property is the distance between two atoms, i.e.

$$O = d_{ij} = |\boldsymbol{x}_i - \boldsymbol{x}_j|. \tag{10.5}$$

With the frozen Gaussian propagator (9.14) this leads to the expression

$$\begin{aligned} \bar{d}_{ij}^{(\mathrm{FG})} = \frac{1}{Z_{\mathrm{FG}}(\beta)} \mathrm{Tr}(K_{\mathrm{FG}}(\beta) \, |\boldsymbol{x}_i - \boldsymbol{x}_j|) = \frac{1}{Z_{\mathrm{FG}}(\beta)} \det(\boldsymbol{\Gamma}) \exp\left( -\frac{\hbar^2}{4} \mathrm{Tr}(\boldsymbol{\Gamma}) \beta \right) \\ \times \sqrt{\det\left(2\left[\mathbf{1} - \exp(-\hbar^2 \boldsymbol{\Gamma} \beta)\right]^{-1}\right)} \int_{-\infty}^{\infty} \frac{\mathrm{d}\boldsymbol{q}^{3N}}{(2\pi)^{3N}} \exp\left( -2 \int_0^{\beta/2} \mathrm{d}\tau \langle V(\boldsymbol{q}(\tau)) \rangle \right) \\ \times \int_{-\infty}^{\infty} \mathrm{d}\boldsymbol{x}^{3N} \exp\left( -[\boldsymbol{x} - \boldsymbol{q}(\beta/2)]^{\mathrm{T}} \boldsymbol{\Gamma} [\boldsymbol{x} - \boldsymbol{q}(\beta/2)] \right) |\boldsymbol{x}_i - \boldsymbol{x}_j| \ , \end{aligned} \tag{10.6}$$

in which an explicit integration over the $3N$ position variables $\boldsymbol{x}$ remains in addition to the evaluation of the partition function (9.15). As mentioned in chapter 9 it is very important to reduce the numerical effort as much as possible for many-particle systems. In particular, the position space integrations require an expensive Monte Carlo sampling in a high-dimensional configuration space.

For usual applications a numerical evaluation of the $\boldsymbol{x}$ integration can be avoided in a reasonable approximation. This can be seen with the variable $\boldsymbol{y} = \boldsymbol{x} - \boldsymbol{q}(\beta/2)$, which transforms the $\boldsymbol{x}$ integral in (10.6) to

$$\int_{-\infty}^{\infty} \mathrm{d}\boldsymbol{y}^{3N} \exp\left( -\boldsymbol{y}^{\mathrm{T}} \boldsymbol{\Gamma} \boldsymbol{y} \right) |\boldsymbol{y}_i - \boldsymbol{y}_j + \boldsymbol{q}_i(\beta/2) - \boldsymbol{q}_j(\beta/2)| \ . \tag{10.7}$$

The width of the atom's wave functions contribute only at low temperatures significantly to the distance. As we will see, in practical applications a very narrow Gaussian centres all values $\boldsymbol{y}_i$ strongly around zero, i.e. $\boldsymbol{x}_i$ is almost identical with $\boldsymbol{q}_i(\beta/2)$ for a nonvanishing Gaussian weight. Thus, we evaluate the integral (10.7) for the case $|\boldsymbol{y}_i - \boldsymbol{y}_j| \ll |\boldsymbol{q}_i - \boldsymbol{q}_j|$, and obtain

$$|\boldsymbol{y}_i - \boldsymbol{y}_j + \boldsymbol{q}_i - \boldsymbol{q}_j| \approx |\boldsymbol{q}_i - \boldsymbol{q}_j| - (\boldsymbol{y}_i - \boldsymbol{y}_j) \cdot \frac{\boldsymbol{q}_i - \boldsymbol{q}_j}{|\boldsymbol{q}_i - \boldsymbol{q}_j|} + \frac{1}{2}(\boldsymbol{y}_i - \boldsymbol{y}_j)^2 - \frac{1}{2}\frac{\left[(\boldsymbol{y}_i - \boldsymbol{y}_j) \cdot (\boldsymbol{q}_i - \boldsymbol{q}_j)\right]^2}{|\boldsymbol{q}_i - \boldsymbol{q}_j|^3} \,. \quad (10.8)$$

With this expansion the integral (10.7) evaluates to

$$\sqrt{\frac{\pi^{3N}}{\det(\boldsymbol{\Gamma})}}\left[|\boldsymbol{q}_i(\beta/2) - \boldsymbol{q}_j(\beta/2)| + \frac{\mathrm{Tr}\big(\boldsymbol{\Gamma}_{ii}^{-1} + \boldsymbol{\Gamma}_{jj}^{-1} - \boldsymbol{\Gamma}_{ij}^{-1} - \boldsymbol{\Gamma}_{ji}^{-1}\big)}{6|\boldsymbol{q}_i(\beta/2) - \boldsymbol{q}_j(\beta/2)|}\right], \quad (10.9)$$

where $\boldsymbol{\Gamma}_{ij}$ is the $3 \times 3$ submatrix of $\boldsymbol{\Gamma}$ at the rows and columns representing particles $i$ and $j$. In total we obtain

$$\begin{aligned}\bar{d}_{ij}^{(\mathrm{FG})}(\beta) = \frac{1}{Z_{\mathrm{FG}}(\beta)}\mathrm{Tr}(K_{\mathrm{FG}}(\beta)\,|\boldsymbol{x}_i - \boldsymbol{x}_j|) &\approx \frac{1}{Z_{\mathrm{FG}}(\beta)}\sqrt{\det(\boldsymbol{\Gamma})}\exp\left(-\frac{\hbar^2}{4}\mathrm{Tr}(\boldsymbol{\Gamma})\beta\right) \\ &\times \sqrt{\det\left([\mathbf{1} - \exp(-\hbar^2\boldsymbol{\Gamma}\beta)]^{-1}\right)}\int_{-\infty}^{\infty}\frac{\mathrm{d}\boldsymbol{q}^{3N}}{(2\pi)^{3N/2}}\exp\left(-2\int_0^{\beta/2}\mathrm{d}\tau\langle V(\boldsymbol{q}(\tau))\rangle\right) \\ &\times \left[|\boldsymbol{q}_i(\beta/2) - \boldsymbol{q}_j(\beta/2)| + \frac{\mathrm{Tr}\big(\boldsymbol{\Gamma}_{ii}^{-1} + \boldsymbol{\Gamma}_{jj}^{-1} - \boldsymbol{\Gamma}_{ij}^{-1} - \boldsymbol{\Gamma}_{ji}^{-1}\big)}{6|\boldsymbol{q}_i(\beta/2) - \boldsymbol{q}_j(\beta/2)|}\right]. \quad (10.10)\end{aligned}$$

The first term in equation (10.10), $\propto |\boldsymbol{q}_i - \boldsymbol{q}_j|$, reflects the core of the semiclassical approximation, in which the positions of the atoms are given by the centres $\boldsymbol{q}_i$ of the Gaussian wave packets (9.13). It corresponds to

$$O = |\boldsymbol{q}_i - \boldsymbol{q}_j| \,. \quad (10.11)$$

The second term contains a correction due to the finite width of an atom's wave packet. It is completely sufficient to include this lowest-order term, of which the $\boldsymbol{x}$ integration could be done analytically with a simple result, thus reducing the numerical effort drastically. For the frozen Gaussian method any higher terms beyond those included in the approximation (10.10) for the mean distances are of lower interest because the width matrix $\boldsymbol{\Gamma}$ is held constant and any information on the temperature dependence of the wave function's variance is ignored anyway. Indeed, as we will see in the results already the correction term in the approximation (10.10) has almost no significance. From the physical point of view we also expect that the width of the atom's wave functions only plays

a role at very low temperatures at which the structural configuration is unambiguously in a highly symmetric ground state configuration.

To estimate the quality and validity of these mean values we calculate additionally the variances of the distance distributions. With the operator

$$O = v_{ij} = (d_{ij} - \bar{d}_{ij})^2 = (\boldsymbol{x}_i - \boldsymbol{x}_j)^2 - \bar{d}_{ij}^2 \,, \tag{10.12}$$

and the integral

$$\begin{aligned}\frac{1}{Z_{\mathrm{FG}}(\beta)}\mathrm{Tr}\left(K_{\mathrm{FG}}(\beta)\,[\boldsymbol{x}_i - \boldsymbol{x}_j]^2\right) &= \frac{1}{Z_{\mathrm{FG}}(\beta)}\sqrt{\det(\boldsymbol{\Gamma})}\exp\left(-\frac{\hbar^2}{4}\mathrm{Tr}(\boldsymbol{\Gamma})\beta\right)\\ &\times\sqrt{\det\left([\mathbf{1}-\exp(-\hbar^2\boldsymbol{\Gamma}\beta)]^{-1}\right)}\int_{-\infty}^{\infty}\frac{\mathrm{d}\boldsymbol{q}^{3N}}{(2\pi)^{3N/2}}\exp\left(-2\int_0^{\beta/2}\mathrm{d}\tau\langle V(\boldsymbol{q}(\tau))\rangle\right)\\ &\times\left[(\boldsymbol{q}_i(\beta/2)-\boldsymbol{q}_j(\beta/2))^2+\frac{1}{2}\mathrm{Tr}\big(\boldsymbol{\Gamma}_{ii}^{-1}+\boldsymbol{\Gamma}_{jj}^{-1}-\boldsymbol{\Gamma}_{ij}^{-1}-\boldsymbol{\Gamma}_{ji}^{-1}\big)\right]\end{aligned} \tag{10.13}$$

we obtain the standard deviations $\sigma_{ij} = \sqrt{\bar{v}_{ij}^{(\mathrm{FG})}}$ of the distances $\bar{d}_{ij}^{(\mathrm{FG})}$.

#### Sorted distances

For the $Ar_6$ cluster there are 15 possible combinations $i$ and $j$, and thus 15 distances. The clusters are oriented arbitrarily in the simulation, the numbers $i$ and $j$ of the atoms have no meaning for the true configuration, and thus are not appropriate quantities to define the pairwise distances. The average of all calculations simply results in identical values for all $\bar{d}_{ij}$ which correspond to the mean value of all 15 atom-atom distances in a certain configuration. To obtain a meaningful quantity we sort the distances according to their size,

$$d_1 < d_2 < \ldots < d_{15} \,, \tag{10.14}$$

and determine the thermal average of these size ordered distances, i.e. we obtain the thermal mean value of the smallest distance, the second smallest, and so forth. These values can be compared with the expectations of geometrical configurations.

### 10.1.2. Thawed Gaussian propagator

The frozen Gaussian method has proved to provide good results for thermodynamic quantities. We want to know whether or not this is also true for the widths calculated in this chapter. In chapter 9 we have seen that the thawed Gaussian method with a fully coupled width matrix leads to the best agreement with numerically exact mean energies and specific heats, and thus turned out to provide very good reference values. The Gaussian approximation affects mainly the propagator which already has been used for the derivatives of the partition function. Thus, we can expect that also for the distances

the thawed Gaussian method should be very close to the true quantum mechanical result. We use it to evaluate the quality of the distances obtained with the frozen Gaussian semiclassical approximation.

The thawed Gaussian propagator we use is, again, the time evolved Gaussian approximation (TEGA) suggested by Frantsuzov et al. [53, 170] and introduced in section 9.1.2 with a full width matrix $\boldsymbol{G}$. Its symmetrised propagator is

$$\begin{aligned}\langle \boldsymbol{x}|K_{\mathrm{TG}}(\tau)|\boldsymbol{x}'\rangle = \int \frac{\mathrm{d}\boldsymbol{q}^{3N}}{(2\pi)^{3N}} \frac{\exp[2\gamma(\tau/2)]}{\det[\boldsymbol{G}(\tau/2)]} \\ \times \exp\left(-\frac{1}{2}[\boldsymbol{x}-\boldsymbol{q}(\tau/2)]^{\mathrm{T}}\boldsymbol{G}(\tau/2)^{-1}[\boldsymbol{x}-\boldsymbol{q}(\tau/2)]\right) \\ \times \exp\left(-\frac{1}{2}[\boldsymbol{x}'-\boldsymbol{q}(\tau/2)]^{\mathrm{T}}\boldsymbol{G}(\tau/2)^{-1}[\boldsymbol{x}'-\boldsymbol{q}(\tau/2)]\right) \ , \quad (9.8)\end{aligned}$$

and the partition function reads

$$Z_{\mathrm{TG}} = \int \frac{\mathrm{d}\boldsymbol{q}^{3N}}{(2\sqrt{\pi})^{3N}} \frac{\exp[2\gamma(\tau/2)]}{\sqrt{\det[\boldsymbol{G}(\tau/2)]}} \ . \quad (9.10)$$

For the comparison we evaluate the mean value of the distances in the same approximation as for the frozen Gaussian propagator, viz.

$$\begin{aligned}\bar{d}_{ij}^{(\mathrm{TG})}(\beta) \approx \frac{1}{Z_{\mathrm{TG}}(\beta)} \int \frac{\mathrm{d}\boldsymbol{q}^{3N}}{(2\sqrt{\pi})^{3N}} \frac{\exp[2\gamma(\beta/2)]}{\sqrt{\det[\boldsymbol{G}(\beta/2)]}} \\ \times \left[|\boldsymbol{q}_i(\beta/2)-\boldsymbol{q}_j(\beta/2)| + \frac{\mathrm{Tr}\big(\boldsymbol{G}_{ii}(\beta/2)+\boldsymbol{G}_{jj}(\beta/2)-\boldsymbol{G}_{ij}(\beta/2)-\boldsymbol{G}_{ji}(\beta/2)\big)}{6|\boldsymbol{q}_i(\beta/2)-\boldsymbol{q}_j(\beta/2)|}\right] . \quad (10.15)\end{aligned}$$

The thawed Gaussian method provides an additional important information. In contrast to the frozen Gaussian method it is, as described in section 9.1.2, based on a temperature-dependent width matrix $\boldsymbol{G}(\tau)$, which automatically adapts itself to a given temperature, and thus provides easier access to the width of the wave function, which influences the variances of the distances. We expect that the "quantum mechanical part of the variances", i.e. that originating from the spread of the wave function, increases with lower temperatures, which has to be reflected in the Gaussian width matrix. For a frozen Gaussian this increase of the width can only be described correctly if the constant matrix $\boldsymbol{\Gamma}$ is optimised for every single temperature, which is a numerically expensive task. For the thawed Gaussian the variances read

$$\begin{aligned}\bar{v}_{ij}^{(\mathrm{TG})}(\beta) \approx \frac{1}{Z_{\mathrm{TG}}(\beta)} \int \frac{\mathrm{d}\boldsymbol{q}^{3N}}{(2\sqrt{\pi})^{3N}} \frac{\exp[2\gamma(\beta/2)]}{\sqrt{\det[\boldsymbol{G}(\beta/2)]}} \Big[(\boldsymbol{q}_i(\beta/2)-\boldsymbol{q}_j(\beta/2))^2 \\ + \frac{1}{2}\mathrm{Tr}\big(\boldsymbol{G}_{ii}(\beta/2)+\boldsymbol{G}_{jj}(\beta/2)-\boldsymbol{G}_{ij}(\beta/2)-\boldsymbol{G}_{ji}(\beta/2)\big)\Big] - \left(\bar{d}_{ij}^{(\mathrm{TG})}\right)^2 . \quad (10.16)\end{aligned}$$

We are mainly interested in the quantum mechanical part of the variances, viz.

$$\bar{v}_{ij}^{(\mathrm{TG,qm})}(\beta) \approx \frac{1}{Z_{\mathrm{TG}}(\beta)} \int \frac{\mathrm{d}\boldsymbol{q}^{3N}}{(2\sqrt{\pi})^{3N}} \frac{\exp[2\gamma(\beta/2)]}{\sqrt{\det[\boldsymbol{G}(\beta/2)]}} \times \frac{1}{2}\mathrm{Tr}\big(\boldsymbol{G}_{ii}(\beta/2) + \boldsymbol{G}_{jj}(\beta/2) - \boldsymbol{G}_{ij}(\beta/2) - \boldsymbol{G}_{ji}(\beta/2)\big) \ . \quad (10.17)$$

# 10.2. Structural information about the $Ar_6$ cluster

## 10.2.1. Representation of the system

The main differences of $Ar_6$ to the argon trimer considered in chapter 9 is the number of atoms. The numerical representation of the system can be done in the same way. We use the Hamiltonian

$$H = -\frac{\hbar^2}{2}\sum_{i=1}^{N}\Delta_i + \sum_{j<i} V(|\boldsymbol{r}_i - \boldsymbol{r}_j|) \ , \quad (9.2)$$

where the pairwise interaction is given by a Morse potential (9.21) with the parameters given in table 9.1.

Also the artificial confinement required for the convergence of the position space integrals is done in the same way as for the trimer. According the procedure of section 9.2.1 all six particles are confined within a sphere around the centre of mass $\boldsymbol{R}_{\mathrm{cm}}$ by the condition $|\boldsymbol{q} - \boldsymbol{R}_{\mathrm{cm}}| < R_{\mathrm{c}}$, where $R_{\mathrm{c}}$ is the confining radius.

Of course, an additional potential influences the results and can crucially change the behaviour of the cluster [52, 62]. If only bound configurations are investigated $R_{\mathrm{c}}$ is usually chosen such that the bound configurations are not affected, i.e. $R_{\mathrm{c}}$ is larger than the extension of the bound cluster. However, we are interested also in the dissociation process, for which the choice of $R_{\mathrm{c}}$ is nontrivial as we have seen in chapter 9. A larger radius $R_{\mathrm{c}}$ always allows for a dissociation at lower temperatures. In principle it has to be adopted to the physical conditions as, e.g. the pressure. We are interested in the *qualitative behaviour* at the dissociation and checked carefully that our choice $R_{\mathrm{c}} = 35\,\text{Å}$ does not influence the *qualitative* change of the observables we are investigating, i.e. the mean energy, the specific heat, the mean values of the inter-atomic distances and their variances.

While in a thawed Gaussian calculation the initial condition for the width matrix is defined (cf. equation (9.12)) the constant matrix $\boldsymbol{\Gamma}$ has to be chosen carefully. It is a free parameter of the system and its actual choice has a critical impact on the quality of the results [69]. However, as has been mentioned above the structure (9.20) with the $3 \times 3$ submatrices (10.3) is reasonable and has proved to give excellent results in section 9.2.2. Thus, only the two parameters $D_1$ and $D_2$ need to be chosen. The parameter $D_2$ providing the lowest value for the mean energy in the zero temperature limit has shown to lead to the best agreement with numerically exact calculations and the more flexible

thawed Gaussian approximation. This result is almost independent of the temperature at which the partition function, mean energy or specific heat of all methods are compared. Thus, the simple minimisation of the frozen Gaussian approximation to the ground state energy gives us a reliable way of determining $D_2$. For the $Ar_6$ cluster in this chapter we found that $D_2 = 32\,\text{Å}^{-2}$ is the best choice. It is known from section 9.2.1 that $D_1 = 0.1\,\text{Å}^{-2}$ is a good description of the free centre of mass motion. This value will be used in this chapter. In agreement with chapter 9 we denote the two-parameter frozen Gaussian propagator 2P-FG, and its fully-coupled thawed Gaussian counterpart FC-TG.

## 10.2.2. Mean energy and specific heat

To compare the $Ar_6$ cluster with the trimer considered in chapter 9 we first look at the mean energy and the specific heat. They are shown in figure 10.1 for the two-parameter frozen Gaussian propagator and the derivatives of the classical partition function (9.23). The observations are very similar to those obtained in section 9.2.1. At very low temperatures the classical calculation tends to the potential minimum. At $T = 1\,\text{K}$ we find a mean energy of $E = -1216\,\text{cm}^{-1}$. The frozen Gaussian is at this temperature already in a very flat regime, in which the mean energy is almost independent of the temperature and approximates the quantum mechanical ground state energy. The method leads to $E \approx -1015\,\text{cm}^{-1}$. In the inset of figure 10.1 (a) we compare it with the more flexible fully-coupled thawed Gaussian propagator for which we get a value of $E \approx -1040\,\text{cm}^{-1}$, i.e. the difference is approximately only 2.4%. Thus, we may conclude that also for the larger $Ar_6$ cluster the quality of the frozen Gaussian propagator is comparable to that of the numerically more expensive thawed Gaussian variant even for the low-temperature limit in which, with the knowledge of chapter 9, it is known to lead to the worst results.

The dissociation appears, similarly to the argon trimer, in the mean energy as a step. The energy raises almost directly to that of six free particles. This indicates a dissociation of all atoms at once as we observed it for the trimer. The same information can be gained from the specific heat, which is shown around the dissociation in figure 10.1 (b). One broad peak indicates that the dissociation is occurring in one step. The classical calculation shows a transition at a slightly lower temperature, and the difference between the two maxima in the specific heat is approximately 0.5 K, which is lower as for the trimer, where we observed a difference of 1.5 K. Certainly the difference can again be related to the zero point energy in quantum mechanics. This is larger for six atoms than for three and one could expect that consequently also the temperature difference could be larger. However, one has to keep in mind that this energy also has to be distributed among a larger number of atoms during the dissociation.

Since aside from the small shift in the temperature the dissociation process is almost identical in the classical and the frozen Gaussian calculation we may, again, conclude that it is a purely classical phenomenon. The temperature at which it occurs is, of course, dependent on the choice of the confining sphere we made. As mentioned above

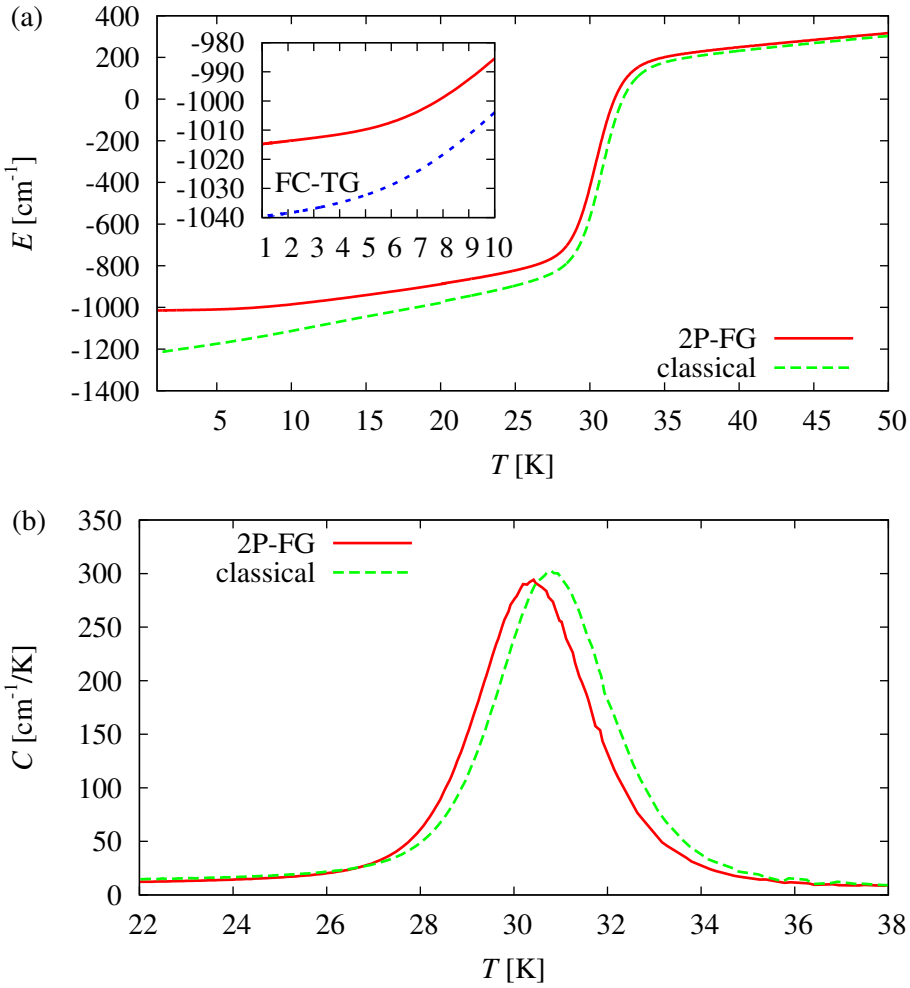


Figure 10.1.: (a) Mean energies of the $Ar_6$ cluster calculated with the two-parameter frozen Gaussian propagator (2P-FG) and its classical counterpart. For the high-temperature limit both results agree well. At low temperatures the classical mean energy tends to the potential minimum and the frozen Gaussian propagator approximates the quantum mechanical ground state. The inset shows a comparison of the 2P-FG method with the fully coupled thawed Gaussian method (FC-TG). The energies differ by a few percent. (b) Specific heat around the dissociation, which seems to happen in one step.

for a specific case one is interested in, one would have to translate the radius $R_c$ to a given situation with, e.g. a given pressure. We checked, however, that we are in a regime, in which the qualitative behaviour does not change and also the quantitative data, i.e. the temperature of the dissociation, depends only weakly on the radius. In particular, we assured that the case of a completely dissociated cluster is present for temperatures above 40 K.

### 10.2.3. Structural information for low temperatures and for the dissociation

In addition to the information of the simple derivatives of the partition function we now wish to study the mean distances. Since so far the dissociation seems to be purely classical it is interesting to also compare the structural information with the classical one. To do so, we add the classical mean distances

$$\bar{d}_{ij}^{(\text{classical})} = \frac{1}{Z_{\text{cl}}} \left( \frac{\mathrm{k}T}{2\pi\hbar^2} \right)^{3/2N} \int \mathrm{e}^{-\beta V(\boldsymbol{q})} |\boldsymbol{q}_i - \boldsymbol{q}_j| \, \mathrm{d}\boldsymbol{q}^{3N} \tag{10.18}$$

in the calculations below.

#### Structure at low temperatures

The mean distances we obtain for temperatures below 20 K, i.e. significantly below the dissociation process, are shown in figure 10.2, where we first compare the frozen Gaussian method 2P-FG with the classical calculation in figure 10.2 (a), and then add the fully-coupled thawed Gaussian approximation in figure 10.2 (b). The most striking observation is that the distances appear in the low-temperature limit in two groups. We have a group of three "long" distances of which the values are always above 5 Å for $T \to 0$ and a second group of the 12 remaining "short" distances which converge to a value below 4 Å. This already gives a clear answer to the question about the ground state configuration of $Ar_6$. It is consistent with the distances in an octahedron, or in other words, the atoms are located at the centres of the surfaces of its dual polyhedron, viz. the cube. For this we expect twelve short distances $d_s$ from the atoms on neighbouring surfaces and three longer distances $d_l$ between the atoms on opposite surfaces. The ratio of the distances is expected to be $d_l = \sqrt{2} d_s$, which we find to be fulfilled excellently in both the classical and semiclassical calculations.

The classical distances are in the limit $T \to 0$ always lower than the results of the two semiclassical approximations. This is not surprising. In the classical case the atoms seek directly the potential minima, whereas in the quantum case we always have a wave function with a finite width leading automatically to larger mean distances. We also find that in the classical case the fixed octahedron configuration is only observable for $T \to 0$. This is a consequence of the fact that classically every nonvanishing energy

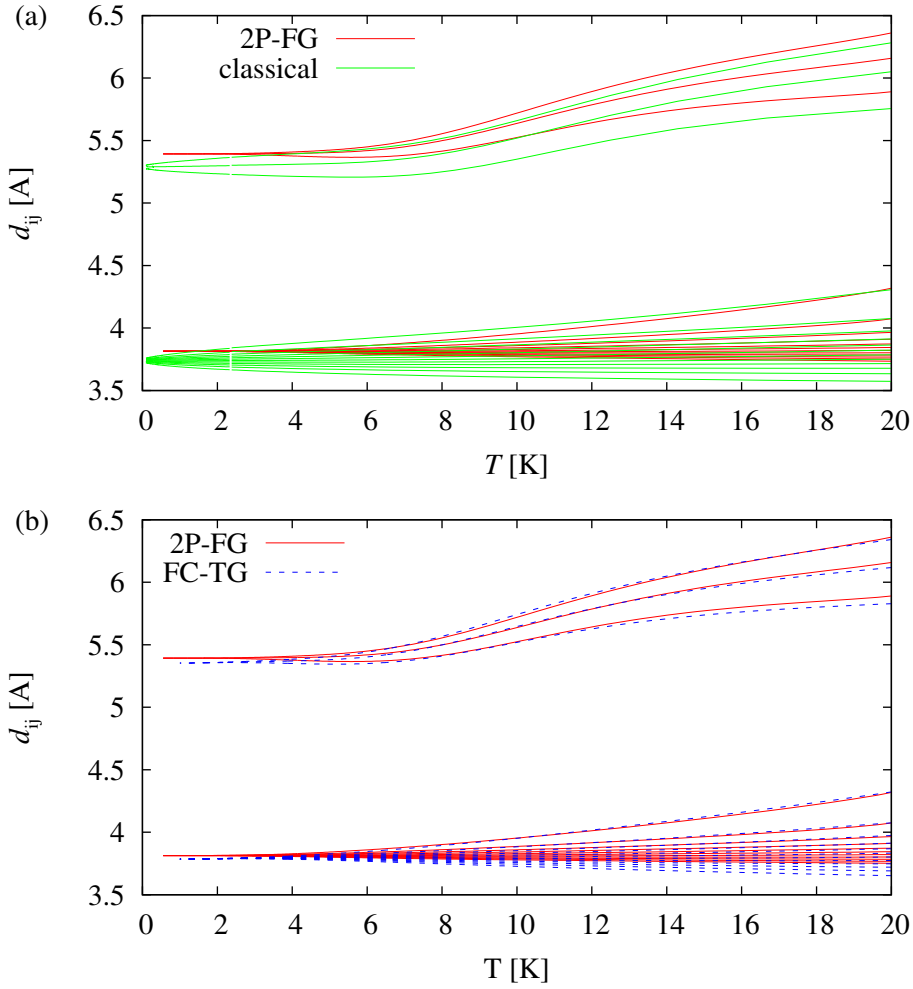


Figure 10.2.: (a) Comparison of the mean values of all 15 distances calculated with the frozen Gaussian method (2P-FG) and a classical calculation at temperatures $T \leq 20$. The distances appear in groups. Three distances converge for $T \to 0$ to values above 5 Å, wheres the remaining 12 are below 4 Å. (b) A comparison of the frozen Gaussian and thawed Gaussian method (FC-TG) shows that the mean distances agree very well.

allows for a thermal excitation. In contrast to this there should be no excitation possible if k$T$ is clearly below the energy difference between the ground state and the first excited state in the quantum mechanical case. This is also reflected in the mean distances. For temperatures below $T \approx 3\,\mathrm{K}$ we do not observe any differences between the distances in one group, and the distances do not change for even lower temperatures. This indicates that we are already in the ground state configuration.

A comparison of the frozen Gaussian method with the fully-coupled thawed Gaussian propagator reveals that the distances agree very well. This is in particular true for all larger distances. Also the low temperature limit shows an excellent agreement. The edge length of the cube containing the octahedron is $d_l = 5.39\,\text{Å}$ in the frozen Gaussian calculation and $d_l = 5.35\,\text{Å}$ in the thawed Gaussian approximation. The difference is below 1 %, and thus even smaller than that of the mean energy. Obviously the structural information of the frozen Gaussian method is less affected by the constant Gaussian width approximation.

With the data of figure 10.2 we are also able to estimate the quality of the approximation (10.8), in which we introduced the power series expansion of the distances. The first-order term we retained in the expansion is of the size

$$\frac{\mathrm{Tr}\left(\mathbf{\Gamma}_{ii}^{-1} + \mathbf{\Gamma}_{jj}^{-1} - \mathbf{\Gamma}_{ij}^{-1} - \mathbf{\Gamma}_{ji}^{-1}\right)}{6|\boldsymbol{q}_i - \boldsymbol{q}_j|}\,, \tag{10.19}$$

where for the width matrix (10.2) we obtain $\mathrm{Tr}\left(\mathbf{\Gamma}_{ii}^{-1} + \mathbf{\Gamma}_{jj}^{-1} - \mathbf{\Gamma}_{ij}^{-1} - \mathbf{\Gamma}_{ji}^{-1}\right)/6 = D_2^{-1} = (32\,\text{Å}^{-2})^{-1} = 0.031\,\text{Å}^2$. With the knowledge that the typical distances $|\boldsymbol{q}_i - \boldsymbol{q}_j|$ are even in the bound phase in the order of a few Ångströms we find that this correction is approximately of the size of less than 1 % of the leading order. Hence, it has at most the same size as the difference between the two semiclassical propagators. Higher orders in the series expansion (10.8) would lead to even smaller corrections, which do not need to be taken into account since they are below the quality of the semiclassical approxmation. Thus, we conclude that the numerically important reduction of the position space integrals does not influence the quality of the results for the distances.

### Dissociation to six free atoms

The distances around the dissociation are shown in figure 10.3, where the classical and 2P-FG results are compared. Since the frozen Gaussian approximation is known to provide good results at these temperatures (cf. chapter 9), a comparison with the thawed Gaussian propagator does not give any new information. Figure 10.3 confirms the finding of the consideration of the mean energy and the specific heat in figure 10.1. The dissociation effect is classical. The semiclassical approximation of the quantum mechanical propagator and the purely classical calculation lead to the same behaviour. Apart from a small shift in temperature both diagrams agree very well.

The calculation of the distances gives additional insight into the dissociation process. For temperatures $T \lessapprox 23\,\mathrm{K}$ the groups of short and long distances are unchanged. Above

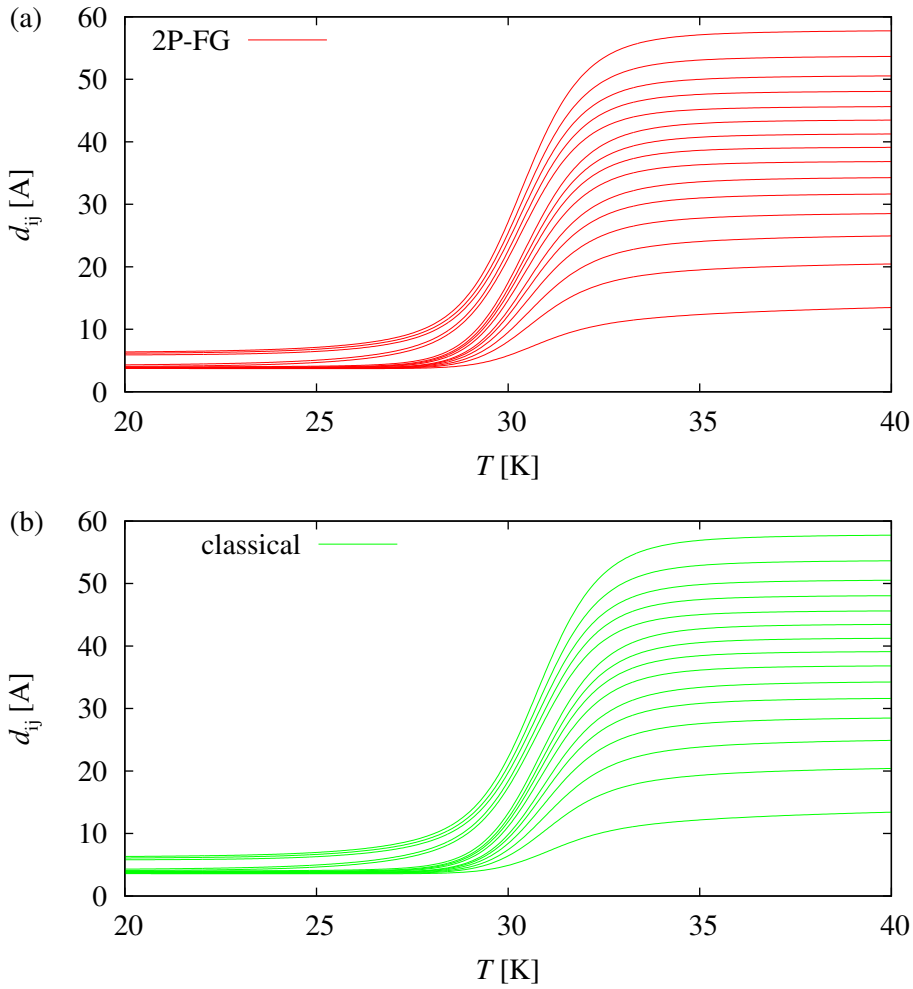


Figure 10.3.: (a) Mean values of all 15 distances calculated with the frozen Gaussian method (2P-FG) around the dissociation. Two of the smaller distances join the group of the three larger distances starting with $T \approx 23\,\mathrm{K}$, but then the dissociation occurs at once. (b) The same behaviour is observed for the classical calculation.

this temperature two of the twelve distances $d_s$ are separating from the others and join the three longer distances $d_l$. Two new groups with five and ten distances appear. This could correspond to the beginnings of a rearrangement of the atoms. However, it is questionable whether this is really the case. A new structure cannot arise since the whole process does not finish before all distances raise drastically and indicate with this increase the dissociation of the cluster. It is more likely that we observe the precursors of the total destruction of the cluster. The dissociation happens then at once as it was already found for the trimer in section 9.2.4. After the dissociation the distances obtain new almost constant values which correspond to the distribution of atoms moving freely within the confining sphere.

### Variances of the distances

In the previous sections we considered the mean values of the distances. To learn more about their actual distribution we show their standard deviations in figure 10.4 (a) for the classical and the 2P-FG method. The most significant feature is the drastic increase of the standard deviations around the transition. At this temperature range parts of the simulated clusters are still in a bound configuration whereas others are already dissociated. The effect is similar and of the same size for the classical and the semiclassical calculation. For temperatures above the dissociation the standard deviations are almost the same for all distances, which is also expected for six free atoms.

Of more interest is the behaviour of the standard deviations below the dissociation. The longer distances are expected to show more fluctuations. Additionally we observe that two of the shorter distances join the group of the three long distances for increasing temperatures. We can also expect that these two show higher standard deviations than the short distances since the the separation of the two distances does not happen abruptly at one temperature as can be seen in figure 10.3. Consequently we find that below the dissociation the standard deviations form two groups. One group combines the standard deviations of five distances, i.e. the three longer ones and the two joining them. The other group consists of the standard deviations of the 10 short distances which stay together up to the temperature of the dissociation.

In figure 10.4 (a) it seems that the standard deviations are always decreasing for lower temperatures. This is definitely expected for the classical calculation. The frozen Gaussian approxmation can, since the width of the wave function is determined by the constant values of $\mathbf{\Gamma}$, not reflect the quantum mechanical expectation that the wave function stretches at lower temperatures. To cover also this effect we plot in figure 10.4 (b) the quantum mechanical part according to equation (10.17) of the variances in the thawed Gaussian approximation. We show only the variance of one of the distances since this part is almost identical for all of them in the highly symmetric situation of a monoatomic cluster. At $T \approx 20\,\mathrm{K}$ the variance has approximately the same size as that following from the frozen Gaussian method $v_{ij}^{(\mathrm{FG,qm})} = \mathrm{Tr}\big(\mathbf{\Gamma}_{ii}^{-1} + \mathbf{\Gamma}_{jj}^{-1} - \mathbf{\Gamma}_{ij}^{-1} - \mathbf{\Gamma}_{ji}^{-1}\big)/2 =$

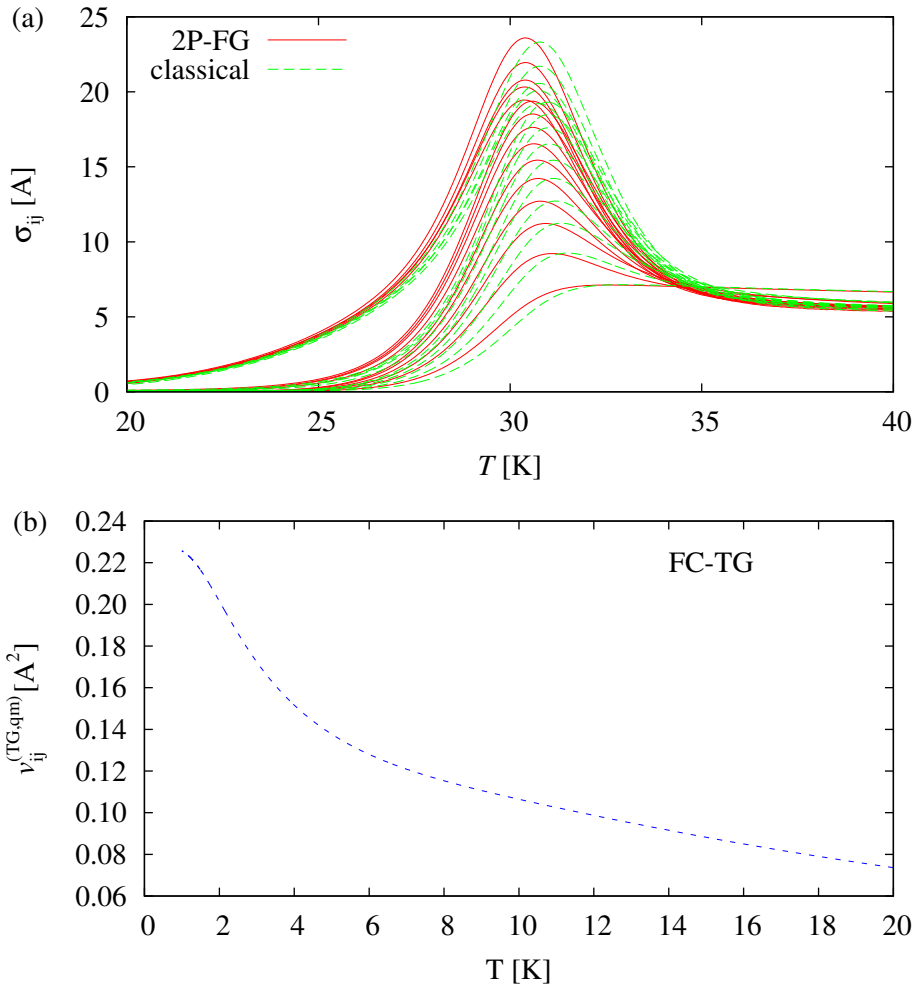


Figure 10.4.: (a) Standard deviations $\sigma_{ij}$ of the distances in the frozen Gaussian approximation (2P-FG) and of the classical calculation. They increase drastically around the dissociation. (b) Quantum mechanical part (10.17) of the variances for the fully coupled thawed Gaussian propagator. For low temperatures it increases due to an increasing width of the Gaussians.

$3D_2^{-2} = 0.093\,\text{Å}$. In particular, these quantum mechanical parts of the variances are considerably lower than other contributions in equations (10.13) and (10.16). Figure 10.4 (a) would not change with the thawed Gaussian propagator. Only for temperatures $T \lessapprox 10\,\text{K}$ the extension of the wave function becomes important for a measurement of the distances. For temperatures in the range of the dissociation the information from the frozen Gaussian method is completely sufficient.

## 10.3. Discussion

On the methodological side we were in this chapter able to show that structural information about a cluster of atoms can be obtained with the frozen Gaussian semiclassical method. The evaluation of the corresponding integrals can be done in parallel to the evaluation of the partition function, and thus is numerically cheap. Nevertheless the full information about all the distances of all combinations of the atoms can be obtained. A comparison with the more flexible thawed Gaussian propagator revealed that the quality of the distances is on the same level as that of the mean energy or the specific heat, or even better. To avoid inefficient numerical computations of a position space integral an approximation for the distances has been introduced. It was possible, however, to show that this approximation does not reduce the quality of the results below that obtained in the semiclassical approximation of the propagator.

On the physical side we found that with increasing temperatures the $Ar_6$ cluster undergoes a direct transition to six free atoms around $T \approx 31\,\text{K}$. However, it shows precursors in the distances. At temperatures slightly below the dissociation a reordering of the atoms seems to start, but then vanishes in the increasing distances at the dissociation. The dissociation is a purely classical effect. The semiclassical approximation shows exactly the same behaviour with just a small shift in the temperature of 0.5 K. Around the dissociation the standard deviations of the distances are almost only determined by classical effects. Only for lower temperatures the extension of the wave functions becomes important as has been seen in a thawed Gaussian approximation.

At low temperatures the cluster assumes the shape of an octahedron, where the longer distance of the atoms is $d_l = 5.4\,\text{Å}$, and the shorter has the value $d_s = d_l/\sqrt{2} = 3.8\,\text{Å}$. Classically the fixed configuration is only obtained in the limit $T \to 0$ whereas in the quantum mechanical case the ground state configuration is present for all temperatures $T \lessapprox 3\,\text{K}$.

# 11. First-order corrections to the frozen Gaussian imaginary time propagator

In the last chapters we have seen that the imaginary time or Boltzmann operator belongs to the important quantities needed for understanding the equilibrium properties of multi-dimensional systems at finite temperatures. The derivatives of its trace give access to basic thermodynamic quantities as the mean energy and specific heat, which allow for the investigation of thermodynamic properties of atomic clusters. Since for systems with many degrees of freedom it is a challenge to evaluate the Boltzmann operator we have introduced a numerically much cheaper frozen Gaussian approximation, which shows qualitatively good results.

Despite the large success and broad applicability of Gaussian methods for the evaluation of the mean energy and the specific heat of clusters one has to keep in mind that they are semiclassical approximations. As pointed out by Liu and Miller [67] they are not expected to be accurate at very low temperatures where quantum effects are large. In the simplest case one observes a shift of the ground state energy away from the exact result as we have seen in chapter 9. The low-temperature range is, however, very often the most important and crucial for the thermodynamic properties of rare gas cluster. For example, Gaussian based computations on clusters of light atoms, e.g. $Ne_{13}$ and $Ne_{38}$ [54, 56], predict novel low temperature quantum effects such as liquid-like zero temperature structures of $Ne_{38}$ as compared to a solid-like structure predicted from classical mechanics [61]. These predictions are based on the Gaussian approximation [53, 56, 67, 170, 171] and have to be verified. It is the purpose of this chapter to introduce a possibility to systematically improve the semiclassical approximation.

A systematic approach connecting the Gaussian semiclassical initial value approximations with exact quantum mechanics is the generalised time-dependent perturbation approach developed by Pollak and coworkers [68, 69]. Within this framework the Gaussian approximations can be considered as a lowest-order approximation of a series converging to the exact quantum Boltzmann operator. It has been shown that both the thawed and frozen Gaussian versions of this series converge rapidly to the numerically exact answer for a one-dimensional double well potential [69, 172]. In this chapter we want to demonstrate that the corrections to the Gaussian imaginary time propagator are also practically applicable to higher-dimensional systems, in particular to atomic clusters. To

do so, we apply the frozen Gaussian series to the partition function of the argon trimer and calculate its first-order correction. We show that the correction helps to estimate the quality of the results and provides objective access to the validity of the Gaussian approximations. With the first-order terms it is possible to identify a border temperature below which the Gaussian results become questionable. This result clearly states that the dissociation process [57] discussed in chapter 9 with Gaussian approximations is correctly described by the frozen Gaussian imaginary time propagator since it appears in the allowed temperature range.

In section 11.1 we introduce the first-order correction to the partition function for clusters of atoms. The theory is then applied to the system studied already in chapter 9, viz. the argon trimer, in section 11.2. We introduce the system (section 11.2.1), show how the first-order correction term may be used to determine the best width parameter (section 11.2.2), consider the influence of an artificial confinement on the correction (section 11.2.3) and present the first-order corrected mean energy and specific heat for the dissociation process of the cluster (section 11.2.4), which allow for a clear statement on the quality of the Gaussian approximation. The required numerical effort is analysed in section 11.3. Finally we discuss the main significance of the first-order correction in section 11.4.

This chapter is based on reference [182], in which the findings presented here were published.

## 11.1. Frozen Gaussian approximation to the partition function and first-order corrections

### 11.1.1. Frozen Gaussian series representation

Zhang et al. [69] proposed a frozen Gaussian form of the imaginary time propagator $K(\beta) = \exp(-\beta H)$ at inverse temperature $\beta = 1/(\mathrm{k}T)$ and developed its higher-order corrections in the framework of the generalised time-dependent perturbation series [68, 179, 180]. The zeroth order of this series corresponds to the frozen Gaussian propagator introduced in section 9.1.3. The frozen Gaussian coherent state has the form (9.13), which leads to the matrix elements (9.14) of the imaginary time propagator. In this formalism there is only one dynamical variable, viz. the position of the centre of the Gaussian, which follows the equation of motion (9.16).

Since the Bloch equation

$$-\frac{\partial}{\partial\tau}|\boldsymbol{q}_0,\tau\rangle = H|\boldsymbol{q}_0,\tau\rangle \tag{9.7}$$

is not solved exactly by the propagator (9.14), one can define the correction operator [68]

$$C(\tau) = -\frac{\partial}{\partial\tau}K_0(\tau) - HK_0(\tau)\ . \tag{11.1}$$

The formal solution of equation (11.1) is

$$K_0(\tau) = K(\tau) - \int_0^\tau \mathrm{d}\tau' K(\tau - \tau') C(\tau') \; . \tag{11.2}$$

With the assumption that the exact propagator $K(\tau)$ can be expressed in terms of a series

$$K(\tau) = \sum_{n=0}^{\infty} K_j(\tau) \; , \tag{11.3}$$

where $K_j(\tau) \sim C(\tau)^j$ are terms with ascending power in the small correction, one can write down the recursion relation

$$K_{j+1}(\tau) = \int_0^\tau \mathrm{d}\tau' K_j(\tau - \tau') C(\tau') \tag{11.4}$$

for the calculation of higher-order terms.

### 11.1.2. First-order corrections to the partition function

In the framework of the series expansion the lowest-order approximation to the quantum partition function is simply the trace of the zeroth-order propagator [69], which has been written down in section 9.1.3:

$$Z_{\mathrm{FG}}(\tau) = \mathrm{Tr}\left[K_{\mathrm{FG}}(\tau)\right] = \sqrt{\det(\mathbf{\Gamma})} \exp\left(-\frac{\hbar^2}{4}\mathrm{Tr}(\mathbf{\Gamma})\tau\right) \sqrt{\det\left(\left[\mathbf{1} - \exp(-\hbar^2\mathbf{\Gamma}\tau)\right]^{-1}\right)} \\ \times \int_{-\infty}^{\infty} \frac{\mathrm{d}\boldsymbol{q}^{3N}}{(2\pi)^{N/2}} \exp\left(-2\int_0^{\tau/2} \mathrm{d}\tau \langle V(\boldsymbol{q}(\tau))\rangle\right) \; . \tag{9.15}$$

Its first-order corrected counterpart

$$Z_1(\beta) = Z_0(\beta) + Z_{\mathrm{C1}}(\beta) \tag{11.5a}$$

is obtained in a similar way. The correction term for the partition function can be combined as

$$Z_{\mathrm{C1}}(\beta) = \mathrm{Tr}\left[K_1(\beta)\right] = \int_0^\beta \mathrm{d}\tau \int \mathrm{d}\boldsymbol{x}'^{3N} \int \mathrm{d}\boldsymbol{x}^{3N} \langle \boldsymbol{x}'|K_0(\beta - \tau)|\boldsymbol{x}\rangle \langle \boldsymbol{x}|C(\tau)|\boldsymbol{x}'\rangle \tag{11.5b}$$

after the explicit representation of the correction operator (11.1) has been evaluated. The frozen Gaussian imaginary time propagator can be written as [69]

$$\langle \boldsymbol{x}'|C(\tau)|\boldsymbol{x}\rangle = \langle \boldsymbol{x}'|\left(-\frac{\partial}{\partial\beta} - H\right)K_0(\tau)|\boldsymbol{x}\rangle = \det(\boldsymbol{\Gamma})\exp\left(-\frac{\hbar^2}{4}\mathrm{Tr}(\boldsymbol{\Gamma})\tau\right)$$
$$\times\sqrt{\det\left(2\left[\mathbf{1}-\exp(-\hbar^2\boldsymbol{\Gamma}\tau)\right]^{-1}\right)}\exp\left(-\frac{1}{4}[\boldsymbol{x}'-\boldsymbol{x}]^{\mathrm{T}}\boldsymbol{\Gamma}[\tanh(\hbar^2\boldsymbol{\Gamma}\tau/2)]^{-1}[\boldsymbol{x}'-\boldsymbol{x}]\right)$$
$$\times\int\frac{\mathrm{d}\boldsymbol{q}^{3N}}{(2\pi)^{3N}}\Delta V(\boldsymbol{x}',\boldsymbol{x},\boldsymbol{q}(\tau/2))\exp\left(-2\int_0^{\tau/2}\mathrm{d}\tau'\langle V(\boldsymbol{q}(\tau'))\rangle\right.$$
$$\left.-[\bar{\boldsymbol{x}}-\boldsymbol{q}(\tau/2)]^{\mathrm{T}}\boldsymbol{\Gamma}[\bar{\boldsymbol{x}}-\boldsymbol{q}(\tau/2)]\right), \quad (11.6a)$$

where the energy difference operator is found to be

$$\Delta V(\boldsymbol{x}',\boldsymbol{x},\boldsymbol{q}(\tau/2)) = \frac{\hbar^2}{4}\left(-\mathrm{Tr}(\boldsymbol{\Gamma})+[\boldsymbol{x}'-\boldsymbol{x}]^{\mathrm{T}}\frac{\boldsymbol{\Gamma}^2}{2}[\boldsymbol{x}'-\boldsymbol{x}]\right)+\langle V(\boldsymbol{q}(\tau/2))\rangle$$
$$+\frac{\hbar^2}{2}\left([\bar{\boldsymbol{x}}-\boldsymbol{q}(\tau/2)]^{\mathrm{T}}\boldsymbol{\Gamma}^2[\bar{\boldsymbol{x}}-\boldsymbol{q}(\tau/2)]+[\boldsymbol{x}'-\boldsymbol{x}]^{\mathrm{T}}\boldsymbol{\Gamma}\coth\left(\frac{\hbar^2\tau}{2}\boldsymbol{\Gamma}\right)\boldsymbol{\Gamma}[\bar{\boldsymbol{x}}-\boldsymbol{q}(\tau/2)]\right)$$
$$+[\bar{\boldsymbol{x}}-\boldsymbol{q}(\tau/2)]\cdot\langle\nabla V(\boldsymbol{q}(\tau/2))\rangle - V(\boldsymbol{x}'), \quad (11.6b)$$

and again $\bar{\boldsymbol{x}} = (\boldsymbol{x}'+\boldsymbol{x})/2$.

Since most parts of the propagator (9.14) and of the correction operator (11.6a) include only simple Gaussians or polynomials in $\boldsymbol{x}$ and $\boldsymbol{x}'$ the matrix element of the product of the zeroth-order propagator and the correction operator needed for the computation of the first-order correction term may be calculated analytically. Only the parts including the potential require in general a numerical computation. However, assuming a Gaussian form (9.5) for the potential enables one to calculate this part analytically as well. That is, all $\boldsymbol{x}'$ and $\boldsymbol{x}$ integrations can be performed analytically, and only the $\boldsymbol{q}$ and $\tau$ integrations remain for the numerical evaluation.

After evaluating the $\boldsymbol{x}'$ and $\boldsymbol{x}$ integrations in equation (11.5b) we can finally write the first-order correction as

$$Z_{\mathrm{C1}}(\beta) = \frac{\det(\boldsymbol{\Gamma})^2}{(2\pi)^N}\exp\left(-\frac{\hbar^2}{4}\mathrm{Tr}(\boldsymbol{\Gamma})\beta\right)\int_0^\beta\mathrm{d}\tau\sqrt{\det\left([\mathbf{1}-\exp(-\hbar^2\boldsymbol{\Gamma}(\beta-\tau))]^{-1}\right)}$$
$$\times\sqrt{\det\left([\mathbf{1}-\exp(-\hbar^2\boldsymbol{\Gamma}\tau)]^{-1}\right)}\int\mathrm{d}\boldsymbol{q}_1^{3N}\int\mathrm{d}\boldsymbol{q}_2^{3N}\Delta V_{\mathrm{S}}(\boldsymbol{q}_1,\boldsymbol{q}_2,\beta,\tau)$$
$$\times\exp\left(-2\int_0^{(\beta-\tau)/2}\mathrm{d}\tau'\langle V(\boldsymbol{q}_1(\tau'))\rangle\right)\exp\left(-2\int_0^{\beta/2}\mathrm{d}\tau'\langle V(\boldsymbol{q}_2(\tau'))\rangle\right), \quad (11.7)$$

where the single trajectory contribution to the energy difference operator is denoted as

$$\Delta V_{\mathrm{S}}(\boldsymbol{q}_1,\boldsymbol{q}_2,\beta,\tau) = \exp\left(-\frac{1}{2}\Delta\boldsymbol{q}(\beta,\tau)^{\mathrm{T}}\boldsymbol{\Gamma}\Delta\boldsymbol{q}(\beta,\tau)\right)\left\{\frac{1}{\sqrt{\det(\boldsymbol{B}(\beta,\tau))\det(2\boldsymbol{\Gamma})}}\right.$$
$$\times\left[\frac{\hbar^2}{4}\left(-\frac{1}{2}\mathrm{Tr}(\boldsymbol{\Gamma})+\frac{1}{4}\mathrm{Tr}(\boldsymbol{B}(\beta,\tau)^{-1}\boldsymbol{\Gamma}^2)+\frac{1}{2}\Delta\boldsymbol{q}(\beta,\tau)^{\mathrm{T}}\boldsymbol{\Gamma}^2\Delta\boldsymbol{q}(\beta,\tau)\right)\right.$$
$$\left.\left.+\langle V(\boldsymbol{q}_2(\tau/2))\rangle+\frac{1}{2}\Delta\boldsymbol{q}(\beta,\tau)^{\mathrm{T}}\langle\nabla V(\boldsymbol{q}_2(\tau/2))\rangle\right]-V_{\mathrm{SG}}(\bar{\boldsymbol{q}},\beta,\tau)\right\}, \quad (11.8)$$

the difference trajectory is defined as

$$\Delta\boldsymbol{q}(\beta,\tau) = \boldsymbol{q}_1((\beta-\tau)/2)-\boldsymbol{q}_2(\tau/2)\,, \quad (11.9a)$$

and the middle point is

$$\bar{\boldsymbol{q}}(\beta,\tau) = \frac{1}{2}(\boldsymbol{q}_1((\beta-\tau)/2)+\boldsymbol{q}_2(\tau/2))\,. \quad (11.9b)$$

The integrated potential $V_{\mathrm{SG}}(\bar{\boldsymbol{q}},\beta,\tau)$ can be written in a form similar to the Gaussian average of the Gaussian fitted potential (9.5), which was introduced by Frantsuzov et al. [53] for a fully-correlated multi-dimensional Gaussian propagator. It consists of a sum of Gaussians,

$$V_{\mathrm{SG}}(\bar{\boldsymbol{q}},\beta,\tau) = \sqrt{\frac{\det(\boldsymbol{C}(\beta,\tau))}{\det(\boldsymbol{B}(\beta,\tau)+\boldsymbol{\Gamma}/2)}}\sum_{j<i}\sum_{p}c_p\sqrt{\frac{\det(\boldsymbol{D}_{ij}(\beta,\tau))}{\det(\boldsymbol{D}_{ij}(\beta,\tau)+\alpha_p)}}$$
$$\times\exp\left(-\left[\bar{\boldsymbol{q}}_i(\beta,\tau)-\bar{\boldsymbol{q}}_j(\beta,\tau)\right]^{\mathrm{T}}\boldsymbol{F}_{ij}^{(p)}(\beta,\tau)\left[\bar{\boldsymbol{q}}_i(\beta,\tau)-\bar{\boldsymbol{q}}_j(\beta,\tau)\right]\right)\,, \quad (11.10)$$

with the matrices

$$\boldsymbol{B}(\beta,\tau) = \frac{1}{4}\boldsymbol{\Gamma}\left[\tanh(\hbar^2\boldsymbol{\Gamma}(\beta-\tau)/2)^{-1}+\tanh(\hbar^2\boldsymbol{\Gamma}\tau/2)^{-1}\right] \quad (11.11a)$$

and

$$\boldsymbol{C}(\beta,\tau) = \frac{1}{2}\left(\boldsymbol{B}(\beta,\tau)+\frac{\boldsymbol{\Gamma}}{2}\right)\left[\boldsymbol{B}(\beta,\tau)\boldsymbol{\Gamma}\right]^{-1}\,. \quad (11.11b)$$

The submatrices $\boldsymbol{C}_{ij}(\beta,\tau)$ for the particles $i$ and $j$ of $\boldsymbol{C}(\beta,\tau)$ are required for

$$\boldsymbol{D}_{ij}(\beta,\tau) = \left(\boldsymbol{C}_{ii}(\beta,\tau)+\boldsymbol{C}_{jj}(\beta,\tau)-\boldsymbol{C}_{ij}(\beta,\tau)-\boldsymbol{C}_{ji}(\beta,\tau)\right)^{-1} \quad (11.12a)$$

and

$$\boldsymbol{F}_{i,j}^{(p)}(\beta,\tau) = \alpha_p-\alpha_p^2\left(\alpha_p+\boldsymbol{D}_{ij}(\beta,\tau)\right)^{-1}\,. \quad (11.12b)$$

Note that the first-order correction term (11.5b) is not symmetric. Here we use the "left" correction operator defined by Zhang et al. [69]. This has, however, no influence on the partition function due to the trace in equation (11.5b).

## 11.2. First-order calculations for the argon trimer

### 11.2.1. Potential and confinement

To be consistent with chapter 9 we model the pairwise interaction of the argon atoms by the Morse potential (9.21) with the same parameters as introduced in section 9.2.1. Since the Gaussian averaged quantities according to equation (9.3) and the $\boldsymbol{x}'$ and $\boldsymbol{x}$ integrations in the first-order correction term (11.5b) can be performed analytically if the potential can be expressed in terms of Gaussians, we use again the fit (9.5) with the parameters listed in table 9.1. Thus, similar to the zeroth-order case of chapters 9 and 10 there are only two integrations, which have to be done numerically, viz. the integration in the $\boldsymbol{q}$ space and the imaginary time integration in equation (11.5b). It is the latter one which is added due to the correction. It is one-dimensional and can be performed with a standard integrator. The multi-dimensional Monte Carlo sampling in the $\boldsymbol{q}$ variables is done with a standard Metropolis algorithm as outlined in reference [53].

To converge the integrals the $\boldsymbol{q}$ space is restricted by the condition $|\boldsymbol{q} - \boldsymbol{R}_{\mathrm{cm}}| < R_{\mathrm{c}}$, where $R_{\mathrm{c}}$ is a confining radius and $\boldsymbol{R}_{\mathrm{cm}}$ is the centre of mass of the cluster. This necessary procedure was outlined in section 9.2.1. As has been shown in section 9.2.3 the value of $R_{\mathrm{c}}$ has a critical influence on the thermodynamic properties. For the first-order correction term (11.5b) two $\boldsymbol{q}$ integrations, viz. in the propagator and in the correction operator, have to be taken into account. Here, the restriction on $\boldsymbol{q}$ is applied for the propagator part (9.14). Due to the coupling via $\boldsymbol{x}'$ and $\boldsymbol{x}$ in equation (11.6a) the restriction automatically affects also the $\boldsymbol{q}$ variable in the correction operator.

For the first-order study in this chapter we concentrate on a confinement of $R_{\mathrm{c}} = 10\,\text{Å}$. It is known from section 9.2.3 that this confinement does not describe the dissociation process fully since it is too restrictive. However, the restricted cluster shows a very broad transition from the bounded system to three free particles, and thus allows for a clear analysis of the correction term's influence on the results around the dissociation, which is the interesting physical effect.

### 11.2.2. Choice of the width parameter

In the frozen Gaussian ansatz the matrix of width parameters $\boldsymbol{\Gamma}$ is constant in imaginary time $\tau$, however, the choice of $\boldsymbol{\Gamma}$ has a critical influence on the quality of the results [69]. In chapter 9 we found that the width matrix

$$\boldsymbol{\Gamma} = \begin{pmatrix} (\boldsymbol{D}_1 + 2\boldsymbol{D}_2)/3 & (\boldsymbol{D}_1 - \boldsymbol{D}_2)/3 & (\boldsymbol{D}_1 - \boldsymbol{D}_2)/3 \\ (\boldsymbol{D}_1 - \boldsymbol{D}_2)/3 & (\boldsymbol{D}_1 + 2\boldsymbol{D}_2)/3 & (\boldsymbol{D}_1 - \boldsymbol{D}_2)/3 \\ (\boldsymbol{D}_1 - \boldsymbol{D}_2)/3 & (\boldsymbol{D}_1 - \boldsymbol{D}_2)/3 & (\boldsymbol{D}_1 + 2\boldsymbol{D}_2)/3 \end{pmatrix} \tag{9.20}$$

with two $3\times3$-submatrices $\boldsymbol{D}_1 = D_1\mathbf{1}$ and $\boldsymbol{D}_2 = D_2\mathbf{1}$, where $\mathbf{1}$ is the $3\times3$ identity matrix, provides results competitive with thawed Gaussian calculations using a single-particle

ansatz. The parameter $D_1$ represents the free centre of mass motion and should be chosen as small as possible. The Gaussian width for the relative coordinates is represented by $D_2$. In section 9.2.1 an optimum value of $D_2 = 25\,\text{Å}^{-2}$ was found. It yields the best approximation to a numerically exact path integral Monte Carlo calculation [57] and thawed Gaussian approximations. It was also found that all choices of $D_1$ below a certain value lead to the same mean energies and that $D_1 = 0.1\,\text{Å}^{-2}$ belongs to this range in which $D_1$ is small enough. These parameters also provide the best and lowest approximation to the ground state energy. Thus, the minimum of the ground state energy could also be used to search for the optimum value of the width parameters. It provides, however, no access to the quality of the results if the exact ground state energy is unknown.

A systematic, objective and internally consistent approach to the determination of the optimum width parameter is made possible by considering the first-order correction. The definition of the correction operator in equation (11.1) makes clear that it measures the deviation of the zeroth-order term from the exact result. One should thus minimise the ratio of the first-order [equation (11.5b)] and zeroth-order [equation (9.15)] contributions to the partition function by varying the width parameter matrix to find the optimum value.

In figure 11.1 (a) we plot the ratio $Z_{\text{C1}}/Z_0$ for several values of the parameters $D_2$ and $D_1 = 0.1\,\text{Å}^{-2}$. The data was calculated for a cluster with a confinement of $R_\text{c} = 10\,\text{Å}$. The zeroth- and first-order mean energies in figure 11.1 (b) visualise the transition from a bounded to an unbounded cluster. For temperatures at which the system is bounded, i.e. $T \lessapprox 30\,\text{K}$ an optimum range for the width parameter at which the contribution of the correction term $Z_{\text{C1}}$ is minimal can be found. Below the transition temperature the lines for $D_2$ between $20\,\text{Å}^{-2}$ and $30\,\text{Å}^{-2}$ are close to each other, the smallest value is found for $D_2 = 25\,\text{Å}^{-2}$. This confirms our previous zeroth-order study of the argon trimer in chapter 9, where the same value of $D_2 = 25\,\text{Å}^{-2}$ provided the best agreement with numerically exact path integral Monte Carlo methods. At higher temperatures, where the cluster passes through a transition to three almost free atoms, the situation changes. The ratio becomes smaller as the magnitude of $D_2$ decreases. In the limit of three free particles, the frozen Gaussian approximation is exact, in the limit that the width matrix vanishes. One thus expects that in this limit, the smaller values of the width parameters would provide a better approximation.

### 11.2.3. Influence of the confining sphere

As already mentioned, for free particles, the frozen Gaussian propagator yields the exact partition function in the limit $\mathbf{\Gamma} \to \mathbf{0}$. Thus, one expects that the free centre of mass motion, described by $D_1$, demands $D_1$ to be as small as possible. In practice one observes, however, that $D_1$ shows a minimum correction at a finite value. This is a result of the confinement of the atoms, which has the same effect as adding a confining potential

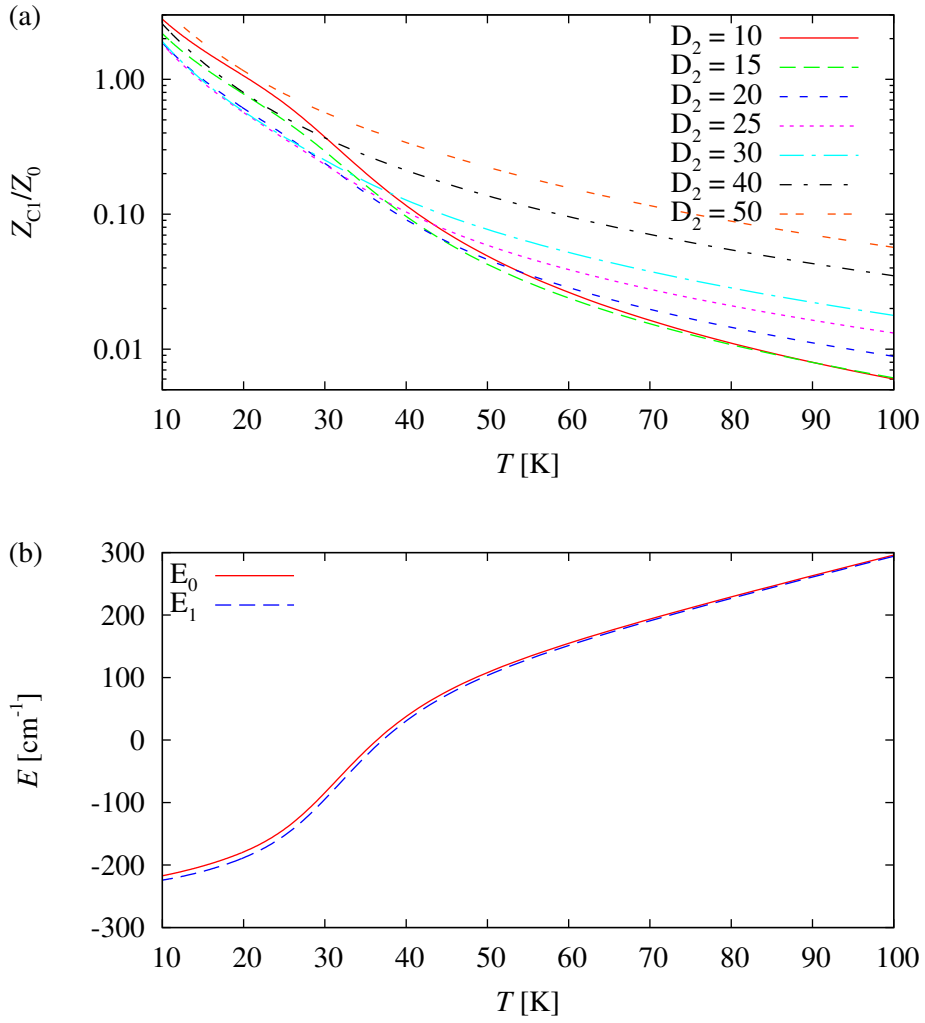


Figure 11.1.: (a) The ratio of the contribution of the first- and zeroth-order terms in the series expansion of the partition function is plotted as a function of the temperature $T$ for varying values of the width parameter $D_2$ (given in units of $\text{Å}^{-2}$) and $D_1 = 0.1\,\text{Å}^{-2}$. For the bounded system ($T \lessapprox 30\,\text{K}$) the range $D_2 = 20 \ldots 30\,\text{Å}^{-2}$ leads to the minimal ratio whereas for temperatures above the transition temperature smaller values of $D_2$ lead to smaller relative corrections. (b) The zeroth-order approximation to the mean energy $E_0$ and its first-order corrected counterpart $E_1$ is shown to visualise the transition from the bounded to the unbounded system for $D_1 = 0.1\,\text{Å}^{-2}$ and $D_2 = 25\,\text{Å}^{-2}$.

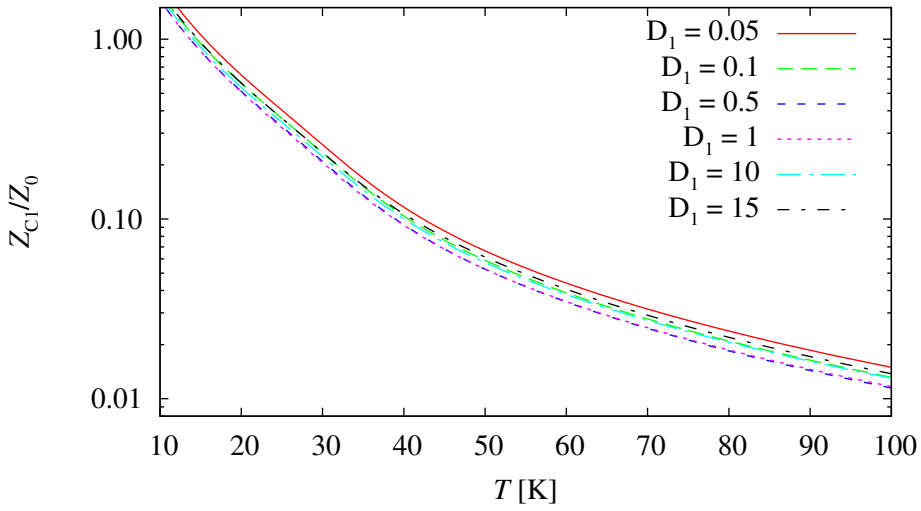


Figure 11.2.: The ratio of the contribution of the first- and zeroth-order terms in the series expansion of the partition function is plotted as a function of the temperature $T$ for varying values of the width parameter $D_1$ (given in units of $\text{Å}^{-2}$) and $D_2 = 25\,\text{Å}^{-2}$. The minimal ratio is found in the range $D_1 = 0.5 \ldots 1\,\text{Å}^{-2}$. The cluster is limited by a confinement with $R_c = 10\,\text{Å}$.

(9.22), i.e. the particles are not really free. The effect can be observed in figure 11.2, where the ratio $Z_{C1}/Z_0$ is plotted for several choices of $D_1$ and $D_2 = 25\,\text{Å}^{-2}$. As can be seen the minimum correction is achieved for the finite values $D_1 = 0.5 \ldots 1\,\text{Å}^{-2}$ if a confinement of $R_c = 10\,\text{Å}$ is used.

The influence of the confinement can also be found in the study of the width parameter $D_2$ for the internal degrees of freedom. For high temperatures, i.e. in the limit of three free particles a smaller value of $D_2$ should provide a better approximation. Thus, one expects always a smaller contribution $Z_{C1}$ for smaller values of $D_2$. However, the strengths of the first-order corrections for $D_2 = 10\,\text{Å}^{-2}$ and $D_2 = 15\,\text{Å}^{-2}$ are almost the same in the high-temperature limit, even beyond the temperatures shown in figure 11.2.

### 11.2.4. Correction at low temperatures and the first-order corrected mean energy

Figures 11.1 (a) and 11.2 already indicate that the correction term increases in importance as the temperature is lowered. This is not surprising since an imaginary time propagation is performed approximately and the difference between the approximate and exact solutions is expected to increase with (imaginary) time. The behaviour be-

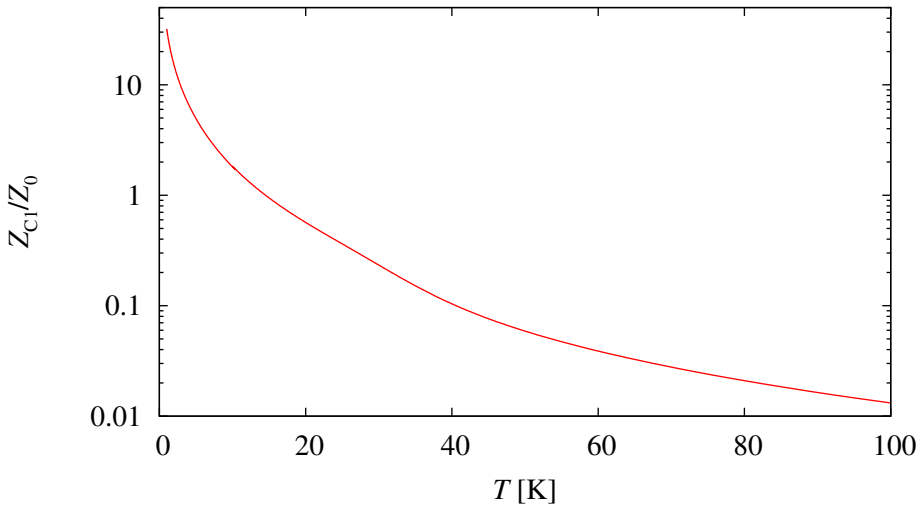


Figure 11.3.: Relative strength of the first-order correction to the partition function at lower temperatures for $R_c = 10\,\text{Å}$, $D_1 = 0.1\,\text{Å}^{-2}$, and $D_2 = 25\,\text{Å}^{-2}$. It diverges in the limit $T \to 0$.

comes even clearer in figure 11.3, where the relative strength of the first-order correction $Z_{C1}/Z_0$ is plotted for the argon trimer with a confinement $R_c = 10\,\text{Å}$ and width parameters $D_1 = 0.1\,\text{Å}^{-2}$, $D_2 = 25\,\text{Å}^{-2}$ down to a temperature of $T = 1\,\text{K}$. It increases drastically and shows a diverging behaviour in the limit $T \to 0$, i.e. $\beta \to \infty$. The increasing importance of the first-order correction term at low temperatures is consistent with our previous zeroth-order study of the system in chapter 9, where we found that the accuracy of the frozen Gaussian approximation gets worse as $T \to 0$ and the cluster approaches the ground state. At low temperatures, quantum effects are strong and, in particular, the Gaussian (zeroth-order) approximations cannot reproduce the exact ground state energy $E_{GS}$ of the cluster. The Gaussian form imposed on the wave function is too severe and the ground state energy obtained from the zeroth-order approximation is found to be slightly higher than the exact ground state energy ($E_0 = E_{GS} + \Delta E$ and $\Delta E > 0$).

To further understand the divergence of the first-order term, we may assume that for large $\beta$ only the ground state contributes to the partition function and that the exact partition function $Z$ and its zeroth-order approximated counterpart $Z_0$ behave as

$$Z \approx \mathrm{e}^{-\beta E_{GS}}, \qquad Z_0 \approx \mathrm{e}^{-\beta(E_{GS}+\Delta E)}\,. \tag{11.13}$$

Thus, a first-order correction which is valid also for large $\beta$ would be expected to diverge, since $Z/Z_0 \approx \mathrm{e}^{\beta\Delta E}$.

More interesting is, however, the influence of the first-order correction on the deriva-

tives of the partition function, which are required for the physically meaningful average energy

$$E = \mathrm{k}T^2 \frac{\partial \ln Z}{\partial T} \tag{11.14a}$$

and specific heat

$$C = \frac{\partial E}{\partial T} \,. \tag{11.14b}$$

Figure 11.4 shows the temperature dependence of the mean energy and specific heat of the argon trimer for $R_\mathrm{c} = 10\,\text{Å}$, $D_1 = 0.1\,\text{Å}^{-2}$, and $D_2 = 25\,\text{Å}^{-2}$, i.e. the same parameters as in figure 11.3. The frozen Gaussian results for the zeroth- and first-order approximations are compared with a fully-coupled thawed Gaussian approximation which, as discussed in chapter 9 is expected to be more accurate than the frozen Gaussian approximation. As one can see in figure 11.4 (a) the first-order correction for the frozen Gaussian approximation brings the resulting estimate closer to the fully-coupled thawed Gaussian estimate over most of the temperature range studied. However, for temperatures $T \lessapprox 12\,\text{K}$ the first-order correction to the energy becomes smaller and vanishes in the limit $T \to 0$. This also influences the specific heat as can be seen in figure 11.4 (b). In the temperature range of the transition from bounded to unbounded motion, the first-order corrected frozen Gaussian calculations agree well with the fully-coupled thawed Gaussian counterpart. For lower temperatures this is no longer true. The divergence is especially noticeable in the low temperature limit for the specific heat where the first-order correction significantly increases the difference between the fully-coupled thawed Gaussian estimate (which is rather accurate as known from numerically exact computations, see chapter 9) and the frozen Gaussian based estimate.

Interestingly, although the first-order correction term at very low temperatures is much larger than the zeroth-order frozen Gaussian estimate (see figure 11.3), it does not lead to any change in the estimate of the ground state energy. As may be seen from figure 11.4 (a) the increase of the correction to the partition function is not "fast enough". This is further demonstrated in figure 11.5, where the difference between the first derivatives of the logarithms of the zeroth-order and first-order partition functions,

$$D = \frac{\partial \ln Z_0}{\partial T} - \frac{\partial \ln Z_1}{\partial T} \tag{11.15}$$

is plotted vs. the temperature. From figure 11.3 one expects this difference to diverge and this is evidently the case. However, the first-order correction term can lead to a correction for the estimate of the ground state energy only if the temperature derivative diverges as $T^2$, as can be seen from equation (11.14a). We find, however, that below a critical temperature the difference of the derivatives behaves as $D \sim T^{-0.91}$, and this is not sufficient. As a result the first-order correction to the ground state energy vanishes as found in figure 11.4.

Although the first-order correction term does not lead to a corrected estimate for the ground state energy, it does provide information on the quality of the frozen Gaussian

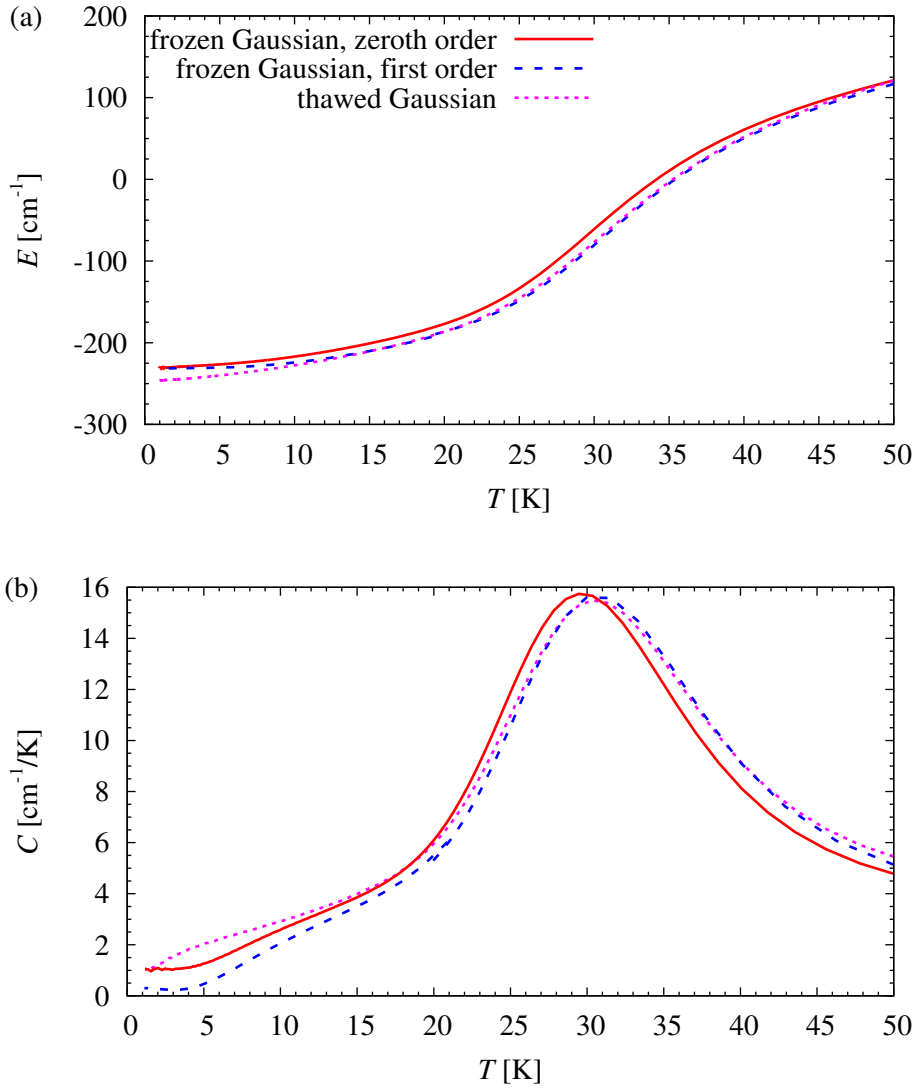


Figure 11.4.: (a) Temperature dependence of the mean energy of the argon trimer for $R_c = 10\,\text{Å}$, $D_1 = 0.1\,\text{Å}^{-2}$, and $D_2 = 25\,\text{Å}^{-2}$. Shown are the zeroth-order (solid line) and first-order (dashed line) frozen Gaussian results, and the fully-coupled thawed Gaussian approximation (dotted line). (b) Specific heat for the same parameters. Both calculations indicate a substantial improvement due to the first-order correction in the temperature region of the transition and above. For lower temperatures the correction breaks down, indicating that the frozen Gaussian approximation is no longer sufficiently accurate.

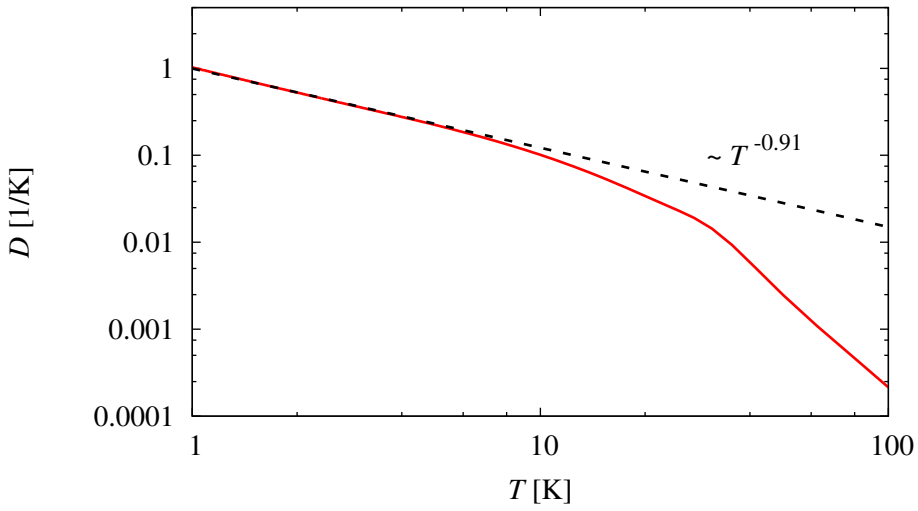


Figure 11.5.: Double logarithmic plot of the difference $D$ between the first derivatives of the logarithms of the zeroth- and first-order partition functions as defined in equation (11.15). In the limit of low temperatures the divergence behaves as $D \sim T^{-0.91}$, which is not strong enough to compensate for the $T^2$ term in equation (11.14a) needed to obtain a nonvanishing energy correction.

approximation. The ratio $Z_{C1}/Z_0$ (cf. figure 11.3) and the temperature behaviour of the correction to the mean energy [cf. figures 11.4 (a) and 11.5] provide an objective measure for the correctness of the values as estimated from the frozen Gaussian approximation. Only at a temperature $T \approx 12\,\mathrm{K}$ and below it, the correction becomes comparable with the zeroth-order estimate, and thus is no longer small. Approximately at the same temperature the energy correction starts to get smaller. Both outcomes indicate that the quality of the approximation is questionable for lower temperatures. However, the dissociation process described in chapter 9 appears only at higher temperatures, indicating that the frozen Gaussian approximation accurately reflects the quantum transition from a bounded moiety to dissociation into three free particles.

## 11.3. Numerical effort for evaluating the first-order correction

The results presented for the mean energy and the specific heat in section 11.2 showed that the quality of the first-order corrected frozen Gaussian approximation is similar to the fully-coupled thawed Gaussian method in the interesting range of temperatures. It is therefore of interest to compare their computational cost.

The numerically most expensive part is the imaginary time propagation of the dynamical variables. Since the positions $\boldsymbol{q}$ in the zeroth-order frozen Gaussian propagator (9.14) and the correction operator (11.1) are the only dynamical variables of a frozen Gaussian propagator, the number of equations of motion for the first-order corrected partition function still scales linearly with the particle number. For $N$ particles one has to solve $6N + 2$ equations of motion, in which the time integrations of the averaged potential in the exponential of the propagator and the correction operator [c.f. equations (9.14) and (11.7)] are included. By contrast the number of dynamical variables of the fully-coupled thawed Gaussian propagator scales always quadratically with the number of particles due to the symmetric time-dependent Gaussian width matrix. Counting all dynamical variables of the time evolved Gaussian approximation [53, 170] one obtains $3N(3N + 3)/2 + 1$ equations of motion. Thus, the imaginary time propagation of the dynamics is cheaper for the first-order frozen Gaussian partition function.

The first-order correction requires, however, also additional numerical effort. The need for propagating pairs of $\boldsymbol{q}$ trajectories for the propagator and the correction operator in equation (11.5b) demands a larger number of sampling points for the Monte Carlo integration in the two sets of positions $\boldsymbol{q}$. Additionally, the time integration in equation (11.5b) has to be evaluated. At this point the importance of an analytical evaluation of the $\boldsymbol{x}'$ and $\boldsymbol{x}$ integrations in equation (11.5b) as described in section 11.1.2 becomes clear. Owing to this simplification one can do without an additional $6N$-dimensional Monte Carlo sampling for the operator product [$\boldsymbol{x}$ integration in equation (11.5b)] and the trace ($\boldsymbol{x}'$ integration). This drastically reduces the numerical costs. Note that a $3N$-dimensional trace integration is already required for the zeroth-order approximation of both the frozen and thawed Gaussian partition functions. It can be and is evaluated analytically in all cases. With the analytical evaluation of the $\boldsymbol{x}'$ and $\boldsymbol{x}$ integrations there remain $6N$ $\boldsymbol{q}$ integrations for the first-order corrected frozen Gaussian partition function and $3N$ for its zeroth-order thawed Gaussian counterpart.

Because of the different numbers of required sampling points there is no general way for estimating the numerical effort. In the case of the argon trimer the additional effort for the first-order correction outweighs the lower number of equations of motion. We used $6.5 \times 10^7$ sampling points for the frozen Gaussian with first-order correction and $1.2 \times 10^7$ for the thawed Gaussian to obtain converged results down to low temperatures of about 1 K. On the same architecture (one Tesla C1060 GPU) the frozen Gaussian first-order calculation resulted in approximately twice the time as the zeroth-order thawed Gaussian. Due to the better scaling of the number of dynamical variables (linear instead of quadratic) one may expect that this relation changes in favour of the first-order frozen Gaussian variant with increasing particle number. However, as the results in this chapter demonstrate, the information the first-order correction provides on the validity of the Gaussian approximations is at least as important as the improvement of the numerical estimate of the physical values.

## 11.4. Significance of the first-order correction

With the results obtained in this chapter we see that the highest value of the correction term is to assess the quality of Gaussian approximations used in the study of thermodynamic properties of high-dimensional systems [51–57, 171]. It is known that these Gaussian approximations are exact in the high-temperature limit but are not necessarily correct at low temperatures. The present study shows that the first-order correction indicates a border temperature below which the results of the approximate propagators become questionable and above which they may be considered to be reliable.

The investigation of the argon trimer revealed that the dissociation process [57] discussed earlier with Gaussian approximations in full detail in chapter 9 is correctly described by the frozen Gaussian imaginary time propagator. It appears in the temperature range for which the first-order correction is small. Furthermore, the first-order corrected results are comparable with a fully-coupled thawed Gaussian investigation of the system, i.e. the addition of the first-order correction term improves the thermodynamic estimates. The numerical cost of the first-order corrected frozen Gaussian values is, however, higher than that of the thawed Gaussian partition function.

Since most effects in rare gas clusters such as structural transformations or dissociations appear at low temperatures [51–57, 171] it will be of value to investigate these properties with the series expansion. The correction term should be used to verify the validity of the Gaussian approximations in these cases, in particular, where strong differences are found between the approximate quantum computations and a purely classical theory [56].

# 12. Conclusions

## 12.1. Summary

The first part of this thesis was devoted to Bose-Einstein condensates in a complex $\mathcal{PT}$-symmetric double-well potential. The antisymmetric imaginary potential contributions model in one well a coherent influx of particles and an outflux from the other. It is known from linear quantum systems with a $\mathcal{PT}$-symmetric potential that real eigenvalue solutions of the time-independent Schrödinger equation exist in certain ranges of the physical parameters. However, the condensed phase of Bose-Einstein condensates is described by the nonlinear Gross-Pitaevskii equation and the nonlinearity introduces new properties which need an extensive study. This investigation is of high value because up to now an experimental verification of the effects of $\mathcal{PT}$ symmetry in a genuine quantum system is still lacking.

The solutions of the time-independent Gross-Pitaevskii equation revealed that real eigenvalue solutions, i.e. true stationary states of the time-dependent Gross-Pitaevskii equation do exist. Thus, the possibility of observing $\mathcal{PT}$ symmetry in quantum mechanics is in principle given. This could be shown in a general calculation in an idealised model, where the double well is formed by two infinitesimally thin delta traps, as well as in a fully three-dimensional calculation of a realistic spatially extended potential. Due to the nonlinearity a new branch point structure, not known from linear $\mathcal{PT}$-symmetric systems, appears. Two real eigenvalue solutions merge in a second-order exceptional point and then vanish completely when the gain-loss parameter is increased. $\mathcal{PT}$-broken complex eigenvalue solutions do not emerge from this point. However, $\mathcal{PT}$-broken states are found. They appear already for a lower gain-loss parameter and branch off from one of the real eigenvalue solutions. This branch point, at which the two complex and complex conjugate $\mathcal{PT}$-broken states and the real $\mathcal{PT}$-symmetric state are identical, could be identified to be a third-order exceptional point. For values of the gain-loss parameter between the two branch points associated $\mathcal{PT}$-symmetric and $\mathcal{PT}$-broken eigenstates coexist.

The $\mathcal{PT}$-broken states with complex chemical potentials are not true stationary states of the time-dependent Gross-Pitaevskii equation, and thus are not observable. However, their appearance has crucial consequences on the dynamics of the states with real eigenvalues. Already a linear stability analysis revealed that the $\mathcal{PT}$-symmetric state, from which the two $\mathcal{PT}$-broken states branch off, gets unstable in the vicinity of the bifurcation. A small discrepancy between the gain-loss parameter of the bifurcation and that

of the stability change could be explained by the norm-dependent nonlinearity of the Gross-Pitaevskii equation. The other $\mathcal{PT}$-symmetric state stays stable until the gain-loss parameter at which it vanishes is reached approximately. The stability properties have a strong impact on the full dynamics of the condensate wave function propagating in the double well. Stable oscillations of the wave function have been observed for small gain-loss contributions to the potential. Due to this gain-loss effect the total norm of the wave in the double well also oscillates with moderate amplitude. At larger gain-loss parameters those oscillations which start their evolution with an increasing norm may exceed a critical value of the norm at which the wave function becomes unstable. The result is a norm growing above all limits and destroying the condensate. In a real physical situation, when, in contrast to the description with a constant imaginary potential, the reservoirs are not infinitely large, the growth will end at a certain norm and the dynamics will be different from that obtained in the description with the $\mathcal{PT}$-symmetric Hamiltonian. However, in the dynamics of the complex potential the growing wave is guided by the complex eigenvalue solution of the time-independent Gross-Pitaevskii equation. The most important result of the dynamical calculations is the verification of the existence of $\mathcal{PT}$-symmetric states which are sufficiently stable to be observable in an experiment.

After the studies with the complex potentials two approaches of possible experimental realisations were investigated. The first approach consists of a closed four-well potential described by a Hermitian Hamiltonian, in which the $\mathcal{PT}$-symmetric double well is embedded as a subsystem. The latter one is formed by the inner two wells and the outer two wells act as source and drain for the wave function. It could be shown that it is possible to adjust the optical potential of the four-well setup such that a $\mathcal{PT}$-symmetric stationary state of the double well is possible with the same properties as studied before in the non-Hermitian description. Even the stable oscillations for a non-stationary initial condition could be reproduced. An experimentally feasible procedure leading to the $\mathcal{PT}$-symmetric situation was found. The experimental prerequisites, e.g. partially tilted multi wells, are accessible with today's techniques [152–154].

In a second approach the possibility of an in- and outflux of atoms by an unbound condensate state was studied. It was assumed that an external reservoir of atoms in the condensed phase exists and that these atoms can be in- and outcoupled to and from the double-well setup by a directed flow of unbound particles. This investigation was on an elementary level. However, it could be shown that it is in principle possible to replace the imaginary potentials of the non-Hermitian description by coupling terms of two or more wave functions. That is, it seems possible to create the $\mathcal{PT}$-symmetric potential by a simultaneous in- and outcoupling of atoms even though the calculations with the double-delta potential turned out to be challenging.

In total the first part showed that Bose-Einstein condensates are indeed an excellent candidate for a first experimental realisation of a $\mathcal{PT}$-symmetric quantum system. Stable stationary states fulfilling the conditions of $\mathcal{PT}$-symmetric systems are observable and can be created with today's experimental methods.

A different topic was the study of the decay behaviour of resonances in a linear quantum system at an exceptional point. It was demonstrated that the resonances forming the branch point singularity do not possess a purely exponential decay but include a polynomial contribution. This decay signal is unique and not observable without exceptional points. The numerically exact calculations for resonances of the hydrogen atom in crossed electric and magnetic fields revealed that it is possible to excite an adequate superposition such that the non-exponential decay will be observable in the survival probability.

A semiclassical approximation to the Boltzmann operator using a frozen Gaussian propagator was the topic of the second part of the thesis. For systems with a large number of degrees of freedom these approximations are important because exact quantum computations are too expensive. It was possible to extend the frozen Gaussian propagator such that it is applicable to multi-dimensional systems and well suited for the description of clusters of atoms. A quantitatively precise approximation to the mean values of the distances of the atoms could be added to the simple approximations of the partition function studied earlier. For all accessible values a comparison with similar but numerically more expensive methods showed that the frozen Gaussian propagator can compete with them. Furthermore, it was possible to show for the argon trimer that the propagator provides a quantitatively good approximation to the true quantum mechanical result obtained with numerically exact methods.

The investigation of the dissociation processes of $Ar_3$ and $Ar_6$ revealed two main results. Firstly, it could be shown that an artificial confinement of the atoms, which is necessary to converge numerical calculations, is often chosen too restrictive to obtain the correct dissociation process. Secondly, it could be shown that both clusters perform a direct dissociation in one step after which all atoms behave like free particles. This dissociation is almost purely classical. The influence of quantum mechanics is only found in a convergence to the ground state energy instead of the classical potential minimum for $T \to 0$ and in a slight shift of the dissociation threshold to higher classical temperatures, which can be attributed to the zero point energy.

Since the frozen Gaussian propagator is a semiclassical approximation to quantum mechanics it is not expected to be accurate at low temperatures when quantum effects become strong. It can, however, be considered as the leading order of a time-dependent perturbation theory. The first order of this correction was developed and implemented for the frozen Gaussian operator adapted to rare gas clusters. It was demonstrated that its highest value is to assess the quality of Gaussian approximations used in the study of thermodynamic properties of high-dimensional systems. For the investigation of the argon trimer the calculations revealed that all physically relevant effects occur in a temperature range in which the frozen Gaussian approximation describes correctly the imaginary time propagator and the first-order correction is small. In total, the results tell that for many applications the frozen Gaussian propagator is the method of choice. Its calculation is numerically cheap as compared to other methods, its quality can be objectively measured without the need for any other method, and it turned out to work

sufficiently correct for the physical effects observable in the thermodynamics of rare gas clusters.

## 12.2. Outlook

The present thesis showed that Bose-Einstein condensates are good candidates for the first experimental observation of a $\mathcal{PT}$-symmetric quantum system. However, there are still some questions which have to be answered. The prospects for a realisation of a $\mathcal{PT}$-symmetric setup are the most interesting subject from an experimental point of view. The calculations shown here are very promising and in particular the four-well model has been considered with realistic parameters. However, it relies on some simplifications, e.g. the matrix model on which the realistic physical parameters have been mapped. A fully three-dimensional solution of the Gross-Pitaevskii equation will be necessary to really pin down experimentally relevant parameters. This requires the development of grid computations especially adapted to complex potentials. It will also be important to investigate how the subtle interplay between the nonlinearity and the gain-loss effect observed in the stability properties found in the case of the $\mathcal{PT}$-symmetric potential will manifest itself in the dynamics of a closed multi-well system.

Numerically exact dynamical calculations will also be essential to proceed the study of the second realisation concept, viz. the in- and outcoupling of a directed atom flow. To go beyond the simple one-dimensional model based on the double-delta potential we need a geometry in which a reservoir exists that can be coupled to both wells. Then the directed atom flow, e.g. created by Bragg beams [91], must be modelled and the coupling to the condensate in the double well has to be implemented. It will be important to analyse how the condensate behaves if the strict conditions which have been found for the coupling have to be fulfilled in a larger extended region of the position space and not only at single coupling points in a delta-shaped trap. It is a nontrivial question whether this setup can then still be brought in agreement with the description provided by a complex $\mathcal{PT}$-symmetric potential. The answer will require a full dynamical study of the process.

Extensions of the $\mathcal{PT}$-symmetric double-well setup are also thinkable and will probably lead to new physical effects. Possible is the inclusion of a spatially modulated scattering length forming the double-well structure instead of the external potential [121, 183]. Even more interesting seems to be the addition of a long-range inter-atomic interaction. Bose-Einstein condensates with a dipole-dipole interaction have in many situations shown qualitatively new effects [120]. In particular, in multi-well setups the long-range forces lead to couplings of condensate fractions in non-adjoining wells. This could lead to new cases of $\mathcal{PT}$ symmetry or $\mathcal{PT}$-symmetry breaking in the presence of gain-loss terms.

On the theoretical side it would be desirable to understand how a coherent in- or outcoupling of atoms can be understood on a microscopic level. This should also be

important for a realistic description of experimental situations and will require considerations beyond the mean-field limit. Possible starting points along these lines could be the studies of the transition to the mean-field limit of a non-Hermitian Bose-Hubbard Hamiltonian [9, 23, 24] or the investigation of the coherently outcoupled atom density [91]. The relation with master equations [89, 90] could also help to obtain more insight.

There are also a few open mathematical questions. For example, a clear predictability of the critical values leading to $\mathcal{PT}$-symmetry breaking would be of high value. Since the $\mathcal{PT}$-symmetric potential barrier in the double-well setup used in this thesis can be considered as a perturbation of the harmonic trap confining the condensate, studies of perturbed harmonic oscillators [184, 185] might provide a good basis for such an investigation as it has already been done for delta perturbations [186]. Furthermore, insight to mathematical properties in terms of analytical expressions has so far only been obtained in the mean-field limit of the Bose-Hubbard dimer [9, 23, 24, 112], of which the dynamics differs from that of the Gross-Pitaevskii equation, or linearisations in matrix models [118, 147]. It would be interesting to get analytical expressions directly for a nonlinear system comparable to the Gross-Pitaevskii equation for the $\mathcal{PT}$-symmetric double well. A model with $\mathcal{PT}$-symmetric Robin boundary conditions at the edges of a square well [187, 188] might be helpful to answer this question.

The frozen Gaussian method developed in the second part of the thesis has proved to provide reliable results for quantum mechanical calculations with low numerical effort. There is a large number of investigations which can be done with it. In particular, the results for $Ar_3$ and $Ar_6$ indicate that the confinement to very small spheres usually applied in the calculation of the partition function and values deduced from it [52–54, 171] might be too restrictive to fully understand the low-temperature behaviour of the clusters. The dissociation can set in before structural changes or a melting can be observed. To make a clear statement on this question it is necessary to advance the investigations done here to clusters with higher numbers of atoms. In particular, the cases of $Ar_{13}$ [176–178], $Ne_{13}$ [53] or $Ne_{38}$ [54] examined recently are of special interest.

Also the series expansion of the imaginary time propagator can help to get further insight. Most effects in rare gas clusters such as structural transformations or dissociations appear at low temperatures and it has to be analysed whether the semiclassical approximations used in the calculations correctly reproduce the true quantum mechanical behaviour. An important example will be $Ne_{38}$, for which strong differences are found between the approximate quantum computations and a purely classical theory [56].

Furthermore, the series expansion of the Boltzmann operator exists also for thawed Gaussian propagators [68] and has been applied to a one-dimensional system [172]. The thawed Gaussian propagator is known to approximate the exact mean energy at low temperatures better than its frozen Gaussian counterpart. Thus, it will be interesting to see whether this can be confirmed with the correction term and whether the observed breakdown of the approximation lies at a lower temperature than for the frozen Gaussian results.

# A. Own publications in relation to this thesis

- **Refereed articles:**
  - Holger Cartarius and Eli Pollak:
    *Imaginary time Gaussian dynamics of the* $Ar_3$ *cluster*,
    The Journal of Chemical Physics 134, 044107 (2011)
  - Holger Cartarius and Nimrod Moiseyev:
    *Fingerprints of exceptional points in the survival probability of resonances in atomic spectra*,
    Physical Review A 84, 013419 (2011)
  - Holger Cartarius and Eli Pollak:
    *First-order corrections to semiclassical Gaussian partition functions for clusters of atoms*,
    Chemical Physics 399, 135 (2012)
  - Holger Cartarius and Günter Wunner:
    *Model of a* $\mathcal{PT}$*-symmetric Bose-Einstein condensate in a delta-function double-well potential*,
    Physical Review A 86, 013612 (2012)
  - Holger Cartarius, Daniel Haag, Dennis Dast, and Günter Wunner:
    *Nonlinear Schrödinger equation for a* $\mathcal{PT}$*-symmetric delta-function double well*,
    Journal of Physics A: Mathematical and Theoretical 45, 444008 (2012)
  - Dennis Dast, Daniel Haag, Holger Cartarius, Günter Wunner, Rüdiger Eichler, and Jörg Main:
    *A Bose-Einstein condensate in a* $\mathcal{PT}$ *symmetric double well*,
    Fortschritte der Physik 61, 124 (2013)
  - Manuel Kreibich, Jörg Main, Holger Cartarius, and Günter Wunner:
    *Hermitian four-well potential as a realization of a* $\mathcal{PT}$*-symmetric system*,
    Physical Review A 87, 051601 (2013)
  - W. D. Heiss, H. Cartarius, G. Wunner, and J. Main:
    *Spectral singularities in* $\mathcal{PT}$*-symmetric Bose–Einstein condensates*,
    Journal of Physics A: Mathematical and Theoretical 46, 275307 (2013)

  - Robin Gutöhrlein, Jörg Main, Holger Cartarius, and Günter Wunner:
    *Bifurcations and exceptional points in dipolar Bose-Einstein condensates*,
    Journal of Physics A: Mathematical and Theoretical 46, 305001 (2013)
  - Holger Cartarius, Dennis Dast, Daniel Haag, Günter Wunner, Rüdiger Eichler, and Jörg Main:
    *Stationary and dynamical solutions of the Gross-Pitaevskii equation for a Bose-Einstein condensate in a $\mathcal{PT}$ symmetric double well*,
    Acta Polytechnica 53, 259 (2013)
  - Dennis Dast, Daniel Haag, Holger Cartarius, Jörg Main, and Günter Wunner:
    *Eigenvalue structure of a Bose-Einstein condensate in a $\mathcal{PT}$-symmetric double well*,
    Journal of Physics A: Mathematical and Theoretical 46, 375301 (2013)
  - Daniel Haag, Dennis Dast, Andreas Löhle, Holger Cartarius, Jörg Main, and Günter Wunner:
    *Nonlinear quantum dynamics in a $\mathcal{PT}$-symmetric double well*,
    Physical Review A 89, 023601 (2014)
    (Published between submission and publication of this thesis.)
  - Daniel Haag, Holger Cartarius, and Günter Wunner:
    A Bose-Einstein condensate with $\mathcal{PT}$-symmetric loss and gain in a harmonic trap: A test of rigorous estimates,
    Acta Polytechnica 54, 116 (2014)
    (Published between submission and publication of this thesis.)

- **Contributions to conference proceedings**:
  - Dennis Dast, Daniel Haag, Holger Cartarius, Günter Wunner, Rüdiger Eichler, and Jörg Main:
    *Description of Bose-Einstein condensates in $\mathcal{PT}$-symmetric double wells*,
    Proceedings of the International Symposium on Self-Organization in Complex Systems: The Past, Present, and Future of Synergetics, Delmenhorst 2012, A. Pelster, G. Wunner (Eds.),
    Springer Lecture Notes in Physics, in press (2014), Preprint available at
    `http://itp1.uni-stuttgart.de/institut/arbeitsgruppen/cartarius/publikationen.php`

- **Submitted articles:**
  - Andreas Löhle, Holger Cartarius, Dennis Dast, Daniel Haag, Jörg Main, and Günter Wunner:
    *Stability of Bose-Einstein condensates in a $\mathcal{PT}$ symmetric double-delta potential close to branch points*,
    Acta Polytechnica 54, 133 (2014)
    (Published between submission and publication of this thesis.)

– Jacob Fuchs, Jörg Main, Holger Cartarius, and Günter Wunner:
*Harmonic inversion analysis of exceptional points in resonance spectra*,
Journal of Physics A 47, 125304 (2014)
(Published between submission and publication of this thesis.)

- **Article in preparation:**
  – Holger Cartarius:
  *Structure and dissociation of the* $Ar_6$ *cluster with the frozen Gaussian imaginary time propagator*,
  intended for submission to Physical Review A

# Bibliography


[1] Nimrod Moiseyev. *Non-Hermitian Quantum Mechanics*. Cambridge University Press, Cambridge (2011).

[2] A. Guo, G. J. Salamo, D. Duchesne, R. Morandotti, M. Volatier-Ravat, V. Aimez, G. A. Siviloglou, and D. N. Christodoulides. Observation of $\mathcal{PT}$-Symmetry Breaking in Complex Optical Potentials. *Physical Review Letters* 103, 093902 (2009).

[3] Christian E. Rüter, Konstantinos G. Makris, Ramy El-Ganainy, Demetrios N. Christodoulides, Mordechai Segev, and Detlev Kip. Observation of parity-time symmetry in optics. *Nature Physics* 6, 192 (2010).

[4] C. M. Bender and S. Boettcher. Real spectra in non-Hermitian Hamiltonians having $\mathcal{PT}$ symmetry. *Physical Review Letters* 80, 5243 (1998).

[5] Carl M. Bender. Making sense of non-Hermitian Hamiltonians. *Reports on Progress in Physics* 70, 947 (2007).

[6] K. G. Makris, R. El-Ganainy, D. N. Christodoulides, and Z. H. Musslimani. $\mathcal{PT}$-Symmetric Periodic Optical Potentials. *International Journal of Theoretical Physics* 50, 1019 (2011).

[7] Ali Mostafazadeh. Delta-function potential with a complex coupling. *Journal of Physics A: Mathematical and General* 39, 13495 (2006).

[8] Shachar Klaiman, Uwe Günther, and Nimrod Moiseyev. Visualization of Branch Points in $\mathcal{PT}$-Symmetric Waveguides. *Physical Review Letters* 101, 080402 (2008).

[9] E. M. Graefe, H. J. Korsch, and A. E. Niederle. Mean-field dynamics of a non-Hermitian Bose-Hubbard dimer. *Physical Review Letters* 101, 150408 (2008).

[10] K. G. Makris, R. El-Ganainy, D. N. Christodoulides, and Z. H. Musslimani. Beam Dynamics in $\mathcal{PT}$ Symmetric Optical Lattices. *Physical Review Letters* 100, 103904 (2008).

[11] H. F. Jones. Interface between Hermitian and non-Hermitian Hamiltonians in a model calculation. *Physical Review D* 78, 065032 (2008).

[12] Ali Mostafazadeh and Hossein Mehri-Dehnavi. Spectral singularities, biorthonormal systems and a two-parameter family of complex point interactions. *Journal of Physics A: Mathematical and Theoretical* 42, 125303 (2009).

[13] H. F. Jones and E. S. Moreira Jr. Quantum and classical statistical mechanics of a class of non-Hermitian Hamiltonians. *Journal of Physics A: Mathematical and Theoretical* 43, 055307 (2010).

[14] A. Ruschhaupt, F. Delgado, and J. G. Muga. Physical realization of $\mathcal{PT}$-symmetric potential scattering in a planar slab waveguide. *Journal of Physics A: Mathematical and General* 38, L171 (2005).

[15] Konstantinos G. Makris, Ramy El-Ganainy, Demetrios N. Christodoulides, and Z. H. Musslimani. $\mathcal{PT}$-symmetric optical lattices. *Physical Review A* 81, 063807 (2010).

[16] Ingrid Rotter. Environmentally induced effects and dynamical phase transitions in quantum systems. *Journal of Optics* 12, 065701 (2010).

[17] R. El-Ganainy, K. G. Makris, D. N. Christodoulides, and Ziad H. Musslimani. Theory of coupled optical $\mathcal{PT}$-symmetric structures. *Optics Letters* 32, 2632 (2007).

[18] D. Ananikian and T. Bergeman. Gross-Pitaevskii equation for Bose particles in a double-well potential: Two-mode models and beyond. *Physical Review A* 73, 013604 (2006).

[19] Vit Jakubský and Miloslav Znojil. An explicitly solvable model of the spontaneous $\mathcal{PT}$-symmetry breaking. *Czechoslovak Journal of Physics* 55, 1113 (2005).

[20] Hossein Mehri-Dehnavi, Ali Mostafazadeh, and Ahmet Batal. Application of pseudo-Hermitian quantum mechanics to a complex scattering potential with point interactions. *Journal of Physics A: Mathematical and Theoretical* 43, 145301 (2010).

[21] E. P. Gross. Structure of a Quantized Vortex in Boson Systems. *Il Nuovo Cimento* 20, 454 (1961).

[22] L. P. Pitaevskii. Vortex Lines in an Imperfect Bose Gas. *Soviet Physics JETP* 13, 451 (1961).

[23] E. M. Graefe, U. Günther, H. J. Korsch, and A. E. Niederle. A non-Hermitian $\mathcal{PT}$ symmetric Bose–Hubbard model: eigenvalue rings from unfolding higher-order exceptional points. *Journal of Physics A: Mathematical and Theoretical* 41, 255206 (2008).

[24] E. M. Graefe, H. J. Korsch, and A. E. Niederle. Quantum-classical correspondence for a non-Hermitian Bose-Hubbard dimer. *Physical Review A* 82, 013629 (2010).

[25] Hamidreza Ramezani, Tsampikos Kottos, Ramy El-Ganainy, and Demetrios N. Christodoulides. Unidirectional nonlinear $\mathcal{PT}$-symmetric optical structures. *Physical Review A* 82, 043803 (2010).

[26] Z.H. Musslimani, Konstantinos G. Makris, Ramy El-Ganainy, and Demetrios N. Christodoulides. Optical solitons in $\mathcal{PT}$ periodic potentials. *Physical Review Letters* 100, 30402 (2008).

[27] F. Kh. Abdullaev, V. V. Konotop, M. Salerno, and A. V. Yulin. Dissipative periodic waves, solitons, and breathers of the nonlinear Schrödinger equation with complex potentials. *Physical Review E* 82, 056606 (2010).

[28] Yu. V. Bludov and V. V. Konotop. Nonlinear patterns in Bose-Einstein condensates in dissipative optical lattices. *Physical Review A* 81, 013625 (2010).

[29] R. Driben and B. A. Malomed. Stability of solitons in parity-time-symmetric couplers. *Optics Letters* 36, 4323 (2011).

[30] F. Kh. Abdullaev, Y. V. Kartashov, Vladimir V. Konotop, and D. A. Zezyulin. Solitons in $\mathcal{PT}$-symmetric nonlinear lattices. *Physical Review A* 83, 41805 (2011).

[31] Yu. V. Bludov, V. V. Konotop, and B. A. Malomed. Stable dark solitons in $\mathcal{PT}$-symmetric dual-core waveguides. *Physical Review A* 87, 013816 (2013).

[32] Yaakov Lumer, Yonatan Plotnik, Mikael C. Rechtsman, and Mordechai Segev. Nonlinearly Induced $\mathcal{PT}$ Transition in Photonic Systems. *Physical Review Letters* 111, 263901 (2013).

[33] J. Pickton and H. Susanto. Integrability of $\mathcal{PT}$-symmetric dimers. *Physical Review A* 88, 063840 (2013).

[34] W. P. Reinhardt. Complex Coordinates in the Theory of Atomic and Molecular Structure and Dynamics. *Annual Review of Physical Chemistry* 33, 223 (1982).

[35] Nimrod Moiseyev. Quantum theory of resonances: calculating energies, widths and cross-sections by complex scaling. *Physics Reports* 302, 212 (1998).

[36] W. D. Heiss. Phases of wave functions and level repulsion. *The European Physical Journal D – Atomic, Molecular, Optical and Plasma Physics* 7, 1 (1999).

[37] T. Kato. *Perturbation theory for linear operators*. Springer, Berlin (1966).

[38] C. Dembowski, H.-D. Gräf, H. L. Harney, A. Heine, W. D. Heiss, H. Rehfeld, and A. Richter. Experimental Observation of the Topological Structure of Exceptional Points. *Physical Review Letters* 86, 787 (2001).

[39] B. Dietz, H. L. Harney, O. N. Kirillov, M. Miski-Oglu, A. Richter, and F. Schäfer. Exceptional Points in a Microwave Billiard with Time-Reversal Invariance Violation. *Physical Review Letters* 106, 150403 (2011).

[40] O. Latinne, N. J. Kylstra, M. Dörr, J. Purvis, M. Terao-Dunseath, C. J. Joachain, P. G. Burke, and C. J. Noble. Laser-Induced Degeneracies Involving Autoionizing States in Complex Atoms. *Physical Review Letters* 74, 46 (1995).

[41] Holger Cartarius, Jörg Main, and Günter Wunner. Exceptional Points in Atomic Spectra. *Physical Review Letters* 99, 173003 (2007).

[42] R. Lefebvre, O. Atabek, M. Šindelka, and N. Moiseyev. Resonance Coalescence in Molecular Photodissociation. *Physical Review Letters* 103, 123003 (2009).

[43] E Hernández, A Jáuregui, and A Mondragán. Non-Hermitian degeneracy of two unbound states. *Journal of Physics A: Mathematical and General* 39, 10087 (2006).

[44] K. Rapedius, C. Elsen, D. Witthaut, S. Wimberger, and H. J. Korsch. Nonlinear resonant tunneling of Bose-Einstein condensates in tilted optical lattices. *Physical Review A* 82, 063601 (2010).

[45] Holger Cartarius, Jörg Main, and Günter Wunner. Discovery of exceptional points in the Bose-Einstein condensation of gases with attractive 1/r interaction. *Physical Review A* 77, 013618 (2008).

[46] W. D. Heiss. Time behaviour near to spectral singularities. *European Physical Journal D – Atomic, Molecular, Optical and Plasma Physics* 60, 257 (2010).

[47] Jan Wiersig, Sang Wook Kim, and Martina Hentschel. Asymmetric scattering and nonorthogonal mode patterns in optical microspirals. *Physical Review A* 78, 053809 (2008).

[48] S. Longhi. Spectral singularities and Bragg scattering in complex crystals. *Physical Review A* 81, 022102 (2010).

[49] Eva-Maria Graefe and H. F. Jones. $\mathcal{PT}$-symmetric sinusoidal optical lattices at the symmetry-breaking threshold. *Physical Review A* 84, 013818 (2011).

[50] B. Dietz, T. Friedrich, J. Metz, M. Miski-Oglu, A. Richter, F. Schäfer, and C. A. Stafford. Rabi oscillations at exceptional points in microwave billiards. *Physical Review E* 75, 027201 (2007).

[51] J. P. Neirotti, David L. Freeman, and J. D. Doll. A heat capacity estimator for Fourier path integral simulations. *The Journal of Chemical Physics* 112, 3990 (2000).

[52] Cristian Predescu, Dubravko Sabo, J. D. Doll, and David L. Freeman. Heat capacity estimators for random series path-integral methods by finite-difference schemes. *The Journal of Chemical Physics* 119, 12119 (2003).

[53] Pavel A. Frantsuzov and Vladimir A. Mandelshtam. Quantum statistical mechanics with Gaussians: Equilibrium properties of van der Waals clusters. *The Journal of Chemical Physics* 121, 9247 (2004).

[54] Cristian Predescu, Pavel A. Frantsuzov, and Vladimir A. Mandelshtam. Thermodynamics and equilibrium structure of $Ne_{38}$ cluster: Quantum mechanics versus classical. *The Journal of Chemical Physics* 122, 154305 (2005).

[55] Ronald P. White, Sean M. Cleary, and Howard R. Mayne. Phase changes in Lennard-Jones mixed clusters with composition $Ar_nXe_{6-n}$ (n = 0,1,2). *The Journal of Chemical Physics* 123, 094505 (2005).

[56] Pavel A. Frantsuzov, Dario Meluzzi, and Vladimir A. Mandelshtam. Structural Transformations and Melting in Neon Clusters: Quantum versus Classical Mechanics. *Physical Review Letters* 96, 113401 (2006).

[57] R. Pérez de Tudela, M. Márquez-Mijares, T. González-Lezana, O. Roncero, S. Miret-Artés, G. Delgado-Barrio, and P. Villarreal. A path-integral Monte Carlo study of a small cluster: The Ar trimer. *The Journal of Chemical Physics* 132, 244303 (2010).

[58] B. J. Berne and D. Thirumalai. On the Simulation of Quantum Systems: Path Integral Methods. *Annual Review of Physical Chemistry* 37, 401 (1986).

[59] Nancy Makri. Time-Dependent Quantum Methods for Large Systems. *Annual Review of Physical Chemistry* 50, 167 (1999).

[60] D. M. Ceperley. Metropolis Methods for Quantum Monte Carlo Simulations. *AIP Conference Proceedings* 690, 85 (2003).

[61] D. D. Frantz, D. L. Freeman, and J. D. Doll. Extending J walking to quantum systems: Applications to atomic clusters. *The Journal of Chemical Physics* 97, 5713 (1992).

[62] R. D. Etters and Jaya Kaelberer. Thermodynamic properties of small aggregates of rare-gas atoms. *Physical Review A* 11, 1068 (1975).

[63] David M. Leitner, R. Stephen Berry, and Robert M. Whitnell. Quantum chaos of $Ar_3$: Statistics of eigenvalues. *The Journal of Chemical Physics* 91, 3470 (1989).

[64] David M. Leitner, J. D. Doll, and Robert M. Whitnell. Quantum mechanics of small Ne, Ar, Kr, and Xe clusters. *The Journal of Chemical Physics* 94, 6644 (1991).

[65] Pavel V. Elyutin, Vladimir I. Baranov, Elena D. Belega, and Dmitrij N. Trubnikov. The partition functions and thermodynamic properties of small clusters of rare gas atoms. *The Journal of Chemical Physics* 100, 3843 (1994).

[66] T. González-Lezana, J. Rubayo-Soneira, S. Miret-Artés, F. A. Gianturco, G. Delgado-Barrio, and P. Villarreal. Comparative configurational study for He, Ne, and Ar trimers. *The Journal of Chemical Physics* 110, 9000 (1999).

[67] Jian Liu and William H. Miller. Using the thermal Gaussian approximation for the Boltzmann operator in semiclassical initial value time correlation functions. *The Journal of Chemical Physics* 125, 224104 (2006).

[68] Jiushu Shao and Eli Pollak. A new time evolving Gaussian series representation of the imaginary time propagator. *The Journal of Chemical Physics* 125, 133502 (2006).

[69] Dong H. Zhang, Jiushu Shao, and Eli Pollak. Frozen Gaussian series representation of the imaginary time propagator theory and numerical tests. *The Journal of Chemical Physics* 131, 044116 (2009).

[70] Markus Müller and Ingrid Rotter. Exceptional points in open quantum systems. *Journal of Physics A: Mathematical and Theoretical* 41, 244018 (2008).

[71] Uwe Günther, Ingrid Rotter, and Boris F. Samsonov. Projective Hilbert space structures at exceptional points. *Journal of Physics A: Mathematical and Theoretical* 40, 8815 (2007).

[72] H. Eleuch and I. Rotter. Avoided level crossings in open quantum systems. *Fortschritte der Physik* 61, 194 (2013).

[73] M. V. Berry. Mode degeneracies and the petermann excess-noise factor for unstable lasers. *Journal of Modern Optics* 50, 63 (2003).

[74] T. Stehmann, W. D. Heiss, and F. G. Scholtz. Observation of exceptional points in electronic circuits. *Journal of Physics A: Mathematical and General* 37, 7813 (2004).

[75] W. D. Heiss. The physics of exceptional points. *Journal of Physics A: Mathematical and Theoretical* 45, 444016 (2012).

[76] W. D. Heiss. Chirality of wavefunctions for three coalescing levels. *Journal of Physics A: Mathematical and Theoretical* 41, 244010 (2008).

[77] G. Demange and E. M. Graefe. Signatures of three coalescing eigenfunctions. *Journal of Physics A: Mathematical and Theoretical* 45, 025303 (2012).

[78] Robin Gutöhrlein, Jörg Main, Holger Cartarius, and Günter Wunner. Bifurcations and exceptional points in dipolar Bose-Einstein condensates. *Journal of Physics A: Mathematical and Theoretical* 46, 305001 (2013).

[79] S. Bose. Plancks Gesetz und Lichtquantenhypothese. *Zeitschrift für Physik* 26, 178 (1924).

[80] A. Einstein. Quantentheorie des einatomigen idealen Gases II. *Sitzungsberichte der preußischen Akademie der Wissenschaften, phys.-math. Kl.* Jahrgang 1925, 3 (1925).

[81] M. H. Anderson, J. R. Ensher, M. R. Matthews, C. E. Wieman, and E. A. Cornell. Observation of Bose-Einstein Condensation in a Dilute Atomic Vapor. *Science* 269, 198 (1995).

[82] K. B. Davis, M.-O. Mewes, M. R. Andrews, N. J. van Druten, D. S. Durfee, D. M. Kurn, and W. Ketterle. Bose-Einstein Condensation in a Gas of Sodium Atoms. *Physical Review Letters* 75, 3969 (1995).

[83] Nimrod Moiseyev and Lorenz S. Cederbaum. Resonance solutions of the nonlinear Schrödinger equation: Tunneling lifetime and fragmentation of trapped condensates. *Physical Review A* 72, 033605 (2005).

[84] Peter Schlagheck and Tobias Paul. Complex-scaling approach to the decay of Bose-Einstein condensates. *Physical Review A* 73, 023619 (2006).

[85] T. Paul, M. Hartung, K. Richter, and P. Schlagheck. Nonlinear transport of Bose-Einstein condensates through mesoscopic waveguides. *Physical Review A* 76, 063605 (2007).

[86] Roberto Livi, Roberto Franzosi, and Gian-Luca Oppo. Self-Localization of Bose-Einstein Condensates in Optical Lattices via Boundary Dissipation. *Physical Review Letters* 97, 060401 (2006).

[87] D. Witthaut, E. M. Graefe, S. Wimberger, and H. J. Korsch. Bose-Einstein condensates in accelerated double-periodic optical lattices: Coupling and crossing of resonances. *Physical Review A* 75, 013617 (2007).

[88] K. Rapedius and H. J. Korsch. Resonance solutions of the nonlinear Schrödinger equation in an open double-well potential. *Journal of Physics B: Atomic, Molecular and Optical Physics* 42, 044005 (2009).

[89] F. Trimborn, D. Witthaut, and S. Wimberger. Mean-field dynamics of a two-mode Bose–Einstein condensate subject to noise and dissipation. *Journal of Physcis B: Atomic, Molecular and Optical Physics* 41, 171001 (2008).

[90] D. Witthaut, F. Trimborn, H. Hennig, G. Kordas, T. Geisel, and S. Wimberger. Beyond mean-field dynamics in open Bose-Hubbard chains. *Physical Review A* 83, 063608 (2011).

[91] Y. Shin, G.-B. Jo, M. Saba, T. A. Pasquini, W. Ketterle, and D. E. Pritchard. Optical Weak Link between Two Spatially Separated Bose-Einstein Condensates. *Physical Review Letters* 95, 170402 (2005).

[92] R. Gati, M. Albiez, J. Fölling, B. Hemmerling, and M. K. Oberthaler. Realization of a single Josephson junction for Bose–Einstein condensates. *Applied Physics B* 82, 207 (2006).

[93] T. Gericke, P. Wurtz, D. Reitz, T. Langen, and H. Ott. High-resolution scanning electron microscopy of an ultracold quantum gas. *Nature Physics* 4, 949 (2008).

[94] N. P. Robins, C. Figl, M. Jeppesen, G. R. Dennis, and J. D. Close. A pumped atom laser. *Nature Physics* 4, 731 (2008).

[95] Carl M. Bender, Stefan Boettcher, and Peter N. Meisinger. $\mathcal{PT}$-symmetric quantum mechanics. *Journal of Mathematical Physics* 40, 2201 (1999).

[96] Miloslav Znojil. Exact solution for Morse oscillator in $\mathcal{PT}$-symmetric quantum mechanics. *Physics Letters A* 264, 108 (1999).

[97] Miloslav Znojil. $\mathcal{PT}$-symmetric square well. *Physics Letters A* 285, 7 (2001).

[98] Carl M. Bender, Dorje C. Brody, and Hugh F. Jones. Complex Extension of Quantum Mechanics. *Physical Review Letters* 89, 270401 (2002).

[99] Miloslav Znojil. Decays of degeneracies in $\mathcal{PT}$-symmetric ring-shaped lattices. *Physics Letters A* 375, 3435 (2011).

[100] Miloslav Znojil and Junde Wu. A Generalized Family of Discrete $\mathcal{PT}$-symmetric Square Wells. *International Journal of Theoretical Physics* 52, 2152 (2013).

[101] G. Lévai and M. Znojil. The interplay of supersymmetry and $\mathcal{PT}$ symmetry in quantum mechanics: a case study for the Scarf II potential. *Journal of Physics A: Mathematical and General* 35, 8793 (2002).

[102] Carl M. Bender, Vincenzo Branchina, and Emanuele Messina. Ordinary versus $\mathcal{PT}$-symmetric $\phi^3$ quantum field theory. *Physical Review D* 85, 085001 (2012).

[103] P. D. Mannheim. Astrophysical evidence for the non-Hermitian but $\mathcal{PT}$-symmetric Hamiltonian of conformal gravity. *Fortschritte der Physik* 61, 140 (2013).

[104] Carl M. Bender, H. F. Jones, and R. J. Rivers. Dual-symmetric quantum field theories. *Physics Letters B* 625, 333 (2005).

[105] S. Bittner, B. Dietz, U. Günther, H. L. Harney, M. Miski-Oglu, A. Richter, and F. Schäfer. $\mathcal{PT}$ Symmetry and Spontaneous Symmetry Breaking in a Microwave Billiard. *Physical Review Letters* 108, 024101 (2012).

[106] Joseph Schindler, Ang Li, Mei C. Zheng, F. M. Ellis, and Tsampikos Kottos. Experimental study of active *LRC* circuits with $\mathcal{PT}$ symmetries. *Physical Review A* 84, 040101 (2011).

[107] J. Schindler, Z. Lin, J. M. Lee, H. Ramezani, F. M. Ellis, and T. Kottos. $\mathcal{PT}$-symmetric electronics. *Journal of Physics A: Mathematical and Theoretical* 45, 444029 (2012).

[108] Y. D. Chong, Li Ge, and A. Douglas Stone. $\mathcal{PT}$-Symmetry Breaking and Laser-Absorber Modes in Optical Scattering Systems. *Physical Review Letters* 106, 093902 (2011).

[109] M. Znojil and H.B. Geyer. Smeared quantum lattices exhibiting $\mathcal{PT}$-symmetry with positive $\mathcal{P}$. *Fortschritte der Physik* 61, 111 (2013).

[110] Ali Mostafazadeh. Nonlinear spectral singularities of a complex barrier potential and the lasing threshold condition. *Physical Review A* 87, 063838 (2013).

[111] Ali Mostafazadeh. Nonlinear Spectral Singularities for Confined Nonlinearities. *Physical Review Letters* 110, 260402 (2013).

[112] E. M. Graefe. Stationary states of a $\mathcal{PT}$ symmetric two-mode Bose-Einstein condensate. *Journal of Physics A: Mathematical and Theoretical* 45, 444015 (2012).

[113] Ziad H. Musslimani, Konstantinos G. Makris, Ramy El-Ganainy, and Demetrios N. Christodoulides. Analytical solutions to a class of nonlinear Schrödinger equations with $\mathcal{PT}$-like potentials. *Journal of Physics A: Mathematical and Theoretical* 41, 244019 (2008).

[114] Eva-Maria Graefe and H. F. Jones. $\mathcal{PT}$-symmetric sinusoidal optical lattices at the symmetry-breaking threshold. *Physical Review A* 84, 013818 (2011).

[115] H. F. Jones. Analytic results for a $\mathcal{PT}$-symmetric optical structure. *Journal of Physics A: Mathematical and Theoretical* 45, 135306 (2012).

[116] Li Ge, Y. D. Chong, S. Rotter, H. E. Türeci, and A. D. Stone. Unconventional modes in lasers with spatially varying gain and loss. *Physical Review A* 84, 023820 (2011).

[117] M. Liertzer, Li Ge, A. Cerjan, A. D. Stone, H. E. Türeci, and S. Rotter. Pump-Induced Exceptional Points in Lasers. *Physical Review Letters* 108, 173901 (2012).

[118] Dennis Dast, Daniel Haag, Holger Cartarius, Jörg Main, and Günter Wunner. Eigenvalue structure of a Bose-Einstein condensate in a $\mathcal{PT}$-symmetric double well. *Journal of Physics A: Mathematical and Theoretical* 46, 375301 (2013).

[119] D. O'Dell, S. Giovanazzi, G. Kurizki, and V. M. Akulin. Bose-Einstein Condensates with $1/r$ Interatomic Attraction: Electromagnetically Induced "Gravity". *Physical Review Letters* 84, 5687 (2000).

[120] T. Lahaye, C. Menotti, L. Santos, M. Lewenstein, and T. Pfau. The physics of dipolar bosonic quantum gases. *Reports on Progress in Physics* 72, 126401 (2009).

[121] Thawatchai Mayteevarunyoo, Boris A. Malomed, and Guangjiong Dong. Spontaneous symmetry breaking in a nonlinear double-well structure. *Physical Review A* 78, 053601 (2008).

[122] K. Rapedius and H. J. Korsch. Resonance solutions of the nonlinear Schrödinger equation in an open double-well potential. *Journal of Physics B: Atomic, Molecular and Optical Physics* 42, 044005 (2009).

[123] D. Witthaut, K. Rapedius, and H. J. Korsch. The nonlinear Schoedinger equation for the delta-comb potential: quasi-classical chaos and bifurcations of periodic stationary solutions. *Journal of Nonlinear Mathematical Physics* 16, 207 (2008).

[124] Silvestro Fassari and Fabio Rinaldi. On the Spectrum of the Schrödinger Hamiltonian of the One-Dimensional Harmonic Oscillator Perturbed by Two Identical Attractive Point Interactions. *Reports on Mathematical Physics* 69, 353 (2012).

[125] Ersan Demiralp. Bound states of $n$-dimensional harmonic oscillator decorated with Dirac delta functions. *Journal of Physics A: Mathematical and General* 38, 4783 (2005).

[126] H.F. Jones. The energy spectrum of complex periodic potentials of the Kronig–Penney type. *Physics Letters A* 262, 242 (1999).

[127] Zafar Ahmed. Energy band structure due to a complex, periodic, $\mathcal{PT}$-invariant potential. *Physics Letters A* 286, 231 (2001).

[128] H. Uncu, D. Tarhan, E. Demiralp, and Ö. E. Müstecaplıoglu. Bose-Einstein condensate in a harmonic trap with an eccentric dimple potential. *Laser Physics* 18, 331 (2008).

[129] Holger Cartarius and Günter Wunner. Model of a $\mathcal{PT}$-symmetric Bose-Einstein condensate in a $\delta$-function double-well potential. *Physical Review A* 86, 013612 (2012).

[130] Holger Cartarius, Daniel Haag, Dennis Dast, and Günter Wunner. Nonlinear Schrödinger equation for a $\mathcal{PT}$-symmetric delta-function double well. *Journal of Physics A: Mathematical and Theoretical* 45, 444008 (2012).

[131] Dennis Dast, Daniel Haag, Holger Cartarius, Günter Wunner, Rüdiger Eichler, and Jörg Main. A Bose-Einstein condensate in a $\mathcal{PT}$ symmetric double well. *Fortschritte der Physik* 61, 124 (2013).

[132] Holger Cartarius, Dennis Dast, Daniel Haag, Günter Wunner, Rüdiger Eichler, and Jörg Main. Stationary and dynamical solutions of the Gross-Pitaevskii equation for a Bose-Einstein condensate in a $\mathcal{PT}$ symmetric double well. *Acta Polytechnica* 53, 259 (2013).

[133] Dennis Dast, Daniel Haag, Holger Cartarius, Günter Wunner, Rüdiger Eichler, and Jörg Main. Description of Bose-Einstein condensates in $\mathcal{PT}$-symmetric double wells. In *Proceedings of the International Symposium on Self-Organization in Complex Systems: The Past, Present, and Future of Synergetics, Delmenhorst 2012*, edited by Axel Pelster and Günter Wunner, Springer Lecture Notes in Physics (2014). In press, Preprint available at `http://itp1.uni-stuttgart.de/institut/arbeitsgruppen/cartarius/publikationen.php`.

[134] Dennis Dast. *Variationsrechnungen zu Bose-Einstein-Kondensaten in $\mathcal{PT}$-symmetrischen Doppelmuldenpotentialen.* Master's thesis, Universität Stuttgart (2012). Available at: `http://itp1.uni-stuttgart.de/publikationen/abschlussarbeiten/`.

[135] Daniel Haag. *Numerische Behandlung von Bose-Einstein-Kondensaten im $\mathcal{PT}$-symmetrischen Doppelmuldenpotential.* Master's thesis, Universität Stuttgart (2012). Available at: `http://itp1.uni-stuttgart.de/publikationen/abschlussarbeiten/`.

[136] L. D. Carr, C. W. Clark, and W. P. Reinhardt. Stationary solutions of the one-dimensional nonlinear Schroedinger equation. I. Case of repulsive nonlinearity. *Physical Review A* 62, 63610 (2000).

[137] L. D. Carr, Charles W. Clark, and W. P. Reinhardt. Stationary solutions of the one-dimensional nonlinear Schrödinger equation. II. Case of attractive nonlinearity. *Physical Review A* 62, 063611 (2000).

[138] L. D. Carr, J. N. Kutz, and W. P. Reinhardt. Stability of stationary states in the cubic nonlinear Schroedinger equation: Applications to the Bose-Einstein condensate. *Physical Review E* 63, 66604 (2001).

[139] A. D. McLachlan. A variational solution of the time-dependent Schrodinger equation. *Molecular Physics* 8, 39 (1964).

[140] Eric J. Heller. Classical S-matrix limit of wave packet dynamics. *The Journal of Chemical Physics* 65, 4979 (1976).

[141] Eric J. Heller. Frozen Gaussians: A very simple semiclassical approximation. *The Journal of Chemical Physics* 75, 2923 (1981).

[142] Stefan Rau, Jörg Main, Patrick Köberle, and Günter Wunner. Pitchfork bifurcations in blood-cell-shaped dipolar Bose-Einstein condensates. *Physical Review A* 81, 031605(R) (2010).

[143] Stefan Rau, Jörg Main, and Günter Wunner. Variational methods with coupled Gaussian functions for Bose-Einstein condensates with long-range interactions. I. General concept. *Physical Review A* 82, 023610 (2010).

[144] Stefan Rau, Jörg Main, Holger Cartarius, Patrick Köberle, and Günter Wunner. Variational methods with coupled Gaussian functions for Bose-Einstein condensates with long-range interactions. II. Applications. *Physical Review A* 82, 023611 (2010).

[145] William H. Press, Saul A. Teukolsky, William T. Vetterling, and Brian P. Flannery. *Numerical Recipes in Fortran 77*. Cambridge University Press, New York, second edition (1992).

[146] G. Theocharis, P. G. Kevrekidis, D. J. Frantzeskakis, and P. Schmelcher. Symmetry breaking in symmetric and asymmetric double-well potentials. *Physical Review E* 74, 056608 (2006).

[147] W. D. Heiss, H. Cartarius, G. Wunner, and J. Main. Spectral singularities in $\mathcal{PT}$-symmetric Bose–Einstein condensates. *Journal of Physics A: Mathematical and Theoretical* 46, 275307 (2013).

[148] Fabian Single. *Modelle für $\mathcal{PT}$-symmetrische Bose-Einstein-Kondensate*. Master's thesis, Universität Stuttgart (2013). Available at: `http://itp1.uni-stuttgart.de/publikationen/abschlussarbeiten/`.

[149] Daniel Haag, Dennis Dast, Andreas Löhle, Holger Cartarius, Jörg Main, and Günter Wunner. Nonlinear quantum dynamics in a $\mathcal{PT}$-symmetric double well. *Physical Review A* 89, 023601 (2014). Published between submission and publication of this thesis.

[150] Andreas Löhle, Holger Cartarius, Daniel Haag, Dennis Dast, Jörg Main, and Günter Wunner. Stability of Bose-Einstein condensates in a $\mathcal{PT}$ symmetric double-$\delta$ potential close to branch points. *Acta Polytechnica* 54, 133 (2014). Published between submission and publication of this thesis.

[151] Andreas Löhle. *Stabilitätslücke bei $\mathcal{PT}$-symmetrischen Bose-Einstein-Kondensaten*. Bachelor's thesis, Universität Stuttgart (2013). Available at: `http://itp1.uni-stuttgart.de/publikationen/abschlussarbeiten/`.

[152] T. Salger, C. Geckeler, S. Kling, and M. Weitz. Atomic Landau-Zener Tunneling in Fourier-Synthesized Optical Lattices. *Physical Review Letters* 99, 190405 (2007).

[153] S. Fölling, S. Trotzky, P. Cheinet, M. Feld, R. Saers, A. Widera, T. Müller, and I. Bloch. Direct observation of second-order atom tunnelling. *Nature* 448, 1029 (2007).

[154] K. Henderson, C. Ryu, C. MacCormick, and M. G. Boshier. Experimental demonstration of painting arbitrary and dynamic potentials for Bose-Einstein condensates. *New Journal of Physics* 11, 043030 (2009).

[155] Manuel Kreibich, Jörg Main, Holger Cartarius, and Günter Wunner. Hermitian four-well potential as a realization of a $\mathcal{PT}$-symmetric system. *Physical Review A* 87, 051601(R) (2013).

[156] Qian Niu, Xian-Geng Zhao, G. A. Georgakis, and M. G. Raizen. Atomic Landau-Zener tunneling and Wannier-Stark ladders in optical potentials. *Physical Review Letters* 76, 4504 (1996).

[157] Alessandro Zenesini, Carlo Sias, Hans Lignier, Yeshpal Singh, Donatella Ciampini, Oliver Morsch, Riccardo Mannella, Ennio Arimondo, Andrea Tomadin, and Sandro Wimberger. Resonant tunneling of Bose–Einstein condensates in optical lattices. *New Journal of Physics* 10, 053038 (2008).

[158] S. Wimberger, R. Mannella, O. Morsch, E. Arimondo, A. R. Kolovsky, and A. Buchleitner. Nonlinearity-induced destruction of resonant tunneling in the Wannier-Stark problem. *Physical Review A* 72, 063610 (2005).

[159] D. R. Dounas-Frazer, A. M. Hermundstad, and L. D. Carr. Ultracold bosons in a tilted multilevel double-well potential. *Physical Review Letters* 99, 200402 (2007).

[160] L. D. Carr, D. R. Dounas-Frazer, and M. A. Garcia-March. Dynamical realization of macroscopic superposition states of cold bosons in a tilted double well. *Europhysics Letters* 90, 10005 (2010).

[161] Holger Cartarius and Nimrod Moiseyev. Fingerprints of exceptional points in the survival probability o f resonances in atomic spectra. *Physical Review A* 84, 013419 (2011).

[162] Markus Glück, Andrey R. Kolovsky, and Hans Jürgen Korsch. Wannier-Stark resonances in optical and semiconductor superlattices. *Physics Reports* 366, 103 (2002).

[163] Holger Cartarius, Jörg Main, and Günter Wunner. Exceptional points in the spectra of atoms in external fields. *Physical Review A* 79, 053408 (2009).

[164] P. Schmelcher and L. S. Cederbaum. Two-body effects of the hydrogen atom in crossed electric and magnetic fields. *Chemical Physics Letters* 208, 548 (1993).

[165] D. Delande, A. Bommier, and J. C. Gay. Positive-energy spectrum of the hydrogen atom in a magnetic field. *Physical Review Letters* 66, 141 (1991).

[166] J. Main and G. Wunner. Rydberg atoms in external fields as an example of open quantum systems with classical chaos. *Journal of Physics B: Atomic, Molecular and Optical Physics* 27, 2835 (1994).

[167] Jörg Main. Use of harmonic inversion techniques in semiclassical quantization and analysis of quantum spectra. *Physics Reports* 316, 233 (1999).

[168] Jacob Fuchs, Jörg Main, Holger Cartarius, and Günter Wunner. Harmonic inversion analysis of exceptional points in resonance spectra. *Journal of Physics A* 47, 125304 (2014). Published between submission and publication of this thesis.

[169] Holger Cartarius and Eli Pollak. Imaginary time Gaussian dynamics of the $Ar_3$ cluster. *The Journal of Chemical Physics* 134, 044107 (2011).

[170] Pavel Frantsuzov, Arnold Neumaier, and Vladimir A. Mandelshtam. Gaussian resolutions for equilibrium density matrices. *Chemical Physics Letters* 381, 117 (2003).

[171] Pavel A. Frantsuzov and Vladimir A. Mandelshtam. Equilibrium properties of quantum water clusters by the variational Gaussian wavepacket method. *The Journal of Chemical Physics* 128, 094304 (2008).

[172] Riccardo Conte and Eli Pollak. Comparison between different Gaussian series representations of the imaginary time propagator. *Physical Review E* 81, 036704 (2010).

[173] Hans Feldmeier and Jürgen Schnack. Molecular dynamics for fermions. *Reviews of Modern Physics* 72, 655 (2000).

[174] Ronald A. Aziz and M. J. Slaman. The argon and krypton interatomic potentials revisited. *Molecular Physics* 58, 679 (1985).

[175] E. Pahl, F. Calvo, L. Koči, and P. Schwerdtfeger. Accurate Melting Temperatures for Neon and Argon from Ab Initio Monte Carlo Simulations. *Angewandte Chemie International Edition* 47, 8207 (2008).

[176] G. Franke, E. Hilf, and L. Polley. Quantum mechanics and phase transitions in small noble-gas clusters. *Zeitschrift für Physik D Atoms, Molecules and Clusters* 9, 343 (1988).

[177] Peter Borrmann. How should thermodynamics for small systems be done? *Computational Materials Science* 2, 593 (1994).

[178] C. J. Tsai and K. D. Jordan. Use of the histogram and jump-walking methods for overcoming slow barrier crossing behavior in Monte Carlo simulations: Applications to the phase transitions in the $(Ar)_{13}$ and $(H_2O)_8$ clusters. *The Journal of Chemical Physics* 99, 6957 (1993).

[179] Shesheng Zhang and Eli Pollak. Monte Carlo Method for Evaluating the Quantum Real Time Propagator. *Physical Review Letters* 91, 190201 (2003).

[180] Eli Pollak and Jiushu Shao. Systematic Improvement of Initial Value Representations of the Semiclassical Propagator. *The Journal of Physical Chemisty A* 107, 7112 (2003).

[181] Holger Cartarius. Structure and dissociation of the $Ar_6$ cluster with the frozen Gaussian imaginary time propagator (2014). In preparation.

[182] Holger Cartarius and Eli Pollak. First-order corrections to semiclassical Gaussian partition functions for clusters of atoms. *Chemical Physics* 399, 135 (2012).

[183] Thawatchai Mayteevarunyoo, Boris A. Malomed, and Athikom Reoksabutr. Solvable model for solitons pinned to a parity-time-symmetric dipole. *Physical Review E* 88, 022919 (2013).

[184] James Adduci and Boris Mityagin. Eigensystem of an $L^2$-perturbed harmonic oscillator is an unconditional basis. *Central European Journal of Mathematics* 10, 569 (2012).

[185] Boris Mityagin and Petr Siegl. Root system of singular perturbations of the harmonic oscillator type operators (2013). Preprint arXiv:1307.6245.

[186] Daniel Haag, Holger Cartarius, and Günter Wunner. A Bose-Einstein condensate with $\mathcal{PT}$-symmetric loss and gain in a harmonic trap: A test of rigorous estimates. *Acta Polytechnica* 54, 116 (2014). Published between submission and publication of this thesis.

[187] David Krejčiřík and Petr Siegl. $\mathcal{PT}$-symmetric models in curved manifolds. *Journal of Physics A: Mathematical and Theoretical* 43, 485204 (2010).

[188] Petr Siegl. $\mathcal{PT}$-Symmetric Square Well-Perturbations and the Existence of Metric Operator. *International Journal of Theoretical Physics* 50, 991 (2011).

# Acknowledgements

A thesis of this form is never possible without a lot of support from various people. I would like to thank all who helped to make it possible.

First of all I would like to thank my collaborators at the First Institute of Theoretical Physics of the University of Stuttgart (ITP1) who contributed to the work presented in this thesis. In particular, I am very grateful to Dennis Dast, Daniel Haag, Manuel Kreibich, Andreas Löhle, and Fabian Single for some of the numerical data. I have also greatly benefited from numerous discussions with them about all topics concerning $\mathcal{PT}$-symmetric quantum systems. Fruitful and illuminating conversations have always been possible with the members of the ITP1 working on related topics in the field of non-Hermitian quantum systems, among them Rüdiger Fortanier, Robin Gutöhrlein, and Professor Dr. Jörg Main. I have had always the full support of the head of the Institute, Professor Dr. Günter Wunner, who continuously has given me constructive comments, strong encouragement, and has provided an ideal environment for my habilitation. I highly appreciate this support.

I am thankful to all members of the ITP1 for the pleasant and productive working atmosphere. Christoph Schimeczek has helped me a lot in keeping the computers and other technical components in operation. I thank him, Dr. Sebastian Boblest, and my colleagues at the ITP1 named above for carefully proofreading this manuscript.

The first studies of the rare gas clusters have been done during my stay at the Weizmann Institute of Science from May 2010 to April 2011. I thank Professor Dr. Eli Pollak for the warm welcome, for sharing his knowledge of semiclassical Gaussian propagators and their applications in physics and chemistry with me, for his support, and for the ongoing collaboration. I also thank Asaf Azuri, Dr. Riccardo Conte, Shauli Daon, Dr. Reuven Ianconescu, and Dr. Jeremy Moix for many helpful discussions. Financial support from the Minerva Foundation for a Minerva Fellowship is gratefully acknowledged.

Many topics of this thesis would not have been possible without enlightening and inspiring collaborations with experts in the respective fields of research. I would like to thank Professor Dr. Dieter Heiss and Professor Dr. Nimrod Moiseyev for a large number of valuable conversations. Furthermore, I thank Dr. Eva-Maria Graefe for stimulating discussions on the stability properties of Bose-Einstein condensates in complex potentials. My appreciation goes to Dr. Petr Siegl for helpful explanations on many mathematical aspects. I also wish to thank Dr. Raam Uzdin for enlightening remarks on the decay mechanism of resonances at exceptional points. I have also benefited from insightful comments and suggestions by Professor Dr. Ali Mostafazadeh.

This thesis is one step in the formal habilitation process and I wish to thank the

members of the mentor group Professor Dr. Hans Peter Büchler, Professor Dr. Tilman Pfau, Professor Dr. Udo Seifert, Professor Dr. Hans-Rainer Trebin, and Professor Dr. Günter Wunner for their support during the procedure. In advance I would like to thank the referees, who will be appointed after this thesis will have been filed, for their effort. I am particularly grateful to Professor Dr. Jörg Main, who encouraged me to pursue a scientific career after my PhD.

# Zusammenfassung in deutscher Sprache

Im ersten Teil dieser Habilitationsschrift wird eine besondere Form nichthermitescher Hamiltonoperatoren behandelt. Obwohl die Quantenmechanik auf hermiteschen Operatoren aufbaut, ist die Anwendung nichthermitescher Operatoren oft sinnvoll, da sie einen eleganten Zugang zu offenen Quantensystemen, also Systemen, die mit einer Umgebung in Kontakt stehen, bieten. Einen Überblick über die verschiedenen Anwendungsmöglichkeiten bietet das Buch von Moiseyev [1]. In dieser Habilitationsschrift treten zwei wichtige Anwendungen auf, nämlich die Untersuchung von nichthermiteschen Hamiltonoperatoren mit Paritäts-Zeit-Symmetrie und die Modellierung des Zerfalls von Resonanzen, der mit Hilfe eines nichthermiteschen Hamiltonoperators im Rahmen der zeitunabhängigen Schrödingergleichung behandelt werden kann.

Hamiltonoperatoren mit einer Paritäts-Zeit-Symmetrie, kurz $\mathcal{PT}$-Symmetrie, haben in den letzten Jahren eine stets anwachsende Aufmerksamkeit erfahren, seit Bender und Boettcher [4] gezeigt haben, dass sie bemerkenswerte, für die Physik interessante Eigenschaften besitzen. Sie beschreiben Systeme mit räumlich getrennten Gewinn- und Verlusttermen, die zu einem Anwachsen oder Abfall der Amplitude der Wellenfunktion führen. Eine wesentliche besondere Eigenschaft der $\mathcal{PT}$-symmetrischen Hamiltonoperatoren ist, dass sie ein vollständig reelles Spektrum der Energieeigenwerte erlauben, sie ermöglichen also trotz Gewinn- und Verlusteffekten Wellenfunktionen, die stationär sind. Diese Effekte sind nicht nur in der Quantenmechanik interessant sondern auch in der Optik [6, 8, 10, 14–17]. In optischen Wellenleitern gelangen die ersten experimentellen Umsetzungen $\mathcal{PT}$-symmetrischer Systeme [2, 3].

Trotz des beachtlichen Erfolgs, dass ein experimenteller Beweis der Eigenschaften nichthermitescher $\mathcal{PT}$-symmetrischer Systeme erbracht wurde, bleibt dieser jedoch auf die Optik beschränkt. In einem originären Quantensystem steht ein solcher Beweis noch aus. Zweck des ersten Teils dieser Habilitationsschrift ist es, von theoretischer Seite den Nachweis zu erbringen, dass sich ein Bose-Einstein-Kondensat in einem Doppelmuldenpotential [18], wie von Klaiman und anderen vorgeschlagen [8], dafür eignet. Die $\mathcal{PT}$-Symmetrie wird in diesem System dadurch umgesetzt, dass in einer Mulde Atome in das Kondensat eingekoppelt und auf der anderen Seite ausgekoppelt werden.

Zwar werden $\mathcal{PT}$-symmetrische Quantensysteme schon seit vielen Jahren untersucht [4, 7, 11, 12, 19, 20], Bose-Einstein-Kondensate unterscheiden sich von diesen aber in einem wesentlichen Punkt. Bei ausreichend niedrigen Temperaturen werden sie im Molekularfeldgrenzwert von der Gross-Pitaevskii-Gleichung [21, 22] beschrieben. Diese ist nicht-

linear und damit ist nicht mehr sichergestellt, dass $\mathcal{PT}$-symmetrische Lösungen der stationären Gross-Pitaevskii-Gleichung mit reellen Energien existieren. Die Nichtlinearität kann als reeller Bestandteil des Potentials angesehen werden. Nur wenn dieser invariant unter Raumspiegelungen ist und der lineare Anteil des Operators $\mathcal{PT}$-symmetrisch ist, ist der zugehörige nichtlineare Hamiltonoperator insgesamt $\mathcal{PT}$-symmetrisch. Die $\mathcal{PT}$-Symmetrie des nichtlinearen Operators hängt also von seiner eigenen Lösung ab. Vorherige Untersuchungen eines nichthermiteschen Bose-Hubbard-Dimers [9, 23, 24] und nichtlinearer optischer Systeme [25–31] lassen jedoch auf eine geeignete $\mathcal{PT}$-symmetrische Lösung hoffen. In dieser Habilitationsschrift wird schrittweise, zuerst anhand von Lösungen der zeitunabhängigen Schrödingergleichung, anschließend mit dynamischen Rechnungen, gezeigt, dass Bose-Einstein-Kondensate sich tatsächlich als experimentell realisierbares $\mathcal{PT}$-symmetrisches Quantensystem eignen. Außerdem werden zwei Vorschläge für eine experimentelle Umsetzung gegeben.

Nichthermitesche Quantensysteme enthalten jedoch noch wesentlich mehr Effekte, die in hermiteschen Quantensystemen nicht auftreten können. Dazu gehören exzeptionelle Punkte, also isolierte Punkte in einem mindestens zweidimensionalen Parameterraum, an denen zwei oder mehr Resonanzeigenzustände zusammenfallen, sodass ihre Energien *und* Wellenfunktionen identisch sind [1, 36, 37]. In theoretischen Arbeiten wurden exzeptionelle Punkte in vielen Systemen gefunden [9, 23, 24, 42–45], sie wurden in Mikrowellenexperimenten [38, 39] und elektrischen Schwingkreisen [74] experimentell nachgewiesen, jedoch steht auch in diesem Fall eine experimentelle Beobachtung in einem Quantensystem aus. In dieser Habilitationsschrift wird ein Vorschlag präsentiert, wie dies über ein einzigartiges, nicht rein exponentielles Zerfallsverhalten der Resonanzen [24, 46–50] des Wasserstoffatoms in gekreuzten äußeren elektrischen und magnetischen Feldern an einem exzeptionellen Punkt gelingen kann.

Der zweite Teil der Habilitationsschrift beschäftigt sich mit einem anderen Zugang zu Systemen, in denen eine Verbindung zwischen gebundenen und ungebundenen Zuständen besteht. Edelgascluster sind ein aktives Forschungsgebiet, da sie in recht einfachen Systemen eine große Bandbreite an thermodynamischen Eigenschaften enthalten [51–57]. Dazu gehören insbesondere Umwandlungen ihrer Struktur oder Phasenübergänge bei ansteigender Temperatur. Diese Phänomene treten bei niedrigen Temperaturen und auf atomarer Längenskala auf. Daher sind präzise quantenmechanische Rechnungen nötig, in denen der Boltzmannoperator $K = \exp(-\beta H)$ ausgewertet werden muss. Dafür existieren numerisch exakte Methoden, die jedoch mit steigender Teilchenzahl schnell aufwendig werden und nicht mehr anwendbar sind. Aus diesem Grund werden verlässliche Näherungsverfahren benötigt, die numerisch besser skalieren. In dieser Habilitationsschrift wird eine dieser Näherungen eingeführt, auf mehrdimensionale Systeme erweitert und zur Berechnung der thermodynamischen Effekte der $Ar_3$- und $Ar_6$-Cluster angewandt. Die semiklassische Näherung besteht darin, den Imaginärzeitpropagator durch die Propagation einer gaußschen Wellenfunktion zu ersetzen, deren Breite konstant gehalten wird. Mit ihr lässt sich die Zustandssumme mit geringem numerischen Aufwand auswerten. Aus den Ableitungen der Zustandssumme gewinnt man dann die mittlere

Energie sowie die Wärmekapazität.

Die Anwendung auf so scheinbar einfache Cluster wie $Ar_3$ und $Ar_6$ ist deshalb interessant, weil es trotz ihrer Einfachheit ungelöste elementare Fragen zu ihren thermodynamischen Eigenschaften gibt. So zeigen exakt-numerische Monte-Carlo-Rechnungen [57], dass $Ar_3$ bei steigender Temperatur in einem Schritt zu drei freien Atomen dissoziiert, diese Ergebnisse sind jedoch aufgrund starker numerischer Fluktuationen nicht gesichert. Die semiklassische gaußsche Methode ermöglicht eine Antwort auf diese Frage. Darüber hinaus wird sie bei der Betrachtung des $Ar_6$-Clusters so erweitert, dass man neben der Zustandssumme auch die thermodynamischen Mittelwerte der Abstände der Atome im Cluster berechnen kann, was wichtig ist, um die Struktur aufklären zu können.

Bei Näherungsmethoden stellt sich immer die Frage, ob ihre Genauigkeit für die untersuchten Fragen ausreichend ist. Dies wird für die entwickelte Methode auf mehrere Arten untersucht. Die mit ihr erhaltenen Ergebnisse werden im Fall des $Ar_3$-Clusters mit numerisch exakten Methoden, ansonsten mit einer genaueren, aber auch numerisch aufwendigeren gaußschen Methode, bei der sich die Breitenmatrix frei dynamisch entwickeln kann, verglichen. Darüber hinaus bietet die von Pollak und anderen entwickelte zeitabhängige Störungsrechnung [68, 69] die Möglichkeit die Qualität der gaußschen Näherung intrinsisch, das heißt ohne die Heranziehung anderer Rechnungen, auszuwerten. Im Rahmen dieser Störungsrechnung ist die vorgestellte gaußsche Näherung die führende Ordnung einer Reihenentwicklung. Die Korrekturen erster Ordnung aus dieser Reihe werden für die gaußsche Methode berechnet und es wird gezeigt, wie sie herangezogen werden können, um die Qualität der Näherung einzuschätzen und die Gültigkeit der Ergebnisse objektiv zu bewerten.

## Teil I. Quantensysteme mit nichthermiteschen Hamiltonoperatoren zur Modellierung von Gewinn- und Verlusttermen

**Ausgeglichene Gewinn- und Verlustterme in Quantensystemen** Komplexe Potentiale werden in dieser Habilitationsschrift eingeführt, um Verluste oder Gewinne der Amplitude einer Wellenfunktion beschreiben zu können. Wenn sie auftreten, nimmt die Kontinuitätsgleichung für die Wahrscheinlichkeitsdichte der Quantenmechanik die in Gleichung (2.3) vorgestellte erweiterte Form an. Danach lässt sich interpretieren, dass ein positives imaginäres Potential die Amplitude anwachsen lässt, also einen Gewinn beschreibt, ein negativer Imaginärteil sie abfallen lässt, also einen Verlust bedeutet. Der physikalische Hintergrund dieses Effekts ist in Abbildung 2.1 dargestellt. Wir nehmen an, dass wir ein abgeschlossenes System mit dem in roten Linien in Abbildung 2.1 (a) dargestellten Potential haben. In diesem könnte sich die Wellenfunktion wie in grünen Linien dargestellt ausbreiten. Daraus wird ersichtlich, dass die Dynamik des Systems es sicher erlaubt, dass die Aufenthaltswahrscheinlichkeit sich von einer Mulde in die andere verschiebt. Betrachtet man aber nur die inneren beiden Mulden als eigenes System, in dem die äußeren nicht vorkommen [blaue Linien für das Potential in Abbildung 2.1 (b)], so muss man den Effekt, dass die Aufenthaltswahrscheinlichkeit innerhalb dieser zwei

Mulden zu und abnehmen kann, anders simulieren. Dies gelingt gerade durch komplexe Potentiale und in diesem Sinn sind sie in der Habilitationsschrift zu verstehen.

Als Hamiltonoperatoren $H$ mit einer Paritäts-Zeit-Symmetrie werden solche bezeichnet, die entsprechend Gleichung (2.9a) mit dem $\mathcal{PT}$-Operator vertauschen. Für diese lassen sich verschiedene Eigenschaften zeigen, die jedoch für die Anwendung in dieser Habilitationsschrift überprüft werden müssen, da mit Bose-Einstein-Kondensaten ein nichtlineares Quantensystem untersucht wird und die Eigenschaften nur für lineare Operatoren bewiesen sind. Es lässt sich jedoch mit recht einfachen Rechnungen aus Abschnitt 2.2.2 zeigen, dass die wichtigsten Aussagen für nichtentartete chemische Potentiale in der Gross-Pitaevskii-Gleichung weiterhin gelten. Die chemischen Potentiale sind bei einem $\mathcal{PT}$-symmetrischen linearen Teil des Hamiltonoperators entweder reell oder treten in konjugiert-komplexen Paaren auf. Sie sind genau dann reell, wenn die zugehörige Wellenfunktion $\mathcal{PT}$-symmetrisch ist. Wenn $\psi$ eine Lösung mit komplexem chemischen Potential $\mu$ ist, so ist $\mathcal{PT}\psi$ die Lösung zum dazu konjugiert-komplexen $\mu$.

**Lösungen der zeitunabhängigen Gross-Pitaevskii-Gleichung für ein Bose-Einstein-Kondensat in einer $\mathcal{PT}$-symmetrischen Doppelmulde** Als erstes elementares Modell wird ein Bose-Einstein-Kondensat in einem $\mathcal{PT}$-symmetrischen Doppel-Delta-Potential eingeführt, da es aufgrund seiner Einfachheit einen guten Einblick in die mathematische Struktur verspricht. Es ist durch die eindimensionale Gross-Pitaevskii-Gleichung (3.3) mit dem Energieeigenwert $\mu = -\kappa^2$ gegeben. Die Gewinn- und Verlusteffekte werden durch den Imaginärteil des Potentials beschrieben, dessen Stärke durch den Parameter $\gamma$ definiert wird. Zunächst wird überprüft, ob der lineare Spezialfall $g = 0$ alle Eigenschaften linearer $\mathcal{PT}$-symmetrischer Quantensysteme enthält. Dies ist der Fall und kann für die Eigenwerte $\kappa$ in Abbildung 3.1 abgelesen werden. Unterhalb eines kritischen Wertes $\gamma_{\mathrm{EP}}$ des Gewinn-Verlust-Parameters treten zwei reelle Energieeigenwerte auf, die zugehörigen Zustände fallen bei $\gamma_{\mathrm{EP}}$ in einem exzeptionellen Punkt zusammen. Für größere Werte von $\gamma$ treten zwei komplexe und zueinander konjugiert-komplexe Eigenwerte auf. Die zugehörigen Eigenzustände erfüllen die oben genannten Beziehungen. Das Modell ist somit für die Untersuchung des nichtlinearen Falls gut geeignet.

Im Fall der Gross-Pitaevskii-Gleichung, also $g \neq 0$, ergeben sich in den Spektren Ähnlichkeiten aber auch deutliche Unterschiede zum linearen Fall. Die Eigenwerte sind in Abbildung 3.3 aufgetragen. Als erstes wichtiges Ergebnis stellt man fest, dass reelle Werte für das chemische Potential $\mu$ weiterhin bestehen. Nach den allgemein oben festgestellten Beziehungen müssen die zugehörigen Wellenfunktionen $\mathcal{PT}$-symmetrisch sein. Dies wird in den Abbildungen 3.4 (a) und (b) bestätigt. Die Wellenfunktionen besitzen einen symmetrischen Real- und einen antisymmetrischen Imaginärteil. Wie im linearen Fall vereinigen sich die beiden reellen Lösungen in einem exzeptionellen Punkt. Aus diesem gehen bei weiterer Erhöhung des Gewinn-Verlust-Parameters allerdings keine komplexen Energieeigenwerte hervor. Diese treten bereits bei einem kleineren Wert von $\gamma$ auf und spalten vom Grundzustand ab [oberer Zweig in Abbildung 3.3, da $\kappa$ und nicht das che-

mische Potential $\mu$ aufgetragen ist]. Diese Energien sind zueinander konjugiert-komplex und die zugehörigen Wellenfunktionen in den Abbildungen 3.4 (c) und (d) erfüllen die erwartete Symmetrie $\mathcal{PT}\psi_1 = \psi_2$.

Die gefundenen Spektren sind nicht auf den idealisierten Fall des Doppel-Delta-Potentials beschränkt. Ein dazu vollkommen analoges Verhalten lässt sich für das dreidimensionale Potential (3.12) finden. In Abbildung 3.7 werden zunächst die Spektren für die eindimensionale Projektion aus Abbildung 3.6 über dem Gewinn-Verlust-Parameter $\Gamma$ aufgetragen. Sie unterscheiden sich qualitativ nicht von denen für das Doppel-Delta-Potential. Auch die gefundenen Wellenfunktionen in den Abbildungen 3.8 und 3.9 zeigen die erwartete Form. In einem variationellen Näherungsverfahren werden die Eigenzustände des vollen dreidimensionalen Problems berechnet. Dabei zeigt sich, dass die zwei zusätzlichen Raumdimensionen, wie zu erwarten war, keine zusätzliche Information einbringen, da der $\mathcal{PT}$-symmetrische imaginäre Potentialanteil nur auf eine Richtung bezogen ist. Oder anders ausgedrückt, man verliert durch die Reduktion der Rechnungen auf eine Dimension keine physikalisch relevanten Effekte und sie ist für alle weiteren Betrachtungen ausreichend. Es ist sogar möglich, die Ergebnisse für das dreidimensionale Problem mit sehr guter quantitativer Übereinstimmung aus den eindimensionalen Rechnungen zu gewinnen.

Abbildung 3.10 fasst die wichtigsten Resultate aus den Spektren des nichtlinearen Falles in Form eines Phasendiagramms zusammen. In Abhängigkeit der Parameter $g$ für die Nichtlinearität und $\Gamma$ für den Gewinn-Verlust-Effekt beobachtet man drei Bereiche. Es gibt die bereits aus linearen Systemen bekannten Fälle, dass nur $\mathcal{PT}$-symmetrische oder nur $\mathcal{PT}$-gebrochene Lösungen auftreten. Darüber hinaus stellt man zwischen dem Wert $\Gamma_{\mathrm{cr}}$, an dem die $\mathcal{PT}$-gebrochenen Zustände vom Grundzustand abspalten, und dem Wert $\Gamma_{\mathrm{EP}}$, an dem die $\mathcal{PT}$-symmetrischen verschwinden, die Koexistenz zusammengehöriger $\mathcal{PT}$-symmetrischer und $\mathcal{PT}$-gebrochener Lösungen fest. Diese Tatsache sowie die ungleiche Anzahl an Lösungen bei Variation von $g$ oder $\Gamma$ erscheint zunächst ungewöhnlich und mathematisch unvollständig. Mit einer geeigneten komplexen Erweiterung lässt sich das jedoch aufklären. Diese wurde für das Doppel-Delta-Potential durchgeführt. Dazu trennt man nach Gleichung (4.7) die Gross-Pitaevskii-Gleichung in ihren Real- und Imaginärteil auf und erlaubt dann den darin vorkommenden reellen Koeffizienten, komplex zu werden, wie es in den Gleichungen (4.8a) bis (4.8d) angegeben ist. Das Ergebnis sind die Spektren aus Abbildung (4.4), in denen, anders als in Abbildung 3.3, die Zahl der Lösungen nicht mehr von $\gamma$ abhängt. Das scheinbar ungewöhnliche Verhalten aus Abbildung 3.3 lässt sich also auf die nichtanalytische Form der Gross-Pitaevskii-Gleichung zurückführen. Darüber hinaus gelingt es, mit der analytischen Erweiterung nachzuweisen, dass der kritische Punkt $\Gamma_{\mathrm{cr}}$ ein exzeptioneller Punkt dritter Ordnung ist. Wählt man einen geeigneten Asymmetrieparameter aus Gleichung (4.11), der eine Asymmetrie des Realteils des Potentials beschreibt, und umkreist ihn gemäß Gleichung (4.12) in der komplexen Ebene, so findet man das Verhalten aus Abbildung 4.7 (b). Für einen vollständigen Kreis im Parameterraum beobachtet man eine Permutation aller drei Eigenwerte, die am kritischen Punkt zusammenfallen. Das ist ein charakteristisches Signal

für einen exzeptionellen Punkt dritter Ordnung.

**Stabilität und Dynamik in der $\mathcal{PT}$-symmetrischen Doppelmulde** Bevor auf die Dynamik eines Bose-Einstein-Kondensats eingegangen wird, wird die Stabilität der gefundenen stationären Zustände untersucht. Dabei sind nur die Zustände mit reellem chemischem Potential interessant. Die gefundenen Zustände mit komplexem chemischem Potential wachsen entweder an (positiver Imaginärteil) oder fallen ab (negativer Imaginärteil), sind also keine stationären Lösungen, auch wenn sie die zeitunabhängige Gross-Pitaevskii-Gleichung lösen. Die Stabilitätsanalyse erfolgt mit Hilfe der Bogoliubov-de Gennes-Gleichungen (5.2). In ihnen tritt ein Stabilitätseigenwert $\omega$ auf. Dieser ist im Ansatz (5.1b) so gewählt, dass ein rein reeller Wert anzeigt, dass der Zustand dynamisch stabil auf kleine Störungen reagiert, und ein Imaginärteil auf ein exponentielles Anwachsen der Störung hindeutet.

Die Stabilitätsanalyse zeigt, dass der angeregte Zustand bis kurz vor seinem Verschwinden stabil bleibt, wie aus seinen Stabilitätseigenwerten in Abbildung 5.1 abgelesen werden kann. Komplizierter ist das Verhalten des Grundzustands, wie Abbildung 5.2 verdeutlicht. Dieser ist bei kleinen Werten des Gewinn-Verlust-Parameters $\Gamma$ stabil. Etwa dort, wo von ihm die komplexen Zustände abspalten, wird er jedoch instabil. Dieser Wechsel ist grundsätzlich nicht überraschend, da die Zustände mit komplexem chemischem Potential wie oben beschrieben dynamisch instabil sind, der Stabilitätswechsel wäre jedoch exakt am kritischen Punkt $\Gamma_{\mathrm{cr}}$ erwartet worden. Man findet allerdings, dass dies nur in der Nähe dieses Punktes geschieht. Dieses Verhalten wurde für die Zustände im Doppel-Delta-Potential, das sich als Testkandidat dafür gut eignet, genauer untersucht. Auch hier tritt die Unstimmigkeit zwischen dem kritischen Punkt $\gamma_{\mathrm{cr}}$ und dem Stabilitätswechsel bei $\gamma_\omega$ auf. Der Unterschied $\Delta\gamma = \gamma_{\mathrm{cr}} - \gamma_\omega$ hängt von der Stärke $g$ der Nichtlinearität ab und ist in Abbildung 5.4 dargestellt. Dies legt die Vermutung nahe, dass die Nichtlinearität für das Verhalten verantwortlich ist. Tatsächlich kann man es darauf zurückführen, dass die Nichtlinearität in der Gross-Pitaevskii-Gleichung von der Norm abhängt. Beseitigt man diese Abhängigkeit nämlich über die Transformation (5.6), so stellt man fest, dass die Unstimmigkeit verschwindet, also $\Delta\gamma = 0$. Ein Beispiel dafür ist in Abbildung 5.5 dargestellt.

Die dynamischen Rechnungen werden mit einer Superposition aus den beiden Lösungen mit reellen Eigenwerten gestartet. Beispiele sind in den Abbildungen 6.2 (a) bis (c) für das nichtlineare Doppel-Delta-System und in den Abbildungen 6.3 (a) bis (c) für die ausgedehnte Doppelmulde gezeigt. Für verschwindende Gewinn- und Verlusteffekte beobachtet man die typischen Rabi-Oszillationen der Zweizustandssysteme [Abbildungen 6.2 (a) und 6.3 (a)]. Mit Gewinn- und Verlusteffekten ändert sich das Bild leicht. Die Oszillationsfrequenz sinkt und die Phasenbeziehung der Wellenfunktionen in den beiden Mulden beträgt nicht mehr $\pi$. Letzteres bedeutet, dass die Wahrscheinlichkeit, das durch die Wellenfunktion beschriebene Teilchen in beiden Mulden zusammen zu finden, zu manchen Zeiten höher ist als zu anderen. Dies ist durch die Gewinn- und Verlustef-

fekte möglich, eine Erhaltung der Wahrscheinlichkeit muss nicht mehr gelten, wie oben beschrieben wurde. Auch in den Abbildungen 6.2 (d) und 6.3 (d) startet die Dynamik mit einer Superposition der beiden Eigenzustände mit reellem chemischem Potential, sie verhält sich jedoch vollkommen verschieden von den vorherigen Beispielen. Bevor eine Oszillation beginnen kann, kommt es zu einem ungebremsten Anwachsen der Amplitude in der Mulde mit Gewinn. Das passiert, obwohl sich das Kondensat zu Beginn nahezu ausschließlich in der Mulde mit Verlust befindet.

Eine genauere Untersuchung dieses Verhaltens deckt auf, dass der Anfangszustand sehr entscheidend für die Art der Dynamik (stabile Oszillation oder ungebremstes Anwachsen) ist. Ist der Anfangszustand so gestaltet, dass die Norm zu Beginn der Zeitentwicklung ansteigt, kann es passieren, dass die Wellenfunktion in die instabile Dynamik gerät. Die Ursache dafür wird bei einem Blick auf die Spektren in den Abbildungen 3.3 oder 3.7 ersichtlich. Steigt die Norm $N$ der Wellenfunktion an, so kann man das auch als eine Lösung der Gross-Pitaevskii-Gleichung mit Norm 1 und einer nach Gleichung (5.8) reskalierten Stärke der Nichtlinearität $g$ auffassen. Zu dieser gehört aber ein neues Eigenwertdiagramm mit zu kleineren Werten verschobenem kritischen Punkt $\gamma_{\mathrm{cr}}$ oder $\Gamma_{\mathrm{cr}}$. Das heißt, die komplexen Lösungen, die die Instabilität hervorrufen, treten möglicherweise beim vorliegenden Wert von $\gamma$ oder $\Gamma$ auf, wenn die Norm ansteigt. Sobald sie in Erscheinung treten, dominiert das Ansteigen in der Mulde mit Gewinn die Dynamik und man beobachtet das explosionsartige Verhalten aus den Abbildungen 6.2 (d) und 6.3 (d).

**Vorschläge für eine experimentelle Umsetzung eines Bose-Einstein-Kondensats in einer $\mathcal{PT}$-symmetrischen Doppelmulde** In dieser Habilitationsschrift werden zwei Vorschläge für eine experimentelle Umsetzung eines $\mathcal{PT}$-symmetrischen Potentials für ein Bose-Einstein-Kondensat gegeben. Der erste Vorschlag greift die Idee auf, die schon bei der Einführung der komplexen Potentiale gegeben wurde. Er beruht auf der Annahme, dass ein Kondensat sich in einer Vierfachmulde, wie sie in Abbildung 7.1 dargestellt ist, befindet und die Dynamik in diesem System betrachtet wird. Basierend auf einer Rechnung mit einem einfachen Matrixmodell lässt sich zeigen, dass bei einer zeitabhängigen Variation des Potentials in diesem System für die inneren beiden Mulden exakt die gleiche Dynamik erhalten werden kann wie in einer Doppelmulde aus den vorherigen Betrachtungen, in der ein komplexes Potential wirkt. Ein Beispiel für einen stationären $\mathcal{PT}$-symmetrischen Zustand ist in Abbildung 7.2 dargestellt. Wenn man das Potentialminimum der äußeren beiden Mulden und die Breite der Barrieren verändert, kann man erreichen, dass die Besetzung der inneren beiden Mulden [$n_1$ und $n_2$ in Abbildung 7.2 (a)] konstant bleibt. Dabei weisen das Abfallen der Besetzung der linken äußeren Mulde und das Ansteigen der Besetzung der rechten äußeren Mulde [$n_0$ und $n_3$ in Abbildung 7.2 (b)] nach, dass es einen Teilchenstrom in das und aus dem inneren Doppelmuldensystem gibt, d.h. die Gewinn- und Verlusteffekte sind vorhanden, gleichen sich aber aus, wie es in einem $\mathcal{PT}$-symmetrischen Fall zu erwarten ist. Auch die stabilen Oszillationen

unter Gewinn- und Verlusteffekten, wie sie die dynamischen Rechnungen in komplexen Potentialen gezeigt haben, können in einem solchen System gefunden werden, was in Abbildung 7.3 (a) dargestellt ist.

Die Rechnungen zu den Abbildungen 7.2 und 7.3 beruhen auf einer einfachen Matrixdarstellung, sie können jedoch mit dem Ansatz aus Gleichung (7.10), bei dem man annimmt, dass in jeder Mulde das Kondensat durch eine Gaußfunktion beschrieben wird, mit der dreidimensionalen Gross-Pitaevskii-Gleichung in Verbindung gebracht werden. Damit kann gezeigt werden, dass dieses Verfahren auch für experimentell mögliche Aufbauten umgesetzt werden kann. Abbildung 7.5 zeigt ein auf diesem Weg berechnetes Beispiel für ein Kondensat aus $^{87}$Rb-Atomen. Dabei wird mit einem symmetrischen Grundzustand (siehe Abbildung 7.4) begonnen. Anschließend wird das Potential so variiert, dass sich ein Teilchenstrom aus der linken äußeren Mulde in die Mitte und aus der Mitte in die rechte äußere Mulde ergibt. Nach der Zeit $t \approx 70$ stellt sich in den mittleren beiden Mulden der gewünschte $\mathcal{PT}$-symmetrische Zustand ein, wie in Abbildung 7.5 (e) zu erkennen ist.

Als zweite Möglichkeit für eine experimentelle Umsetzung wird vorgeschlagen, dass man den experimentell bereits umgesetzten [91] Vorgang nutzt, dass ein Bose-Einstein-Kondensat mit einer Bragg-Streuung aus einer Mulde ausgekoppelt werden kann. Man nimmt an, dass man ein Bose-Einstein-Kondensat in einer Doppelmuldenstruktur vorliegen hat. Eine weitere Mulde wird als Reservoir genutzt. Dies ist in Abbildung 7.6 (a) skizziert. Aus diesem Reservoir werden Atome ausgekoppelt und in eine Mulde des Doppelmuldensystems eingekoppelt. Umgekehrt koppelt man aus der anderen Mulde Atome aus und führt sie wieder dem Reservoir zu. Auf Basis des Doppel-Delta-Potentials konnte mit Modellrechnungen gezeigt werden, dass dieses Vorgehen prinzipiell funktioniert. Abbildung 7.7 zeigt eine numerisch exakte Simulation dazu. Insbesondere der angeregte Zustand mit reellem chemischem Potential, der in Abbildung 7.7 links oben dargestellt ist, lässt sich über eine recht lange Zeit stabil simulieren. Also gelingt es auch in diesem Fall, den effektiv von einem komplexen Potential beschriebenen Gewinn- und Verlusteffekt durch eine echte Kopplung an eine Umgebung zu simulieren.

**Charakteristisches Zerfallsverhalten von Resonanzen an exzeptionellen Punkten**
Resonanzen zerfallen unter normalen Umständen mit einem rein exponentiellen Zeitverhalten, d.h. ihre Besetzungswahrscheinlichkeit nimmt mit $\mathrm{e}^{-\Gamma t}$ ab. An einem exzeptionellen Punkt stellt man jedoch fest, dass dies nicht mehr zwangsweise gilt. Wird nämlich eine Überlagerung der beiden Resonanzen, die am exzeptionellen Punkt zusammenfallen, angeregt, so fällt die Besetzungswahrscheinlichkeit dieser Überlagerung exakt mit dem Zeitverhalten $|1 - at|^2\mathrm{e}^{-\Gamma t}$ ab, es enthält also einen zusätzlichen polynomialen Anteil. Gleichung (8.7) zeigt wie diese Zeitentwicklung zustande kommt.

Dieses Verhalten kann tatsächlich in einem echten Quantensystem gefunden werden. Dazu wird in dieser Habilitationsschrift eine exakt-numerische Rechnung für das Wasserstoffatom in gekreuzten elektrischen und magnetischen Feldern durchgeführt. Die

beiden äußeren Felder werden so eingestellt, dass zwei Resonanzen fast einen exzeptionellen Punkt bilden. Anschließend wird eine Überlagerung dieser beiden Resonanzen so gewählt, dass das nichtexponentielle Verhalten möglichst ausgeprägt ist. Das daraus erhaltene Zeitverhalten ist in Abbildung 8.1 dargestellt. Man erkennt deutlich, dass die Besetzungswahrscheinlichkeit zunächst sogar ansteigt und dann erst abfällt. Dieses Signal stimmt exakt mit dem überein, das man nach Gleichung (8.7) erwartet. Es beschreibt allerdings eine rein mathematische Konstruktion einer geeigneten Überlagerung beider Resonanzen. Jedoch lässt sich zusätzlich zeigen, dass dieser Effekt auch beobachtet werden kann, wenn man nur annimmt, dass man mit einem Laser ein Elektron aus dem $2p$, $m = 0$-Orbital so anregt, dass seine Energie genau den beiden gewünschten, fast entarteten Resonanzen entspricht. Abbildung 8.3 (b) zeigt das Ergebnis dieses Anregungsprozesses. Der angeregte Zustand zerfällt erneut exakt nach $|1 - at|^2 \mathrm{e}^{-\Gamma t}$, wobei der Wert von $a$ mit $(0.226 + 5.25\mathrm{i}) \cdot 10^{-5}$ so klein ist, dass er sich nur schwach bemerkbar macht. Er ist jedoch vorhanden, eindeutig nachweisbar und charakteristisch für einen exzeptionellen Punkt. Ohne einen exzeptionellen Punkt kann dieses Verhalten nicht auftreten.

## Teil II. Von gebundenen zu ungebundenen Zuständen – Dissoziationseffekte von kleinen Clustern

**Dissoziationseffekte von $\mathrm{Ar}_3$ und $\mathrm{Ar}_6$** Gaußsche Näherungsverfahren sind weit verbreitet, um thermodynamische Eigenschaften von Vielteilchensystemen zu berechnen. Sie bauen im wesentlichen darauf auf, die Imaginärzeitdynamik der Blochgleichung (9.7) näherungsweise durch eine gaußsche Wellenfunktion zu lösen und aus dieser Lösung den Imaginärzeitpropagator oder Boltzmannoperator (9.6) aufzubauen. Dabei kommt üblicherweise ein Ansatz nach Gleichung (9.8) zur Anwendung, bei dem man der Breitenmatrix der Gaußfunktion erlaubt, sich in der Imaginärzeit zu ändern. Dies führt auf die Bewegungsgleichungen (9.11a) bis (9.11c), deren Lösung, obwohl es sich bereits um eine semiklassische Näherung handelt, bei großen Teilchenzahlen sehr aufwendig werden kann. Ein Ansatz nach Gleichung (9.14), bei dem eine Gaußfunktion mit fester Breitenmatrix $\mathbf{\Gamma}$ verwendet wird, ist in dieser Hinsicht weitaus weniger aufwendig. Für die Imaginärzeitpropagation muss nur die vektorielle Bewegungsgleichung (9.16) gelöst werden.

In einem Ansatz mit einer festen Breitenmatrix stellt sich aber die Frage, wie diese gewählt werden soll, denn dafür gibt es keinen allgemeinen Ansatz. Jeder Fall muss einzeln untersucht werden. Oft bleibt als einzige Möglichkeit, mit Testrechnungen für Spezialfälle, in denen ein Ergebnis bekannt ist, durch Variation der einzelnen Matrixelemente zu bestimmen, was die beste Wahl ist. Man muss jedoch meist nicht alle Matrixelemente verwenden. In dieser Habilitationsschrift wird gezeigt, dass für einen monoatomaren Cluster die Wahl aus Gleichung (9.20) ideal ist. Sie besteht nur aus zwei Parametern, die man bestimmen muss, und trotzdem kann auch eine kompliziertere Form der Matrix kein besseres Ergebnis erzeugen. Die beiden Variationsparameter entsprechen im wesent-

lichen einer Breite der Wellenfunktion der Schwerpunktkoordinate und einer identischen Breite für alle Wellenfunktionen, die die Relativkoordinaten beschreiben.

Mit diesem gefundenen Ansatz werden zunächst die thermodynamischen Eigenschaften von $Ar_3$ untersucht. Dieser kleine Cluster eignet sich besonders, da die Methode mit anderen verglichen werden kann. Darunter sind auch numerisch exakte Rechnungen, die eine gute Einschätzung der Qualität der gaußschen Näherung ermöglichen. Solche Vergleichsrechnungen werden in den Abbildungen 9.1 und 9.2 gezeigt. Für diese wird die Zustandssumme als Spur des Boltzmannoperators berechnet und daraus werden die mittlere Energie und die Wärmekapazität aus Ableitungen gewonnen. Man erkennt deutlich, dass die gaußsche Näherung mit einer festen Breitenmatrix der oben genannten Form (2P-FG) im Bereich von Temperaturen $T \geq 20\,\mathrm{K}$ sehr gut mit allen Methoden übereinstimmt. Darunter weicht sie von den numerisch exakten Rechnungen und der flexibleren Gaußfunktion mit einer zeitlich variablen Breitenmatrix ab. Insgesamt stellt man in den Vergleichen jedoch fest, dass die Methode gut funktioniert und die kleinen numerischen Unterschiede vertretbar sind. Insbesondere ist sie vergleichbar gut wie eine Variante der Gaußnäherung mit zeitlich variabler Breitenmatrix, bei der eine Blockdiagonalstruktur der Breitenmatrix erzwungen wird (SP-TG), damit sie numerisch besser skaliert. Da die Rechnung mit der konstanten aber vollen Breitenmatrix (9.20) keine Teilchen-Teilchen-Korrelationen ignoriert, aber trotzdem numerisch weniger anspruchsvoll ist, ist sie der SP-TG-Methode überlegen.

Nach diesen Betrachtungen der Methode können die thermodynamischen Eigenschaften des $Ar_3$-Clusters untersucht werden. Dabei stellt man einen wesentlichen Effekt fest. Beim Erhöhen der Temperatur dissoziiert der Cluster in einem Schritt zu drei freien Atomen. Dies ist in Abbildung 9.3 gut zu erkennen. Die mittlere Energie weist eine Stufe auf und die Wärmekapazität zeigt eine deutliche Erhöhung in diesem Temperaturbereich. Ein Vergleich mit der klassischen Rechnung zeigt zudem, dass im Fall der quantenmechanischen Rechnung die Dissoziation bei einer um $\Delta T = 1{,}5\,\mathrm{K}$ höheren Temperatur stattfindet. Dies kann auf die Nullpunktenergie der Quantenmechanik zurückgeführt werden. Insgesamt ist der Vorgang jedoch nahezu klassisch, qualitativ ergibt sich in einer klassischen Rechnung kein anderes Verhalten.

Ein wichtiger Punkt bei den durchgeführten Rechnungen zur Dissoziation von Clustern ist ein künstliches Potential, das eingeführt werden muss, um die numerischen Integrationen beherrschbar zu machen. Der Propagator (9.14) enthält ein Integral über die Ortsvariable $\boldsymbol{q}$, das einer Mittelung über alle möglichen Anfangsorte der Imaginärzeitentwicklung entspricht. Dieses Integral muss mit Monte-Carlo-Methoden numerisch integriert werden und konvergiert nur, wenn der Raumbereich künstlich eingeschränkt wird. Dazu wird üblicherweise eine Sphäre um den Massenmittelpunkt des Clusters gewählt, als Parameter geht ihr Radius ein. Wird dieser zu eng gewählt, hat das dramatische Auswirkungen auf den Dissoziationseffekt, wie in Abbildung 9.4 ersichtlich wird. Erst ab einem Radius von $R_\mathrm{c} = 20\,\text{Å}$ wird überhaupt der Fall erreicht, dass sich die Atome frei bewegen können, wie aus der Konvergenz gegen die schwarze Linie bei $E = 9\mathrm{k}T/2$, also der thermischen Energie von drei freien Teilchen, erkannt werden kann. Ab einem Radi-

us $R_c = 32\,\text{Å}$ erhält man sinnvolle Ergebnisse, die die Dissoziation richtig wiedergeben. Dies ist ein wichtiges Ergebnis, denn oft wird der Radius zu klein gewählt.

Bei der Untersuchung des $Ar_6$-Clusters ergibt sich ein ähnliches Bild wie bei $Ar_3$. Aus Abbildung 10.1 erkennt man, dass auch dieser eine Dissoziation in einem Schritt durchführt, die jedoch aufgrund der höheren dafür benötigten Energie bei höheren Temperaturen stattfindet. Zusätzlich ist aber hier auch interessant, wie sich die einzelnen Atome im Cluster verhalten. Das ist nicht mehr so einfach wie beim $Ar_3$-Cluster. Dazu wird die gaußsche Methode 2P-FG in den Gleichungen (10.10) und (10.13) so erweitert, dass die thermodynamischen Mittelwerte aller Abstände zwischen den Atomen und deren Standardabweichungen berechnet werden können. Ein Ergebnis für tiefe Temperaturen findet man in Abbildung 10.2. Aus dieser kann man ablesen, dass der Cluster im Grundzustand die Form eines Oktaeders annimmt, an dessen Ecken die Atome sitzen. Dazu gehören Längen, die in Gruppen von drei und zwölf auftreten. In der quantenmechanischen Rechnung wird der Grundzustand ab $T \approx 3\,\text{K}$ eingenommen, in der klassischen Rechnung wird erst für $T \to 0$ das Potentialminimum angenommen, wie zu erwarten war. Bei der Dissoziation zeigt sich, dass zwei Abstände ansteigen, bevor es alle anderen tun. Dies könnte den Beginn einer Deformation des Clusters darstellen, die jedoch in der Dissoziation aufgeht, da sie keine klaren Strukturen annimmt, bevor aufgrund des Dissoziationsvorgangs alle Abstände ansteigen und sich letztendlich alle Atome frei bewegen.

**Korrekturen erster Ordnung zur gaußschen Näherung mit einer festen Breitenmatrix** Die gaußsche Näherungsmethode zeigt für die betrachteten Beispiele gute Ergebnisse, die nahe an numerisch exakten Rechnungen liegen und mit numerisch aufwendigeren Näherungsverfahren mithalten können. Will man jedoch in Fällen, in denen andere Verfahren nicht anwendbar sind, ihre Qualität beurteilen können, benötigt man eine intrinsische Methode. Einen Ansatz dafür bietet die Tatsache, dass nach Gleichung (11.1) ein Korrekturoperator eingeführt werden kann, der auf die Rekursionsgleichung (11.4) für höhere Ordnungen in einer zeitabhängigen Störungstheorie führt. Dieses Verfahren wird angewandt, um für die gaußsche Methode mit einer festen Breitenmatrix den Korrekturoperator (11.6a) und schließlich die Korrektur erster Ordnung zur Zustandssumme (11.7) zu bestimmen. Dies gelingt in einer Form, in der weitere numerische Integrationen im Ortsraum vermieden werden, was für die Anwendung in Vielteilchensystemen notwendig ist.

Die Korrekturen erster Ordnung werden in dieser Habilitationsschrift für den $Ar_3$-Cluster berechnet. Dabei werden drei wichtige Ergebnisse erhalten. Wie oben erwähnt wurde, müssen für die gewählte Form der festen Breitenmatrix zwei freie Parameter so eingestellt werden, dass sich die beste Näherung des quantenmechanischen Ergebnisses ergibt. Wie in den Abbildungen 11.1 und 11.2 dargestellt ist, kann als objektives Kriterium die Korrektur erster Ordnung herangezogen werden. Es werden die Parameter gewählt, die die kleinste Korrektur ergeben und somit bereits am nächsten am besten

Ergebnis liegen. Als zweites wichtiges Ergebnis erhält man aus Abbildung 11.3 eine Aussage, wann die gaußsche Näherung quantitativ gute Ergebnisse liefert. Dies kann nur dann der Fall sein, wenn die Korrektur erster Ordnung signifikant kleiner ist als das Ergebnis der führenden Ordnung. In der Abbildung ist das Verhältnis beider Ordnungen für die Zustandssumme aufgetragen. Wie man erkennt, divergiert es für $T \to 0$, allerdings ist es klein in dem Bereich, der physikalisch interessant ist, also bei Temperaturen, bei denen die Dissoziation aus Abbildung 9.3 stattfindet. Ein Vergleich in Abbildung 11.4 zeigt dann auch, dass die Korrektur erster Ordnung um die Dissoziation eine deutliche Verbesserung in der mittleren Energie und der Wärmekapazität ergibt und mit der gaußschen Näherung mit einer zeitlich variablen Breitenmatrix hervorragend übereinstimmt. Für $T \to 0$ ergibt die Korrektur erster Ordnung jedoch keine Verbesserung gegenüber der führenden Ordnung. Dies scheint auf den ersten Blick erstaunlich zu sein, da die Korrektur für die Zustandssumme divergiert. Es wird gezeigt, dass diese Divergenz stärker ausfallen müsste, um einen Korrekturbeitrag zur mittleren Energie erzeugen zu können. Als drittes wichtiges Ergebnis kann man jedoch festhalten, dass die Korrektur erster Ordnung im physikalisch interessanten Temperaturbereich der Dissoziation eine deutliche Verbesserung der mittleren Energie und der Wärmekapazität ergibt.

**Zentrale Aussagen und Ausblick** Die wichtigste Aussage des ersten Teils dieser Habilitationsschrift ist die Feststellung, dass Bose-Einstein-Kondensate tatsächlich ein hervorragender Kandidat für eine erstmalige experimentelle Umsetzung eines $\mathcal{PT}$-symmetrischen Quantensystems sind. Stabile Zustände in einem Doppelmuldenpotential mit Gewinn- und Verlusteffekten existieren, sie erfüllen alle notwendigen Bedingungen $\mathcal{PT}$-symmetrischer Systeme, sind beobachtbar und mit heutigen experimentellen Methoden zugänglich. Im Vergleich zu linearen Quantensystemen zeigen sie darüber hinaus durch das Wechselspiel zwischen der Nichtlinearität und den Gewinn- und Verlusteffekten interessante Eigenschaften wie exzeptionelle Punkte dritter Ordnung, ein kompliziertes Stabilitätsverhalten der stationären Zustände und eine reichhaltige Dynamik.

Es gibt allerdings auch noch viele interessante offene Fragen. Dabei stehen aus experimenteller Sicht sicher die Möglichkeiten einer Umsetzung im Vordergrund. Die bisherigen Rechnungen sind vielversprechend, allerdings enthalten sie noch Näherungen wie das einfache Matrixmodell, in dem das Viermuldensystem gelöst wurde, und die Beschränkung auf das eindimensionale Doppel-Delta-System für den Kopplungsansatz. Zur Weiterentwicklung und der Berechnung tatsächlicher Laborbedingungen sind neue numerische Verfahren wie besonders angepasste Gitterrechnungen erforderlich. Darüber hinaus sind Erweiterungen des $\mathcal{PT}$-symmetrischen Doppelmuldensystems denkbar, z.B. eine räumlich modulierte Streulänge, die statt eines externen Potentials verwendet wird, oder die Einbeziehung langreichweitiger interatomarer Wechselwirkungen wie der Dipol-Dipol-Wechselwirkung, was oft zu neuen physikalischen Effekten führt [120]. Von theoretischer Seite ist darüber hinaus von Interesse, wie das kohärente Ein- und Auskoppeln der Atome auf mikroskopischer Skala verstanden werden kann. Ausgangspunkt dafür können

der Molekularfeldgrenzwert eines Bose-Hubbard-Systems [9, 23, 24], die Betrachtung des direkten kohärenten Auskoppelns des Kondensats aus einer Mulde [91] oder die Beziehung zu Mastergleichungen [89, 90] sein. Es ergeben sich zusätzlich mathematische Fragen wie der Wunsch nach einer Vorhersagbarkeit des Bruchs der $\mathcal{PT}$-Symmetrie bei Verstärkung des Gewinn- und Verlusteffekts. Dafür könnten die Störungsrechnungen für ein Oszillatorpotential [184–186] von hohem Wert sein. Ein Einblick in analytische Lösungen in einem System, das der hier verwendeten Gross-Pitaevskii-Gleichung ähnlich ist [187, 188], könnte bei der Beantwortung vieler mathematischer Fragen sehr hilfreich sein.

Die Untersuchung der thermodynamischen Eigenschaften von kleinen Edelgasclustern mit der gaußschen Näherungsmethode zeigt, dass eine Gaußfunktion mit einer festen Breitenmatrix für viele Anwendungen die Methode der Wahl ist. Die zugehörigen numerischen Rechnungen sind im Vergleich zu anderen verfügbaren Verfahren mit wesentlich geringerem Aufwand durchführbar, hinreichend genau in den Temperaturbereichen, in denen die interessanten physikalischen Effekte auftreten, und die Qualität ihrer Ergebnisse kann mit Hilfe der Korrekturen erster Ordnung aus einer erweiterten zeitabhängigen Störungsrechnung objektiv eingeschätzt werden, ohne ein Vergleichsverfahren hinzuziehen zu müssen. Die Methode ermöglicht ein Verständnis wichtiger grundlegender Fragen wie die Aufklärung der Dissoziation des $Ar_3$-Clusters in einem Schritt oder den Einfluss des künstlichen Potentials, das eingeführt wird, um die numerische Integration beherrschbar zu halten.

Nachdem die gaußsche Methode gezeigt hat, dass sie gute Näherungen quantenmechanischer Ergebnisse liefert, bietet sie sich an, weitere offene Fragen zu thermodynamischen Eigenschaften von Edelgasclustern anzugehen. Insbesondere sollte die Wahl des künstlichen Potentials zur Einschränkung des Integrationsgebiets überprüft werden, da die Ergebnisse für $Ar_3$ und $Ar_6$ andeuten, dass sie in früheren Rechnungen zu restriktiv ausgefallen sein könnte [52–54, 171]. Es könnte sein, dass eine Dissoziation der Cluster einsetzt, bevor die diskutierten strukturellen Umwandlungen auftreten. Dazu müssen die Betrachtungen aus dieser Habilitationsschrift auf Systeme mit deutlich höheren Dimensionen erweitert werden. Von besonderem Interesse sind die kürzlich betrachteten Cluster $Ar_{13}$ [176–178], $Ne_{13}$ [53] oder $Ne_{38}$ [54].

Die erweiterte zeitabhängige Störungsrechnung kann helfen, ungelöste Fragen in den Fällen zu beantworten, in denen klassische und semiklassische Rechnungen qualitativ unterschiedliche Resultate liefern und der Einfluss von Quanteneffekten überprüft werden muss. So sagen semiklassische Rechnungen für $Ne_{38}$ einen Grundzustand ohne feste Gitterstruktur voraus, was einer klassischen Rechnung widerspricht [56]. Weiterhin existiert die Reihenentwicklung auch für andere, numerisch aufwendigere gaußsche Näherungsverfahren [68, 172]. Es wäre interessant, die Qualität dieser Verfahren damit zu überprüfen und festzustellen, ob sie tatsächlich bei tieferen Temperaturen zuverlässige quantenmechanische Näherungswerte liefern.